Deposition of La-Mn-O and Nd-Mn-O Based Thin Films and Study of Their Electrical Transport and Magnetic Properties

A Thesis Submitted

By

Ranganadha Gopalarao T

Roll Number: 11612111

In Partial Fulfillment of the Requirements for the Award of the Degree of

Doctor of Philosophy in Physics

Department of Physics

Indian Institute of Technology Guwahati

Guwahati-781039, India

August 2017

TH-1726_11612111

TH-1726_11612111

Statement

The work contained in the thesis entitled "**Deposition of La-Mn-O and Nd-Mn-O Based Thin Films and Study of Their Electrical Transport and Magnetic Properties**" has been carried out by me under the supervision of Prof. S. Ravi, Department of Physics, Indian Institute of Technology Guwahati. This work has not been submitted elsewhere for the award of any degree.

21st August, 2017

(Ranganadha Gopalarao T)
Department of Physics
Indian Institute of Technology Guwahati
Guwahati – 781039, India

TH-1726_11612111

TH-1726_11612111

Certificate

It is certified that the work contained in the thesis entitled **"Deposition of La-Mn-O and Nd-Mn-O Based Thin Films and Study of Their Electrical Transport and Magnetic Properties"** by Mr. Ranganadha Gopalarao T, a PhD student of the Department of Physics, Indian Institute of Technology Guwahati for the award of the degree of *Doctor of Philosophy* has been carried out under my supervision. This work has not been submitted elsewhere for the award of any degree.

21st August, 2017

(S. Ravi)
Professor, Department of Physics
Indian Institute of Technology Guwahati
Guwahati – 781 039, India

TH-1726_11612111

TH-1726_11612111

TH-1726_11612111

Dedicated

to

My mother

TH-1726_11612111

TH-1726_11612111

TH-1726_11612111

Acknowledgments

I would like to express my sincere gratitude for enormous support of my guide, doctoral committee members, well-wishers, friends and family members to accomplish my doctoral thesis.

First of all, I would like to thank my thesis supervisor Prof. S. Ravi, for spending his valuable time on lot of discussions over the technical ideas to sort out the problems faced while doing the experiments, and for his assessment and insightful comments on my writing skills, that put me to accomplish the great task of writing this thesis. I couldn't even imagine a better advisor and mentor than him for creation of such a nice atmosphere to fulfil my Ph.D. thesis.

Besides my supervisor, I sincerely thank to my thesis monitoring committee members Prof. A. Perumal, Dr. Subhash Thota and Dr. M. Qureshi for their suggestions, thought provoked comments and encouragement during the presentations of my thesis work. I would like to thank Dr. D. Pamu for helping me to use the RF magnetron sputtering unit and its extension.

I am very much thankful to Head of the Department of physics, Prof. Poulose for his help in extending departmental facilities. I would like to thank former heads of department of physics Prof. S. Basu and Prof. S. Ravi for their cooperation during the tenure of my Ph.D. thesis. I am also thankful to all faculty members of Physics department. My special thanks go to Dr. Sidananda Sarma for helping me to carry out experiments and Mr. Basab Bijoy Purakayasthya for interfacing the instruments through LabView software. I am also thankful to other staff members of my department.

I am thankful to Central Instrumental Facility (CIF), IIT Guwahati, for enabling me to avail several sophisticated instruments to perform the experiments during my PhD tenure. Department of Science and Technology for facilitating Vibrating Sample Magnetometer and TTRAX III diffractometer are gratefully acknowledged.

TH-1726_11612111

I really thank my friends Dr. Murali Gedda, Dr. Santhosh Kumar, Dr. Subbarao and Dr. Ravi Kumar Birouju, Ramakrishna Madaka, Ravi kumar Patta and Bipul Deka for lots of discussions, arguments and technical help.

I thank my lab-mates Junmoni Barman, Bibuthi Dash, Pratap Behera and Akansha singh for their support and helpful nature in all scenarios. I am thankful to my seniors Dr. Tribedi Bora, Dr. Akhilesh Kumar Singh, Dr. Bhargab Deka, Dr. Padam Rajendar, Dr. Shyni P.C. I would like to thank my group members Dr. Mahesh, Anabil Gayan, Arnab Das, Raj kumar, Bhagaban Kishan, Anil Kumar, Srinivas Pattipaka, Camelia, Susmita, Anitha.

I thank my family for their strong support. I am sincerely thankful to my uncle V. S. Murty and my cousins Madhurima and Sai for their great motivation, support, suggestion and encouragement to achieve my desires.

Last but not the least, I am grateful to Indian Institute of Technology Guwahati and Ministry of Human Resource and Development for giving me the financial support to carry out the present thesis work. Department of Science and Technology, New Delhi and Board of Research in Nuclear Science Mumbai are acknowledged for financial support through research projects for various experimental facilities.

Lastly I would like to thank Almighty God who has given me the strength to believe my passion and pursue my dreams.

Ranganadha Gopalarao T

IIT Guwahati

TH-1726_11612111

Abstract

The electronic industry and our day to day electronic gadgets depend on semiconducting devices and whose properties depend on the type of charges (electrons or holes) and their concentration. In order to further improve the efficiency and the miniaturization of electronic devices, one more parameter i.e. the spin of the electrons is used as an additional tuning parameter. Devices incorporating all such three degrees (type, concentration and spin) of freedom are known as spin-electronic or spintronic devices. The ferromagnetic materials which can completely polarize the spin of the electrons play a major role in the above development. The ferromagnetic materials are already being used in memory devices such as hard drives, memory sticks, etc. The discovery of giant magneto-resistance (GMR) in the year 1988 by Albert Fert and Peter Grunberg has led to the increase of density of storage devices by several fold.

Subsequent to the discovery of GMR in multi-layered magnetic materials, colossal magneto-resistance was discovered by Jonker and Van Santen in bulk perovskite oxide materials of the type $R_{1-x}A_xMnO_3$ (Here, R = rare earths such as La, Nd, Pr etc., A = alkaline earth such as Ca, Ba, Sr etc.). These materials exhibit ferromagnetic and metal-insulator transitions due to Zener double exchange interaction across Mn^{3+} - O^{2-} - Mn^{4+} networks. Even though bulk samples are studied extensively, development of these materials in thin film form is essential for applications. Since thin film samples are very sensitive to nature of substrate, deposition conditions and post-deposition processing condition, etc. and hence a detailed work is needed to optimise the CMR films, for large T_C, colossal magneto-resistivity, etc. Therefore in an attempt to prepare best quality CMR films several authors have carried out the deposition of various CMR films by choosing appropriate substrate such that the lattice mismatch induced lattice strain is minimum, by varying substrate temperature and gaseous mixture during the deposition, by growing films of different thicknesses, etc..

Recently, a few authors have deposited hetero-structure thin films such as ferromagnetic and anti-ferromagnetic films in a bilayer or multilayer form to study the effect of interface coupling. The bilayer $La_{0.7}Sr_{0.3}MnO_3/SrRuO_3$ and $La_{0.7}Sr_{0.3}MnO_3/SrTiO_3$ are reported to show peculiar micro magnetic and electrical transport properties. Such change in electrical and magnetic properties are due to the manifestation of exchange coupling of the spins across their interfaces.

TH-1726_11612111

As mentioned above, the growth of $La_{0.7}Sr_{0.3}MnO_3$ and $La_{0.7}Ca_{0.3}MnO_3$ thin films by various techniques was extensively studied to attain their electrical and magnetic properties comparable to those of bulk counterpart. $Nd_{0.7}Sr_{0.3}MnO_3$ is one of the well-known CMR materials having T_C value around 250 K and moreover it contains a magnetic rare earth element. It would be interesting to study the interface effects of manganite thin films in a hetero structure configuration as a bilayer form of ferromagnetic and AFM or charge-ordered phases such as $Nd_{0.7}Sr_{0.3}MnO_3/Nd_{0.8}Na_{0.2}MnO_3$ and $La_{0.7}Sr_{0.3}MnO_3/LaFeO_3$. We have chosen RF-magnetron sputtering technique to deposit various manganite films as follows,

- $Nd_{0.7}Sr_{0.3}MnO_3$ films on 001-Al_2O_3 substrate by varying the post annealing temperature in the range of 700 ℃ to 900 ℃.
- $Nd_{0.7}Sr_{0.3}MnO_3$ films on 001-$LaAlO_3$ substrate by varying the film thickness in the range of 12-200 nm and by post annealing in air and oxygen atmosphere separately.
- $Nd_{0.7}Sr_{0.3}MnO_3$ films on 001-MgO substrate by varying the thickness in the range of 60-200 nm and by annealing them separately in air and oxygen environments.
- $Nd_{0.8}Na_{0.2}MnO_3$ films on 001-$LaAlO_3$ substrate by varying the thickness in the range of 30 nm- 100 nm.
- Bilayer of $Nd_{0.7}Sr_{0.3}MnO_3/Nd_{0.8}Na_{0.2}MnO_3$ on 001-$LaAlO_3$ substrate for different thickness of $Nd_{0.7}Sr_{0.3}MnO_3$ layer.
- Bilayer of $La_{0.7}Sr_{0.3}MnO_3/LaFeO_3$ on (001)-$LaAlO_3$ substrate for different thicknesses of $La_{0.7}Sr_{0.3}MnO_3$ layer.

The above samples were characterised by using X-ray diffractometer (XRD) and Raman spectrometer to determine the phase purity and structural distortion, atomic force microscope to study surface morphology and roughness, and energy dispersive spectrometer (EDS) for composition analysis. To understand the magnetic properties as a function of temperature and field, Lakeshore make vibrating sample magnetometer of model no: 7410 is used. The electrical resistivity measurements were carried out by using the standard four probe method and the magneto-resistance was measured by using Quantum Design physical properties measurement system.

TH-1726_11612111

Chapter 1 presents the literature survey of the perovskite manganites, and their structural behaviour, functional properties like ferromagnetic metallic transition, charge ordering and colossal magneto-resistance etc. The role of crystal structure, crystal field effect, Jahn-Teller distortion, electron–phonon coupling etc. on the functional properties are discussed. The reported magnetic as well as electrical transport properties and proposed mechanism in various manganites are also presented. Perovskite thin films and various factors affecting their electrical and magnetic properties are also reviewed.

Chapter 2 discusses the various experimental techniques followed in sample preparation, thin film fabrication, their characterisation and various physical measurements and analysis. Bulk targets were synthesised by solid state reaction and sol gel method. Furthermore, these target samples were utilised to deposit thin films by using Radio-frequency (RF) magnetron sputtering. The crystal structure and its phase purity was confirmed by Rigaku TTRAX III X-ray diffractometer and Raman spectrometer. Temperature variation of electrical resistivity was measured with standard four probe technique, and magnetic properties as a function of temperature and magnetic field were recorded by using Lakeshore make vibrating sample magnetometer with model no:7410. Temperature variation of magneto-resistance measurement is carried out by using Quantum Design physical properties measurement system.

Chapter 3 deals with preparation of $Nd_{0.7}Sr_{0.3}MnO_3$ (NSMO) thin films by varying the annealing temperature, substrate and film thickness. NSMO target was prepared by using the solid state reaction method in single phase form with Pbnm space group. It exhibits a ferromagnetic transition at 225 K and metal-insulator transition at 185 K. This target was used to grow the NSMO thin films by using RF-magnetron sputtering. NSMO film with a thickness of 120 nm was grown on (001)-Al_2O_3 substrate. Here, the substrate temperature was kept at 400℃ and the Ar/O_2 flow rate was fixed at 3:1 ratio. During the deposition the working pressure was maintained at 4.3×10^{-2} mbar. A constant RF power of 50 Watts was maintained throughout the deposition. After deposition, the film was separated into three batches and post- annealed at three different temperatures (700 ℃, 800 ℃ and 900 ℃) in air. All films are found to be in single phase polycrystalline form having Pbnm space group. We observed that the strain gets relaxed with increase in annealing temperature and this is clearly noticed by the Raman spectra collected at room temperature. All films exhibit ferromagnetic transition (T_C) as well as metal-insulator transition (T_{MI}). The T_C is found to

TH-1726_11612111

increase in annealing temperature and on the other hand the T_{MI} values are found to shift towards lower temperature.

In order to obtain the improved and good quality films, 200 nm NSMO films were grown on different substrates namely (001)-Al_2O_3 (ALO), (001)-MgO and (001)-$LaAlO_3$ (LAO). The deposition parameters were kept same as described above and the post-deposition annealing was carried out at 700 ℃ in air and oxygen gas environments. In both cases, we have observed the metal – insulator and ferromagnetic transitions. Compared to air annealed films, mostly the oxygen annealed films are found to show higher ferromagnetic transition temperatures. Moreover the NSMO films on LAO substrate have shown better ferromagnetic and metal-insulator transition temperature, i.e. around 192 K. The obtained magnetic and electrical parameters were explained in terms of substrate induced lattice strain and oxygen vacancies created during the annealing process in air and oxygen environments.

We have studied the thickness variation of NSMO thin film on LAO substrate. The effect of strain is correlated with electrical and magnetic properties of the films. NSMO thin films were deposited on *LAO* substrate with different film thickness of 12, 25, 30, 40, 50, 60 and 120 nm. These films were post-annealed in oxygen environment at 700 ℃ for an hour. All films show epitaxial like growth along the substrate orientation (001). Out-of-plane lattice parameter is found to decrease with increase in the film thickness and the lattice strain gets relaxed at higher thickness. The temperature variation of magnetization was measured for H = 2kOe to study the effect of thickness on magnetic properties. Values of T_C and T_{MI} are found to increase with increase in film thickness for 12 to 60 nm and for further increase in film thickness, induced strain gets relaxed as a consequence no appreciable change in T_C is observed. In this series, we have performed the magneto-resistance measurement at an applied field of 5 Tesla for the films of thicknesses 30 nm, 40 nm and 50 nm. The maximum magneto-resistance is found to be -96 %.

Chapter 4 presents the deposition of the bilayer $Nd_{0.7}Sr_{0.3}MnO_3/Nd_{0.8}Na_{0.2}MnO_3$ thin films on LAO substrate and their characterisation. $Nd_{0.8}Na_{0.2}MnO_3$ (NNMO) target was prepared by using solid state reaction method. The prepared target was used to deposit NNMO single layered thin films on the LAO substrate with the thickness of 30, 40, 50, 75 and 100 nm. All films (excluding 30 and 40 nm films) exhibit ferromagnetic transition around 75 K and the charge ordering around 170 K.

TH-1726_11612111

The bilayer films of NSMO/NNMO were deposited by using the optimised deposition conditions on 001 – LAO substrate. Here the bottom NNMO layer thickness was fixed at 120 nm and the top NSMO layer thickness was varied from 12 nm to 100 nm. For a comparison we have also grown separately the single layer NNMO and NSMO films of thickness 120 nm and 80 nm respectively on LAO substrate. The ferromagnetic transition temperature of single layer NNMO and NSMO are found to be 75 K and 185 K respectively. The T_C values of bilayer films are found to increase with increase in thickness of NSMO layer due to the influence of NNMO layer.

Chapter 5 presents the preparation of bilayer of $La_{0.7}Sr_{0.3}MnO_3$ (LSMO)/$LaFeO_3$ (LFO) thin films on 001 – *LAO* substrate The target of LSMO and LFO were prepared by using sol-gel method and they were well characterised. Initially, individual single layers of LSMO and LFO films were deposited on LAO substrate. Magnetisation and electrical resistivity as a function of temperature show that the LSMO film exhibits ferromagnetic transition and metal-insulator transition around 348 K. Furthermore, influence of thickness of ferromagnetic layer (LSMO) on the characteristic properties of the bilayer are investigated by varying the thickness from 30 to 200 nm. The electrical resistivity measurement as a function of temperature shows the presence of metal-insulator transition. The metallic region of each sample below T_{MI} is analysed in terms of electron-electron scattering as well as weak localization mechanism. In some of the temperature region, the data follow electron-Magnon scattering mechanism. The ferromagnetic and T_{MI} transitions are shifted to higher values with increase in film thickness.

Chapter 6 presents the overall summary of results and conclusions on La-Mn-O and Nd-Mn-O based single and bilayer films. $Nd_{0.7}Sr_{0.3}MnO_3$ films of different thicknesses have been grown on various substrates such as (001)-Al_2O_3, (001)-MgO and (001)-$LaAlO_3$ by varying the post annealing temperature and environment. Epitaxial like films of NSMO were obtained especially on (001)-$LaAlO_3$ substrate. Lattice relaxation and better magnetic and electrical properties are observed at higher thickness of films or under oxygen annealing condition. The maximum magneto-resistance upto -96% was observed. We have successfully grown bilayer of ferromagnetic and antiferromagnetic films such as $Nd_{0.7}Sr_{0.3}MnO_3$/$Nd_{0.8}Na_{0.2}MnO_3$ and $La_{0.7}Sr_{0.3}MnO_3$/$LaFeO_3$. The ferromagnetic resonance study exposed the presence of distribution in ferromagnetic interaction due to the lattice strain and surface pinning behaviour etc. The ferromagnetic resonance peak is

TH-1726_11612111

found to shift towards the lower field as the thickness of the film is increased. A brief write up about future scope of research in this area is also presented.

TH-1726_11612111

List of Abbreviations used in this Thesis

AFM Antiferromagnetic

CMR Colossal Magneto-Resistance

CI Charge Ordered Insulator

CO Charge Ordering

DE Double Exchange

EDS Energy Dispersive Spectroscopy

ESR Electron Spin Resonance

EPR Electron Paramagnetic Resonance

FC Field Cooled

FI Ferromagnetic Insulator

FM Ferromagnetic

FMR Ferromagnetic Resonance

GMR Giant Magneto-Resistance

JT Jahn-Teller

MR Magneto-Resistance

MI Metal Insulator

PM Paramagnetic

PPMS Physical Property Measurement System

PLD Pulsed Laser Deposition

RF Radio Frequency

RMS Root Mean Square

SE Super Exchange

TMO Transition Metal Oxide

VRH Variable Range Hopping

VSM Vibrating Sample Magnetometer

XRD X-ray Diffraction

ZFC Zero Field Cooled

TH-1726_11612111

Table of contents

Page No.

Contents

TH-1726_11612111

TH-1726_11612111

TH-1726_11612111

List of Figures

Page No.

Chapter 1

TH-1726_11612111

Chapter 2

Chapter 3

TH-1726_11612111

TH-1726_11612111

Chapter 4

TH-1726_11612111

TH-1726_11612111

Chapter 5

TH-1726_11612111

List of Tables

Page No.

TH-1726_11612111

TH-1726_11612111

Chapter 1
Introduction

TH-1726_11612111

TH-1726_11612111

Chapter 1

Electronic properties of solids play a major role in the application of microelectronics, magnetic data storage, etc. Electronic properties of 3d transition metal oxides are yet be understood in detail. Unforeseen and highly interesting phenomena have been discovered in some oxides of 3d metals in the last four decades: high temperature superconductivity in cuprates [1-3], colossal magneto-resistance in manganites [4-6], high spin polarisation of conduction electrons in CrO_2, etc. All these phenomena are based on the strong intereaction between charge carriers, lattice, spin and orbital moment of electrons, etc. Colossal magneto-resistive (CMR) oxides, an amazing class of materials are being the subject of research interest for more than two decades, due to their fascinating electrical and magnetic properties and, applications in magnetic recording and spintronics devices [7-10]. The large negative magneto-resistance or the drastic decrease in the electrical resistivity in the presence of an applied magnetic field is known as CMR.

The CMR behaviour is observed in hole-doped manganites with perovskite structure. Here, the prescence of Mn ions in mixed valency play a major role. The above manganites are described by the general chemical formula $R_{1-x}A_xMnO_3$ (R = rare earth cations such as La, Nd, Pr etc., and A= divalent alkaline earth cations such as Ca, Sr, Ba etc.). These materials exhibit the interesting physical properties such as metal-insulator and ferromagnetic to paramagnetic transitions alongwith colossal magneto-resistance in the vicinity of the above transition temperature. These complex metal oxides had been studied way back in 1950 for their interrelated structural, magnetic and electrical transport properties. The early works on $La_{1-x}A_xMnO_3$ compounds with A = Sr, Ca and Ba were carried out by Jonker *et al.* [11] and Van Santen *et al*. [12, 13]. Both end members of the series (x = 0, x = 1) behave as anti-ferromagnetic insulator. However for *x* close to 0.3, ferromagnetism was observed. They found that the onset of ferromagnetic behaviour was coupled with a sharp decrease in electrical conductivity. Zener *et al.* [14] proposed the double exchange interaction in Mn^{3+} - O^{2-} - Mn^{4+} networks to explain the ferromagnetic metallic behaviour. In addtion to Zener – double exchange ferromagnetic interaction, other models such as electron – phonon coupling, etc. have been reported to quantitatively explain the above transition temperature [15].

In this chapter, we present the review of crystal structure of CMR materials, fundamentals of magnetism, electrical transport properties and the experimental work on various manganites with a special emphasize on single layer and multilayer magnetic thin films.

TH-1726_11612111

Chapter 1

1.1 Crystal Structure

The rare earth manganites, $RMnO_3$ generally crystalize in perovskite structure. The general chemical formula of an ideal perovskite is ABO_3, where A atoms occupy the corner positions (0,0,0), the B atoms occupy the body centered position i.e., (1/2,1/2,1/2) and the oxygen atoms occupy the face centered positions (1/2,1/2,0), as shown in Fig.1.1. The structure of $R_{1-x}A_xMnO_3$ oxide is close to that of the cubic perovskite.

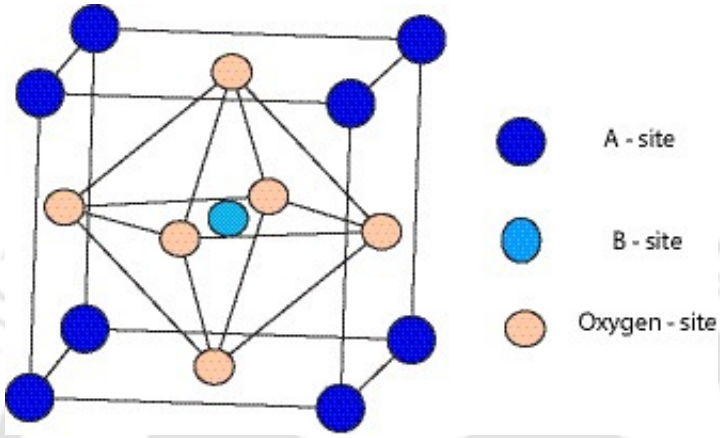

Figure 1.1: An ideal cubic perovskite structure of manganite with general formula ABO_3.

Among all manganite materials, $LaMnO_3$ is widely studied and it forms close to ideal cubic perovskite structure. Here, the Mn is at the center of MnO_6 octahedra with a typical Mn – O – Mn bond angle of 180°. The Mn – O bond length is also found to be equal in all directions. Goldschmith introduced a parameter known as tolerance factor that gives information about the stability of the structure [16]. It is related to the average ionic radii of A and B – site ions and the oxygen ions [16-18]. It is given as,

$$t = \frac{d_{A-O}}{\sqrt{2}d_{Mn-O}} = \frac{(<r_A>+<r_O>)}{\sqrt{2}(<r_{Mn}>+<r_O>)} \quad (1.1)$$

Here, $< r_A >$, $< r_O >$ and $< r_{Mn} >$ are the average ionic radius of rare earth, oxygen and Manganese ions respectively. According to this relation, the ideal cubic structure possesses a tolerance factor value of 1. The tolerance factor of rhombohedral and orthorhombic structures lie in the range of $0.93 < t < 1$ and $t < 0.93$, respectively. The symmetry of crystal structure reduces from cubic to rhombohedral or orthorhombic as a result of tilting and stretching of MnO_6 octahedra. The perovskite structure is stable when the *t* value lies within 0.89 to 1.02. Hwang *et al.* [19] have given a clear picture about the structural properties of manganites, through a phase diagram for temperature versus tolerance factor

TH-1726_11612111

(t) for various A site cations size <r_A>. The phase diagram shows three dominant regions: a paramagnetic insulator at high temperature, a low temperature ferromagnetic metallic region for large tolerance factor above 0.91 and a low temperature ferromagnetic insulator (FMI) behaviour for small tolerance factor. Zhou *et al.* [20] have also investigated the influence of the tolerance factor t in Curie temperature, resistivity, coercive field and magneto-resistance of manganites. They observed that large difference between the ionic radii of the A-site cations is detrimental for magneto-transport properties.

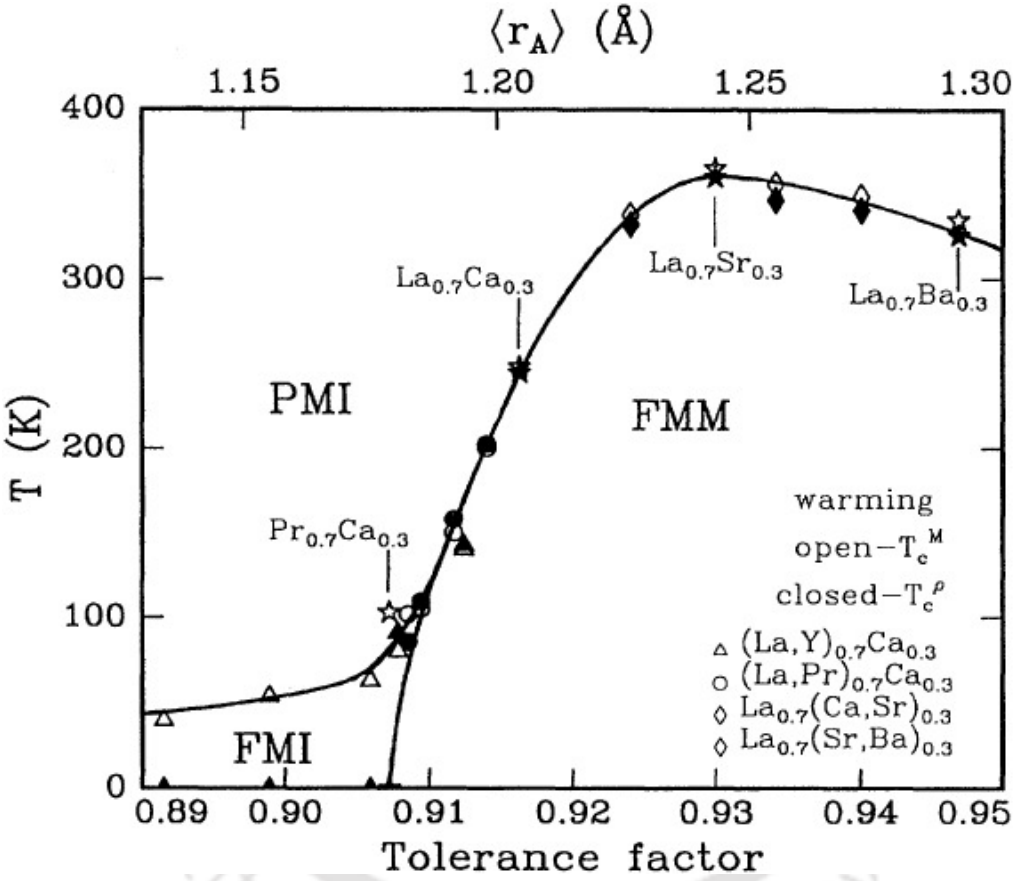

Figure 1.2: Phase diagram of temperature versus tolerance factor for the system $R_{0.7}A_{0.3}MnO_3$, where R is a trivalent rare earth ion and A is a divalent alkaline earth ion. Here, open symbols denote T_c^M measured at 100 Oe. Closed circles denote T_c^ρ.[Reproduced from ref. [19]]

The cubic perovskite structure may transform into orthorhombic or rhombohedral structure due to lattice distortion. One of the possible origins of the lattice distortion is the deformation of MnO_6 octahedra arising from the Jahn–Teller effect. Another lattice deformation comes from the coordinated tilting of MnO_6 octahedra. Typical crystal srtructure of $R_{1-x}A_xMnO_3$ compounds with orthorhombic symmetry is shown in Fig.1.3(a). The unit cell parameters are given in terms of lattice constant of cubic cell a_p. The lattice parameters of the orthorhombic cell with Pnma space group symmetry can be

TH-1726_11612111

approximately written as $a \approx c = \sqrt{2}\, a_p$ and b = $2a_p$. In Pbnm space group, the same parameters can be written as $a \approx b = \sqrt{2}\, a_p$, $c = 2a_p$. The typical lattice parameters of (La, Ca)MnO_3 system is $a = 5.462$ Å, $b = 5.469$ Å and $c = 7.737$Å. Here, the Mn – O – Mn bond angle is in the range of 155° to 160°. Typical rhombohedral crystal structure of $R_{1-x}A_xMnO_3$ is shown in Fig. 1.3(b). Here also, each Mn ion is octahedrally coordinated with O ions. Here the MnO_6 octahedra rotates such that they are along the three fold rotational axis of the ideal cubic structure and it gives rise to rhombohedral symmetry. Unlike the case of orthorhombic cell, there is no buckling of MnO_6 octahedra and hence the Mn-O bond lengths are identical in all three directions.

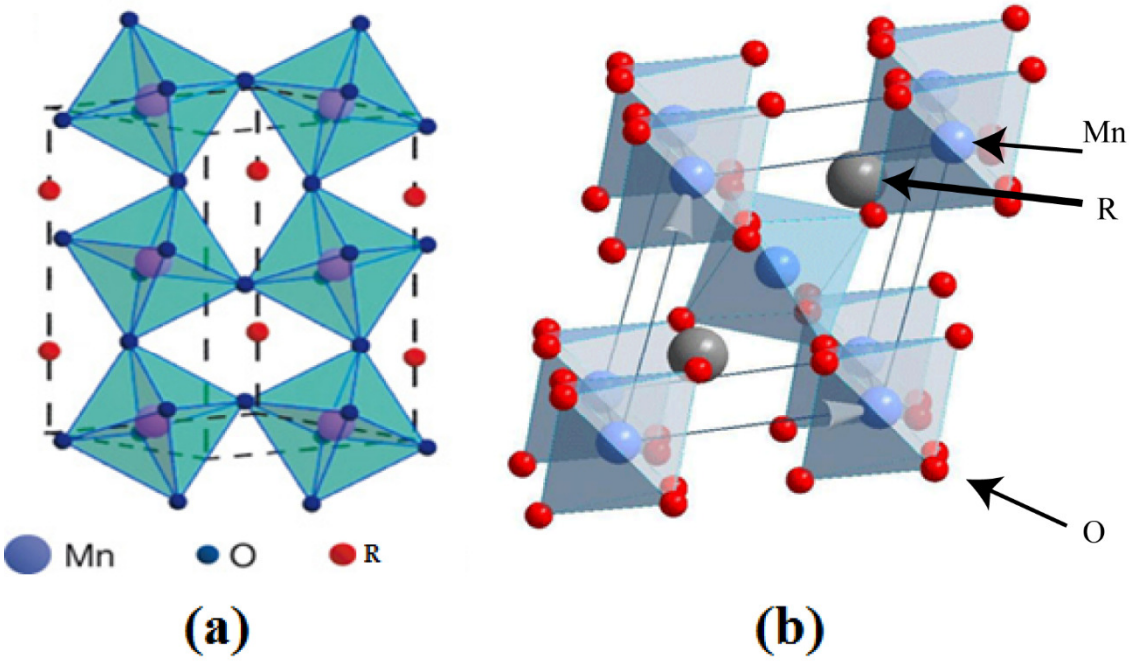

Figure 1.3: Structures of distorted perovskites of manganite: (a) orthorhombic and (b) rhombohedral.

1.2 Magnetism in Manganites

1.2.1 Crystal Field and Jahn – Teller Effect

Perovskite manganites exhibit a complex interplay between the spin, charge, orbital and lattice degrees of freedom, which strongly depend on the site of occupancy of the d orbitals. The basic building blocks of the manganites are the MnO_6 octahedra. Here each Mn ion is under the influence of crystal field due to other surrounding atoms in the crystal and it

TH-1726_11612111

clearly influence the way in which electrons are distributed in Mn – 3d shell. The d-shell electronic structure and the degeneracy states of the shells can be explained as follows.

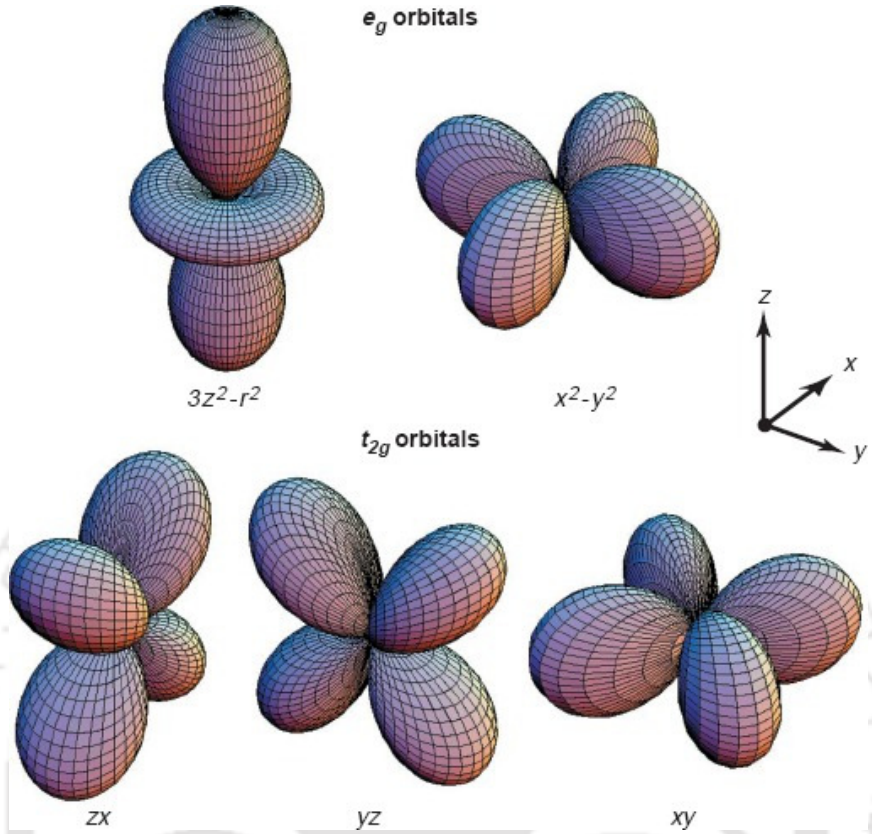

Figure 1.4: Five d orbitals. In the cubic crystal field, this fivefold degeneracy is lifted to two e_g orbitals ((x^2- y^2) and ($3z^2$- r^2)) and three t_{2g} orbitals ((xy), (yz) and (zx)). [Reproduced from the ref [21]].

An isolated Mn^{3+} ion contains four 3d – electrons in five degenerate state. In cubic crystal the degeneracy is lifted by splitting the five 3-d orbital into three t_{2g} and two e_g orbitals as a result of crystal field. The t_{2g} triplet consists of the d_{xy}, d_{yz} and d_{zx} orbitals and the e_g doublet consists of the $d_{x^2-y^2}$ and $d_{3z^2-r^2}$ orbitals. These d orbitals are shown in Fig.1.4. These d-shells form a strong hybridisations by sharing of electrons under the influence of Coulomb interaction with the 2p shell of O-ions. In the case of MnO_6 octahedral coordination in manganites, the e_g - states are lifted over the t_{2g} - state and this is shown in Fig.1.5 [22]. The energy difference between t_{2g} and e_g levels due to crystal field splitting (CFS) for $LaMnO_3$ is approximately 1.5 eV. Spin of each of four electrons in 3d-shell of Mn^{3+} aligns parallel to each other as per Hund's first rule. This results in total spin

TH-1726_11612111

of Mn^{3+} and Mn^{4+} as 2 and 3/2 respectively and their magnetic moments are $4\mu_B$ and $3\mu_B$, respectively.

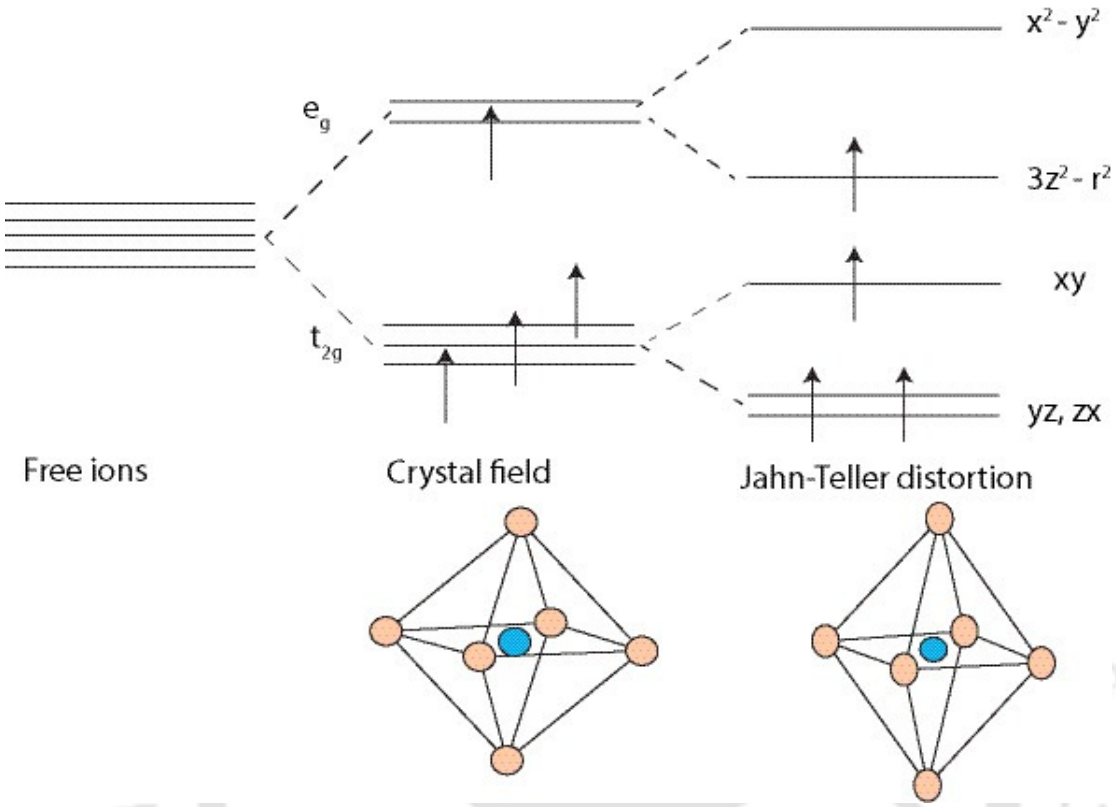

Figure 1.5: 3d - orbitals of Mn^{3+} ion under crystal field and Jahn – Teller distortion.

In addition to crystal field effect some of the ions undergo Jahn – Teller distortion to reduce the overall energy of the system. The Jahn-Teller theorem essentially states that "any non linear molecule with a degenerate electronic state will undergo a geometrical distortion that removes the degeneracy which results in reduction in overall energy of the species".

In manganites, the degeneracy in the $Mn^{3+}O_6$ octahedral are energetically unstable and as a result it tends to distort to reduce the total energy of the system. As a consequence, lifting of degeneracy of the e_g levels is observed. The degree of distortion is determined by the competition between the gain in the energy due to the e_g splitting and the increase of the elastic energy associated to the lattice distortion itself. If the above distortion leads to elongation of MnO_6 along the z-axis, the crystalline field has no more a cubic symmetry around the Mn ion, and the energies of the $d_{x^2-y^2}$ and d_{xy} orbital increase, because they become closer to the 2p - oxygen orbitals. On the contrary, the energy of $d_{3z^2-r^2}$, d_{xz} and

TH-1726_11612111

d $_{yz}$ orbitals decreases, because they move away from the O – 2p orbitals. The distorted system has a lower electronic energy and a higher elastic energy such that the gain in electronic energy is greater than the loss in elastic energy. This distortion is called as Jahn -Teller effect. The JT effect is pronounced when odd number of electrons occupy the e_g state i.e. four electrons in the Mn^{3+} state. On the other hand Mn^{4+} ion is Jahn – Teller inactive due to empty e_g state.

1.2.2 Exchange Interactions

The magnetic properties of manganites are governed by the various exchange interactions between the Mn ions. Exchange interactions are the source of several long range magnetic ordering. Although the consequence of exchange interactions is magnetic in nature but the primarily cause of such interactions has electronstatic origin. If the electrons of nearest neighbour atoms interact directly it is known as direct exchange inteaction and if they interact through a non-magnetic inermediate ion, it is called indireact exchange interaction. However, as far as the manganites are concerned, the indirect exchange interaction is of great relevance because the Mn ions are bonded through O ions in the lattice. In $LaMnO_3$ compound, Mn is mostly in Mn^{3+} state and behaves like Mott-insulator. The super exchange interaction is Mn^{3+} - O^{2-} - Mn^{3+} networks is antiferromagnetic in nature and hence the the parent compound $LaMnO_3$ exhibits A-type anti-ferromagnetic structure. In this magnetic structure, the magnetic ions couple ferromagnetically within the lattice plane but the the neighbouring planes are coupled anti-parallel to each other leading to net antiferromagnetism. The detailed discussion on various exchange interactions are given as follows.

Double Exchange Interaction

Double exchange interaction is an indirect magnetic exchange interaction which is occurred due to the transfer of 3d electrons of transition elements through a nonmagnetic ion like oxygen. This was first proposed by Zener in 1951 and is named as Zener double exchange interaction. The hopping of conducting electron takes place from 3d shell of one ion to 3d shell of another ion, if their core 3d electrons are aligned parallel to each other. In the DE process, two simultaneous transfer of electrons takes place in Mn^{3+}- O^{2-} - Mn^{4+} networks. Here, when core spins of both Mn^{3+} and Mn^{4+} ions are aligned parallel to each other, the e_g electron from Mn^{3+} ion transfers to O^{2-} ion and simultaneously an electron of same spin alignment gets transferred from O^{2-} to adjacent Mn^{4+} ion. At the end of the

TH-1726_11612111

process the network becomes Mn^{4+}- O^{2-} - Mn^{3+}, i.e the position of Mn^{3+} and Mn^{4+} gets interchanged. This process in shown in Fig. 1.6(a).

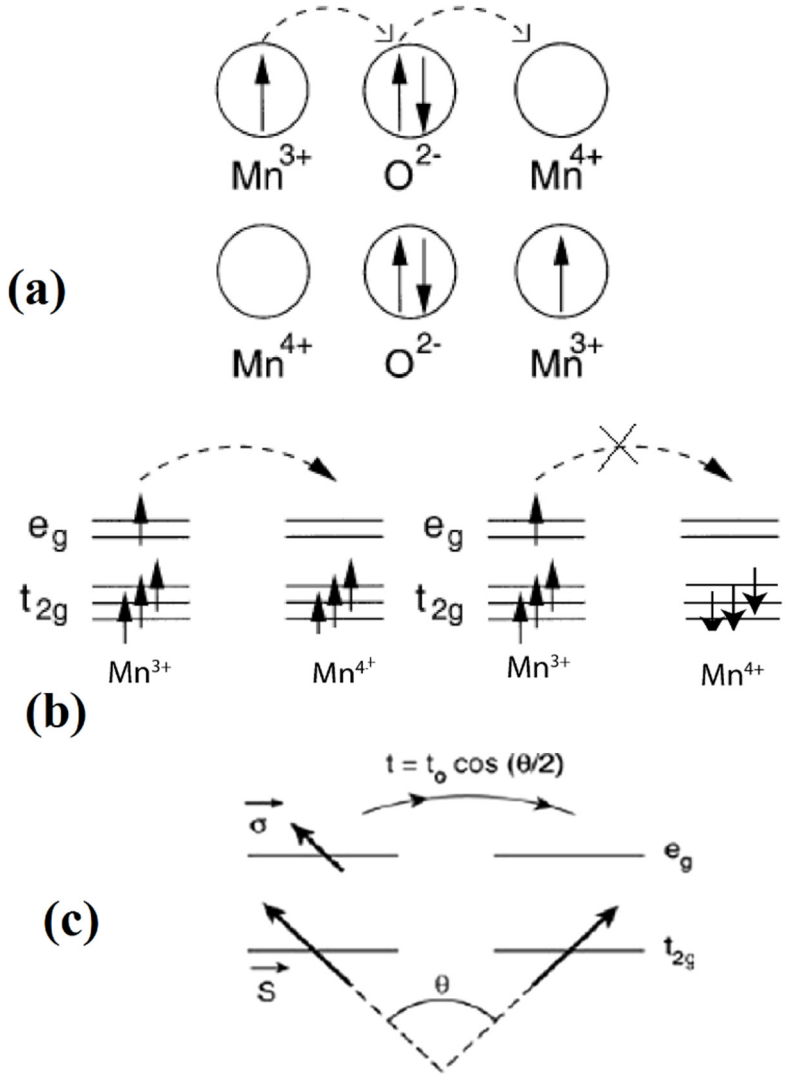

Figure 1.6: Schematic diagram of double exchange interaction across two Mn ions through an oxygen ion.

Super Exchange (SE) Interaction

Super exchange (SE) interaction is one of the indirect exchange interactions, where two magnetic ions interact through a non – magnetic intermediate ion whose electronic orbital overlap with each other. This occurs in ionic solids between two homo-valent magnetic ions through the occupied O – 2p orbital. This exchange phenomenon was first discovered by Goodenough [23] and Kamnamori [24]. In their articles, they have

TH-1726_11612111

demonstrated the origin of ferromagnetic and anti-ferromagnetism. SE interaction explains the magnetic properties as well as insulating behaviour in the transition metal oxides.

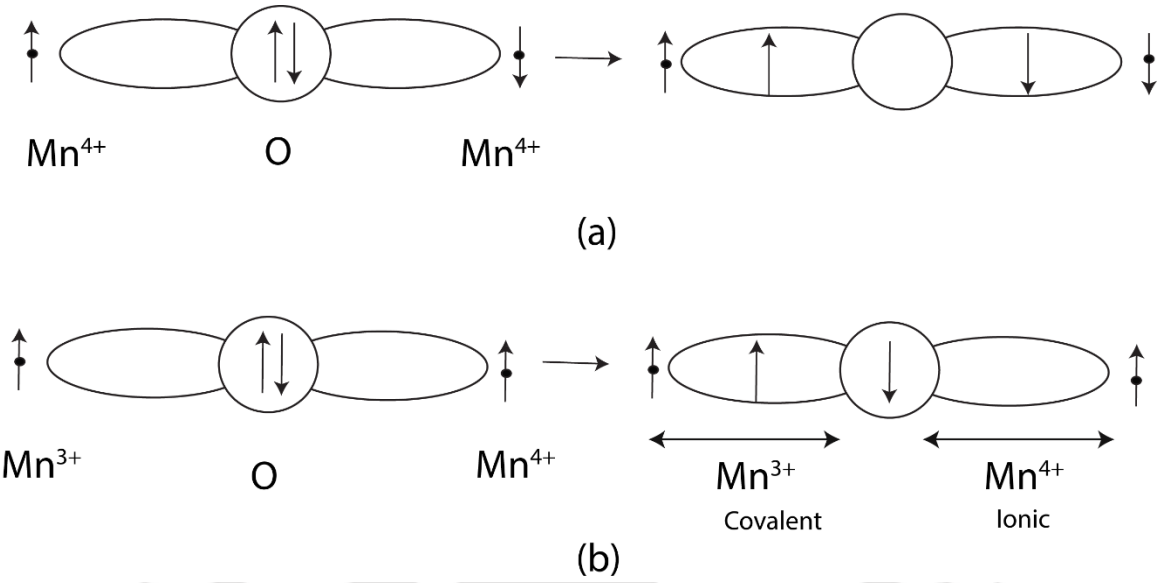

Figure 1.7: Schematic arrangement of spins and orbitals in (a) anti-ferromagnetic super exchange interaction (b) ferromagnetic super exchange interaction in Mn – O – Mn network.

SE interaction favours the anti-ferromagnetic behaviour among two iso-valent Mn ions through the O – 2p orbital. Let two Mn^{4+} ions form a chain arrangement with oxygen as an intermediate ion as shown in Fig.1.7(a). Here unoccupied 3d states of Mn^{4+} ions are overlapped with O-2p orbital. Two spins of oxygen are anti-parallel to each other, these spins are shared and spent some time on each of the unoccupied 3d-orbital of Mn^{4+} ions. Thus it creates bond formation on both sides of oxygen ion due to the hybridization of Mn^{4+} ions. This process leads to a net AFM interaction as shown in Fig.1.17(a). Similar AFM SE interaction is observed in Mn^{3+}- O^{2-} - Mn^{3+} networks.

Goodenough [23] descibed the SE interaction of Mn – O – Mn leads to ferromagnetic behaviour, if one of the Mn – O bond is covalent and other one is ionic, as shown in Fig.1.7(b). Below the Curie temperature, the covalent bond becomes semi covalence (that makes bonding between the parallel spins) and the other electron of O^{2-} ion remains as a single electron.

The Zener double-exchange interaction only explains the transport properties of manganites qualitatively. Millis *et al.* demonstrated that the electron - phonon coupling due to the dynamic Jahn - Teller distortion and Hund's coupling, play an important role for the observed FM properties of manganites [15].

TH-1726_11612111

1.2.3 Magnetic Structure

The magnetic structure represents the magnetic spins arrangement and their association with adjacent spins in the magnetic unit cell. Here volume of the magnetic unit cell is different from the volume of a crystal in a unit cell. Analysis of neutron diffraction pattern generally reveals complete magnetic structure of any magnetically ordered material. Wollan and Koehler [25] carried out the extensive neutron diffraction study to work out the magnetic structure (phase diagram) of $La_{1-x}Ca_xMnO_3$ in the entire composition range. Wollan and Koehler (1955) were among the first to use neutron scattering technique to study magnetism in materials. They found that in addition to FM phase, many other interesting anti-ferromagnetic phases were also present in manganites. Some of the interesting antiferromagnetic structures are A, C and G types and the B-type is of ferromagnetic in nature. They are shown in Fig.1.8.

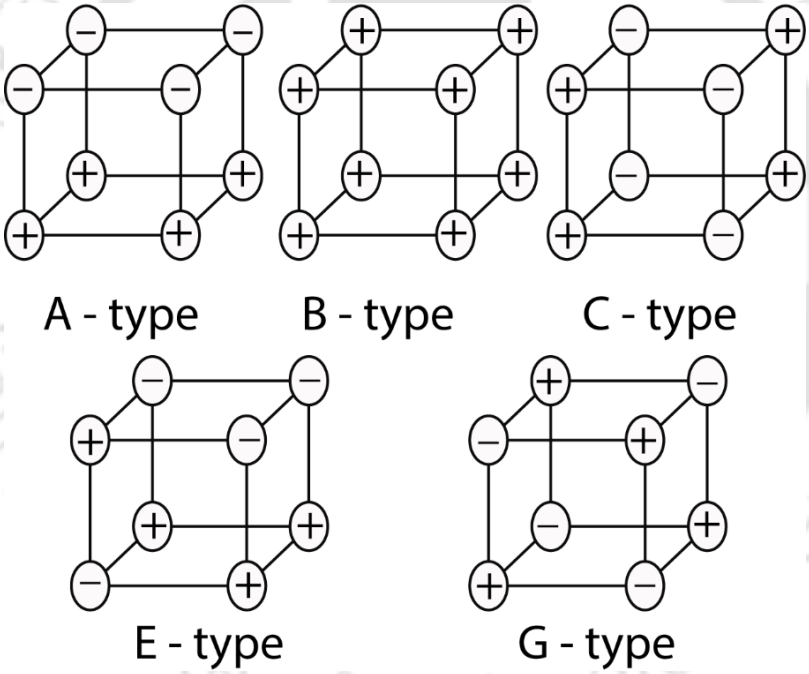

Figure 1.8: Different types of magnetic structure.

A-type magnetic structure generates the anti-ferromagnetic interaction, where the magnetic spins are arranged parallel to each other in (001) plane but the spins in alternative planes are facing opposite to each other. In managanites, $LaMnO_3$ compound exhibits A-type structure. In the case of B-type structure, the six nearest neighbouring magnetic ions are ferromagnetically coupled and gives rise to net FM. In C-type structure, the spins within the planes of (101) and $(\bar{1}10)$ are aligned parallel to each other producing a ferromagnetic interaction within the plane but with an overall antiferromagnetic interaction. In G-type

TH-1726_11612111

magnetic structure, each ion is antiferromagnetically aligned and coupled with six nearest neighbours. Therefore, the periodic atomic arrangement with up and down spin is observed. In E-type magnetic structure, the spins of neighbouring planes along the z -axis are coupled antiferromagnetically, but within the plane, out of four spins three spins are aligned in one direction and the forth one is in opposite direction.

Among them, the most exotic spin arrangement is the CE-type state, which is a mixture of the C phase with the E phase. This CE type structure is also the first evidence of charge ordering and mixed phase (phase separation) tendencies in the manganites. Further progress came somewhat later when the group at Manitoba grew a high quality milli-meter long single crystal of another interesting manganite, (La, Pb)MnO_3 [26]. Jirak *et al*. [27] and Pollert *et al.* [28] studied the structure and magnetic properties of another very popular manganite (Pr, Ca)MnO_3 by X-ray and neutron diffraction techniques. They have also observed charge-ordered phases which are totally different from the ferromagnetic phases of other manganites [27].

1.2.4 Charge - Ordering in Manganites

A fascinating phenomenon of charge ordering (CO) is found to occur in various transition metal oxides (TMOs) wherein electrons become localized due to ordering of cations of different charges (oxidation states) on specific lattice sites. Such ordering generally localizes the electrons in the material, rendering it insulating or semiconducting. This phenomenon of charge ordering (CO) is well known in Fe_3O_4 (magnetite), which undergoes a disorder-order transition accompanied by a resistivity anomaly, popularly known as the Verwey transition, at 120 K. Charge ordering (CO) has been found to occur in a few other TMOs [29, 30] as well, but the evidence of CO in doped rare earth manganites is overwhelming due to the discovery of colossal magneto-resistance and other interesting properties. This peculiar ordering phenomenon is observed by the special arrangement and the interaction of charge, orbital and spins of electrons. The first evidence of CO in doped manganites was observed by Wollan and Koehler [25] through neutron diffraction. They found the CO in $La_{1-x}Ca_xMnO_3$ system for x = 0.5. The charge exchange type anti-ferromagnetic structure causes the CO, when the magnetic spins of Mn^{3+} and Mn^{4+} ions are in a ratio of 1 : 1. The Mn ions are periodically arranged in alternative sites, such that they form a zigzag chain of Mn^{3+} and Mn^{4+} ions and this is shown in Fig.1.9. The intra-chain magnetic moment of Mn^{3+} and Mn^{4+} ions show ferromagnetic trend, while all the neighbouring chains are antiferromagnetically ordered in ab-plane. A similar arrangement

TH-1726_11612111

also takes place in the direction normal to the ab-plane. Three dimensional schematic diagram of charge, orbital and spin ordering in CE-type AFM structure is shown in Fig.1.9(b). Here the Mn^{3+} sublattice represents the electron density distribution and the Mn^{4+} sublattice represents as a dot. Electron diffraction studies of charge ordering in $La_{0.5}Ca_{0.5}MnO_3$ was reported by Cheng and Cheong [31]. Here, the coulomb interaction dominates the kinetic energy of the electrons to form long range CO state. The energy scale of the CO is around 0.5 - 1.0 eV and this is comparable to the unscreened bare nearest neighbour coulomb repulsive. In addition, there exists an orbital degree of freedom of the e_g electrons in Mn^{3+} ions. This orbital ordering can lower the electronic energy through the Jahn–Teller mechanism. Therefore, there exists orbital ordering (OO) in addition to charge ordering in mixed-valent manganites.

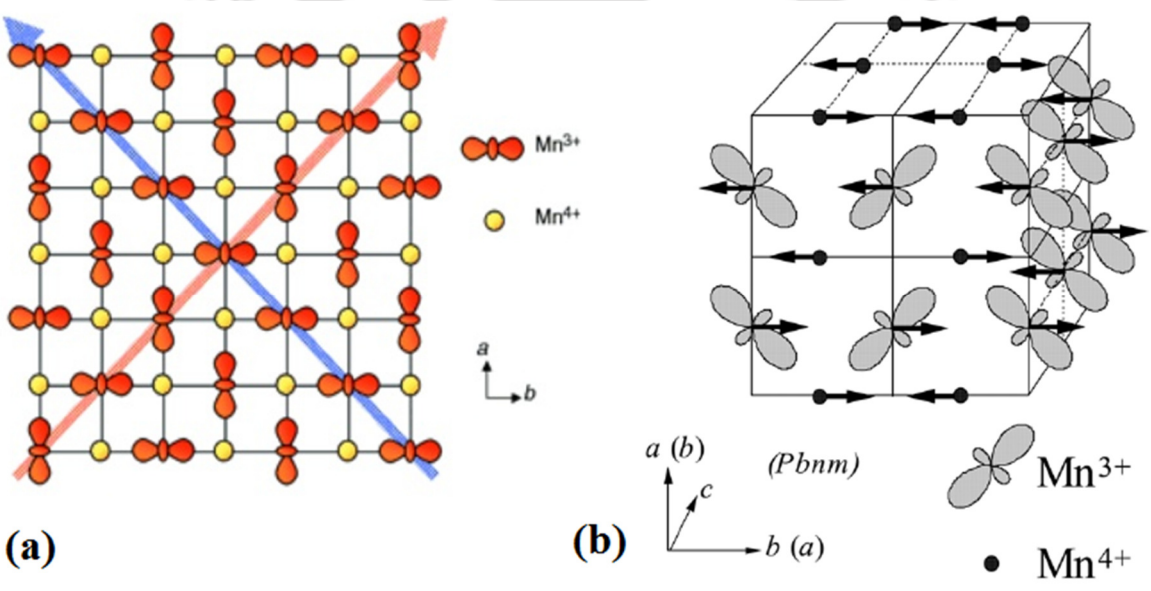

Figure 1.9: (a) Charge and orbital ordering in a-b plane (b) and their ordering in the z-direction.

The charge ordering state can be melted into a metallic ferromagnetic state, by the application of external magnetic field [32-34], pressure [35], exposure to x-ray photons [36], electrical field [37] and laser pulses in visible-IR spectrum [38]. A first order insulator to metal transition is induced when the CO phase is exposed to larger external magnetic field. Rao *et al.* studied the effect of $< r_a >$ value on CO properties and concluded that the T_{CO} increases with decrease $in\ < r_a >$ [39].

TH-1726_11612111

1.3 Electrical Transport in Manganites

The parent compounds of manganites, i.e. $RMnO_3$ and $AMnO_3$ are electrical insulators, where Mn ions are in Mn^{3+} and Mn^{4+} state respectively. A solid solution with the general chemical formula $R_{1-x}A_xMnO_3$ exhibits metal to insulator transition for certain compositions range depending upon the nature of R ion. This is due to e_g electron transfer from Mn^{3+} to Mn^{4+} ions by Zener DE – FM interaction. The simple manganites with strong DE interaction, such as in $La_{1-x}A_xMnO_3$ (A = Ca, Sr, Ba) with $x \approx 1/3$, exhibit a transition from a high temperature paramagnetic (PM) semi-conducting or insulating (I) phase to a low temperature FM – metallic phase. The temperature dependent electrical resistivity plot can be divided into three regions, namely high temperature (insulating region), low temperature (metallic region) and critical (the intermediate region) region. High temperature resistivity data have been explained by the variable range hopping model, small polaron model or thermal excitation model [40-42]. The electrical resistivity data in the ferromagnetic metallic region has been investigated by several models.

Electrical Resistivity in the Metallic Region

The electrical resistivity in the metallic region, i.e., below the metal-insulator transition temperature where $d\rho/dT > 0$ is analysed in terms of various empirical formula with a general relation, [43]

$$\rho = \rho_0 + \rho_m T^m + \rho_n T^n \qquad (1.2)$$

where, ρ_0 the temperature independent residual resistivity due to the scattering by impurities, defects, grain boundaries, and domain walls, etc. Here m and n are exponents and their values are generally 2, 2.5, 3 and 4.5 or 5 depending upon the nature of scattering mechanism. In manganites,the resistivity data in the metallic region follow the empirical relation [44],

$$\rho = \rho_0 + \rho_2 T^2 \qquad (1.3)$$

Here, the second term with the coefficient ρ_2 represents the electron - electron or single magnon scattering mechanism. Many researchers attributed the T^2 dependence to the electron - electron scattering process. The electrical resistivity of $La_{0.7}Ba_{0.3}MnO_3$ is found to follow $T^{2.5}$ dependence and is attributed to single magnon scattering [45]. The analysis of resistivity in the metallic region follows a temperature dependence of $T^{2.5}$ and $T^{1.5}$ above and below the 60 K respectively in [46]. Schiffer *et al.* [47] could successfully fit the low

TH-1726_11612111

temperature resistivity data of $La_{1-x}Ca_xMnO_3$ (x = 0.2, 0.33 and 0.45) samples to the expression,

$$\rho = \rho_0 + \rho_{2.5}T^{2.5} \quad (1.4)$$

On the other hand, the resistance of $La_{0.67}Ba_{0.33}MnO_3$ thin films in the presence of magnetic field follows the $T^{4.5}$ dependence and it represents the two magnon model, where the charge carriers interact with spin waves [48]. A $T^{4.5}$ dependence was observed by Snyder *et al.* [49] in $La_{0.67}Ca_{0.33}MnO_3$ and this was attributed to double magnon scattering mechanism as calculated by Kubo and Ohata [50]. However, the temperatures involved are too high, at which there would be a substantial density of states corresponding to minority spins at the Fermi level and hence single - magnon scattering cannot be ruled out. So, they proposed the expression for resistivity as,

$$\rho = \rho_0 + \rho_2 T^2 + \rho_{4.5}T^{4.5} \quad (1.5)$$

Jaime *et al.*[51] have fitted the low temperature resistivity data of $La_{2/3}(Pb, Ca)_{1/3}MnO_3$ compound to the expression,

$$\rho = \rho_0 + \rho_2 T^2 + \rho_5 T^5 \quad (1.6)$$

Here ρ_2 term refers the single magnon scattering and the T^5 function corresponds to electron-phonon scattering. The experimental resistivity data in the low temperature region of $La_{2/3}Ba_{1/3}MnO_3$ films [52], follow the above model (eq.1.6). The electrical resistivity data of an epitaxially grown LSMO film predominantly follow the polynomial equation of T^5 law, whereas the polycrystalline film having high electrical resistivity and low temperature upturn doesnot follow the T^5dependence [53]. The $\rho - T$ plot of the high quality LSMO film was fitted to eq.1.6 from 10 K to 300 K [54]. The electrical resistivity of $La_{0.67}Ba_{0.33}MnO_3$ films in the presence of different magnetic fields also follow the eq. 1.6 [55].

Electrical Resistivity in the Semiconducting Region

According to Millis *et al.* [15], the existing models based on the DE interaction strongly underestimate the magnitude of electrical resistivity change during the M-I transition. The transition from metallic to insulating phase is described as localisation of itinerant electrons as per Mott-transition. Already, de Gennes [56] demonstrated that for small values of *x* in $R_{1-x}A_xMnO_3$, local distortion of the AFM structure leads to trapping of

TH-1726_11612111

the doped charge carriers. Localisation of charge carriers will lead to enhanced interaction with it neighbours (magnetic) and hence a virtual effective mass is added to the hopping electrons. This transport of lattice or spin distortion corresponds the polaron. Several studies have indicated the charge localisation and the formation of small polarons in perovskite manganites above T_C [57-60]. If the range of association of charge carriers to crystalline distortion is less than the size of unit cell, they are called small polarons. In this case, the charge carriers are always found at lattice site. The temperature variation of electrical resistivity above T_C mostly follow the small polaron model i.e.,

$$\rho = \rho_{sp} T^n e^{(E_{sp}/k_B T)} \tag{1.7}$$

Here, E_{sp} is the hopping energy, T is the temperature and k_B is the Boltzmann constant, n = 1 corresponds to adiabatic small polaron hoping and n = 3/2 corresponds to non-adiabatic small polaron hopping. According to adiabatic small polaron hopping, the charge carriers hop more rapidly and each time the carrier hops, the configuration of vibrating atoms in the adjacent site coincides with that of occupied state. The resistivity data in the paramagnetic region of LBMO thin films were described in terms of adiabatic small polaron model [45]. The variable range hopping and non-adiabatic small polaron hopping models were found to explain the experimental data of polycrystalline, as-deposited thin films with oxygen deficiency. According to three dimensional Mott variable range hoping model, the expression for electrical resistivity can be written as, [61, 62]

$$\rho = \rho_{0m} exp((T_{0m}/T)^{1/4} \tag{1.8}$$

Here ρ_{0m} is Mott residual resistivity and T_{0m} is the Mott temperature. The density of states in the vicinity of Fermi level, $N(E_F)$ and, hopping distance range $R_{0m}(T)$ and hopping energy, E_{hop}(T) can be written as

$$N(E_F) = 18/(k_B T_{0m} a^3) \tag{1.9}$$

$$R_{hop}(T) = (3/8)a((T_{0m}/T)^{1/4} \tag{1.10}$$

$$E_{hop}(T) = (1/4)k_B T^{3/4} T_{0m}^{1/4} \tag{1.11}$$

Here a is the localisation length. According to VRH model, the charge carriers hop from one localised to another localised state having overlapping electron wave function. The energy required for such hopping is taken from phonon.

TH-1726_11612111

Efros and Skhlovskii (ES) [63] have modified the Mott-VRH model by taking into account the coulomb interaction between the charge carriers and the corresponding resistivity expression is,

$$\rho = \rho_{0s} exp(T_{0s}/T)^{1/2} \tag{1.12}$$

where, ρ_{0s} is ES residual resistivity and T_{0s}, the ES characteristic temperature is defined as,

$$T_{0s} = \frac{\beta_1 e^2}{k_B a 4\pi\varepsilon_0\varepsilon_r} \tag{1.13}$$

1.4 Review of Bulk Perovskite Manganites

The present work is focussed on some of the popular manganites and the salient features of these compounds are presented in this section.

$La_{1-x}Sr_xMnO_3$

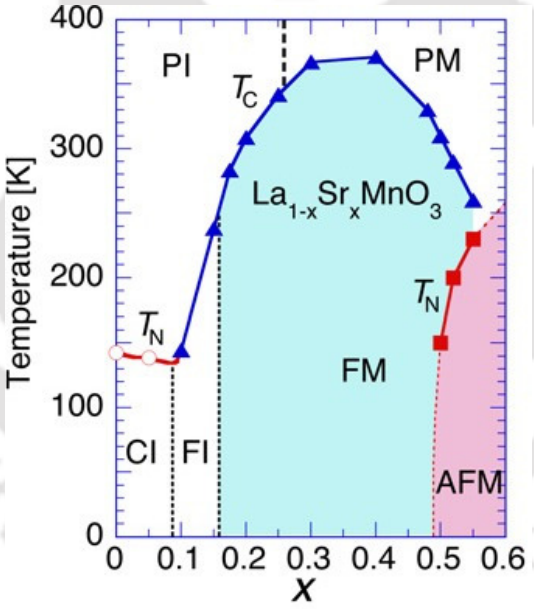

Figure 1.10: The electronic phase diagram of LSMO. PM, PI, FM, FI and CI denote paramagnetic metal, paramagnetic insulator, ferromagnetic metal, ferromagnetic insulator and charge ordered insulating states, respectively [9].

In the study of manganites during the 90's, a considerable emphasis has been given to the analysis of $La_{1-x}Sr_xMnO_3$, a material considered to be representative of the 'large' bandwidth subset of manganese oxides. It is believed that in this compound the hopping amplitude for electrons in the e_g-band is larger than in other manganites.

TH-1726_11612111

The parent compound $LaMnO_3$ (x = 0) and the other substituted compounds $La_{1-x}A_xMnO_3$ (A = Ca, Sr) are strongly affected by both the collective Jahn–Teller effect and the electron correlation effect due to presence of Mn^{3+} ions having single e_g electron. $LaMnO_3$ having orthorhombic structure at room temperature is characterised by the presence of OO due to a cooperative JT effect. This compound undergoes a structural phase transition at 780 K, above which the orbital-ordering(OO) disappears [9, 64].

The undoped $LaMnO_3$ is an orthorhombic anti-ferromagnetic insulator with T_N = 120 K. It consists of the ferromagnetic ab planes and with AFM inter - planar interaction along c. A small canting angle, presumably due to Dzyaloshinski - Moryia antisymmetric interaction [65, 66], was observed from magnetization and ac-susceptibility measurements [67, 68]. In $La_{1-x}Sr_xMnO_3$ compounds, for the doping concentration in the range of $0 < x < 0.1$, insulating canted AFM structure takes place. As the doping level x increases typically above 0.1, the spin state is turned into a ferromagnetic one, while the compound remains insulating or semiconducting up to the critical doping concentration of $x = 0.17$. Above this concentration, ferromagnetic metallic phase is observed with a maximum transition temperature for $x = 0.3$. As explained earlier the transfer of e_g electron from Mn^{3+} to Mn^{4+} ions and hence the double exchange interaction is responsible for the ferromagnetic metallic state. The electronic phase diagram of $R_{1-x}A_xMnO_3$ is explained based on the temperature versus hole doping concentration curve by considering R = La and A = Sr as shown in Fig.1.10. This system with $x = 1/3$ is extensively studied because of it has the maximum transition temperature of T_C = 370 K. With further hole-doping above $x = 0.5$, the materials turn into AFM insulator.

$Nd_{1-x}Sr_xMnO_3$

$Nd_{1-x}Sr_xMnO_3$ material is another interestingly manganite having a smaller e_g – electron bandwidth compared to the LSMO sample. Unlike $LaMnO_3$ series, $NdMnO_3$ exhibits complex behaviour due to the presence of two magnetic sublattices, i.e. Mn and Nd. The perovskite structure of $NdMnO_3$ is orthorhombically distorted due to the tilting of MnO_6 octahedra and it follows Pnma space group. Like $LaMnO_3$, $NdMnO_3$ also exhibits A-type antiferromaganetic structure. The Neel-temperature of this compound is at 78 K due to the Mn sub-lattice and the low temperature magnetic ordering observed at 13 K is due to the presence of Nd sub-lattice [69].

TH-1726_11612111

This series also exhibits CMR behaviour in the vicinity of paramagnetic to ferromagnetic and insulator to metal transition temperature, for the doping concentration in the range of 0.3 and 0.45. However for doping concentration close to 50% i.e. $0.48 < x < 0.51$, the FMM behaviour gets diminished and the AFM and charge/orbital ordering appear, this is shown in magnetic and electronic phase diagram of $Nd_{1-x}Sr_xMnO_3$, Fig.1.11. At $x = 0.5$, the complete transformation of the phase from ferromagnetic metallic (T_C around 250 K) to charge ordered insulating state (nearly 150 K) with decrease in the temperature has been observed. The nominal concentration of Mn^{3+} and Mn^{4+} ions in the ratio of 1:1 would be accompanied by the real space ordering of $d_{x^2-y^2}$ and $d_{3z^2-r^2}$ orbitals leading to charge ordered insulating phase along with the antiferromagnetic ordering [70-73].

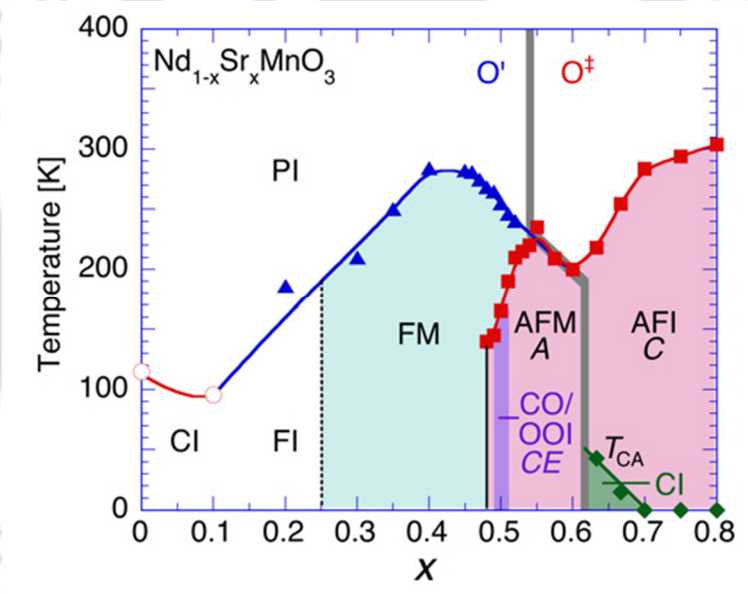

Figure 1.11: The magnetic as well as electronic phase diagram of NSMO.PM, PI, FM, FI and CI denote paramagnetic metal, paramagnetic insulator, ferromagnetic metal, ferromagnetic insulator and charge ordered insulator states, respectively [70].

$Nd_{1-x}Na_xMnO_3$

The mono-valent alkali ion doped, $Nd_{1-x}Na_xMnO_3$ series was studied by a few groups for $x = 0$ to 0.35 [74, 75]. They show charge ordering transition around 180 K with a weak FM transition at 110 K [76]. Samantaray *et al.* [77] explained the magnetic ordering through neutron diffraction studies in $Nd_{1-x}Na_xMnO_3$ compounds for $x = 0$ to 0.2. They observed the A -type AFM structure with the spin canted magnetic moment for $x = 0$. The spin canted ferromagnetism was observed for the composition $x = 0.15$. Further increase in Na concentration to $x = 0.2$ results in CE-type antiferromagnetic structure. This CO

TH-1726_11612111

transition temperature is found to be T_{CO} = 180 K, but Li *et al*. [78] reported the T_{CO} to be 155 K in $Nd_{0.8}Na_{0.2}MnO_3$.

1.5 Manganite Thin Films

Fabrication of high temperature superconducting thin films has stimulated the utility of thin films contribution in the device technology. Thin films are deposited by various methods like Pulsed laser deposition (PLD) [79, 80], sputtering [81-83], laser molecular beam epitaxial growth [84-86] etc. to obtain good quality thin films. In these methods, PLD method is used extensively to synthesize cuprate and HTSCs, which are now routinely made in laboratories, and it has been easily and rapidly adapted for manganites. The discovery of colossal magneto-resistance (CMR) effect in $La_{0.7}Ba_{0.3}MnO_3$ thin films has stiumulated the research to understand and improve the electronic and magnetic properties of these materials. The manganite oxides are highly sensitive to the strain effect, and this offers the possibility of studying its influence upon various properties such as insulator-metal transition temperature (T_{IM}), Curie temperature (T_c), structure and microstructure/morphology. In bulk manganites, strain is induced due to the doping of divalent ions which results in inter atomic lattice strain. Since the interest is to study the strain-induced magneto-transport properties of manganite thin films, this brief review will focus on the transport and magnetic properties of manganites films. In particular, strain effect on the physical properties of manganite thin films will be given more attention. This section will present a brief review of the experimental work done on the manganite thin films in the past few years.

1.6 Role of Deposition Conditions

1.6.1 Post-processing Conditions

In manganite thin films, the most common problem is the reduced T_C and T_{MI} compared to their bulk counterpart due to the deficiency of oxygen content. The films grown at low oxygen pressure result in oxygen deficiency. However, the physical properties of manganite thin films can be modified by depositing thin films under different partial pressures of oxygen [87-89]. Moreover, the oxygen deficiency leads to the structural distortion of the MnO_6 octahedra and hence the appearance of charge ordering phenomenon in the $La_{0.67}Sr_{0.33}MnO_3$ thin films [35, 87]. The oxygen deficiency is influencing the chain arrangement of Mn-O-Mn networks, which impacts the electrical transport behaviour and exchange interaction.

TH-1726_11612111

The parameters such as oxygen deficiency, substrate temperature, nature of substrate etc. strongly influence the lattice strain on films. As grown films have insufficient oxygen quantity, which might cause different structural deformation inducing a large strain [90, 91]. Thus the strain can be relaxed by heat treatment in either in-situ or ex-situ conditions with various environments to improve the functional properties of the thin films. To reduce oxygen deficiency and the structural change, films are annealed in air or oxygen environments. Dorr *et al.* [92] have carried out heat treatment of $La_{0.7}Ca_{0.3}MnO_{3-\delta}$ thin films in vacuum at 600°C. They reported that the vacuum annealing of LCMO films systematically reduce the Mn^{4+} concentration and hence the FM T_C from 270 to 130 K.

Post-annealing under an oxidising or reducing atmosphere strongly affects the oxygen content in manganite films [64, 93-96]. The oxygen content can be improved by subjecting films to high temperatures either during the film deposition or post-deposition of a film. There are two different kinds of heat treatment procedure that can be followed to anneal the films to achieve their characteristic properties i.e. in situ or ex situ. In the first case, a heating filament behind the substrate holding platform is used to maintain the appropriate temperature while depositing the films. The post-deposition annealing process can be carried out either inside the deposition chamber or in an external furnace. In general, the minimum required temperature to get the crystalline nature in manganite thin films is around 650 to 700°C [97, 98] and in some cases temperature is raised upto 800°C to grow epitaxial thin films [99]. Indeed, the poor quality of oxygen content in $La_{0.7}Sr_{0.3}MnO_3$ (LSMO) film grown with substrate temperature of 600°C is modified by annealing them at 950°C in flowing of oxygen pressure, and this process loads to increase in saturation magnetization and the transition temperature [100]. Borges *et al.* have deposited $La_{0.7}Sr_{0.3}MnO_3$ films on MgO substrate, by changing the substrate temperatures in the range of 650°C to 680°C. They found that the magnitude of resistivity is reduced by several orders and the associated T_{MI} shifts towards the high temperature region with increase in the substrate temperature [101]. Reduction in the values of T_C and T_{MI} were observed in earlier reports on $Nd_{2/3}Sr_{1/3}MnO_3$ (NSMO) films grown on $LaAlO_3$. The metal-insulator transition temperature is found to decrease while decreasing the deposition temperature [102].

1.6.2 Substrate Effects

In the previous section, we dealt with the oxygen deficiency related lattice strain and its effect on electrical and magnetic properties. Here we discuss the role of substrate

TH-1726_11612111

on the physical properties of films. This is due to the fact that Mn e_g electrons, which determine most of the physical properties, are coupled to the lattice through the Jahn-Teller distortion of trivalent Mn ions. Thus, strains affect the properties of the manganite films. Consequently, to obtain the desired physical properties, one needs to correctly understand the effects of strains on manganite thin films. In this section, a brief introduction to the origin of different types of strains due to various substrates are discussed.

Selection of the right substrate delivers good quality epitaxial thin films. Indeed, the low lattice mismatch between the substrate and films leads strain relaxation and better properties comparable to that of the bulk materials [103, 104]. Strain induces the structural distortion and it leads to the segregation of impurty phases thereby diminishing overall functional properties of the films. According to Millis [15], the bond length of Mn-O will decide whether given phase behaves as metallic or insulator. This has been confirmed experimentally for (La, Ca)MnO_3 and (La, Sr)MnO_3 thin films deposited on different substrates [105-107].

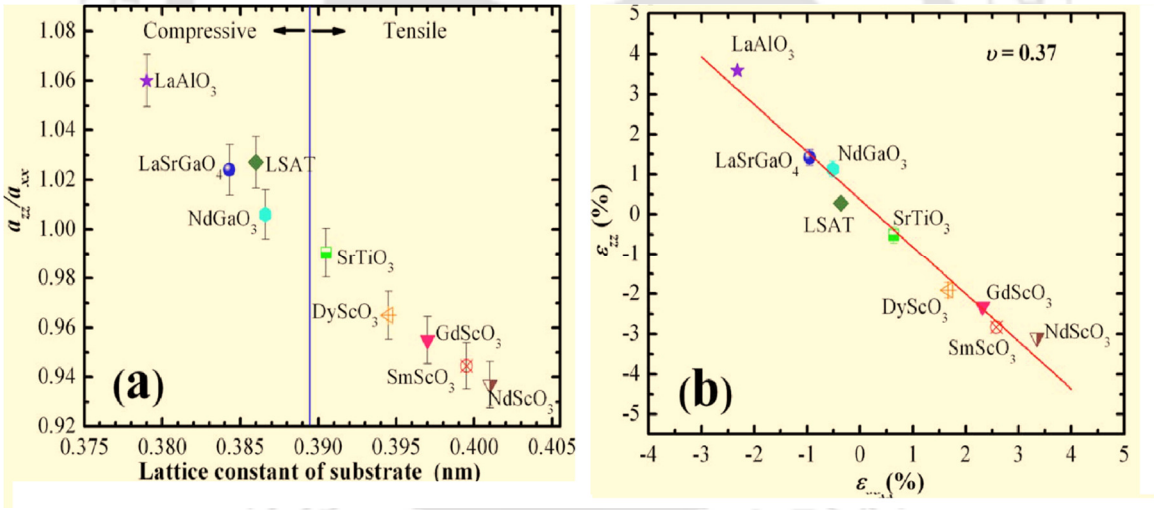

Figure 1.12: (a) Ratio between the out-of-plane and in-plane lattice spacing of $La_{0.7}Sr_{0.3}MnO_3$ films as a function of the pseudocubic in-plane substrate lattice parameter. (b) The out-of-plane lattice strain ε_{zz} as a function of the in-plane lattice strain ε_{xx} [108].

Adamo *et al.* [108] have deposited LSMO films on different substrates and studied the biaxial strain as shown in Fig.1.12. Films experience either tensile or compressive strain depending upon the lattice misfit with the substrate. Both in-plane and out-of-plane lattice parameters are often modified by strain effects when different substrates are used. It is found that the ratio of the out-of-plane lattice constant to in-plane lattice constant decreases as moving from compressive strain to tensile train as shown in Fig.1.12(a) by choosing

TH-1726_11612111

various substrates. The distortion of the tetragonal structure represents the existence of biaxial strain in the lattice of the films. They found Poisson's ratio of LSMO as 0.37 from the straight line fit to the lattice strain along out-of-plane versus in-plane lattice strain of the films as shown in Fig.1.12(b). This is the highest range of substrate induced strain over which Poisson's ratio has ever been calculated for a CMR manganite. Therefore, T_C of the films has been improved more than 10% when the biaxial strain is within 1%.

The right substrate is chosen depending on its chemical compatibility, thermal expansion, surface quality, homogeneity and the cleanliness. If the chemical compatibility is not maintained, there is a probability of contamination of films during the growth as the substrate temperature requires more than 650°C during the growth. Thermal expansion is another important parameter to decide the film growth. Good thermal expansion match between the film and substrate, yields crack free surface and more adhesive nature of films. LSMO thin films are epitaxially grown on the perovskite substrates, having the thermal expansion coefficient (σ) of around 10^{-5} K^{-1}. But the films deposited on Si substrate results in polycrystalline nature with fewer functional properties. On the other hand, the substrate with buffer layer reduces the lattice mismatch, and yield epitaxial growth of the films having bettter functional properties [109]. The surface quality depends on the nature of the film. $La_{2/3}Ca_{1/3}MnO_3$ (LCMO) films on STO substrate exhibit a flat surface but as the thickness is increased islands formation has been observed [110]. The surface cleanliness is another important parameter which depends on the nature of growth. In a general, the substrate may contain residues of manufacturing packaging, finger prints, etc. and this leads to contamination of the substrate. As a result the morphology and the physical properties are strongly influenced.

1.6.3 Epitaxial Growth

The structure of manganite thin films is decided by the choice of substrate [94]. An epitaxial growth of a manganite thin films is achieved on substrate having smooth surface and matching lattice parameter. The commercial substrates having the pseudo tetragonal or pseudo cubic structure with their lattice constant values are shown in Fig.1.13. The commonly used substrates are $SrTiO_3$ (STO, $a = 3.905$Å, cubic), $LaAlO_3$ (LAO, $a = 3.788$Å, pseudo cubic), MgO ($a = 4.205$Å, cubic) and $NdGaO_3$ (NGO, orthorhombic with $a = 5.426$ Å, $b = 5.502$ Å and $c = 7.706$ Å) [111-114]. By using these substrates, a variety of parameters can be optimised to get the appropriate properties equivalent to those

TH-1726_11612111

of bulk manganites. These substrates influence the material growth during the deposition and the annealing process. The lattice mismatch (δ) [115] along the interface is defined in terms of the pseudo cubic lattice constant of the bulk sample and the substrate

$$\delta = \frac{a_{sub} - a_{bulk}}{a_{bulk}} \tag{1.14}$$

Here, a_{sub} and a_{bulk} represent the in-plane lattice constant of the substrate and bulk maagnanite respectively. The negative value of δ corresponds to compressive strain induced along the plane of the film, whereas the positive sign corresponds to tensile strain along the plane of the film and accordingly the perpendicular lattice parameter gets elongated (if it is compressive) or compressed (if it is elongated) as shown in Fig.1.14.

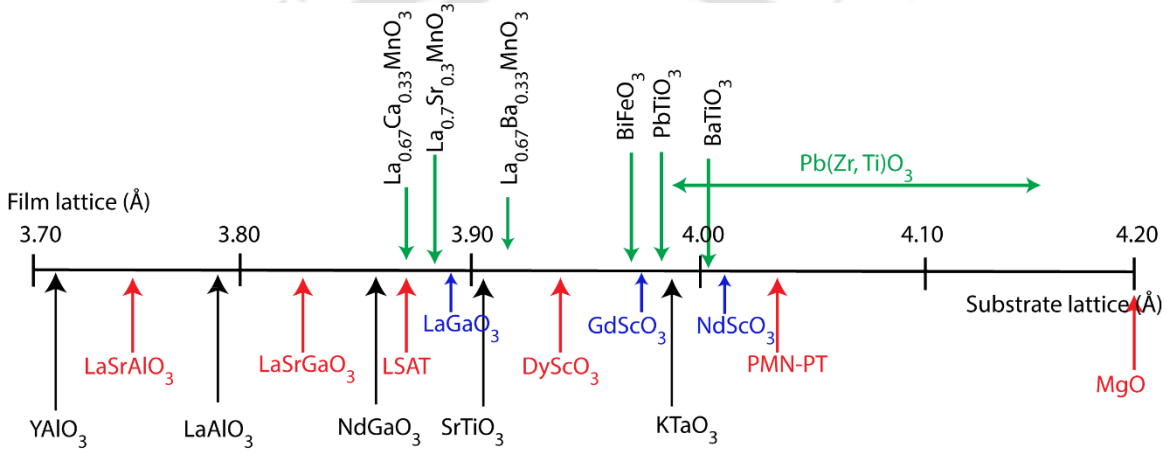

Figure 1.13: The pseudo cubic lattice parameters of several substrates and the lattcie constant of various films [116].

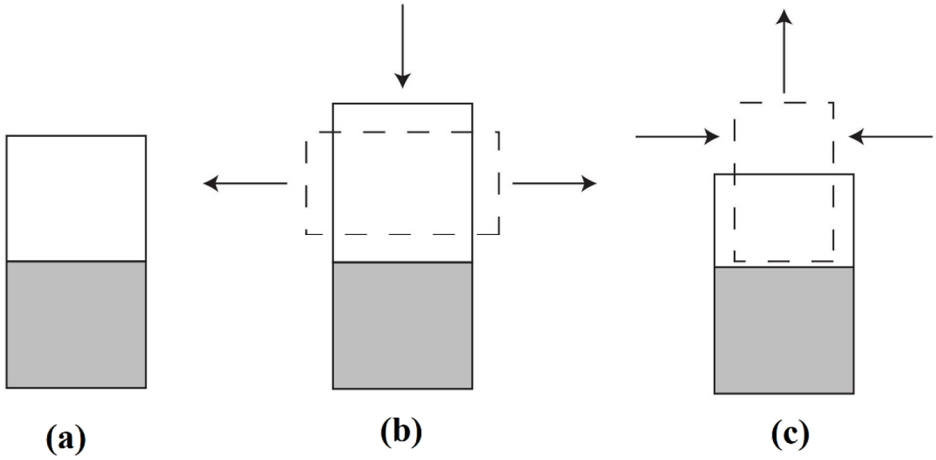

Figure 1.14: The schematic diagram of film (a) without strain (b) in-plane tensile strain and (c) in-plane compressive strain.

TH-1726_11612111

Induced lattice mismatch due to the substrate is estimated by recording X-ray diffraction patterns and high resolution transmission electron microscopy images. The precise value of out-of-plane lattice constant (c) can be easily found out from the analysis of XRD patterns in $\theta - 2\theta$ scan. The cross-sectional view of high resolution transmission electron microscopy images are used to confirm these parameters [117-119]. The most commonly used substrates for preparing LSMO films are LAO and STO. LAO substrate produces compressive strain (this is easily distinguished, in Fig.1.14, depending upon the lattice mismatch between the substrates and film lattice parameters) and STO substrate creates tensile strain. The induced strain is proportional to the out-of-plane lattice constant and it is strongly influenced by variation of other parameters such as thickness of the film, annealing temperature etc. [120]. For example, for $Nd_{2/3}Sr_{1/3}MnO_3$ film grown on $SrTiO_3$ substrate, the out-of-plane parameter increases from 3.8 Å for a 200 Å thick film to 3.86 Å for a 1000 Å film, which is close to the bulk value [121]. In the case of compressively strained films such as in $La_{0.7}Sr_{0.3}MnO_3$ on (100)-oriented $LaAlO_3$ substrate [122]: the out-of-plane parameter decreases from 3.94 Å for a 300 Å thick film to 3.9 Å for a 4500 Å thick film, while at the same time the in-plane parameter changes from 3.82 Å to 3.88 Å .

In order to grow epitaxial manganite films, the substrate should have similar structure (i.e. perovskite) comparable to that of the films. All hole doped manganites have been extensively studied by varying the growth and processing parameters. Li *et al.* [81] have deposited perfect epitaxial LCMO thin film on (100)-LAO.

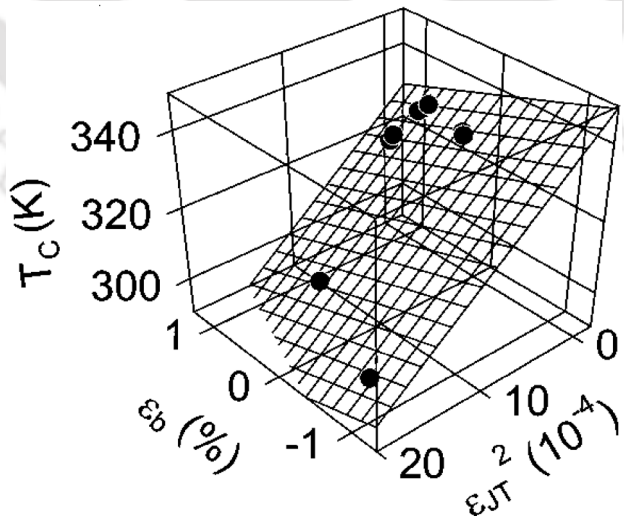

Figure 1.15: The phase diagram of the LSMO films established from the relation 1.15 for the thickness 250 and 500 Å [123].

TH-1726_11612111

The lattice strain can be determined using the relation as $\varepsilon = \frac{a_{film} - a_{bulk}}{a_{bulk}}$. Here a_{film} and a_{bulk} are the lattice constant of film and the bulk sample respectively. The strain is compressive for $\varepsilon < 0$ and tensile for $\varepsilon > 0$. According to Millis *et al.* [124], the transition temperature of colossal magneto-resistance materials is quite sensitive to strains. Hence the biaxial strain (ε_B) can tune the transition temperature. Acoording to them,

$$T_C(\varepsilon) = T_C(\varepsilon = 0)(1 - \alpha\varepsilon_B - \frac{1}{2}\Delta\varepsilon^{*2}) \quad (1.15)$$

Here, ε^* is biaxial distortion, $T_C(\varepsilon)$ and $T_C(\varepsilon = 0)$ are the transition temperature with and without the strain ε, α and Δ are the constants. The constants α and Δ are related as $\alpha = \frac{1}{T_C}\frac{dT_C}{d\varepsilon_B}$. Tsui *et al.* [123] discussed the magnetic properties of LSMO films in terms of biaxial strain, as shown in Fig.1.15. Suppression of T_C might be caused by the biaxial strain, deficiency of oxygen and composition etc. Angeloni *et al.* [125] have explained the suppression of T_{MI} with several mechanisms including the biaxial strain. This strongly depends on various parameters like dead layer effects, imperfect oxygen stoichiometry, and possible finite size effect etc.

Recently a few groups have studied the behaviour of manganite films grown on substrates with high lattice mismatch like MgO. The LSMO films grown on MgO substrate with large lattice mismatch of 8% show that they crystallize in orthorhombic and rhombohedral respectively when the deposition was carried out using sputtering and laser ablation techniques [126]. As discussed above, the surface quality decides the quality of the grown film and it depends on the surface quality of the substrate and its orientation with respect to unit cell dimension of film. The mis-orientation and lattice mismatch may lead to lattice strain which affects the bond angle and Mn – O bondlength. The deviation of Mn – O – Mn bond angle from 180° would affect the electronic bondwidth and hence the DE interaction [127].

1.6.4 Effect of Film Thickness

Thickness of manganite thin film is another important factor, which influences the lattice strain as well as their functional properties. The strain induced due to the oxygen vacancies and substrate choice reduce their T_C and T_{MI}. Saber *et al.* [128] have demonstrated the correlation among the strain, spin disorder and post-annealing temperature of $Sm_{0.55}Sr_{0.45}MnO_3$ (SSMO) thin films as a function of their thickness on $SrTiO_3$ and $LaAlO_3$ - substrates and this is shown in Fig.1.16. They have noticed the out-

TH-1726_11612111

of-plane strain (ε_c) dropped from ≈1.5% to 0.5% and the in-plane strain (ε_a) reduced from ≈ 0.8 to 0.25% as the SSMO films on STO substrates were post-annealed at 900°C.

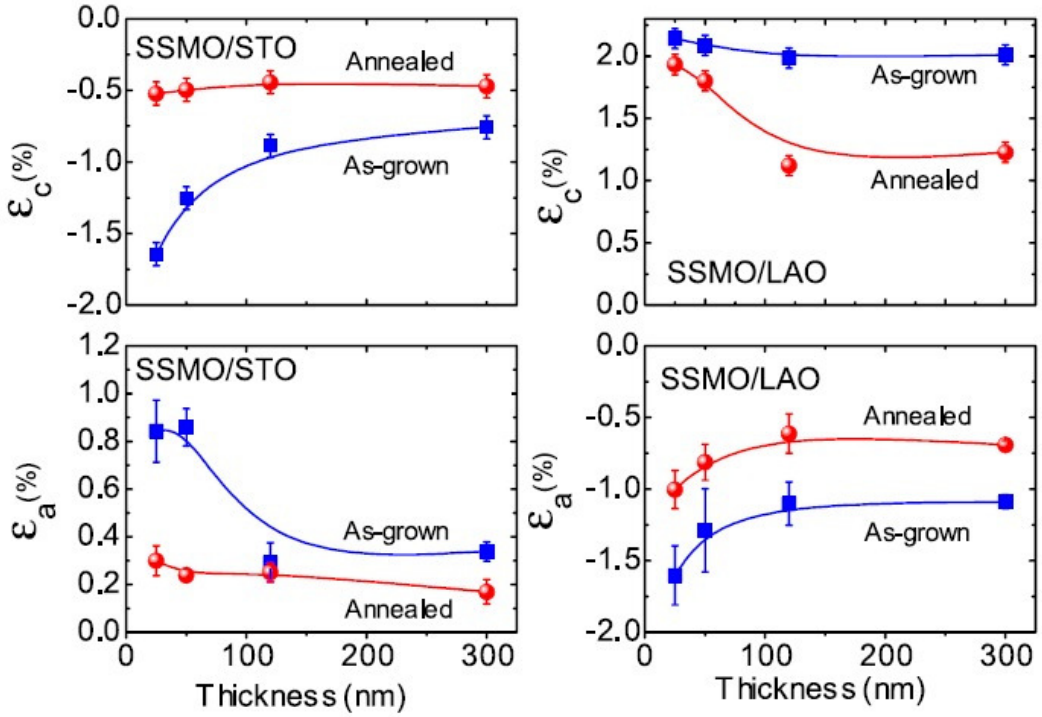

Figure 1.16: ε_C and ε_a for as-grown and annealed films of $Sm_{0.55}Sr_{0.45}MnO_3$ on STO and LAO substrates [128].

One obvious question is what is the minimum thickness required for the film to behave like its bulk material? To find the answer to the above question several researchers have carried out thinkess dependence of physical properties of manganite thin films such as $La_{0.7}Sr_{0.3}MnO_3$ [129], $La_{0.7}Ca_{0.3}MnO_3$ [130], and $La_{0.7}Ba_{0.3}MnO_3$ etc. by varying the thickness in the range of 2 to 200 nm [131-135]. For thickness t > 150 nm, the physical properties behave similar to that of bulk material due to strain relaxation. According to Saber *et al*. [128], in-plane and out-of-plane strain values of annealed films are reduced compared to as-grown films on both substrates. Once the film thickness approaches to critical thickness, the elastic energy exceeds the defects formation energy and as a result, the strain of the film gets reduced [136]. The metal-insulator transition temperature (T_{MI}) of LSMO thin film is reported to decrease from 330 K to 270 K as the strain is induced and their corresponding out-of-plane lattice parameters are 3.88 Å and 3.94 Å respectively [125]. Thus the out-of-plane lattice constant shows larger than the bulk value when the film thickness is a few nano meters. It approaches the bulk value at higher film thicknesses. The T_C and T_{MI} values are reported to increase with increase in film thickness [41, 125].

TH-1726_11612111

The fully strained magnanite thin films are in multiphase form. Bibe *et al.* [137] have experimentally verified the existence of multiphase in $La_{0.7}Ca_{0.3}MnO_3/SrTiO_3$ interface through ^{55}Mn neutron magnetic resonance. The improvement of T_{MI} and saturation magnetization of the thin film is observed with increase in film thickness. The inhomogeneity of magneto-electrical texture, carrier density modification and shrinkage of bandwidth etc. lead to the existence of multiple phase in manganite thin films [138].

Magnetic and electrical transport properties of manganite thin films strongly depend on thickness of the film. At a lower thickness, the metallic nature of the films disappear and the saturation magnetization also decreases [139-144]. This gives rise to an evidence of existence of electrical and magnetic dead layer. The origin of dead layer still under debate, there is no physical interpretation or proof behind the appearance of the dead layer. Borges *et al.* estimated the dead layer of LSMO film on MgO substrate by using a relation i.e. $(\frac{\sigma}{\sigma_B}) \simeq \frac{t-t_D}{t}$ [101] and it was around 4 nm. Here, t and t_D are total thickness of the film and the dead layer thickness and, σ and σ_B is the conductivity of film and bulk sample respectively. The thickness dependent properties are discussed in terms of the strain induced by the substrate.

$La_{1-x}Ba_xMnO_3$ (for x = 0.3 and 0.33) films were reported to exhibit low ferromagnetic transition temperature compared to their respective values in bulk sample due to the biaxial strain [145]. T_C increases with the thickness of the film due to the strain relaxation achieved at higher film thickness. In the biaxial strain of a thin film i.e. (eq 1.15), the biaxial distortion (ε_B) always diminishes the ferromagnetic transition temperture. Therefore, the strain may be relaxed in higher thickness films or films grown on substrate having negligible strain. On the other hand, the easy axis direction of the film switches from strongly in-plane for the film on STO to weakly out-of-plane for the film on LAO [146, 147]. The T_C improvement is observed in compressive strained film of $La_{0.7}Ca_{0.3}MnO_3/SrTiO_3$ [148].

1.7 Homogeneous and Heterogeneous Magnetic Thin Films

In this section, a brief introduction to the fabrication of homo and hetero structure manganite films are given. Several authors have studied the effect of varying the thin film processing. Parameters such as thickness, substrate, substrate temperature etc. to tune their physical properties towards device application. On the other hand, the heterostructure of

TH-1726_11612111

Manganite films are being studied for spintronic devices. Various combination of manganite multilayer films were deposited by using various techniques such as sputtering, pulsed laser deposition etc. to investigate the interactions among the layers. Several authors have reported on the interface interactions between ferromagnetic (FM) and antiferromagnetic (AFM) films in a form of bilayer as well as in multilayer structures and observed the coupling among the charges, spins and lattice degrees of freedom across the interface [149-152]. In recent years, the multiferroic materials with coexistence of at least two ferroic - ordering have dawn ever-increasing interest due to their potential applications as multifunctional devices [153-155]. Specially, the hetero structure of $BiFeO_3$ and $La_{0.7}Sr_{0.3}MnO_3$ exhibits interfacial magnetism at room temperature [156-158]. Interface magnetism is also important for the development of devices with strongly correlated electron oxides. For example, the perfectly spin polarisable ferromagnet $La_{1-x}Sr_xMnO_3$ could be one of the best candidates for random access memory [159]. For example, the upturns of resistivity curves at low temperatures in a tri-layer system progressively diminished due to the replacement ZrO_2 and $LaMnO_3$ by $YBa_2Cu_3O_7$ between the LSMO layers [80]. Moreover, there is no appreciable change in their transition temperature but with a large increment of magneto-resistance near T_C, compared to those single layer. The magnetic properties of LSMO and $La_{0.7}Ca_{0.3}MnO_3$ (LCMO) films grown with different capping layers have shown ferromagnetic transition and saturation magnetization similar to that of bulk samples [146]. Thus, knowledge of the atomic-scale structure in a thin film is a key factor in understanding the structure-property relationship and for providing feedback on the optimized growth conditions to obtain films with excellent crystalline quality.

Recently, a few groups have studied the electrical transport and magnetic properties of bilayer films constructed as a combination of manganite film with other films. Such combination of bilayer films ($La_{0.7}Sr_{0.3}MnO_3$ layer and nonmagnetic metallic layers like Au, Pt, $SrRuO_3$ (SRO) etc.) help to study the spin and the electrical charge transport across their interface. The spin transport in a bilayer system induces a voltage drop across a nonmagnetic layer which is attributed to inverse spin Hall effect. Specially in LSMO/SRO bilayers, dc voltage signals are observed in SRO layer under ferromagnetic resonance [160].

The bilayers of a few nano meters of doped manganite (LSMO) films on $BiFeO_3$ dielectric layer acts as a multiferroic field effect device, where both magnetic as well as

TH-1726_11612111

electrical exchange-bias are observed [161]. The exchange-bias phenomenon is oberved in $La_{0.67}Sr_{0.33}MnO_3/SrTiO_3$ bilayer system when they were deposited under different partial pressures [47]. The hetero-structure of $La_{0.8}Sr_{0.2}MnO_3/TiO_2$ acts as a rectifier at low temperatures due to the manipulation of e_g electrons in $La_{0.8}Sr_{0.2}MnO_3$ films [162]. The hetero-structure configuration of an antiferromagnetic layer either manganite or other perovskite structure sandwiched between two ferromagnetic metallic layers efficiently worked as spin valve devices. The exchange interactions in the supperlattices of $(La,Sr)MnO_3)_m/(LaMO_3)_n$, M = Co, Fe or Co, Ni were studied as a function of composition (m/n) and thickness of each layer [163, 164]. Here m and n represent the number of layers. Anti-ferromagnetic (AF) layers are very important in the fabrication of magneto-electronic devices where the coupling of their spins to adjacent ferromagnetic layers produce an exchange bias coupling. Recently, LFO/LSMO bilayers were grown on Nb-doped $SrTiO_3$ substrate in order to study the effect of nano-structuring and substrate symmetry on the structure of antiferromagnetic domains of $LaFeO_3$ [165]. The magneto-resistance of $LaFeO_3/La_{0.8}Ba_{0.2}MnO_3/LaFeO_3$ tri-layered film is about 74% larger than that of single layer LBMO film, but with reduced transition temperature. Therefore, bilayer of LSMO and LFO is quite interesting to study the spin frustration across the interface that induces abnormal electrical and magnetic properties.

1.8 Motivation of Present Thesis Work

As we mentioned in the above introduction on manganite thin films, the growth of $La_{0.7}Sr_{0.3}MnO_3$ and $La_{0.7}Ca_{0.3}MnO_3$ thin films by various techniques was extensively studied to attain their electrical and magnetic properties comparable to those of bulk counterpart. $Nd_{0.7}Sr_{0.3}MnO_3$ is one of the well-known CMR materials having T_C value around 250 K and moreover it contains a magnetic rare earth element. It would be interesting to study the interface effects of manganite thin films in a hetero-structure configuration as a bilayer form of ferromagnetic and AFM or charge-ordered phases such as $Nd_{0.7}Sr_{0.3}MnO_3/Nd_{0.8}Na_{0.2}MnO_3$ and $La_{0.7}Sr_{0.3}MnO_3/LaFeO_3$. We have chosen RF-magnetron sputtering technique to deposit various manganite films as follows,

- $Nd_{0.7}Sr_{0.3}MnO_3$ films on 001-Al_2O_3 substrate by varying the post annealing temperature in the range of 700°C to 900°C.
- Deposition of $Nd_{0.7}Sr_{0.3}MnO_3$ films on the substrates of Al_2O_3, MgO and $LaAlO_3$ with 001-orientation followed by post–annealing in air and oxygen environments.

TH-1726_11612111

- Structural, electrical and magnetic properties of the $Nd_{0.7}Sr_{0.3}MnO_3$ films on 001-$LaAlO_3$ substrate by varying the thickness in the range of 12 - 200 nm.
- $Nd_{0.8}Na_{0.2}MnO_3$ films on 001-$LaAlO_3$ substrate by varying the thickness in the range of 30 nm - 100 nm.
- Bilayer of $Nd_{0.7}Sr_{0.3}MnO_3$/$Nd_{0.8}Na_{0.2}MnO_3$ on 001-$LaAlO_3$ substrate for different thickness of $Nd_{0.7}Sr_{0.3}MnO_3$ layer.
- Bilayer of $La_{0.7}Sr_{0.3}MnO_3$/$LaFeO_3$ on (001)-$LaAlO_3$ substrate for different thicknesses of $La_{0.7}Sr_{0.3}MnO_3$ layer.

TH-1726_11612111

Chapter 2
Experimental Techniques

TH-1726_11612111

TH-1726_11612111

Chapter 2

In order to understand functional properties of manganite materials, various techniques are required to get the information related to their crystal structure, micro structure along with magnetic and electrical properties. Such studies will give the complete idea to construct high quality materials for applications. This chapter describes the various preparation techniques followed for preparing the bulk materials as well as the fabrication of thin films followed by the characterisation techniques.

Manganite targets were prepared by using the standard solid state route and sol gel methods. Well calibrated target samples were used to grow thin films by using radio frequency (RF) magnetron sputtering system. The prepared bulk as well as thin film samples were characterised by recording X-ray diffraction patterns to check their phase purity and to determine lattice parameters. Disorderness in the crystal structure was analysed with the help of Raman spectrometer and the morphology of thin films was studied by recording the surface images by using atomic force microscope. The electrical and the magnetic properties of samples were studied by measuring the temperature variation of electrical resistivity and temeprature and field variations of magnetization.

2.1 Sample Preparation

2.1.1 Preparation of Sputtering Target

Solid State Route

Solid state route is one of the most common methods used to prepare the polycrystalline oxide samples. The stoichiometric ratio of starting compounds and/or elements were weighed using an electronic balance supplied by Mettler Toledo model no: AG135 with an accuracy of 0.01 mg. The weighed compounds were grinded under the acetone medium using an agate mortar and pestle. The homogeneous mixture of starting compounds was then transferred to an alumina crucible and pre-sintered in the temperature range of 400 to 900°C for over 24 hrs, followed by furnace cooling to room temperature. Thereafter, the presintered compound was pressed into cylindrical shape pellets by using a 13 mm die and a hydraulic press supplied by Techno Search instruments, Thane, India with a maximum load of 6 ton/cm^2. The sintering in pellet form was carried out in air at different temperatures with several intermediate grindings and repelletizing. The final sitnering temperature depends on the nature of composition and is discussed in chapters 3, 4 and 5 for respective series of materials.

TH-1726_11612111

Chapter 2

Sol-Gel Method

Sol-Gel route is a chemical method in which nitrates or acetates of cationic materials are dispersed in a solvent and converted into a gel form through the hydrolysis reaction of polymerisation. The combustion process of a gel yields fine dry powder as a product material. There are a few advantages of the sol-gel technique compared to the solid state route : (1) molecular level mixing of starting compounds can be easily obtained by the materials dissolved in the solvent. (2) The homogeneous doping mixture of the materials can be achieved by incorporating the dopant in the molecular level. (3) The required temperature for annealing is relatively small compared to the case of a solid state route.

In this method, the stoichiometric ratio of the starting compounds and/or elements is converted into metal nitrates by adding nitric acid. They are then converted into citrate by adding excess amount of citric acid and ethylene glycol. The uniform mixture of the above solution is slowly evaporated in a hot plate at 75 to 100°C until a gel is formed. The polymeric gel is completely dried up by keeping at 75°C for 12 hours. The product is then heated to 200°C to decompose the remaining organic reagents. The obtained precursor powder is sintered in pellet form. The final sintering temperature and the duration of sintering is decided depending on the nature of compounds.

2.1.2 Thin Film Growth Techniques

In general, there are many techniques used to grow thin films. They are classified as chemical vapour deposition (CVD) and physical vapour deposition (PVD) depending upon the type of materials used to prepare thin films. Chemical vapour deposition (CVD) method is suitable for the volatile compound. In this technique, material is evaporated thermally to decompose the starting compounds and they chemically react with the substrate surface to form a non-volatile product. This technique was developed to deposit non-metallic hard coatings, dielectric films, and single-crystal semi-conductor films. PVD is a process in which ionised gaseous mixture make collision with the target material and eject the atoms such that they can get deposited on a substrate. This is the most versatile technique to deposit metallic, oxide semiconductors and dielectric thin films. The manganite thin films can be deposited by any one of the technique such as pulsed laser deposition (PLD), magnetron sputtering, molecular beam epitaxy (MBE) etc. In PLD technique, strong energetic laser ablates the material into vapours and then gets condensed

TH-1726_11612111

into a thin solid layer on the substrate. Molecular beam epitaxy is also a method that follows the evaporation process. High quality epitaxial films are grown by using this technique. Here, the respective materials are placed in separate crucibles and heated to an elevated temperature until they begin to sublime. Therefore, the gaseous elements are evaporated and get condensed on a substrate. In the sputtering technique as a gaseous vapour is stimulated by the bombardment of high energy ions in a high vacuum region. This mechanism was discovered by Sir W. R. Grove in 1852. The sputtering process transfer the momentum of positive ions on the cathode surface. Thus atoms are ejected from its surface and deposited on the substrate. The schematic diagram of a sputtering process is shown in Fig. 2.1.

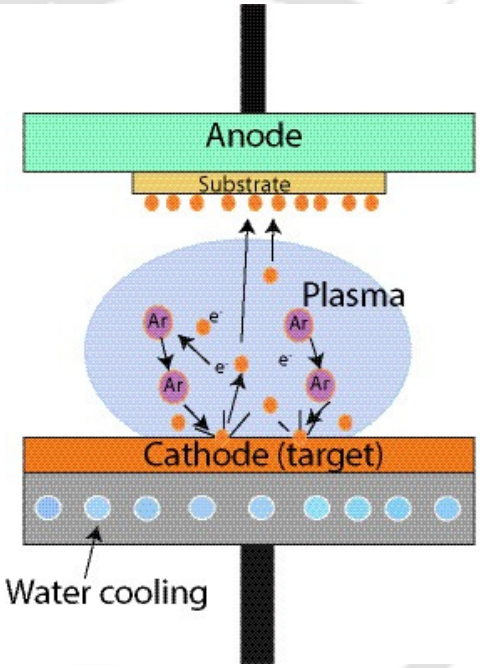

Figure 2.1: Schematic diagram of sputtering process

Plasma of an inert gas is created when the gas enters into the chamber where the electrical field is maintained between two electrodes under high vacuum conditions. As a consequence, discharge of ionised inert gas is generated and they get accelerated towards the cathode by causing multiple scattering with the target material. Hence transfer of momentum from the plasma to surface cathode leads to ejection of the surface atoms. Therefore a cascade scattering process will be continued for a couple of times to impinge the surface atoms. Such process will transfer the energy to the surface atoms. Once their energy is larger than the surface binding energy of an atom, the atom will release from its surface. The ejected atoms passing through the plasma of the inert gas are thermally

TH-1726_11612111

stabilised on the surface of a substrate to form a thin solid layer structure. The trajectory followed by the ionised atoms are random and this can be explained based on glow discharge source, as shown in Fig.2.2. As we have mentioned above, the glow discharge depends on the work function of target materials and pressure surrounded by the environment. Fig.2.2 illustrates the gradient in the plasma with alternating dark and bright regions between the cathode and anode. First region nearby the cathode is an Aston dark space that contains both low energy electrons and high positive energy ions, and they move in the opposite direction. Beyond Aston dark space, a bright luminous region is seen and is known as cathode glow. Sequently a low quality glow known as Crookes or cathode dark space is found next to the cathode glow. Beyond that, a negative glow is appeared due to a mixed interaction of the secondary electrons and neutrals. Subsequently Faraday dark space, positive column region then the anode are observed.

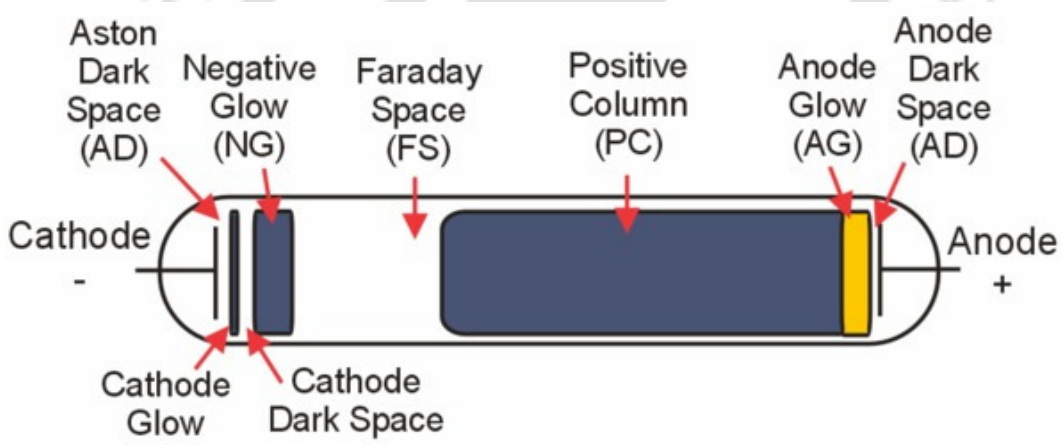

Figure 2.2: Schematic diagram of glow discharge tube under electric field.

Sputtering Yield (S)

Sputtering is a process which ejects bunch of atoms from a target surface when the high energetic particles are bombarded. The sputtering yield can be defined as,

$$S = \frac{Number\ of\ sputtering\ atoms}{Incident\ particles} \tag{2.1}$$

Some of main parameters that influence the sputtering yield are explained below

Energy of Incident Particles :

Fig.2.3 illustrates variation of sputtering yield (S) as a function of the incident ion energy. The minimum energy required to sputter a metal ion from its surface is around 20 ≈ 30 eV. As the energy exceeded threshold energy of a bounded atom, the sputtering yield

TH-1726_11612111

depends on $\sqrt{E}$ upto the ion energy of E = 100 eV [166]. The sputtering yield is directly related to the ion energy for E >100 eV [167]. Moreover, S saturates at higher ion energy and above 10 keV, this will decrease due to the energy dissipation of the incident ions deep in the target.

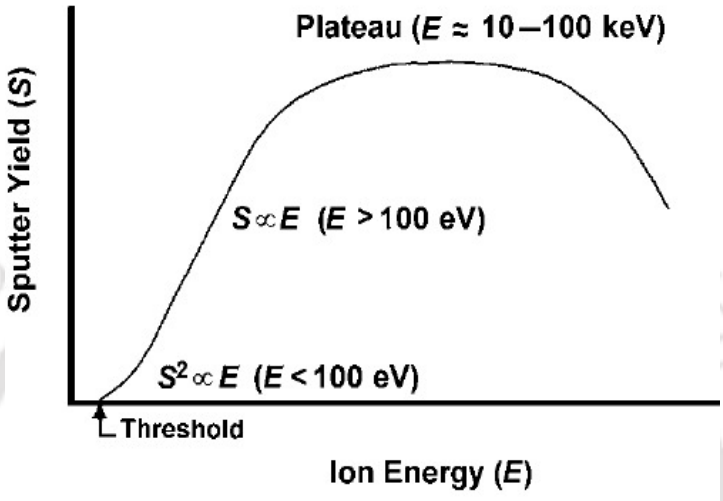

Figure 2.3: Sputtering yield as a function of incident ion energy [168].

Target Materials:

Enormous experimental results have given different yield values and the yield increases with increase in d – shell electrons and reaching a maximum value for gold, silver and copper [169]. Conversely, elements with the most open electronic structure result in the least sputtering yields. The sputtering yields are directly proportional to the energy transfer factor and the hardness of the atoms since hard collisions increase the yield.

Incident Angles of Particles:

The angle of incident is another parameter that governs the sputtering yield. This yield increases with increase in angle of incident (θ_i) and a maximum yield is obtained for θ_i in the range of 60° and 80° [169].

Formation of glow discharge plasma depends upon the type of voltage supplied to the electrodes. Various types of voltage source and/or reactive gas is used to generate the plasma. The sputtering process is distinguished as DC, RF, Magnetron and reactive gas sputtering. The DC-Sputtering is often used to deposit the metallic films and the RF Sputtering i.e. with AC voltage is used to deposit dielectric and oxide related

TH-1726_11612111

semiconducting films. In DC Sputtering, the voltage is set from 3-5 kV and in the case of RF Sputtering, a standard RF power supply set at a frequency of 13.56 MHz is used with a typical power of 50 W.

DC-Sputtering

The DC-sputtering looks similar that shown in Fig. 2.1 but here the power is given through a dc source. Here, the target and the substrate are faced to each other with a separation of a few centimetres distance. The target is connected to a negative terminal of a DC power supply which acts as a cathode and the other terminal is connected to the substrate which acts as a anode. The DC-power is supplied across the electrodes that would generate plasma once Ar gas enters in between the electrodes. The Ar^+ ions in the plasma (ionized by the energetic electrons confined by the magnetic field around the target) will be accelerated toward the cathode such that they hit the target and transfer the energy. As a result the plasma starts sputtering the target. The above sputtering is achieved after maintaining the vacuum pressure of 1-100 mTorr in the chamber. DC sputtering suffers from two major drawbacks as compared to conventional evaporation: (i) low deposition rates and (ii) high thermal load of the substrate due to bombardment of secondary electrons. DC sputtering works with all conductive target materials. However, it is difficult to sputter the insulating materials by this technique because the positively charged ions can't flow through the insulator and hence the electric circuit is interrupted.

Magnetron Sputtering

In magnetron sputtering, the magnetic field helps to enhance the efficiency of initial ionisation process and also helps to trap the electrons in the vicinity of target. A bar magnet mounted on the back side of target is shown in Fig.2.4. The magnetic field lines start from a north pole of the magnet that creates an arch over the target. These lines reach the opposite pole of the magnet passing through the target surface. Once the ionisation process started, the trajectory of emitted electrons is in spiral path when they encountered parallel magnetic field. Here, the component of magnetic field is established parallel to the target surface and perpendicular to the electrical field. Thus, the ejected electrons are confined over the surface of the target. Therefore, the trapped electrons substantially increase the probability of ionizing by electron-atom collisions. This process leads to the formation of dense plasma around the target to produce high deposition rate. In addition to higher deposition rate, the

TH-1726_11612111

magnetron helps to create plasma at low operating pressures (10^{-3} mbar) and low operating voltage (around - 300 V).

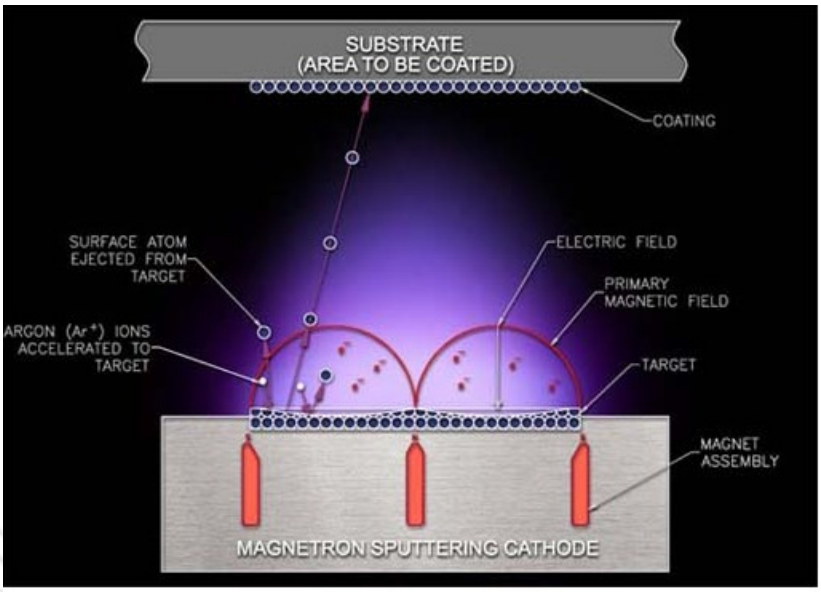

Figure 2.4: Schematic representation of magnetron sputtering gun process.

Reactive Sputtering

In reacting sputtering, the sputtering takes place in the presence of a reactive gas, such as oxygen or nitrogen etc., along with gaseous mixture of starting compounds to maintain the appropriate chemical composition of the thin film This is often used to improve the deposition rate of insulating oxide thin films. Therefore, the addition of reactive gases to the sputtering chamber can importantly affects the deposition rate and stoichiometry of the compound.

RF-Magnetron Sputtering

RF-sputtering also follows the ion bombardment mechanism which results in the erosion of the surface of respective target. The DC-sputtering glow discharge cannot be sustained for insulator target because of the immediate build up of a surface charge of positive ions on the front side of the insulator. Hence a stable glow discharge will be achieved in the insulator targets once the DC power supply is replaced by a RF power supply and the system is called as RF sputtering system. Robertson and Clapp noticed sputtering in the RF discharge in 1933, while the glass surface of the discharge tube was sputtered during the RFdischarge. This system requires an impedance matching between the power supply and glow discharge. The impedance of the power supply is mostly maintained at 50 Ω and the glow discharge is having magnitude of the orders 1 to 10 kΩ.

TH-1726_11612111

The cathode current density is given by $i_s = C\frac{dV}{dt}$, here C is the capacitance between the discharge plasma and the target, and dV/dt denotes the time variations of the target surface potential. This indicates that the increase of the frequency increases the cathode ion currents. In practical systems, the frequency used is 13.56 MHz. We have used a RF magnetron sputtering supplied by Advanced Process Technology, Pune, India, to deposit single and bilayer thin films as shown in Fig.2.5.

Figure 2.5 : Photographic view of the RF magnetron sputtering system.

The upper flange of sputtering system is connected to the chamber such that it can be lifted easily for accessing the chamber. There is a water feed through given from top to the substrate platform in order to prevent any damage to the o-ring while heating the substrate. The substrate is fixed on the substrate holder by using the clamps. Entire platform can be rotated along the axis perpendicular to the plane of the substrate. Inside chamber, two cathodes are mounted with facility for water feed through. The RF power inlets are taken from the bottom surface of the chamber. The optimized distance of separation between the substrate holder and the target on the cathode is around 4.5 cm. The chamber is connected to a high vacuum pump, to pump down the chamber pressure to the base pressure 3×10^{-6} mbar. Thereafter argon gas is allowed to enter into the chamber by monitoring the percentage of the gas mixture with mass flow controllers (MFC). The chamber pressure is constantly maintained on a desired pressure by controlling through high vacuum valve attached to the chamber. In RF magnetron sputtering, the chamber pressure is fixed around 4×10^{-2} mbar, whereas RF power is maintainedat 50 W. The

TH-1726_11612111

substrate temperature is set at two different temperatures, 400°C and 650°C. Uniform thickness and homogeneous composition of thin film can be achieved due to stable plasma which is controlled by the magnetron. It helps to maintain the localised plasma over the target material.

2.2 Characterisation Techniques

2.2.1 X-ray diffractometer

X-ray diffraction patterns help to understand the crystal structure of the materials. In this technique, a beam of X-ray is incident on the powder or thinfilm samples, which contain the lattice planes separated by a distance of a few Angstroms unit that is comparable to the wave length of the monochromatic X-ray. The scattered X – ray from the surfaces of several parallel lattice planes undergo constructive interference depending on the interplanar distance and the inclination angle (θ) of the X – ray and they obey Bragg's diffraction law as follows

$$n\lambda = 2dsin\theta \tag{2.2}$$

Here n is order of the spectrum, λ is wavelength of incident X-ray beam, d stands for the lattice spacing between the two consecutive planes corresponding to particular Miller indices, (hkl) [170].

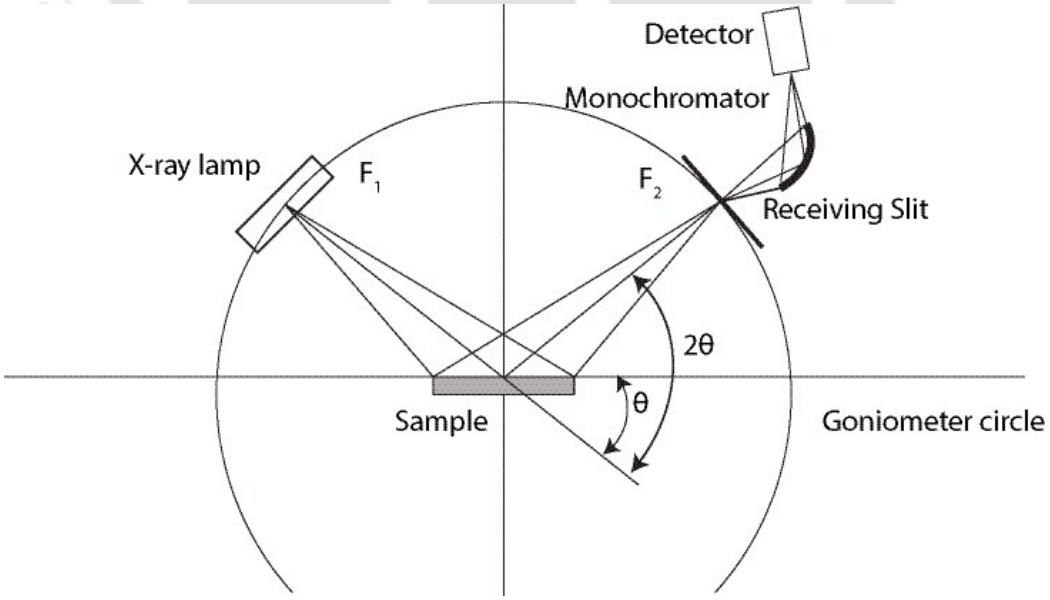

Figure 2.6: Ray diagram of X-ray diffractometer.

TH-1726_11612111

Chapter 2

In the present thesis work, we have recored XRD patterns of bulk and thin films with the help of Rigaku make TTRAX III diffractometer with CuK $_{\alpha}$radiation ($\lambda = 1.5406$ Å). In the present investigation, XRD patterns were collected on each of a sample with a setting of 50 kV voltage and 200 mA tube current of X-ray generator. The ray diagram is shown in Fig.2.6. In this geometry, the source to sample distance and sample to detector distance are kept equal.

The XRD patterns of bulk samples are analysed by using FullProf suite software with the help of Rietveld refinement technique. The background was refined by choosing a polynomial function and the peak shape was fitted to Pseudo Voigt function. The global parameters, such as coefficients of background polynomial, scaling factor, half width parameters (u,v,w) and lattice paramters (a,b,c) were mainly varied during refinement. In addition to that nuclear structure variables such as fractional atomic coordinates (x,y,z), isotropic displacement parameters and occupancy values are varied. Here, occupancy is the chemical occupancy normalised to the multiplicity of the general positions of the group. The occupancy of oxygen was taken as 1 (100%) for all the refined parameters and it was not varied during the refinement. The quality of refinements are known based on the values of reliability factors such as R $_{p}$, R $_{wp}$, R $_{exp}$, R $_{Bragg}$, R $_{F}$ and χ^2 and they are defined as follows

$$\text{Profile factor } R_F = \frac{\sum_{i=1,n} |y_i - y_{c,i}|}{\sum_{i=1,n} y_i} \times 100 \qquad (2.3)$$

Here, y $_{i}$ is the observed data and y $_{c}$, i is the calculated data and n represents the number of data points. Weighed profile factor,

$$R_{wp} = \left[\frac{\sum_{i=1,n} \omega_i |y_i - y_{c,i}|^2}{\sum_{i=1,n} \omega_i y_i^2}\right]^{1/2} \times 100 \qquad (2.4)$$

Here, $\omega_i = \frac{1}{\sigma_i^2}$, σ_i^2 is the variance of y_i.

Expected weight factor,

$$R_{exp} = \left[\frac{|n-p|}{\sum_{i=1,n} \omega_i y_i^2}\right]^{1/2} \times 100 \qquad (2.5)$$

Here, (n-p) is the number of degrees of freedom, n is the total number of experimental data points and p is the number of refined parameters.

TH-1726_11612111

$$\text{Reduced chi-square, } \chi^2 = \left[\frac{R_{wp}}{R_{exp}}\right]^2$$

$$\text{Bragg factor, } R_B = \frac{\sum_h |I_{obs,h} - I_{calc,h}|}{\sum_h I_{obs,h}} \times 100 \quad (2.6)$$

Here h is the vector which levels the Bragg reflections. The $I_{obs,h}$ is the observed integrated intensities and $I_{calc,h}$ is the calculated intensities.

$$\text{Crystallographic R}_\text{F}\text{factor, } R_F = \frac{\sum_h |F_{obs,h} - F_{calc,h}|}{\sum_h F_{obs,h}} \times 100 \quad (2.7)$$

$F_{obs,h}$ is the observed structural factor and $F_{calc,h}$ is the calculated structural factor.

XRD Patterns of Thin Films

Thin film is a two dimension object grown on a substrate and the thickness of the film is very small compared to the other two dimensions. Therefore, the conventional powder diffraction technique does not yield high quality diffraction patterns on thin films due to the strong background signal. Hence the methods like $\theta - 2\theta$ scan, grazing angle incident, ϕ - scan and rocking curves, etc. give information about the crystal structure and the epitaxial nature of films etc. Additional tehcnique such as X – ray reflectivity gives information about film thickness, inter – layer diffusion etc. A thin film can be either grown on amorphous, polycrystalline or single crystal substrate. In the first two cases the films can be mostly in polycrystalline form and in some cases, we even end up getting only amphorous films. In the third case, one can achieve epitaxial growth of films similar to that of single crystalline material. Before starting the X-ray scan of a thin film, the sample and mounting platform have to be aligned in the direction of z - axis and the tilting angle of platforms, i.e. R_x and R_y, must be adjusted to the goniometer and detector. This alignment is required to get the noise free high intensive XRD patterns. X-ray diffraction measurements can be performed on thin films is by two different methods, i.e. out-of-plane and in-plane setting as described below.

Out-of-Plane XRD Measurement

This is the most common technique used for studying the crystal structure of a powder sample as well as of thin films. Out-of-plane XRD patterns are obtained from both symmetrical and asymmetrical measurements. Symmetrical measurement is a method to collect the diffraction patterns from the thin film perpendicular to the plane of the thin film

TH-1726_11612111

surface. The symmetric reflections of a thin film can be obtained once the incident angle and the diffracted angle of the x-ray beam are equivalent against the plane of the film. This is shown in Fig.2.7(a). Well known $2\theta - \theta$ technique is used for symmetrical reflection measurement. Fig.2.7(b) illustrates the asymmetric measurement. This measurement is performed under a specific diffraction geometry in which the X-ray beam is kept at small angle with respect to the film surface and the detector on 2θ axis to record diffraction intensities from the film.

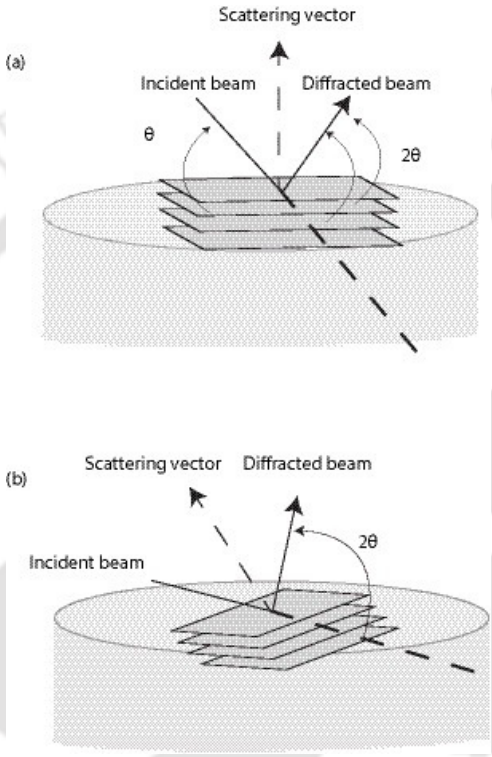

Figure 2.7: Different geometries of out-of-plane XRD measurement in (a) symmetric and (b) asymmetric axes

In-Plane XRD Measurement

This technique is basically used to improve the intensity of the films with minimising substrate contribution. In this technique, the X-ray beam is allowed to incident along the grazing axis of film, which successfully increase the intensity of the film. This technique is able to measure the lattice planes normal to surface of film. In this measurement (thin film measurement), the scattering vector (the normal vector of the lattice planes) of the planes is pointed out from the sample surface but in case of the in-plane measurement the scattering vector lies parallel to surface of the thin film. Here, the incident angle ($\omega = 2\theta/2$) of the x-ray beam can be controlled independent of sample rotating angle

TH-1726_11612111

(φ) as well as the detector position ($2\theta_\chi$). Fig.2.8 depicts the grazing incident arrangement of X-ray Diffraction.

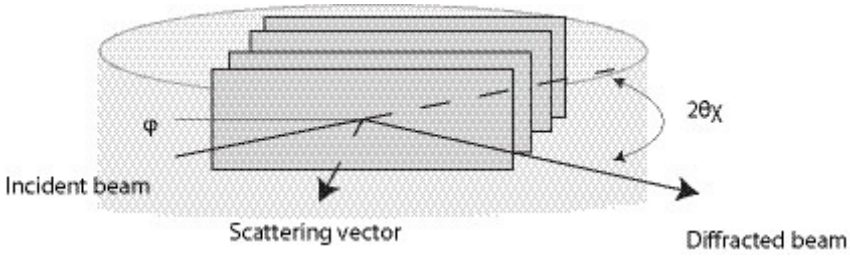

Figure 2.8: In-plane geometry XRD measurement.

2.2.2 Raman Spectroscopy

Raman spectroscopy is a versatile tool for studying the crystal structure and their bonding information. Raman spectroscopy is a form of vibrational spectroscopy, much like infrared spectroscopy. Nevertheless, the infrared bands arise from a change in the dipole moment of a molecule due to an interaction of light with the molecule, Raman bands arise from a change in the polarizability of the molecule due to the same interaction. This means that these observed bands (corresponding to specific energy transitions) take place from specific molecular vibrations.They can be used to identify the molecule as they provide a fingerprint of the molecule being observed. Certain vibrations that are allowed in Raman spectroscopy are forbidden in IR spectroscopy, whereas other vibrations may be observed by both techniques although at considerably different intensities thus this techniques can be a complementary. The Raman spectrum provides details about various frequency at which the radiation is absorbed by the molecule for transition into higher vibrational energy states. When light is scattered from a molecule or crystal, the majority of photons are elastically scattered. The scattered photons have the same energy (frequency) and, wavelength, as that of incident photons. On the other hand, a small fraction of light (approximately 1 in 107 photons) is scattered at optical frequencies different from the incident photon, i.e. typically lower than, the frequency of the incident photons. This process of inelastic scattering is termed as the Raman effect. Raman scattering can occur with a change in vibrational, rotational or electronic energy of a molecule. If the scattering is elastic, the process is called Rayleigh scattering. If it's not elastic, the process is called Raman scattering. Since the discovery of the Raman effect in 1928 by Sir. C.V. Raman, for which he got the Nobel Prize in 1930, Raman spectroscopy has become an established as well as a practical method of chemical analysis and this method is applicable to many

TH-1726_11612111

different chemical species. If the substance being studied is illuminated by monochromatic light, for example by a laser beam, the spectrum of the scattered light consists of a strong line (the exciting line) of the same frequency as the incident illumination together with weaker lines on either side shifted from the strong line by frequencies ranging from a few cm^{-1} to about 3500 cm^{-1}. The lines of frequency less than the exciting lines are called Stokes lines, the others anti-Stokes lines. Raman spectroscopy is very significant practical tool for quickly identifying molecules and minerals. Raman spectroscopy also has important scientific applications in studying molecular structure. To characterize the samples with Raman spectroscopy, samples may be in the form of solids (particles, pellets, powders, film, and fibers), liquids (gels, pastes), and gases.

The Raman studies reported here are performed using Haribo Labram Raman spectrometer with Ar^{+} laser with excitation wavelength of 488 nm and 514 nm. However, for a given series of samples all the measurements are done with the same spectrometer under the same condition. These studies are done on the single layer films deposited on Al_2O_3, MgO and $LaAlO_3$ substrates and the spectra are recorded in the range of 150 - 1000 cm^{-1}.

2.2.3 Atomic Force Microscopy

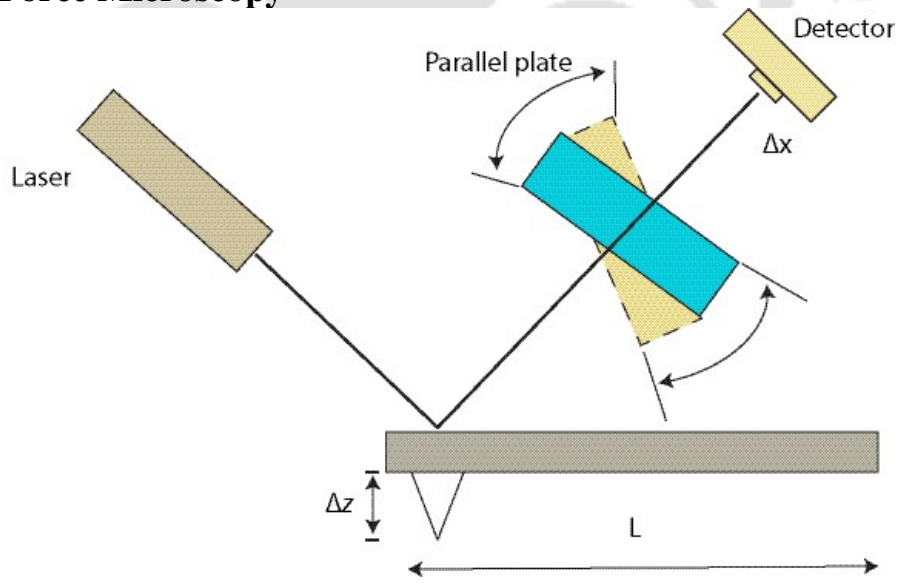

Figure 2.9: Schematic diagram of atomic force microscope instrument.

Atomic force microscope was used to record the topographic images of sample surface. AFM is developed based on the method of scanning tunnel microscope (STM). STM is capable of recording 3-dimensional surface image down to the atomic level. In

TH-1726_11612111

STM, the tunnelling current is sensed from the conducting solid surface to the metallic cantilever with the separation of 0.3 - 1 nm. The STM senses upto 0.2 nm in parallel and 0.01 nm along the normal to the surface. STM is more capable to give high resolution images than AFM, but this technique is used only for the conducting surface. Therefore, AFM gives the high resolution 3-dimensional images compared to other techniques like SEM, FESEM, optical microscopy. AFM is far better than the surface profilometry, because it can quantitatively measure the physical, chemical, magnetic, frictional and electrostatic interface forces with high spatial resolution. However, AFM has to measure the ultra low forces in the range of $10^{-3} - 10^{-9}$ N.

The schematic diagram of the AFM is shown in Fig.2.9. In this technique, there is small tip arranged on rear part of cantilever and it helps to measure resonant frequency of cantilever while it is rapidly moved onto the sample surface. Topographic images of all thin films were measured with silicon nitrade tip. In general, the tip has diameter of a few nano meters. The set up is arranged such that reflected laser beam from the contilever is focussed to the photo – detector. The measured force gradient between tip and surface of the sample is related to the number of photons (in terms of volts) reaching the detector. The reflected photons vary due to the imbalance created by deflections of the cantilever and hence it is seen as change in photo – current. Topographic image is taken based on operating mode of the instrument. They are contact (tapping) mode and non-contact mode. Both techniques are used to measure the topographical image of the sample from the interactive force (force gradient) between tip and sample surface. There is a small difference between these two methods. In contact mode, the image is measured by the interaction force of the cantilever oscillations. But in the case of non-contact mode, the imaging is obtained from the force gradient obtained by the cantilever oscillations and by measuring the shifting of resonant frequency of the cantilever. In this thesis work, all films are characterised in non-contact mode with Agilent made AFM model no:5500.

2.3 Electrical Resistivity Measurements

Temperature variation of electrical resistivity, in the temperature range of 30 K to 300 K, was measured by the standard four probe method. In order to cool down the sample, a top loading helium exchange gas cooled type closed cycle helium refrigerator cryostat fabricated by: Advanced Research System, USA using a helium compressor and cold head motor has been used. The temperature was recorded by using a Lakeshore temperature

TH-1726_11612111

controller, Model no: 335 and also a Lakeshore calibrated Si-diode sensor mounted on the cold head.

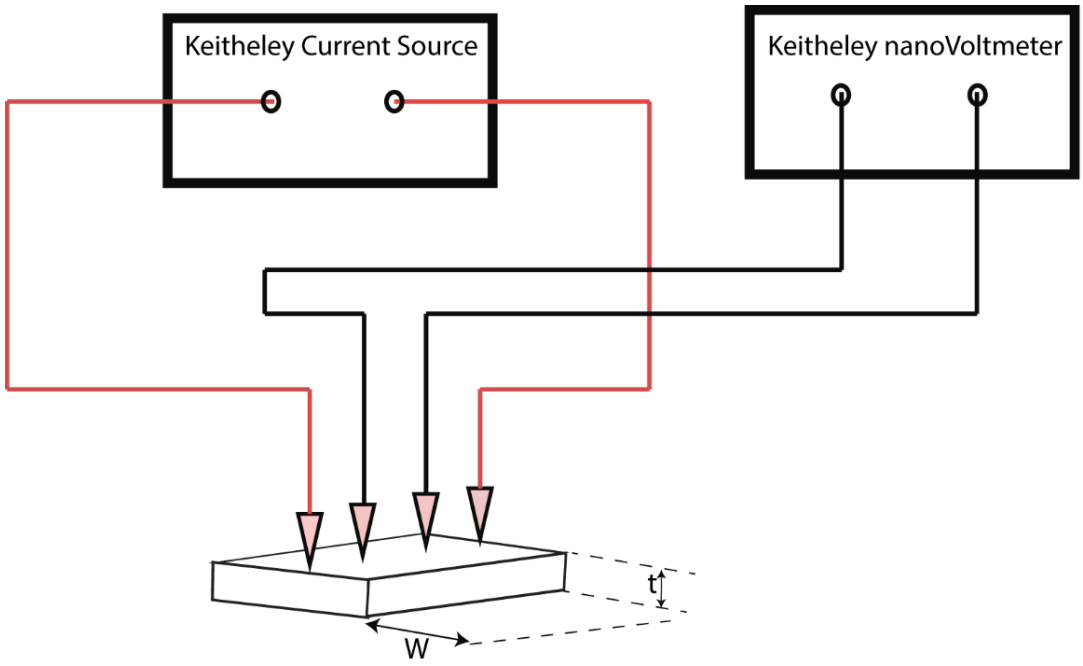

Figure 2.10: Block diagram of resistivity setup using the standard four probe method.

Standard four probe technique was used to eliminate the contribution from contact resistance and lead resistance coming into picture. A constant current (fixed in the range of 1 - 0.01 micro Amp, depending upon the sample nature) was passed through the sample using Keitheley current source of model no-224. The voltage drop across the sample was measured by the Keitheley nano volt meter, model no-2182. Block diagram of the standard four probe method is shown in Fig.2.10. To eliminate the thermo-emf generated across the voltage leads, measurements were carried out for both positive and negative currents. The experimental data were collected using a personal computer equipped with GPIB board.

In order to record the temperature variation of electrical resistivity, the sample was mounted on the fabricated sample holder attached to the CCR cryostat and is shown in Fig.2.11. The enlarged view of the thin film coated with four silver stripes to measure the film resistivity is shown in Fig. 2.11. For calculation of electrical resistivity, the dimension of the samples determined by using vernier caliper and the thickness of the film determined from Stylus Profilometer are used.

TH-1726_11612111

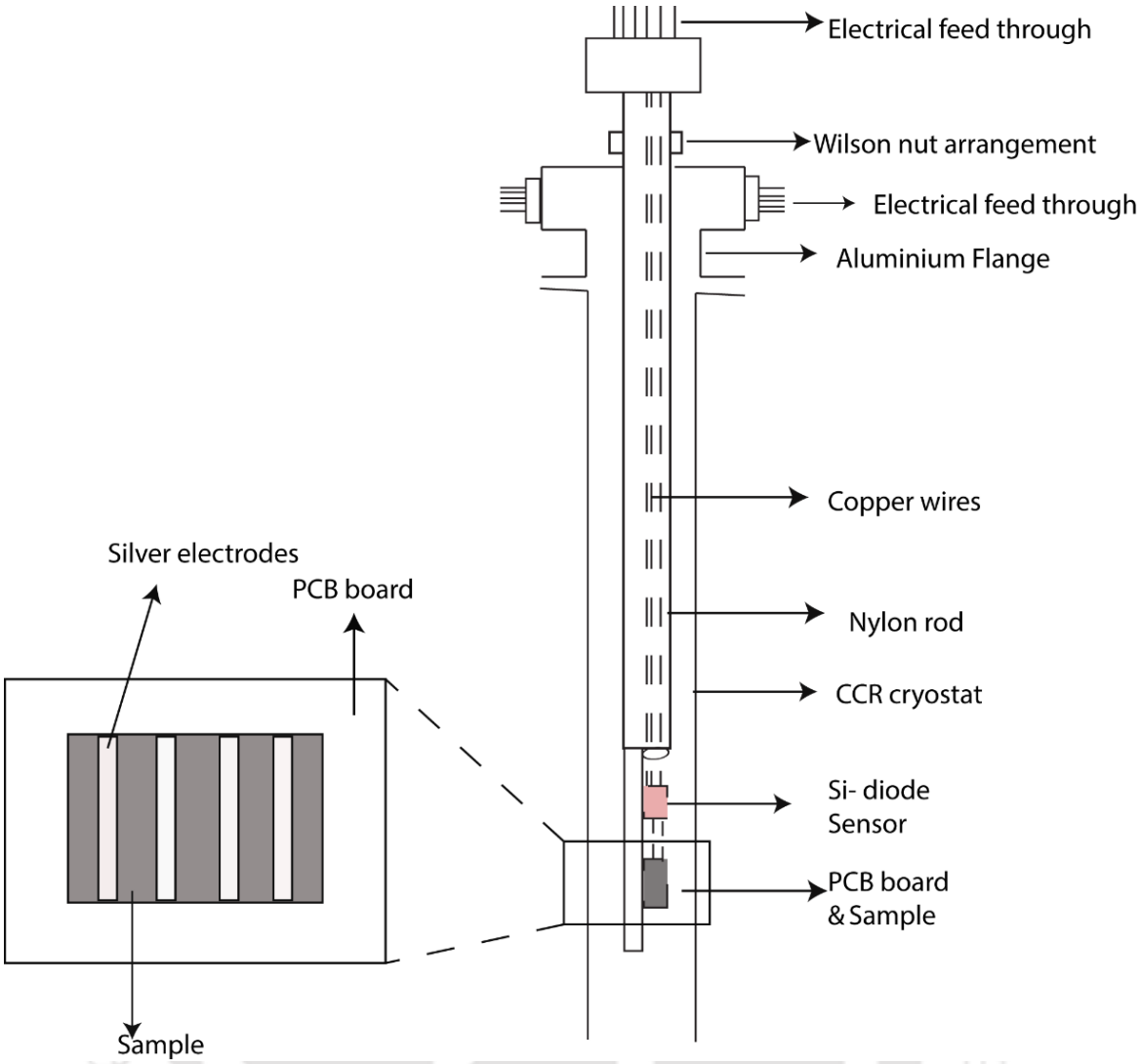

Figure 2.11: A block diagram of the four probe method along with the CCR cryostat and the zoomed view of sample with electrical contacts.

2.3.1 Magneto-Resistivity Measurements

Transport property of a few manganite thin films were measured using standard four-terminal method with the help of a Quantum Design PPMS-6000 system. The PPMS-6000 system can facilitate the measurements in the temperature range of 2 - 300 K. Temperature sweep capability allows measurements to be taken while sweeping the temperature at a user defined rate (0.01-6 K/min). The PPMS has a superconductor magnet, which can provide a magnetic field up to 9 Tesla with the uniformity of ±0.01% over a 5 cm x 5 cm diameter square volume. The low noise, bi-polar power supply allows continuous charging through zero field with current compensation and over-voltage protection. A schematic illustration of the PPMS 6000 probe is shown in Fig.2.12 and a sample mount puck is shown in inset.

TH-1726_11612111

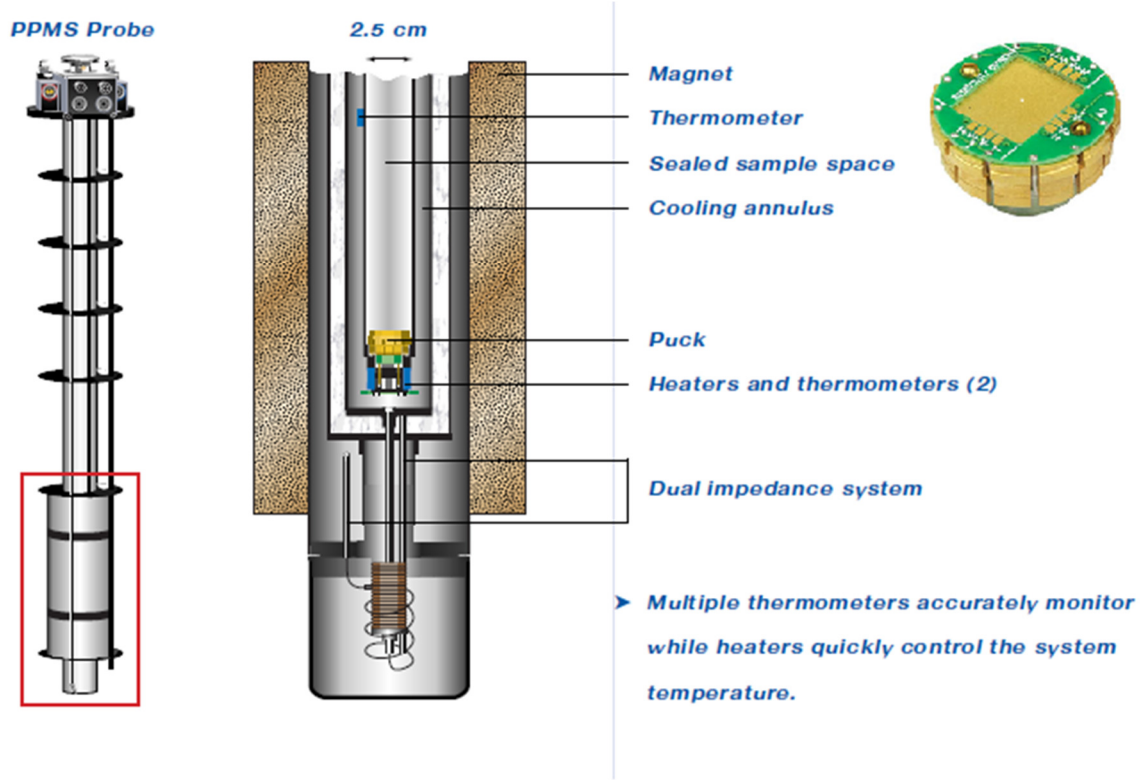

Figure 2.12: A schematic diagram of PPMS (As per Quantum Design)

As we mentioned above, the magneto-resistance was measured using standard four probe method. Before starting the measurement, thin films were mounted on a puck which helps in maintaining the electrical contact with samples then the samples were introduced (as shown in Fig.2.12) into the chamber at room temperature. The chamber was cooled down from room temperature to 10 K with cooling rate of 12 K/min, thereby the cooling rate of the chamber changed to 2 K/min until the required temperature reaches 2 K. After a stable temperature achieved at 2 K, 1 micro Ampere current was allowed to pass through the sample and the voltage drop across other two leads were measured. Magneto-resistance measurement was carried out in the warming mode from 2 K to 300 K in absence of field and in another run of the sample in the presence of 5 Tesla magnetic field applied along the plane of the film.

2.4 Magnetic Properties

2.4.1 Vibrating Sample Magnetometer

Vibrating Sample Magnetometry (VSM) is a versatile measurement technique which allows to determine the magnetic moment of a sample with high precision. This is the most common technique to get the information about the magnetic properties of magnetic materials. VSM works based on Faraday's law which states that an

TH-1726_11612111

electromagnetic force is generated in a coil when there is a change in flux through the coil. The sample which is fixed to the sample rod vibrates with a given frequency and amplitude. It is centered between the two pole pieces of an electromagnet that generates a magnetic field *H* of high homogeneity. As a result, a dipole moment is induced that is proportional to the product of sample susceptibility and applied magneticfield. The oscillation provides an electrical signal that is collected by the pick up coils. Lock-in amplifier and feedback techniques is used to convert the signal from the pickup coil into magnetic moment.

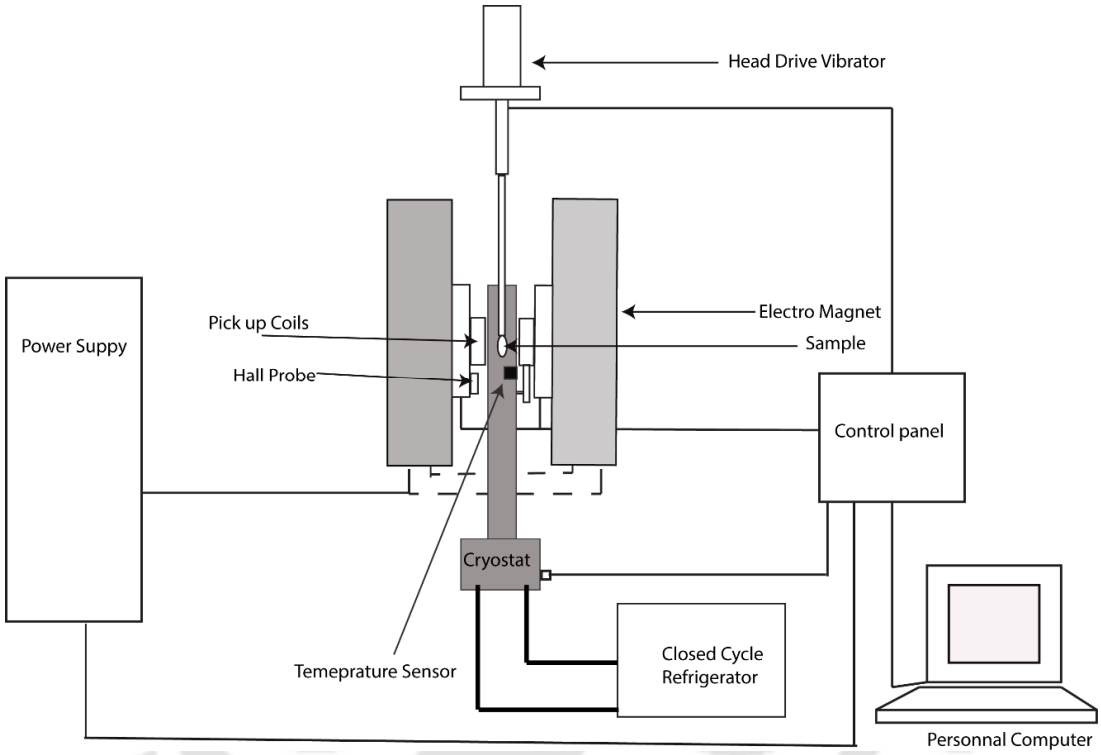

Figure 2.13: Block diagram of the vibrating sample magnetometer

The thin film sample was fixed at lower end of the sample rod aligning the plane of the film parallel to the applied field. Before starting the measurement of a sample, vibrating sample magnetometer was calibrated by using a standard Ni sample. Fig. 2.13 illustrates the block diagram of the vibrating sample magnetometer. Once the magnetic sample is mounted on the sample holder in between the poles of the magnet. The magnet is switched on to generate the required field to induce a dipole moment. As a result, there is an electro motive force induced in the pick up coils, which is proportional to the magnetic moment of the sample. Voltage can be detected to high resolution and accuracy by means of suitable VSM signal detector. VSM (Lakeshore, model no: 7410) was used to measure the temperature variation of magnetic properties in the temperature range of 25 K to 300 K. Oxford make closed cycle refrigerator (CCR) cryostat was used to cool down the

TH-1726_11612111

temperature of the sample down to 25 K. The magnetic moment is recorded either as a function of temperature or field to study the various magnetic properties. A maximum magnetic field of about 1 T is used to measure the hysteresis loops.

2.4.2 Electron Spin Resonance Spectrometer

Electron spin resonance (ESR) is a technique used to record electromagnetic wave absorbed by the magnetic sample under the influence of external DC magnetic field. ESR works based on the principle of Zeeman effect, where the electronic energy level split into several components in the presence of the magnetic field. The energy difference between the two energy levels is

$$\Delta E = g\,\mu_B\,B \tag{2.8}$$

where, g, μ_B and B represent the Lande g-factor, Bohr magneton and the applied DC magnetic field respectively. As the sample is exposed to the microwave radiation some of the electrons in the lower energy state are excited to higher energy levels when the sample is placed in between the magnetic poles. Once the magnetic field tunes the two spin states, the energy difference matches the energy of radiation. As a result an absorption peak will occur.

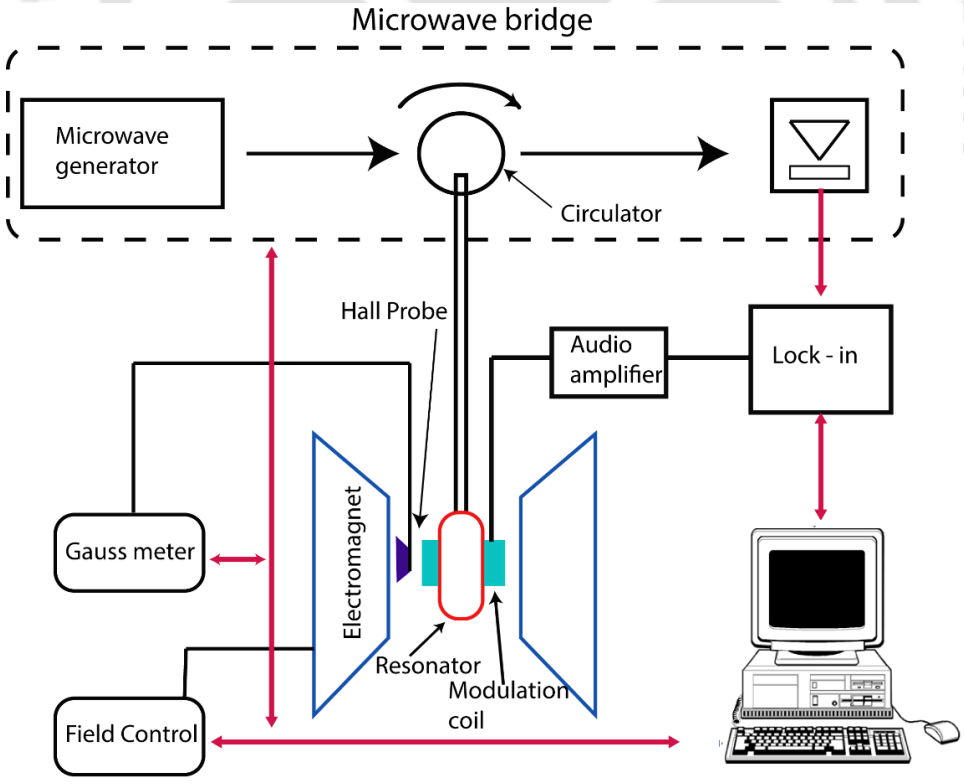

Figure 2.14: Schematic diagram of electron spin resonance spectrometer

TH-1726_11612111

Fig. 2.14 depicts the block diagram of ESR spectrometer. Microwave bridge is an integrated set up which contains the source, detector, protected electronics etc. The sample is mounted inside the chamber of the resonator which lies between the poles of an electromagnet. Once the microwave absorbed by the sample, the detector receives the change in the signal due to either transmittance or reflectance of the microwave while varying the magnetic field. Typically a commercial spectrometer works by varying the magnetic field and holding the frequency constant. ESR spectrometers working at frequencies ranging from several hundred MHz to several hundred GHz are in use. Depending upon the operating frequency, the ESR spectrum is classified into L-band (1-2 GHz) and S-band (2-4 GHz), X-Band (8-10 GHz), Q-band (35 GHz) and W-band (95 GHz). The most commonly used ESR spectrometer is in the range of 9-10 GHz (X-band). In thesis work, we have used, the operating frequency fixed at 9.4 GHz.

TH-1726_11612111

TH-1726_11612111

Chapter 3
Deposition and Characterisation of $Nd_{0.7}Sr_{0.3}MnO_3$ Thin Films

TH-1726_11612111

TH-1726_11612111

Chapter 3

3.1 Introduction

Hole doped perovskite manganite thin films continue to draw the research attention due to their rich physical properties such as ferromagnetic metallic behavior around room temperature and the existence of huge magnetoresistance in the vicinity of metal – insulator transition temperature. The physical properties of La-Mn-O films doped with 30 at.% of divalent ions such as Sr, Ca, Ba etc. depend strongly on growth conditions, thickness of the film and post-deposition annealing temperature, etc. [171, 172].

The functional properties of manganites films strongly depend on the nature of substrates and the subtrate induced lattice strain [173]. The lattice strain depends on the lattice mismatch between the film and the substrate and is generally estimated using the relation $\frac{as-af}{as}$, where a_s and a_f are lattice constant of the substrate and the film respectively. For $a_s < a_f$ films undergo in-plane compressive strain and for $a_s > a_f$ films undergo in-plane tensile strain [173]. A large lattice mismatch between substrate and film leads to growth of films in polycrystalline form and it severely affects their electrical and magnetic properties. Small lattice mismatch between substrate and thin film gives rise to epitaxial growth of thin films with superior functional and physical properties comparable to that of their bulk counter part [174, 175].

In this chapter, we report the study of structural, electrical transport and magnetic properties of $Nd_{0.7}Sr_{0.3}MnO_3$ (NSMO) thin films by varying the post-annealing conditions and by choosing different substrates such as Al_2O_3, MgO, and $LaAlO_3$. In addition to that the effect of film thickness on electrical and magnetic proeperties of NSMO films are studied.

3.2 Preparation and Characterisation of $Nd_{0.7}Sr_{0.3}MnO_3$ Target

Bulk $Nd_{0.7}Sr_{0.3}MnO_3$ (NSMO) was prepared as a target material by using conventional solid state reaction method. Nd_2O_3, $SrCO_3$ and $C_4H_6MnO_4.4H_2O$ of 99.9% purity were taken as starting materials. The stoichiometric ratio of the above compounds were weighed, grinded under acetone medium and pre-sintered in the temperature range 400°C -800°C. Thereafter, the presintered power was pressed into cylindrical target of two inch diameter with a thickness of around 3 mm by using a cylindrical die of appropriate dimension and a hand operated hydraulic press with a pressure of 5 tons/cm^2. The above

TH-1726_11612111

target was annealed at 1100°C for 24 hours followed by furnace cooling to room temperature.

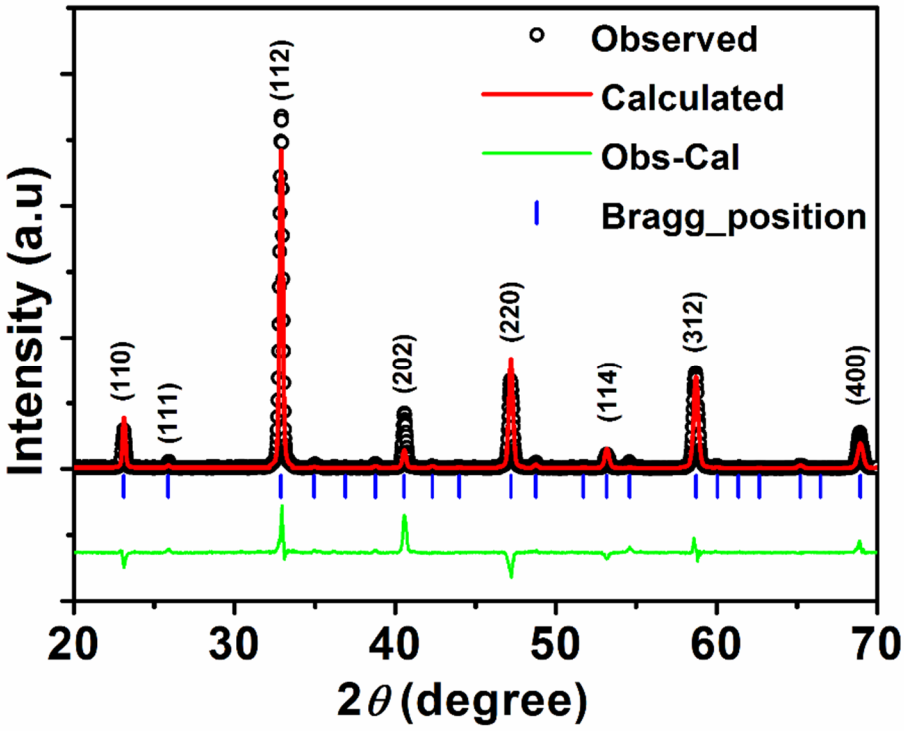

Figure 3.1: XRD pattern of the bulk NSMO target material.

Fig.3.1 illustrates the phase nature of the sample with Pbnm space group as per Rietveld refinement using Fullprof program. The lattice parameters of the sample are found to be a'= 5.544 Å, b'= 5.441 Å and c'= 7.697 Å. The pseudo cubic lattice constant of the target material within the *ab* - plane is found to be *a* (= $a'/\sqrt{2}$) = 3.850 Å, b (= $b'/\sqrt{2}$) = 3.847 Å and c (= $c'/2$) = 3.848 Å.

Temperature variation of magnetization (*M*) was measured for an applied field of 200 Oe and is shown in Fig. 3.2 (a). NSMO material exhibits the ferromagnetic transition and the transition temperature (T_C) is found to be 225 K. The T_C is determined from the plot of dM/dT versus temperature plot as shown in the inset of Fig.3.2(a). The T_C is comparable to that reported in literature [176, 177]. Temperature variation of electrical resistivity was measured from 30 K to 300 K and it a exhibits metal-insulator transition at 185 K as shown in Fig. 3.2 (b). Thus the prepared NSMO target is of single phase in nature with best physical properties comparable to that of standard bulk NSMO.

TH-1726_11612111

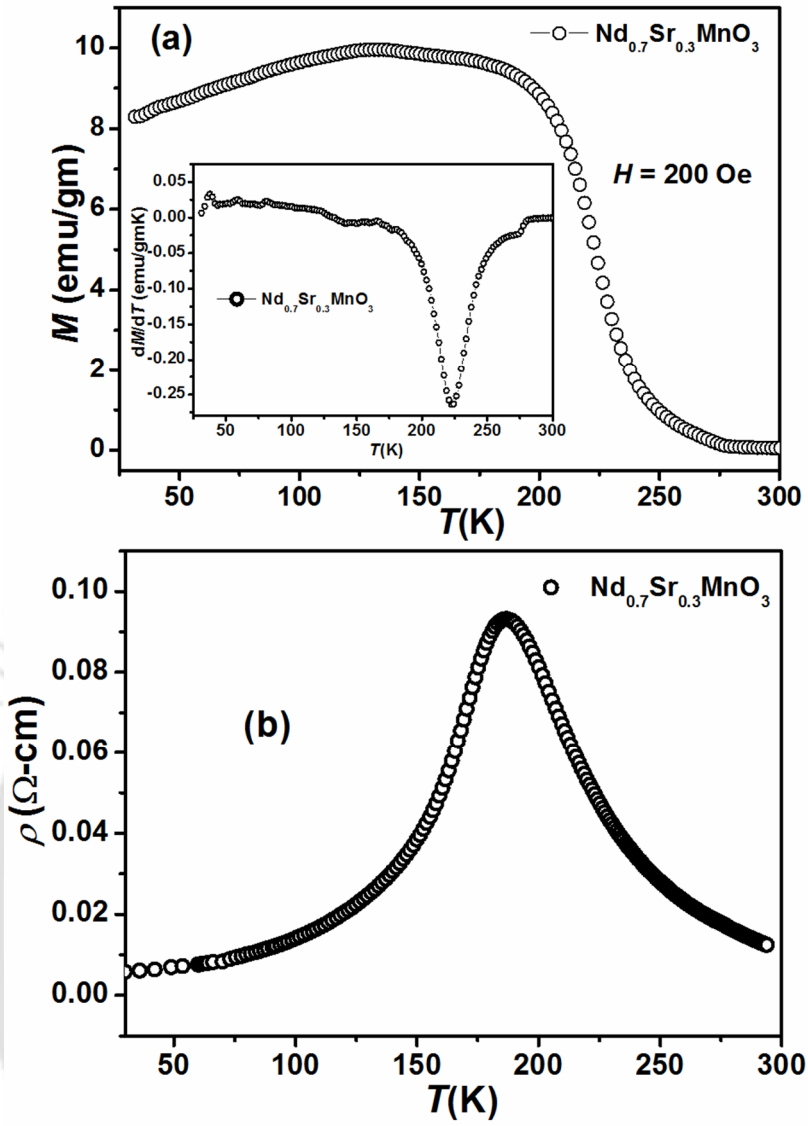

Figure 3.2: Temperature variations of (a) magnetization for the applied field of 200 Oe with plot of d*M*/d*T* vs *T* in the inset and (b) electrical resistivity for the bulk NSMO target material.

The above well characterized target was utilised to deposit thin films of NSMO by using RF magnetron sputtering unit. Deposition and growth of these films were optimized by tuning deposition parameters such as nature of substrate, substrate temperature, thickness of films, post-annealing temperature and post-annealing environment. In the following sections, they are described in detail. The NSMO films were deposited under various experimental conditions and were characterized by recording XRD patterns, atomic force microscope images, and Raman spectra and, by measuring electrical resistivity and magnetization data as a function of temperature and magnetic field.

TH-1726_11612111

3.3 $Nd_{0.7}Sr_{0.3}MnO_3$ Films under Different Post-annealing Temperature

3.3.1 Thin Film Preparation

$Nd_{0.7}Sr_{0.3}MnO_3$ (NSMO) thin films were deposited by using RF-magnetron sputtering unit on (001) oriented sapphire substrate (Al_2O_3). The well characterized NSMO target as discussed in section 3.2 was used to deposit the films. Initially the chamber was evacuated to the base pressure of 3×10^{-6} mbar and then Ar : O_2 gas mixture in the ratio of 3:1 ratio was allowed in the chamber to maintain a working pressure of 4.3×10^{-2} mbar. The substrate temperature was maintained at 400°C throughout the deposition and the RF power was set at 50 W. The deposited films were separated into three different batches and were post-annealed separately at 700°C, 800°C and 900°C in air for an hour. They are named as NSM7, NSM8 and NSM9, respectively.

3.3.2 Structural Properties

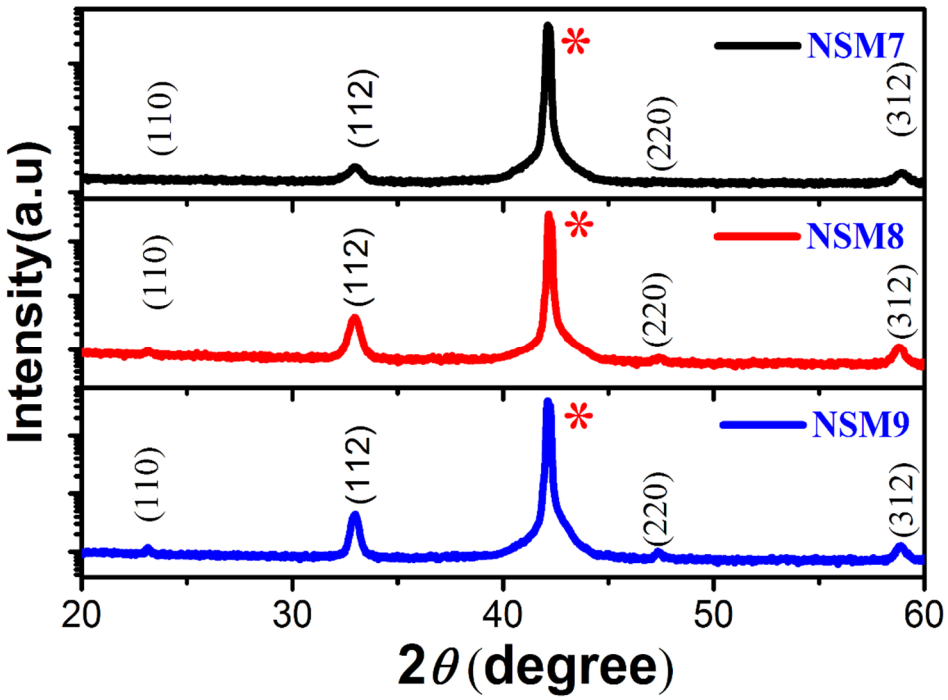

Figure 3.3: The θ–2θ scan of XRD patterns of NSM7, NSM8 and NSM9 thin films.The star mark represents (006) peak of the substrate.

TH-1726_11612111

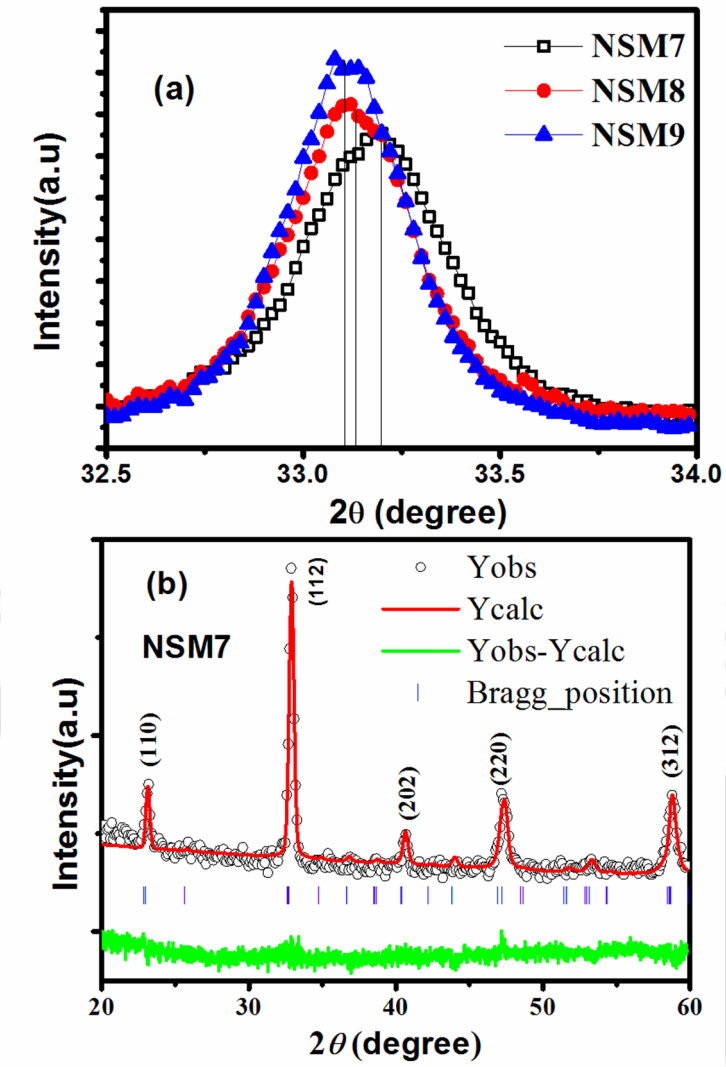

Figure 3.4: (a) Enlarged view of (112) peak of different films. (b) XRD pattern of NSM7 film along with Rietveld refinement. Here the petterns were recorded by using grazing incidence technique.

XRD patterns recorded at room temperature for NSMO films annealed at different temperatures are shown in Fig. 3.3. They are found to be in single phase form. The enlarged view of (112) peak of different films recorded by grazing incidence technique is shown in Fig.3.4(a). This peak is found to shift towards lower 2θ values with increase in annealing temperature. These patterns were refined by using Rietveld refinement method and Fullprof program by choosing Pbnm space group in orthorhombic cell. Typical XRD pattern along with refined data for NSM7 film is shown in Fig.3.4(b). The lattice parameter values are found to increase with increase in annealing temperature. The lattice parameters for NSM7, NSM8 and NSM9 films are found to be a = 5.440 Å, b = 5.432 Å and c = 7.618 Å ; a = 5.454 Å, b = 5.440 Å and c = 7.661 Å and a = 5.463 Å, b = 5.452 Å and c = 7.688 Å, respectively. Lattice strain on the films were calculated by using the relation [178],

TH-1726_11612111

$$\frac{(d-d_0)}{d_0} \times 100\% \quad (3.1)$$

where d is the lattice spacing of the film corresponding to (112) peak having high intensity and d_0 is the lattice spacing of the target material corresponding to same (hkl) value. These values are found to be -0.63, -0.46 and -0.39%, respectively and the negative sign indicates that the films exhibit compressive strain. The average crystallite size values of annealed films were determined with the help of Debye-Scherrer's formula i.e. $t = \frac{K\lambda}{\beta \cos\theta}$. Here, K is the dimensionless shape factor, λ is X-ray wavelength, β is full width half maximum intensity and θ is the Bragg angle. Here K was taken as 0.89 by assuming circular grain.The average crystalline sizes are found to be 21, 23 and 25 nm for NSM7, NSM8 and NSM9, respectively.

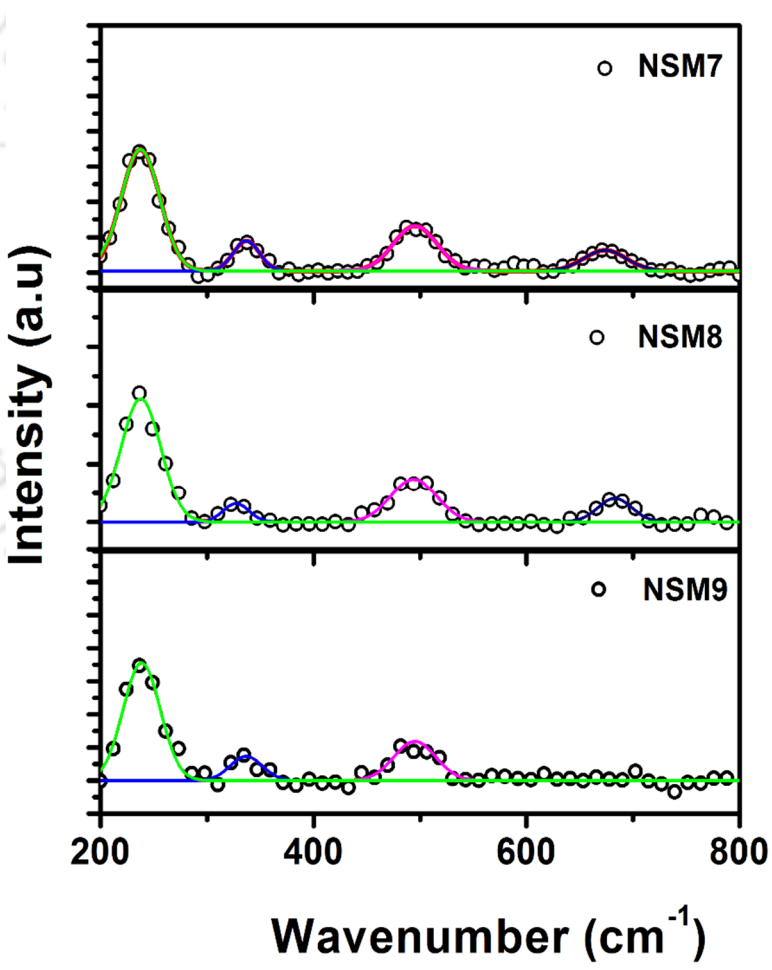

Figure 3.5: Room temperature Raman spectra of NSM7, NSM8 and NSM9 films along with Larentzian fit.

TH-1726_11612111

As per lattice dynamical calculations in orthorhombic perovskite structure, Iliev *et al.* [179] have shown the presence of 24 Raman active modes ($7A_g + 5B_{1g} + 7B_{2g} + 5B_{3g}$). In order to further understand the crystal structure and lattice distortion, we have recorded Raman spectra at room temperature for these three NSMO thin films over the wave number range from 200 to 800 cm^{-1}. Four well resolved Raman lines at 230, 330, 490 and 670 cm^{-1} are observed as shown in Fig.3.5. By comparing the lattice dynamical calculation of Iliev *et al.* [179] the lines at 230 cm^{-1} and 490 cm^{-1} can be attributed to A_g modes due to in phase y-rotation ($A_g(2)$) and out of phase bending of ($A_g(3)$) MnO_6 octahedra, while the line at 330 cm^{-1} is assigned to $B_{3g}(4)$ mode due to in-phase z-rotation and the line at 670 cm^{-1} is due to in-phase stretching ($B_{2g}(1)$). The line corresponding to in phase stretching mode of MnO_6 in xz plane at 670 cm^{-1} disappears upon annealing the film at 900°C, i.e. for NSM9 film shown in Fig.3.5. This can be attributed to reduction in compressive strain as per XRD analysis for the 900°C annealed film and the band at 670 cm^{-1} is probably sensitive to the above strain and lattice defect. This band is considered as disorder induced Raman feature due to oxygen deficiency by Podobedov *et al.* [174] in LCMO thin film. This is also supported by the observation of the shift in the frequency of this mode upon annealing under different oxygen partial pressures in $La_{0.7}Ca_{0.3}MnO_3$ [175]. The observed Raman lines in the present set of samples are comparable to those reported on bulk $Nd_{0.7}Sr_{0.3}MnO_3$ [180].

3.3.3 Morphology of NSMO Films

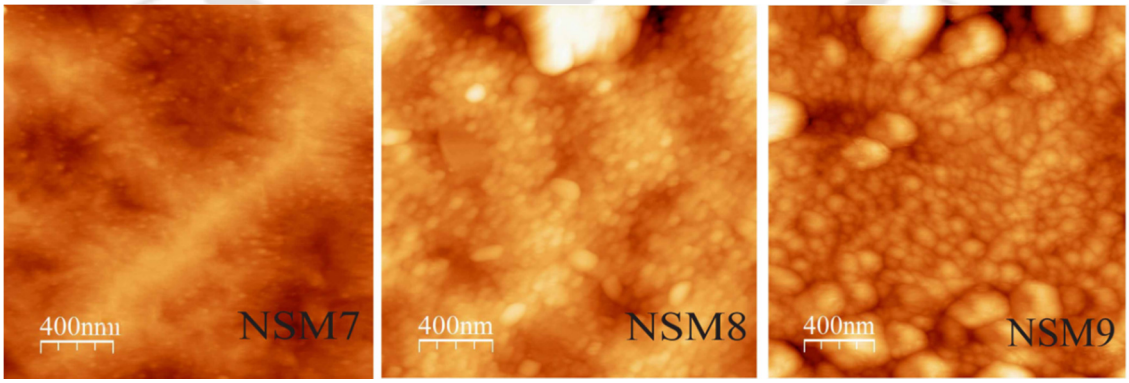

Figure 3.6: Atomic force microscope images of the annealed films NSM7, NSM8 and NSM9

The surface morphology of the NSMO films over the span of $2\mu m \times 2\mu m$ region are shown in Fig.3.6. Here, the average grain size of the films is progressively increased with increase in the post-annealing temperature and the root mean square roughness values are found to be 3.7, 4 and 5.5 nm for NSM7, NSM8 and NSM9, respectively.

TH-1726_11612111

3.3.4 Electrical Resistivity

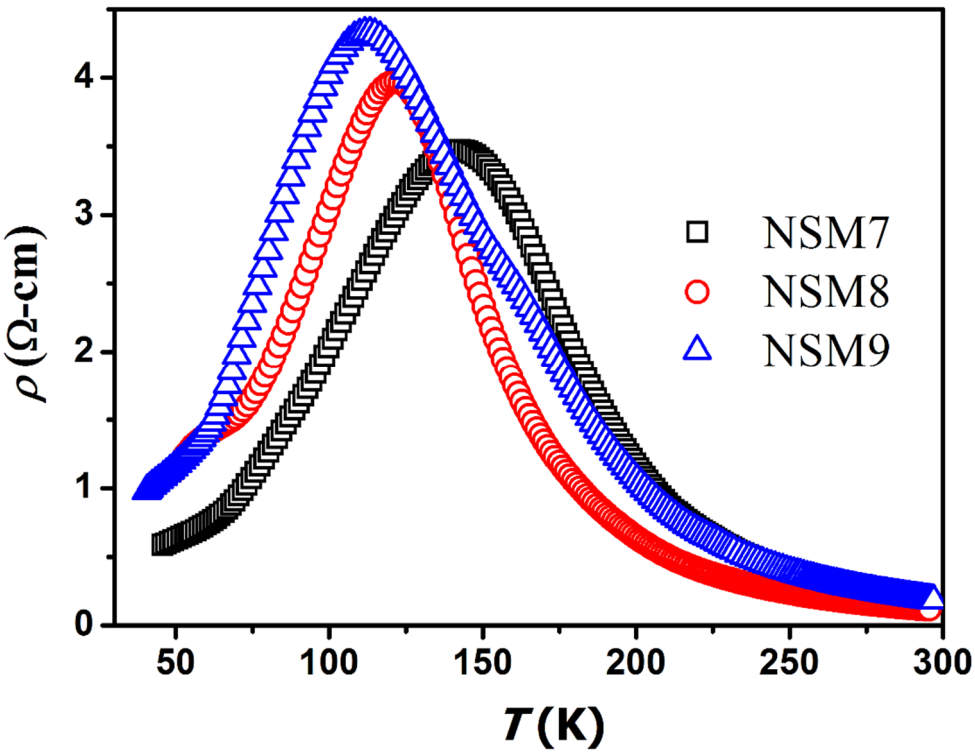

Figure 3.7: Variation of resistivity as a function of temperature for different $Nd_{0.7}Sr_{0.3}MnO_3$ films.

Temperature variations of electrical resistivity of all the three post annealed films are shown in Fig.3.7 and they exhibit metal-insulator transition (T_{MI}) at 142 K, 122 K and 111 K, respectively. The increase in post-annealing temperature is found to decrease T_{MI} values. Eventhough we observed decrease in lattice strain as the annealing temperature is increased, we have found reduction in T_{MI} value and increase in resistivity of the sample. This anomaly can be attributed to possible poor quality of grain boundaries or micro-cracks at grain boundaries as the annealing temperature is increased.

In order to further understand the resistivity behavior, the resistivity data in the metallic region were fitted to the empirical equation,

$$\rho = \rho_0 + \rho_n T^n \qquad (3.2)$$

Here the temperature exponent n takes different values depending on the nature of conduction mechanism. Here n = 2 represents the electron-electron scattering while n = 2.5 is generally attributed to the combination of electron-electron, electron-phonon and

TH-1726_11612111

electron-magnon scattering mechanism [181]. The resistivity data could be best fitted by taking n = 2.5 as shown in Fig.3.8(a). The residual resistivity (ρ_0) increases from 0.26 $\Omega - cm$ to 0.43 $\Omega - cm$ with increase in annealing temperature and $\rho_{2.5}$ is in the order of 20 $\mu\Omega - cm$. The increase in residual resistivity with increase in annealing temperature can be attributed to defects at grain boundaries as discussed in the previous paragraph.

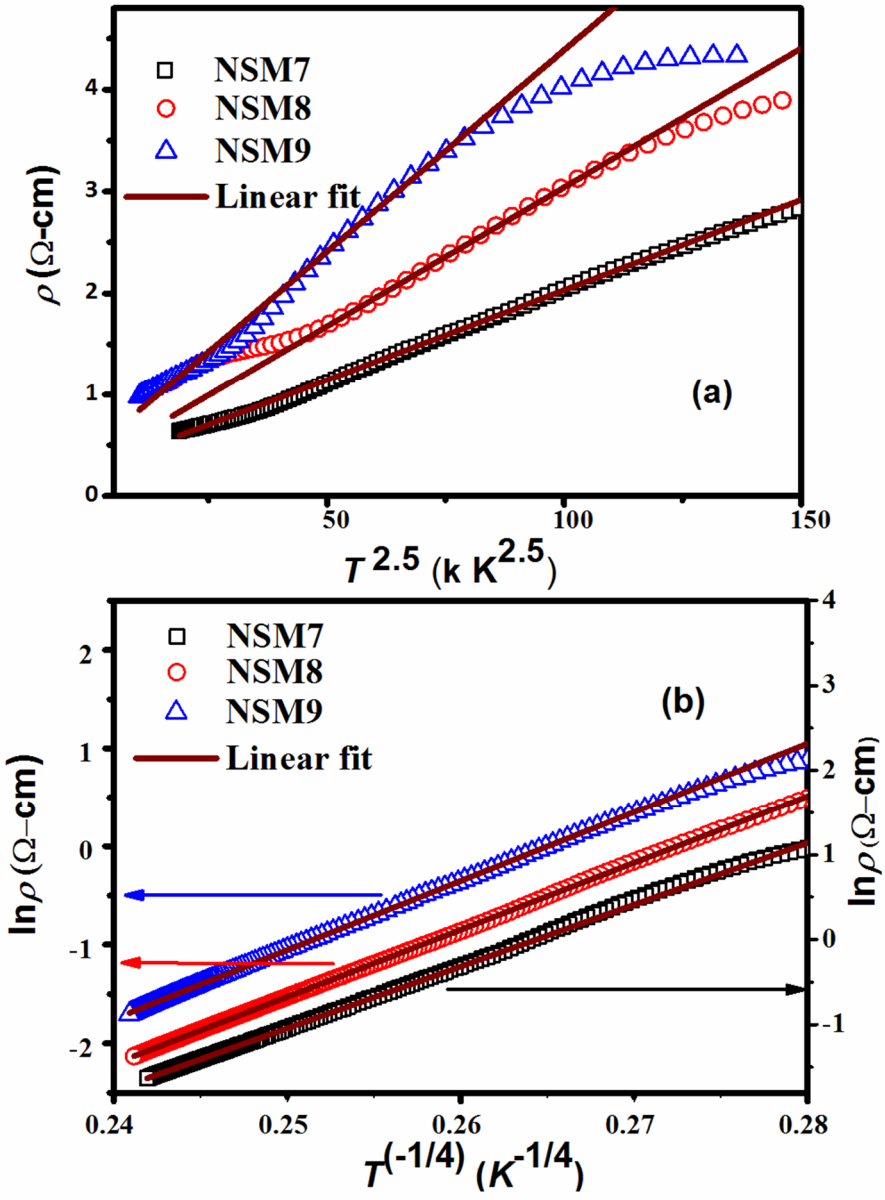

Figure 3.8: (a) Resistivity data in the metallic region and the fit to eq.3.2. (b) Plots of lnρ versus $T^{-1/4}$ and the fit to Mott-VRH model.

The resistivity data in the semiconducting region could be fitted by taking Mott variable range hopping model (Mott-VRH) [182],

TH-1726_11612111

$$\rho = \rho_{om} exp(T_{0m}/T)^{1/4} \quad (3.3)$$

Here ρ_{om} is the Mott residual resistivity and T_{0m} is the Mott characteristic temperature. Fig.3.8(b) shows lnρ versus $T^{-1/4}$ plots, where we can see the linear behaviour for all the three films. The fitted data are shown as solid line and they closely follow the experimental data. The values of ρ_{0m} are found to be in the order of $10^{-3}\mu\Omega - cm$. The hopping energy at 300 K was determined by using the fitted values of T_0 and the relation

$$E_h(T) = (1/4)k_B T^{3/4} T_{0m}^{1/4} \quad (3.4)$$

as per ref [182] and it is found to vary from 112 meV for the film NSM7 to 118 meV for the film NSM9. These hopping values are compable to the literature [183, 184].

3.3.5 Magnetic Properties

In order to study the magnetic properties, temperature variation of magnetization (M) for the applied magnetic field H = 2 kOe and magnetic hysteresis loops at a few selected temperatures were measured. *M-T* plots are shown in Fig.3.9(a) and all the three films show ferromagnetic transition. The ferromagnetic transition temperature (T_C) determined from the plots of dM/dT versus temperature are found to be 163 K, 180 K and 192 K for NSM7, NSM8 and NSM9, respectively and they are shown in Fig.3.9(b). Typical *MH*-loops recorded at 50 K are shown in Fig.3.9(c). The saturation magnetization (M_s) values are estimated from the analysis of initial magnetization curves using the relation based on law of approach to saturation magnetization [185],

$$M = M_S \left[1 - \frac{a}{H^{1/2}} - \frac{b}{H^2}\right] \quad (3.5)$$

M_S values are found to be 600 emu/cc, 620 emu/cc and 640 emu/cc, respectively for the above thin films and their coercivity values are found to be 607, 396 and 355 Oe respectively. Thus with increase in annealing temperature, both the ferromagnetic T_C and M_S values increase while the H_c value decreases. The above improvement in magnetic properties upon increasing the annealing temperature can be attributed to the reduction in lattice strain and oxygen defect. However, they contradict the electrical resistivity results, where decrease in T_{MI} and increase in resistivity values are observed with increase in annealing temperature. So even though, there is an improvement in the quality of the film in terms of reduced lattice strain and improved oxygen stoichiometry, there is a possibility of clustering or agglomeration of films into grains with weak inter grain coupling and it

TH-1726_11612111

gives rise to deteriorated electrical conductivity behaviour. The susceptibility data in the paramagnetic region were fitted to modified Curie-Weiss law,

$$\chi = \chi_0 + \frac{C}{T-\theta_C} \tag{3.6}$$

The temperature independent susceptibility (χ_0) values are found to be -0.13 emu/(mol.Oe), -0.48 emu/(mol.Oe) and -0.75 emu/(mol.Oe) and the Curie temperatures obtained from the above fit are 172 K, 190 K and 196 K, respectively.

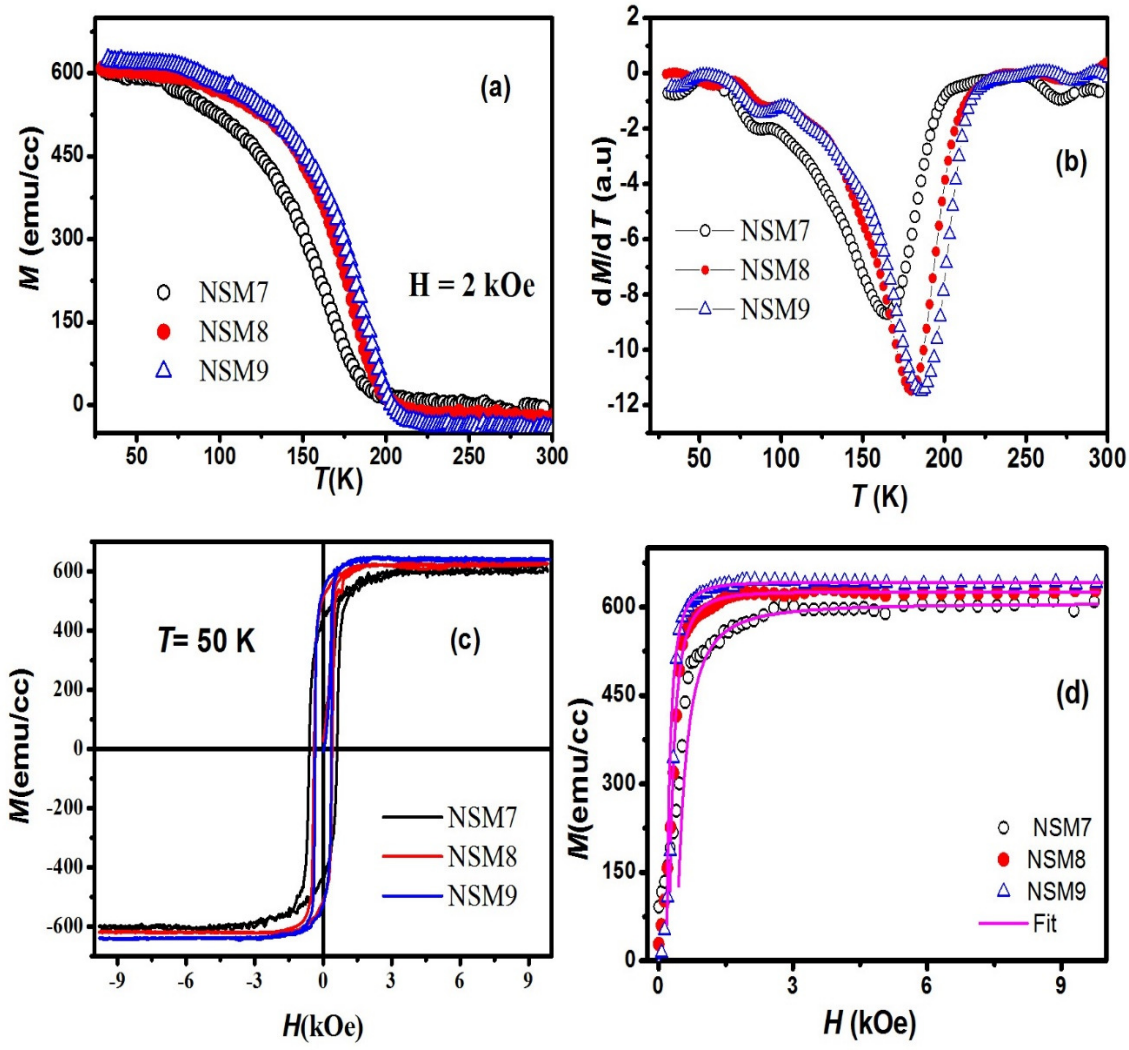

Figure 3.9: (a) Temperature variation of magnetization for H = 2 kOe. (b) dM/dT vesus T plots of NSM7, NSM8 and NSM9 films. (c) Typical MH-hysteresis recorded at 50 K. (d) Initial magnetization curves fitted to the law of approach to saturation magnetization.

3.3.6 Conclusions

The effect of post-annealing on electrical and magnetic properties of NSMO thin films are discussed. NSMO thin films were deposited on Al_2O_3 substrate by RF-sputtering technique and these films were annealed at different temperatures. Films exhibit

TH-1726_11612111

orthorhombic structure and the compressive strain on the films is reduced with increase in annealing temperatures. Room temperature Raman spectra show the standard lines expected for orthorhombic structure with A_g, B_{2g} and B_{3g} modes; one of the lines is found to be sensitive to lattice strain and it disappears upon annealing at 900°C. All prepared samples exhibit metal-insulator transition and the values are found to decrease from 142 K for 700°C annealed film to 111 K for 900°C annealed film. The resistivity in the metallic region could be fitted to the equation with the combination of electron – electron, electron – phonon and electron - magnon scattering mechanisms while the resistivity in the semiconducting region were fitted to Mott-VRH model. Double exchange FM transition was observed and the T_C value is found to increase from 163 K for 700°C annealed film to 192 K for 900°C annealed film. The saturation magnetization values are also found to increase with increase in annealing temperature. The improvement in the magnetic properties is attributed to reduced lattice strain and improved oxygen stoichiometry.

3.4 $Nd_{0.7}Sr_{0.3}MnO_3$ Films on Different Substrates

3.4.1 Thin Film Deposition

In this section, we report the impact of substrate induced lattice strain in NSMO films. Here we have studied the structural, electrical and magnetic properties of NSMO thin films on different substrates. $Nd_{0.7}Sr_{0.3}MnO_3$ (NSMO) film of 200 nm thickness was deposited on three different substrates namely Al_2O_3 (AlO), MgO and $LaAlO_3$ (LAO) oriented along (001) direction. The sputtering chamber was maintained at a working pressure of 4.3×10^{-2} mbar by allowing Ar : O_2 gas flow at 3:1 ratio. RF power was fixed at 50 W and the substrate temperature was kept at 400°C throughout the deposition. Thereafter, these films were divided into two batches. One set was post-annealed at 700°C in air and the another batch was annealed in oxygen atmosphere at the same temperature. The air annealed films on AlO, MgO and LAO substrates are named as SA-200, MA-200 and LA-200, respectively. On the other hand, these films annealed under flowing oxygen gas environmnet are named as SO-200, MO-200 and LO-200, respectively.

TH-1726_11612111

3.4.2 Structural Properties

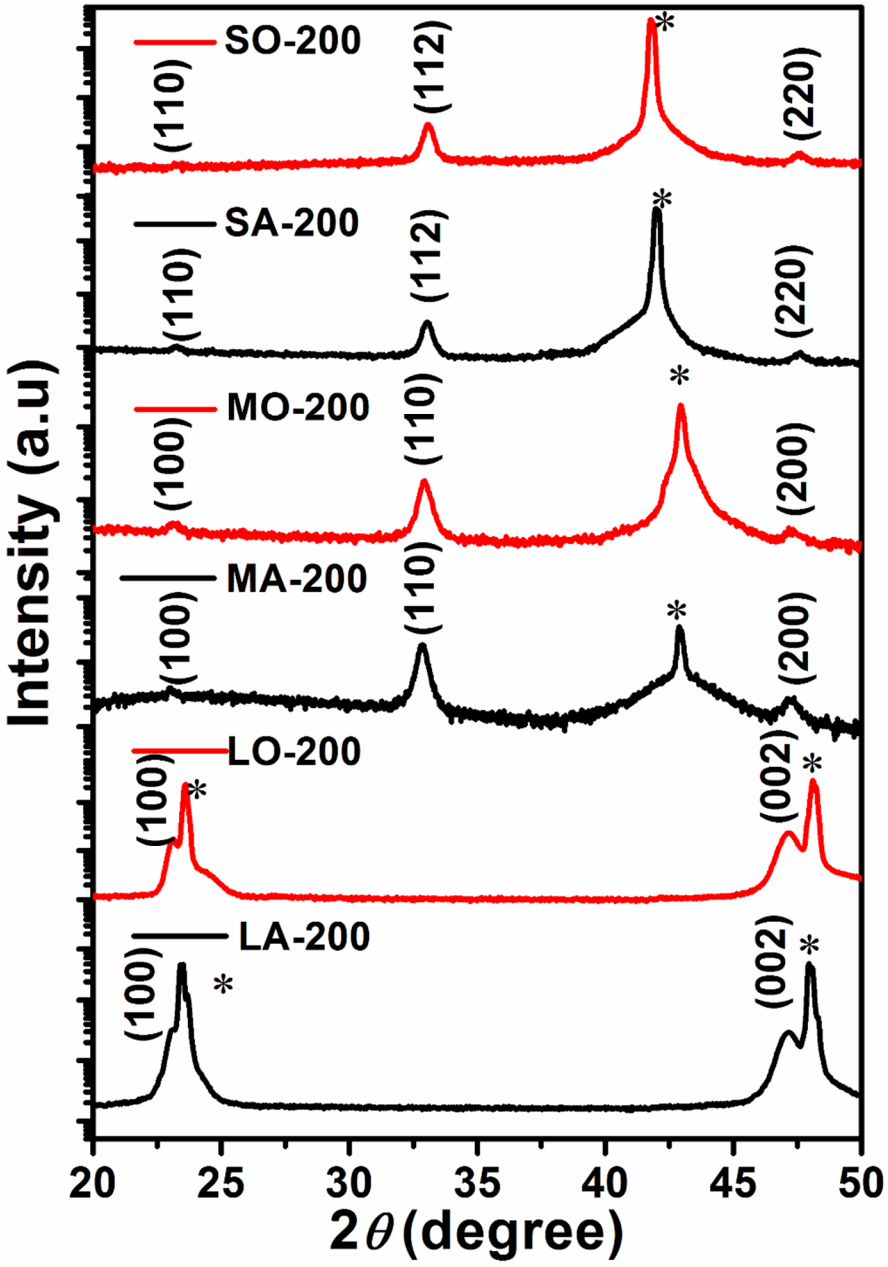

Figure 3.10: The θ –2θ scan of XRD patterns of NSMO thin films on different substrates. Star mark represents (00*l*) peak of the substrates.

XRD patterns of NSMO films grown on AlO, MgO and LAO substrates are shown in Fig.3.10. Films on AlO and MgO substrates show polycrystalline behaviour with orthorhombic and cubic structures, respectively. On the otherhand, the film on LAO substrate is found to be in single crystal nature with complete orientation of the cell along c-axis of the substrate, i.e. along (001) direction. MA-200 and MO-200 samples show polycrystalline behaviour with a maximum intensity of the (110) peak along with other

TH-1726_11612111

peaks in the direction of <100> This signifies the poor growth of the (00*l*) peak aligned along the substrate direction which is observed due to a huge lattice mismatch (8.3%) between the NSMO film and MgO substrate. However, unlike the bulk sample, here the films are found to be crystallised in cubic cell. Lattice constants of the polycrystalline films were determined from the Rietveld refinement by choosing Pm3m space group in the cubic cell. These values are found to 3.854 Å and 3.860 Å for MA-200 and MO-200 films respectively. On the other hand, the lattice constants of films deposited on AlO are found to be a = 5.454 Å, b = 5.435 Å and c = 7.647 Å for SA-200 and a = 5.449 Å, b = 5.433 Å and c = 7.652 Å for SO-200 films. Films on LAO show texturing along c-directon of the unit cell, i.e. along the orientation of the substrate and the the lattice constant perpendicular to the plane of the film was estimated from the observed (*00l*) peaks. The lattice constant is found to be 3.851 Å both for LA-200 and LO-200 films.

Lattice stain (ε) on the film was estimated using the eq.3.1. The lattice strain values of the films are found to be 0.15% and 0.31% for MA-200 and MO-200 and, 0.64% and 0.57% for SA-200 and SO-200 respectively. There is no appreciable change in lattice strain is observed in both air and oxygen annealed films on LAO substrate. The lattice mismatch between the film and substrate is deduced from the relation,

$$\frac{a_{sub}-a_{bulk}}{a_{sub}} \quad (3.7)$$

The mismatch is found to be -2.4%, 8.3% and -1.5% for AlO, MgO and LAO substrates respectively. The films grown on LAO substrate are highly oriented along the direction of single crystalline substrate due to the low lattice mismatch between the lattice parameters of substrate and the film.

Fig.3.11 shows Raman spectra of both air and oxygen annealed films on three substrates in the frequency range of 200 cm^{-1} – 800 cm^{-1}. Raman peaks are observed at 230 cm^{-1}, 330 cm^{-1}, 490 cm^{-1} and 670 cm^{-1} respectively. The obtained spectrum is comparable to that reported in (La-Ca)-Mn-O system [186]. The Raman peak at 230 cm^{-1} corresponds to $A_g(2)$ mode, i.e., in-phase rotation of MnO_6 and the peak at 330 cm^{-1} corresponds to $B_{3g}(4)$ mode of in-phase rotation. Peaks at 490 cm^{-1} and 670 cm^{-1} are attributed to out-of-phase bending ($A_g(3)$) and in-phase stretching ($B_{2g}(1)$) modes respectively [179]. In the case of air annealed films, the peaks at 230 cm^{-1} and 670 cm^{-1} are found to shift towards lower frequency compared to that of oxygen annealed films. A marginal increase in the

TH-1726_11612111

intensity of 330 cm^{-1} peak is observed for the film on both LAO and MgO substrates, and it can be attributed to the increase of in-phase rotation of MnO_6. A similar trend is observed in the Raman spectra of oxygen annealed films.

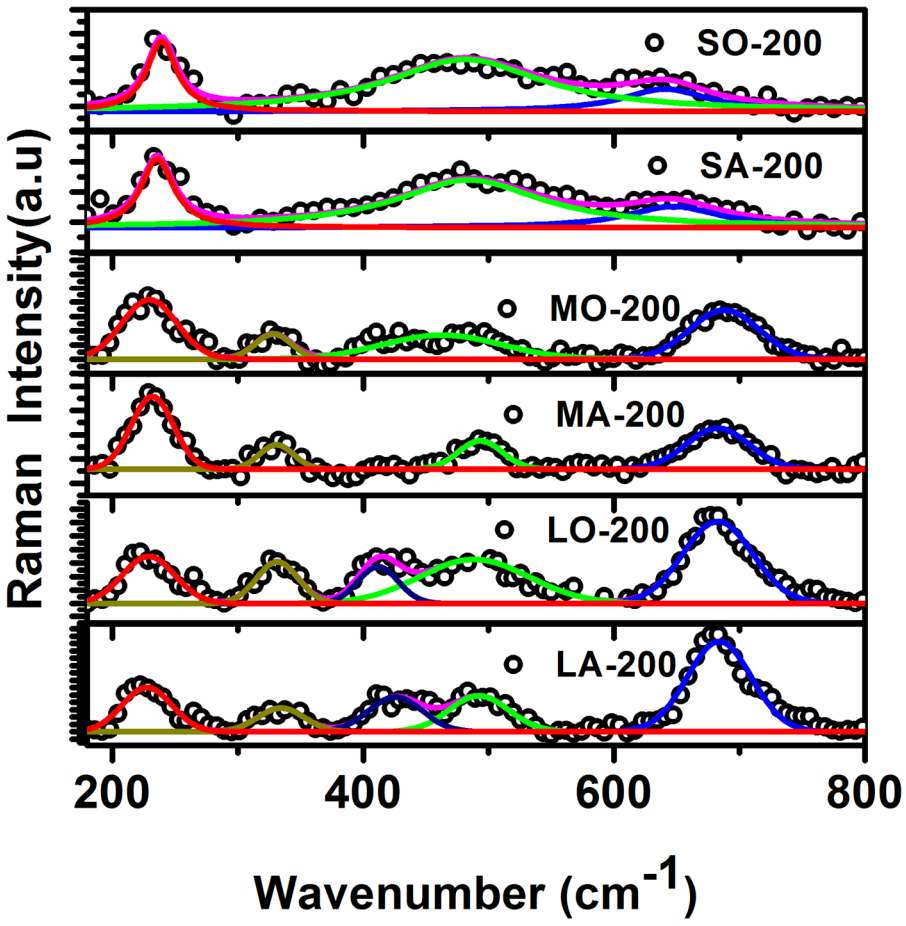

Figure 3.11: Raman spectra of air and oxygen annealed NSMO films on different substrates.

In the spectrum of NSMO/LAO film, in addition to the regular four prominent peaks, an additional peak is observed around ~ 450 cm^{-1}. It is attributed to B_{1g} or B_{3g} symmetric mode. It is due to the bending behaviour of MnO_6 octahedra that originates from in-plane compressive strain. This peak doesn't appear in the films grown on other two substrates due to a huge lattice mismatch and their polycrystalline nature. In the spectrum of NSMO/AlO, there are three peaks observed at 230, 480 and 640 cm^{-1}. Here 640 cm^{-1} peak is attributed to the $B_{2g}(1)$ mode due to the in-phase stretching of MnO_6 octahedra. Among these three peaks, the peak 480 cm^{-1} has shown a huge broadening over the frequency range 300 to 600 cm^{-1}. The peak around 330 cm^{-1} is low intense and it is not clearly visible on AlO substrate.

TH-1726_11612111

3.4.3 Electrical Resistivity

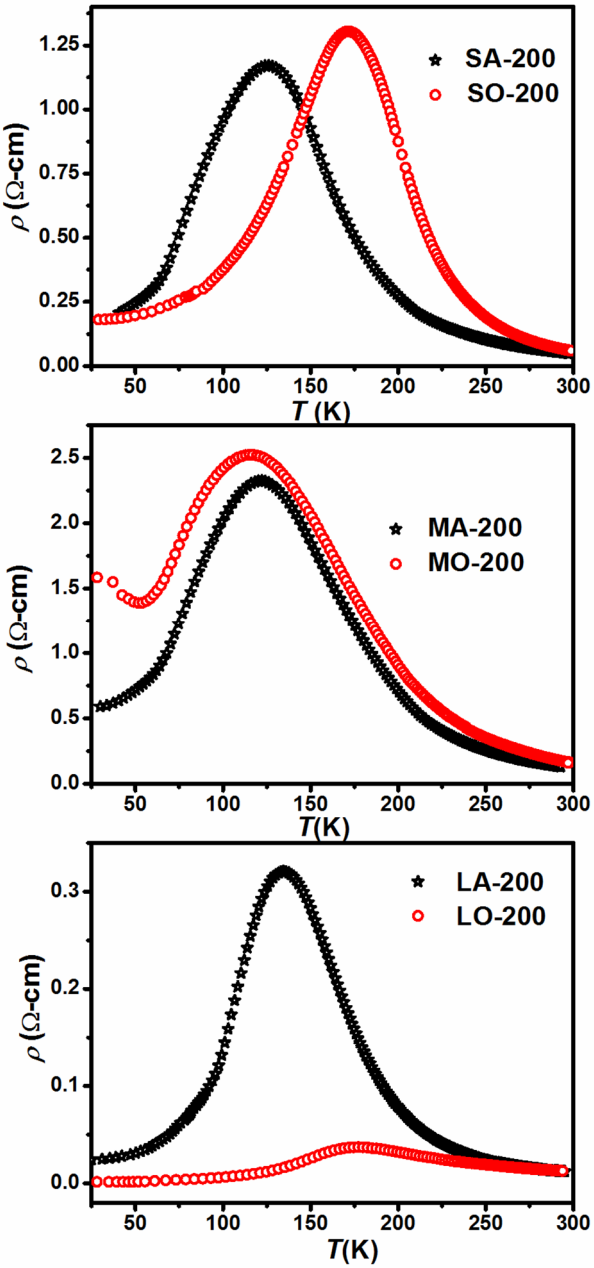

Figure 3.12: Temperature variation of electrical resistivity of both air and oxygen annealed NSMO films grown on AlO, MgO and LAO substrates.

Fig.3.12 shows the electrical resistivity data as a function of temperature for films grown on three different substrates and annealed under both air and oxygen gas environments. All these films exhibit metal-insulator transitions and the transition temperature (T_{MI}) values are found to be 124 K, 123 K and 137 K for SA-200, MA-200 and LA-200 films, respectively. On the other hand T_{MI} values are found to be 171 K, 116 K and 180 K for SO-200, MO-200 and LO-200 films respectively. The maximum resistivity

TH-1726_11612111

values for SA-200 and SO-200 are around 1.5 Ω-cm and those of MA-200 and MO-200 are around 2.5 Ω-cm. For the film on LAO substrate, the maximum resistivity values of the oxygen and air annealed films are 30 *m*Ω-cm and 320 *m*Ω-cm respectively. Here, the T_{MI} values of oxygen annealed films are higher than those of air annealed films. This could be due to the improvement of Mn^{4+} concentration that leads to enhanced double exchange interaction. Therefore, the oxygen annealing effectively reduces the oxygen vacancies in the NSMO films. Moreover, the T_{MI} values of films deposited on LAO substrate are found to be quite large compared to other films and in addition to that they exhibit smaller electrical resistivity. This is mainly due to small lattice mismatch with substrate and the associated relaxation of lattice.

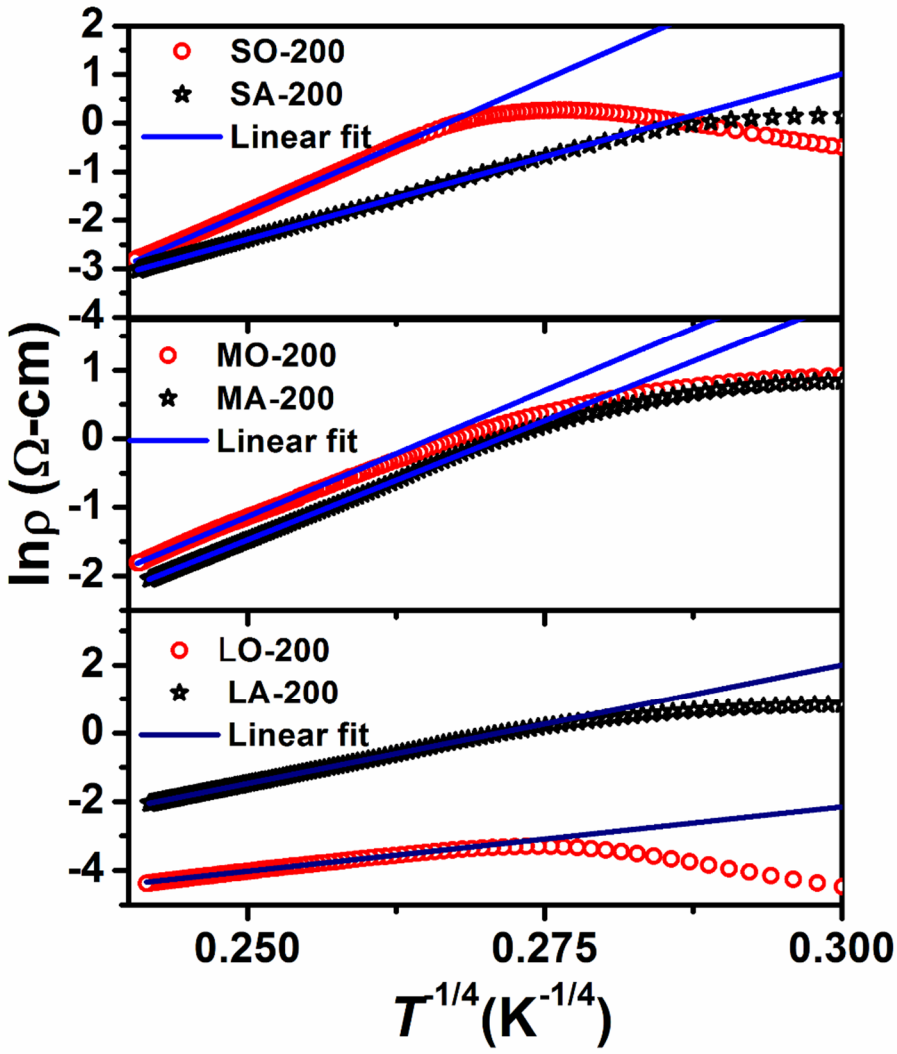

Figure 3.13 : ln ρ versus $T^{-1/4}$ plots along with fit to Mott-VRH model.

TH-1726_11612111

Electrical resistivity data in the insulating region were analysed using eq. 3.3. Here ρ_{0m} and T_{0m} are characteristic constants of the VRH model. Typical plots of $ln(\rho)$ vs $T^{-1/4}$ for all films are shown in Fig.3.13 and they were fitted to the above model by taking ρ_{0m} and T_{0m} as free parameters of the fit. The fitted data are shown as a solid line and they closely follow the experimental data. Similar behaviour is observed for other films. The activation energy for hopping (E_h) at 300 K was determined by using the eq. 3.4 and they are given in table-3.1.

Table 3.1: Metal-insulator transition temperature (T_{MI}), peak resistivity at T_{MI} and activation energy of the films on different substrates.

Samples	T_{MI}(K)	ρ_{peak} (Ω-cm)	E_h(meV)
SA-200	124	1.17	105
SO-200	171	1.31	110
MA200	123	2.31	108
MO-200	116	2.51	108
LA-200	137	0.32	118
LO-200	180	0.03	58

3.4.4 Magnetic Properties

Temperature (T) variation of magnetization (M) was measured under zero field cooled condition by applying a magnetic field of $H = 2$ kOe parallel to the plane of the film. M-T plots of both air annealed and oxygen annealed films on three different substrates are shown in Fig.3.14 and they are found to exhibit ferromagnetic transition. The ferromagnetic transition temperature, T_C values determined from the plots of dM/dT versus T are tabulated in table-3.2. The T_C values for oxygen annealed samples are found to be larger than those of air annealed films. Susceptibility data in the paramagnetic region were fitted to eq.3.6 by taking χ_0, C and θ_c as free parameters of the fit. The estimated θ_c values are given in table-3.2 and they follow the same trend as that of T_C. The large difference between the T_C and the θ_C values for a particular film can be attributed to the broad magnetic transition.

TH-1726_11612111

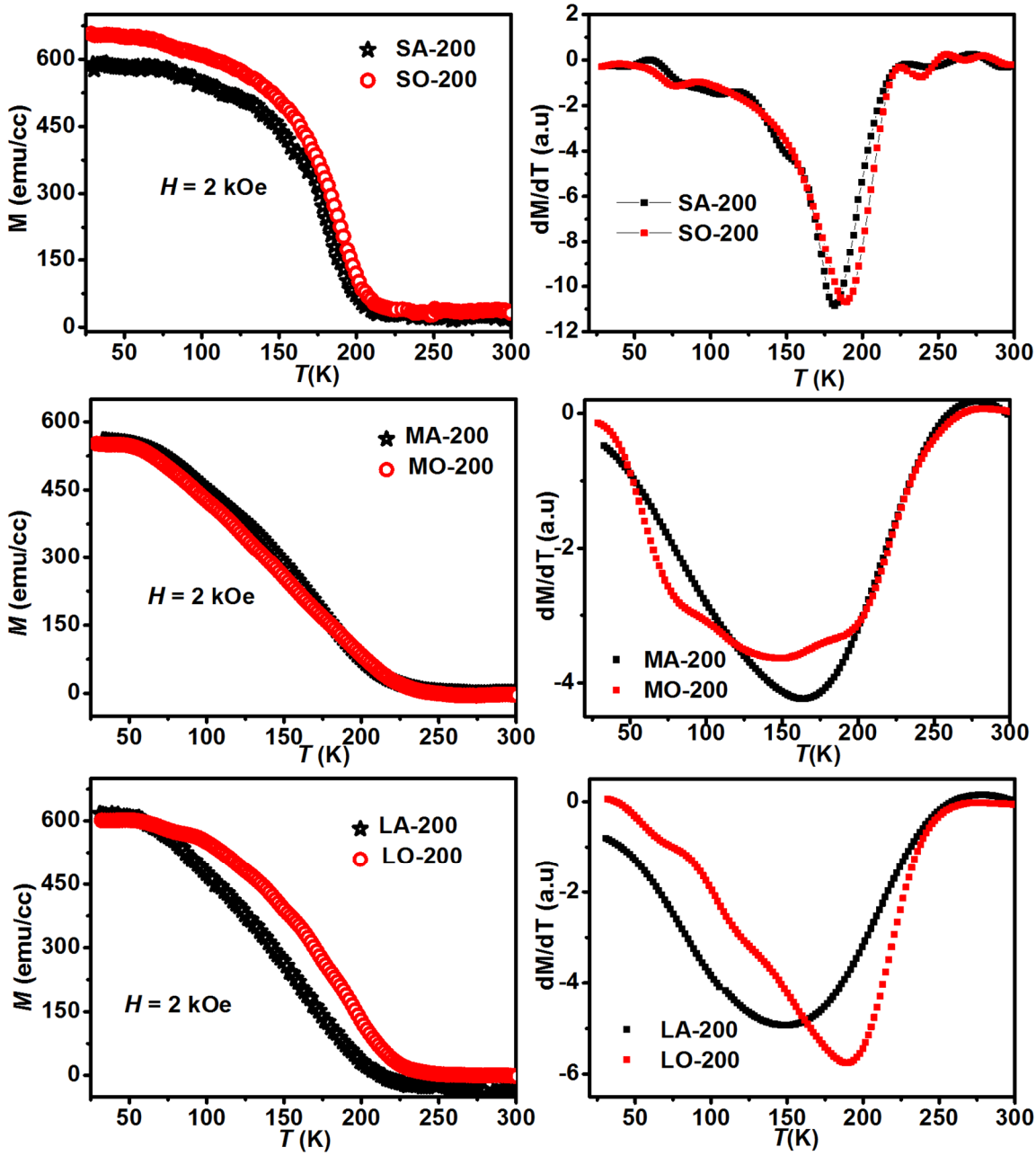

Figure 3.14: Temperature variation of zero field cooled (H = 2 kOe) magnetization for both air and oxygen annealed NSMO films on AlO, MgO and LAO substrates.

TH-1726_11612111

Table 3.2: Ferromagnetic transition temperature (T_C), Curie temperature (θ_C), saturation magnetization (M_s), and magnetic anisotropy constant.

Samples	T_C (K)	θ_C (K)	Ms (μ_B/f.u)	$K\times10^5$ (erg/cc)
SA-200	170	183	3.4	2.6
SO-200	174	190	3.9	2.7
MA-200	140	170	3.6	1.0
MO-200	144	178	3.2	1.0
LA-200	150	182	4.1	1.9
LO-200	194	201	3.8	1.0

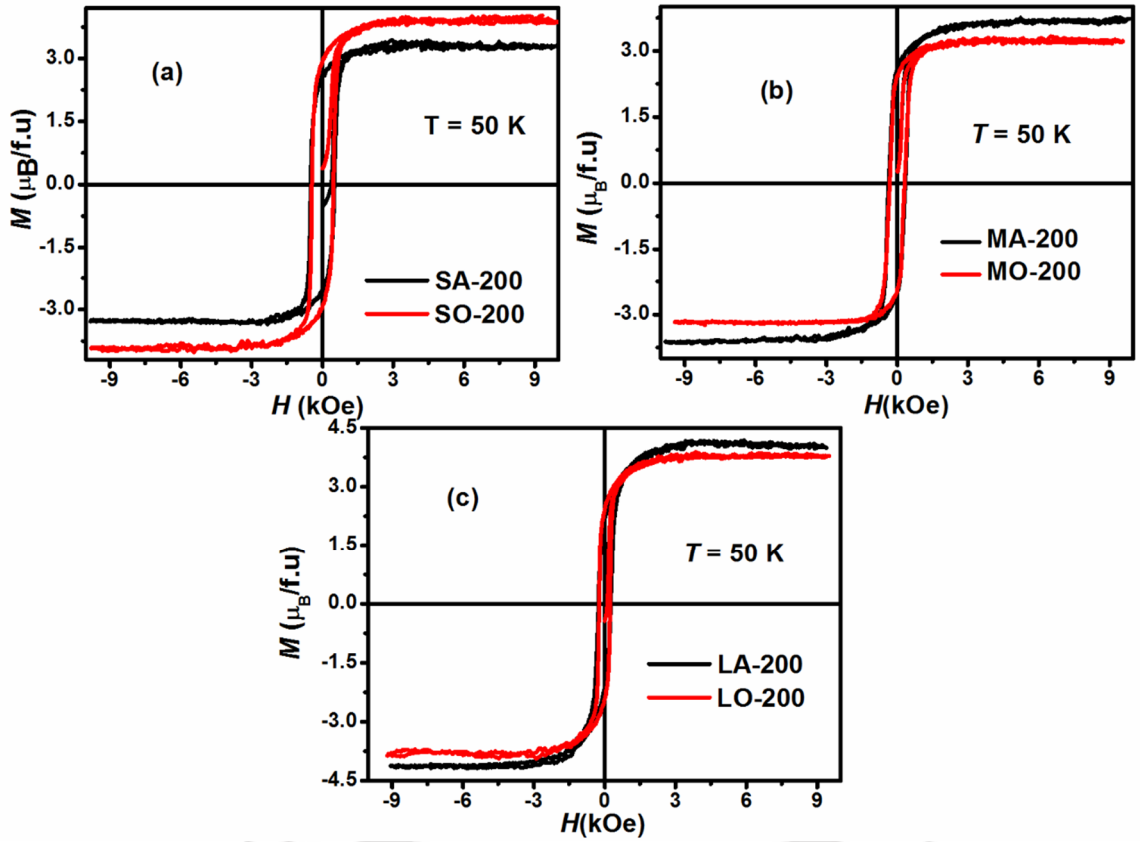

Figure 3.15: *MH*-loops recorded at 50 K for NSMO films on different substrates

Typical *M-H* loops recorded at 50 K are shown in Fig.3.15 for films on different substrates and they all show clear ferromagnetic behaviour with magnetic saturation. The saturation magnetization of the films were determined from the initial magnetization curves by fitting them to the empirical relation of law of approach to saturation magnetization i.e. eq.3.5 [187]. Here *a* and *b* are constants and they are taken as free fitting parameters of fit along with M_S. The saturation magnetization value of all films are tabulated in table-3.2. The maximum saturation magnetization (M_S) value is 4.1 μ_B and is comparable to the expected value. From the fitted parameter *b* and using the relation [188]

TH-1726_11612111

$$b = (4/15)\,(K/Ms)^2 \qquad (3.8)$$

The effective anisotropy constant (K) was determined and its values are tabulated in table-3.2. The K values of present films are comparable to those of LCMO films on MgO substrate [189].

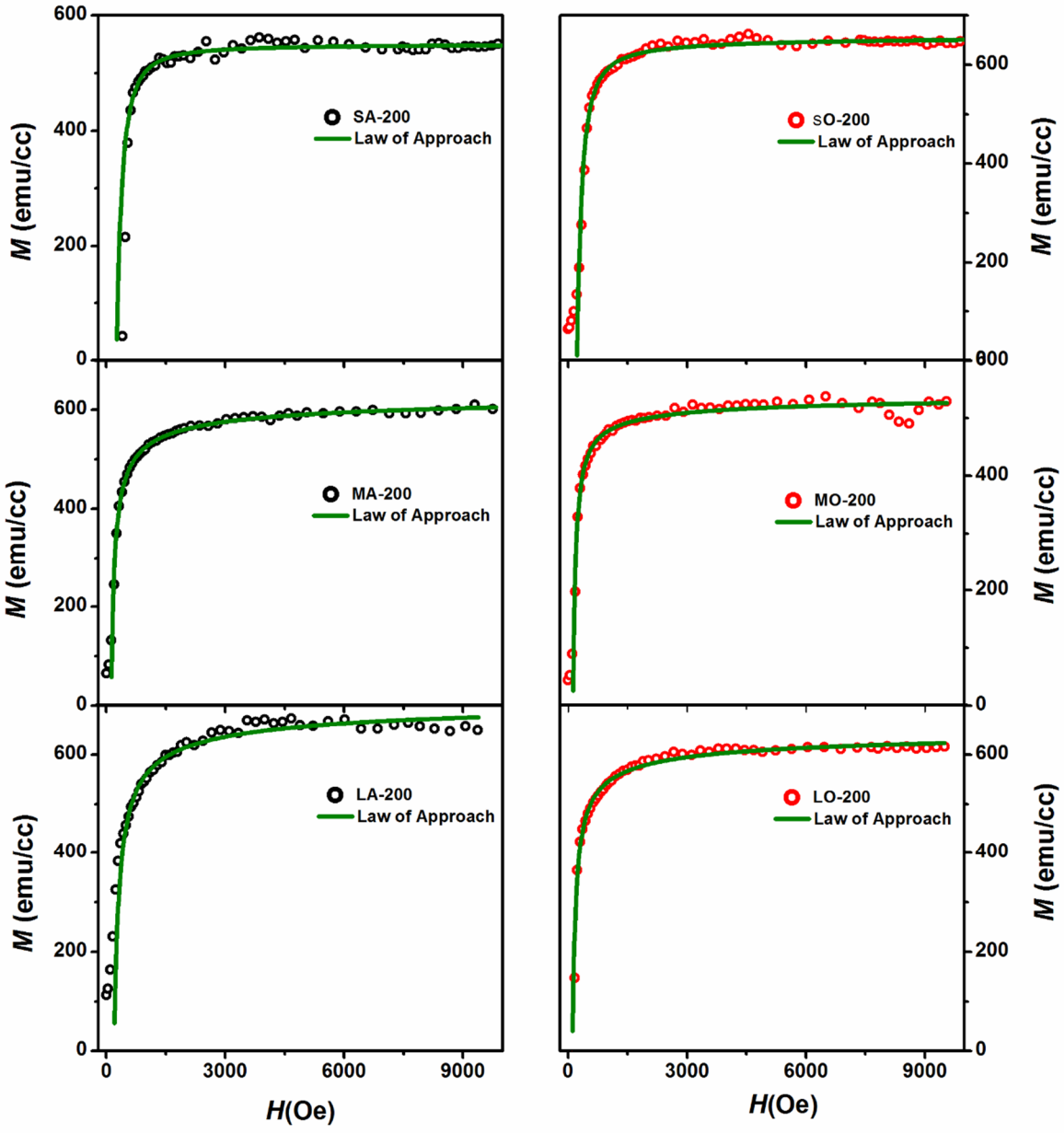

Figure 3.16: The initial magnetization curves fitted to the eq. 3.5 for NSMO films on different substrates.

TH-1726_11612111

3.4.5 Conclusions

$Nd_{0.7}Sr_{0.3}MnO_3$ thin films of 200 nm thickness were deposited on (001) oriented Al_2O_3, MgO and $LaAlO_3$ substrates by using RF-magnetron sputtering technique. They were separately annealed in air and flowing oxygen gas environments. XRD patterns of both air annealed and oxygen annealed films on AlO and MgO substrates demonstrate that they are in polycrystalline nature. These films on AlO substrate crystallize in orthorhombic structure while those on MgO substrate crystallize in cubic structure. They were Rietveld refined by choosing Pbnm and Pm3m space group, repsectively. All films exhibit ferromagnetic transition and the T_C of oxygen annealed samples is higher than that of air annealed films. *M-H* loop measurements show ferromagnetic behaviour with a maximum saturation magnetization of 4.1 μ_B. The effective anisotropy constant *K* was estimated from the analysis of initial magnetization data. Electrical resistivity data of both air and oxygen annealed films show metal-insulator transition; howerver the T_{MI} values of oxygen annealed films are found to be larger and comparable to the bulk value. The resistivity data in the insulating region were analysed by using Mott-VRH model. Thus the oxygen annealing and the substrate play a major role in tuning the electrical resistivity and magnetization data of NSMO films.

3.5 Effect of Film Thickness in $Nd_{0.7}Sr_{0.3}MnO_3$

3.5.1 Thin Films preparation

$Nd_{0.7}Sr_{0.3}MnO_3$ (NSMO) films with different film thicknes were deposited on $LaAlO_3$ substrate by using the RF magnetron sputtering system. The RF power of 50 W, substrate temperature of 400°C and a working pressure of 4.3×10^{-2} mbar with an Ar/O_2 gas mixture in 3:1 ratio were maintained during the growth. Thin films of different thicknesses in the range of 12 nm to 120 nm were deposited by adjusting the duration of deposition. The deposited films were post-annealed at 700°C under a flowing oxygen gas environment.

3.5.2 Structural Properties

We have grown c – axis oriented NSMO films on (001)-LAO substrate with thickness 12 nm, 25 nm, 30 nm, 40 nm, 50 nm ,60 nm and 120 nm. These films were post annealed at 700°C for 1 hr in flowing O_2 gas environment and are named as LO-12, LO-25, LO-30, LO-40, LO-50, LO-60 and LO-120 respectively. XRD patterns of films with

TH-1726_11612111

different thickness are shown in Fig.3.17, where the evolution of (002) peak around the 2θ value of 47.7° is clearly seen.

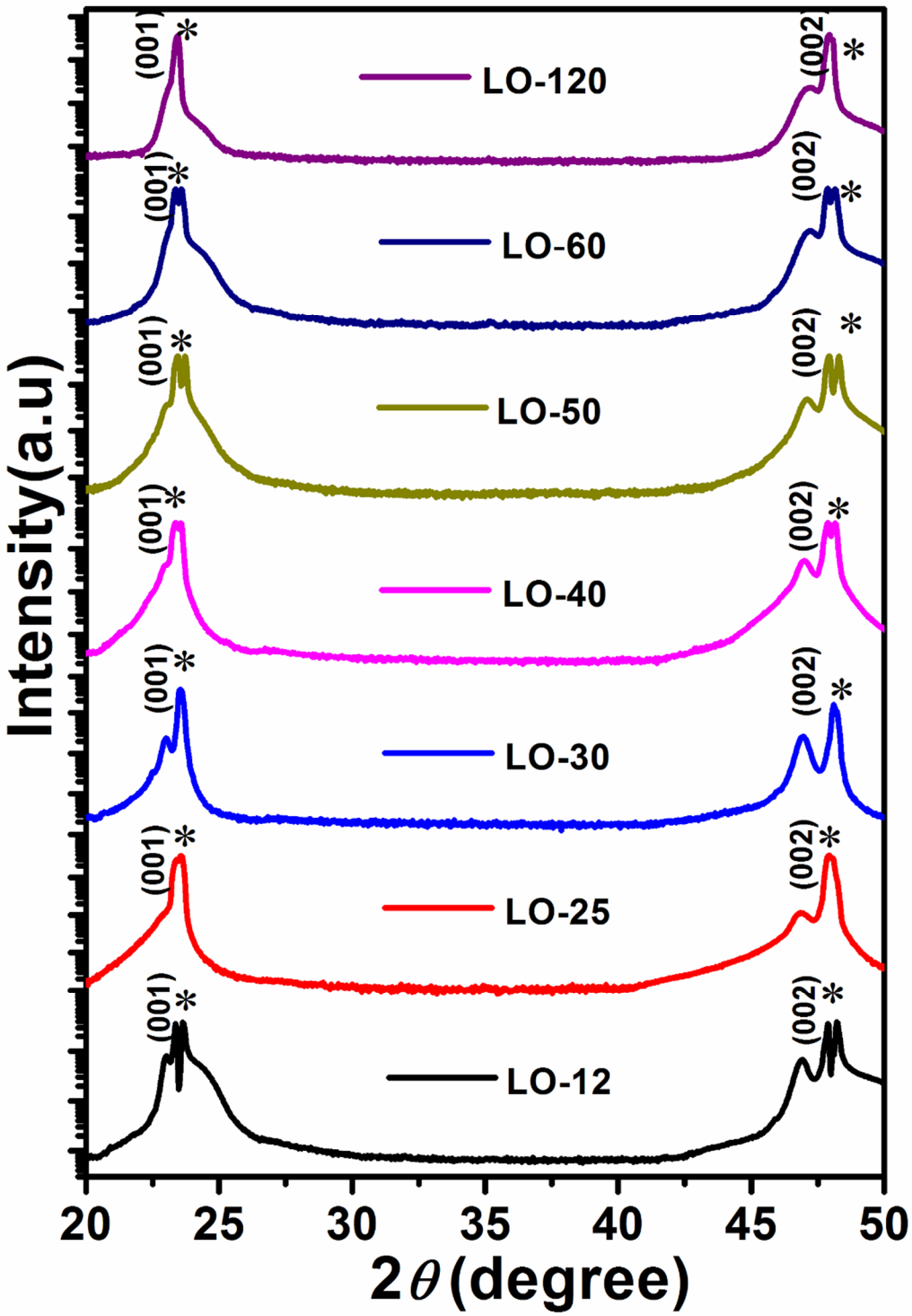

Figure 3.17: XRD patterns of NSMO films of different thicknesses.

TH-1726_11612111

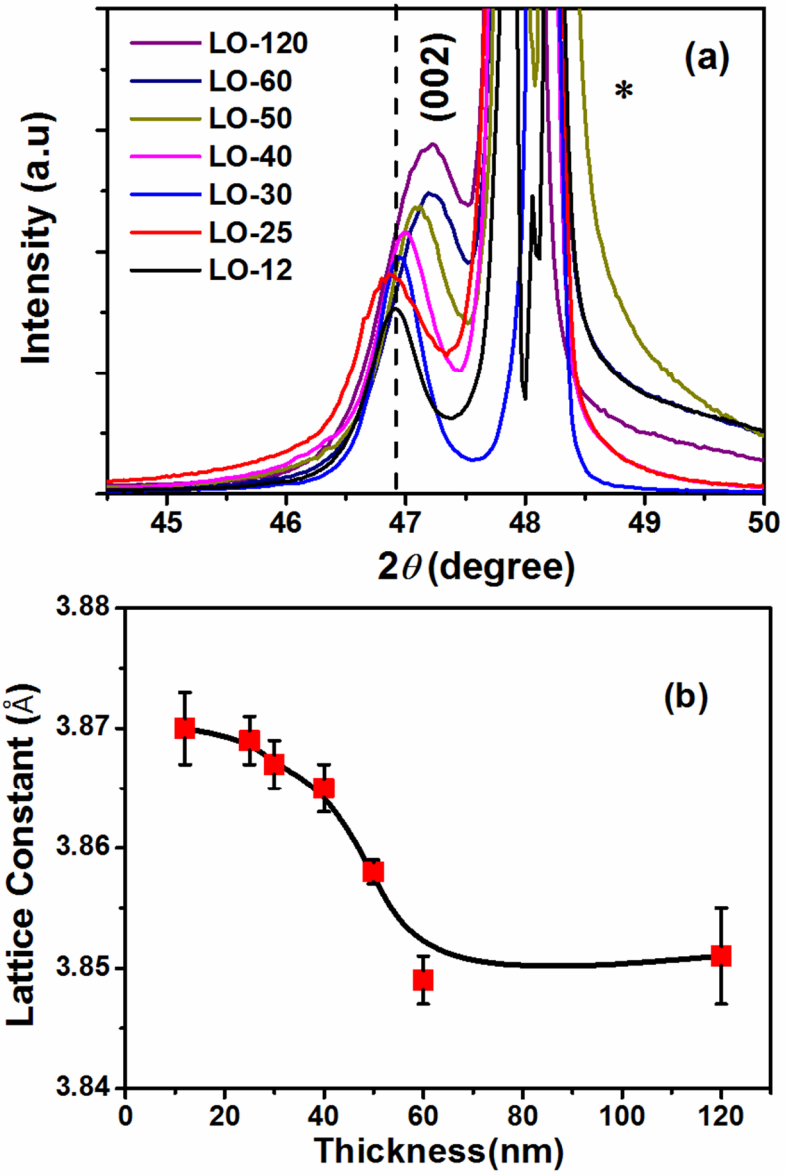

Figure 3.18: (a)The enlarged view of the (002) peak of NSMO films and (b) the out-of-plane lattice constant as a function of film thickness.

For higher thickness due to improved crystallize size, the (001) peak can also be easily distinguishable from the (001) peak of LAO substrate. Thus even for a substrate temperature of 400°C during the growth, c-axis oriented single crystalline NSMO films are obtained. The enlarged view of the (002) peak is shown in Fig. 3.18(a). This peak is shifted to higher 2θ angle with increase in thickness of the films. The out-of-plane lattice constant, a_c obtained from the (002) peak of NSMO is shown in Fig.3.18(b) as a function of film thickness. The a_c value is found to decrease with increase in film thickness up to 60 nm

TH-1726_11612111

and beyond that it remains almost constant. The a_c value for films of lower thickness is found to be quite large compared to that of bulk sample (c = 3.848 Å). They indicate the presence of out-of-plane tensile strain (ε) and it was estimated using the eq. $\varepsilon = (c_f - c)/c$ by taking c_f as a_c. The estimated ε values are tabulated in table-3.3. The lattice constants of LAO substrate (a_s = 3.788 Å) is lower than that of bulk NSMO (c = 3.848 Å) with a lattice mismatch of -1.6%. The above lattice mismatch leads to an in-plane compression and an out-of-plane elongation of lattice parameters.

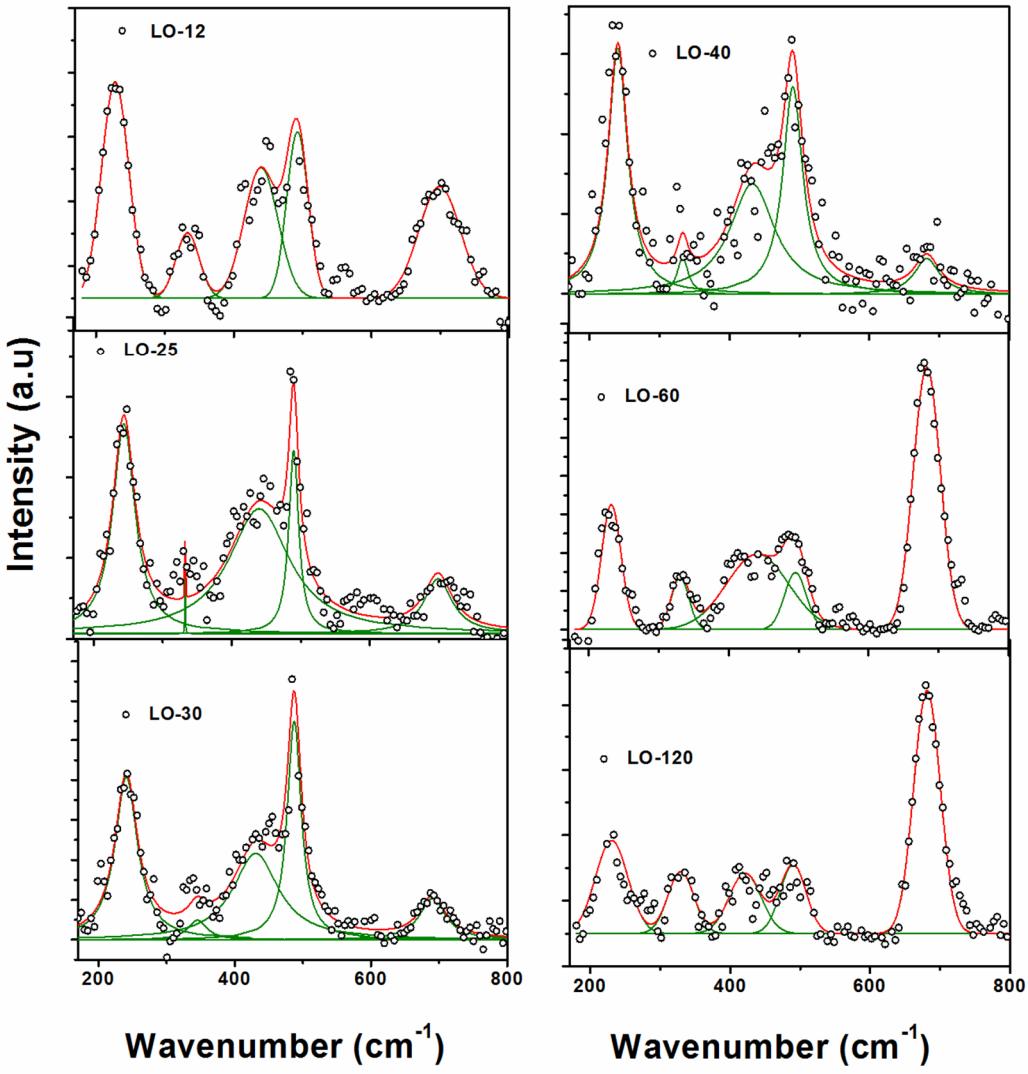

Figure 3.19: Raman spectra of NSMO films with different thicknesses.

The Raman spectra were recorded for the films in the frequency range of 200 cm^{-1} to 800 cm^{-1} and they are shown in Fig. 3.19. The LO-12 film shows four Raman peaks at 230 cm^{-1}, 450 cm^{-1} , 490 cm^{-1} and 670 cm^{-1} respectively. The obtained spectrum is comparable to that reported for (La, Ca)-Mn-O system [10]. Out of four peaks, the most

TH-1726_11612111

intense peak is at 230 cm^{-1} and it can be attributed to $A_g(2)$ mode, i.e. in-phase rotation of MnO_6 octahedra [179]. The twin peaks at 450 cm^{-1} and 490 cm^{-1} are due to out of phase bending of MnO_6 octahedra with $B_{2g}(3)$ and $A_g(3)$ modes respectively. The peak at 670 cm^{-1} can be attributed to in-phase oxygen stretching, i.e. $B_{2g}(1)$ mode [186] and in addition to that it is considered as disorder induced Raman feature due to oxygen deficiency [174]. With increase in film thickness (LO-12 to LO-120), the intensity of peaks in the range 200 cm^{-1} to 500 cm^{-1} is found to decrease with respect to the peak at 670 cm^{-1}. No appreciable change in the intensity of 670 cm^{-1} is observed. So, the predominant lattice strain at lower thickness of film leads to large rotation (230 cm^{-1}) and stretching (450 cm^{-1} and 490 cm^{-1}) of MnO_6 octahedra. Like the 12 nm thick film (LO-12), other films show an additional peak at 330 cm^{-1} and it is attributable to in-phase rotation of MnO_6 with $B_{3g}(4)$ mode symmetry as per the reported value based on lattice dynamics calculation [179].

3.5.3 Surface Morphology of NSMO Films

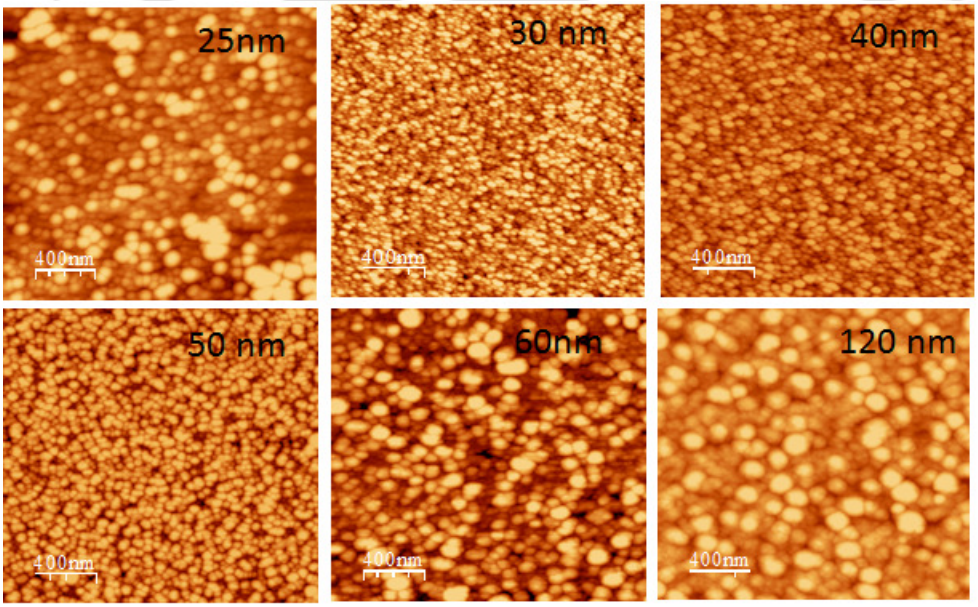

Figure 3.20: Topographical images of NSMO films of different thicknesses

Fig.3.20 shows surface morphologies of NSMO films deposited with various film thickness. In thinner films, the grain growth is randomly arranged on the surfaces of the films. As the thickness is increased, the grains are uniformly distributed on the substrate and the grain size progressively increases at higher film thickness. The root mean square (RMS) roughness R(t) of the films is determined by using WSxM software and it is gradually increased with increase in film thickness. The RMS roughness is dependent on

TH-1726_11612111

the relative surface height of the film (h(x, t)), i.e. R(t) = $\sqrt{|h(x,t)|^2}$. Here, x represents the lateral position at the deposition time t. The surface roughness of a film is expressed in terms of a power law [190],

$$R = t^{\beta} \quad (3.9)$$

Here, t represents the duration of deposition and β corresponds the growth exponent. Fig. 3.21 depicts the evolution of surface roughness as a function of film thickness. The growth exponent parameter is found to be 1.13 from the fitting, which is comparable to the literature [191].

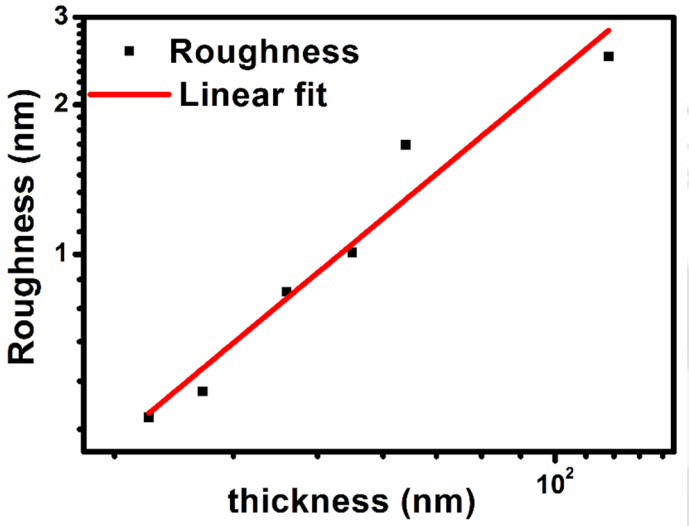

Figure 3.21: Roughness as a funciton of film thickess along with fit to eq. 3.9.

3.5.4 Magnetic Properties

Typical plots of temperature variation of magnetization of oxygen annealed NSMO films are shown in Fig. 3.22, where we can see the ferromagnetic transition with T_C around 200 K. The T_C values obtained from dM/dT versus T plots are tabulated in table-3.3. The T_C value is comparable to that reported by Jin *et al.* [80] in 60 nm thick NSMO films on LAO substrate and moreover it is close to that of bulk sample [192]. However, we have not observed any measurable ferromagnetic signal on 12 nm thick NSMO film. So, it falls within the magnetic dead layer. Similar order of magnetic dead layer (10 nm) has been reported by Borges *et al.*[193] in LSMO thin films. Temperature variation of susceptibility in the paramagnetic region was fitted to the modified Curie-Weiss law (eq.3.6). The temperature independent susceptibility (χ_0) values are found to be in the range of -0.0056 emu/(cc.Oe) to -0.0246 emu/(cc.Oe). The Curie temperature (θ_C) values obtained from the fit are given in table – 3.3. and they closely follow their respective T_C.

TH-1726_11612111

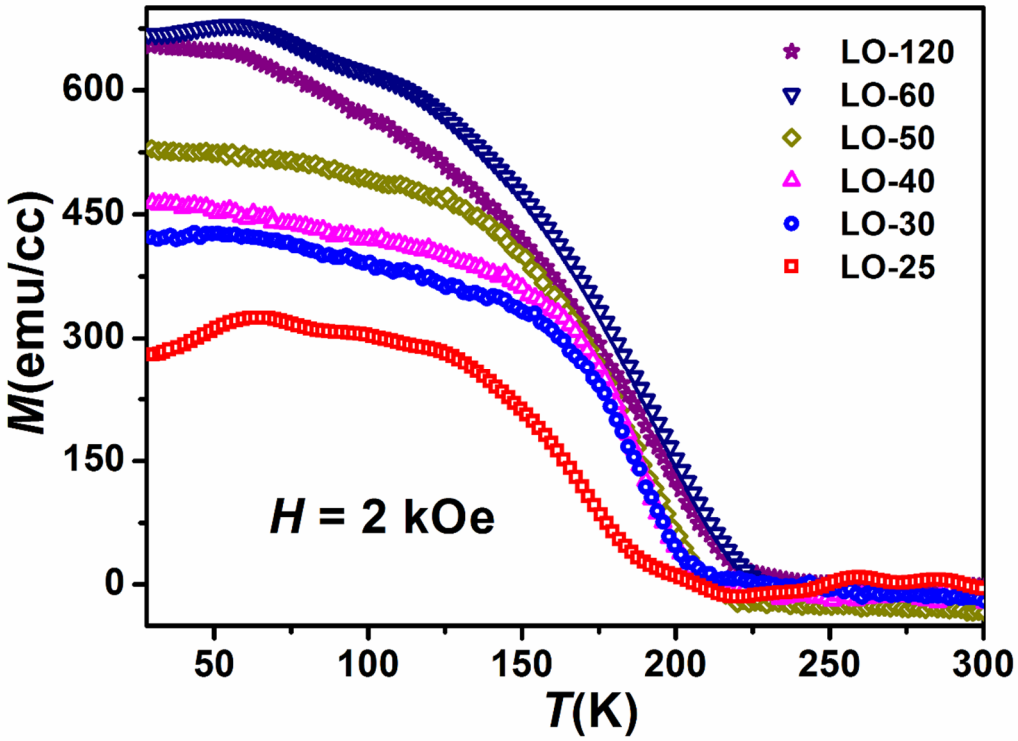

Figure 3.22: Temperature variation of zerofield cooled (H = 2 kOe) magnetization for the oxygen annealed NSMO films on LAO substrate.

M-H loops recorded at 50 K for NSMO films are shown in Fig. 3.23. All of them show typical ferromagnetic behaviour with saturation magnetization M_S close to $4\mu_B$.The M_S values obtained for different films are shown in table-3.3. The M_S value of thinner films are relatively smaller than that of thicker films and this could be mainly due to the large out-of-plane tensile strain and the corresponding distortion in MnO_6 octahedra. Such distortion is expected to affect the double exchange ferromagnetic interaction. The maximum M_S value ($4\mu_B$) obtained in NSMO film is found to be larger than the expected value ($3.7\mu_B$) due to spin only contribution of ferromagnetically ordered Mn ions. Such a large M_S value is reported in other Nd-Mn-O based bulk sample [194] and in $La_{0.7}Sr_{0.3}MnO_3$ thin films [195]. This could be due to possible contribution from orbital magnetic moment or weak ferromagnetic moment contributed by Nd^{3+} ions.

In order to further understand the magnetic behaviour, the data of initial magnetization as a function of field H were analysed by fitting to the law of approach to saturation, i.e. eq. 3.5, as per ref [196]. Here M_S, a and b are taken as the free parameters of fit. Typical plots of fitted initial magnetization curves along with the experimental data for all films are shown in Fig. 3.24. The fitted data closely follow the experimental data. From the fitted parameters and using the relation eq. 3.8. the effective magnetic anisotropy

TH-1726_11612111

constant (K) was estimated and is given in table-3.3. The anisotropy constant is found to decrease with increase in film thickness and is consistent with decrease in lattice strain. The K value is comparable to that reported by Suzuki *et al.* in LSMO film on (110)-STO substrate at room temperature [197].

Table 3.3: strain (ϵ), T_C, Curie temperature (θ_C), saturation magnetization (M_s), effective magnetic anisotropic constant (K) and T_{MI} values for films LO-25, LO-30, LO-40, LO-50, LO-60 and LO-120 films.

Film	ε(%)	T_C(K)	θ_C(K)	Ms(μ_B/f.u)	K×10^5(erg/cc)
LO-12	0.57	-	-	-	-
LO-25	0.54	165	172	2.5	3.8
LO-30	0.49	182	177	2.7	2.6
LO-40	0.44	187	182	3.2	1.9
LO-50	0.25	190	191	3.8	1.7
LO-60	0.02	200	208	4.0	1.4
LO-120	0.07	198	203	3.8	1.3

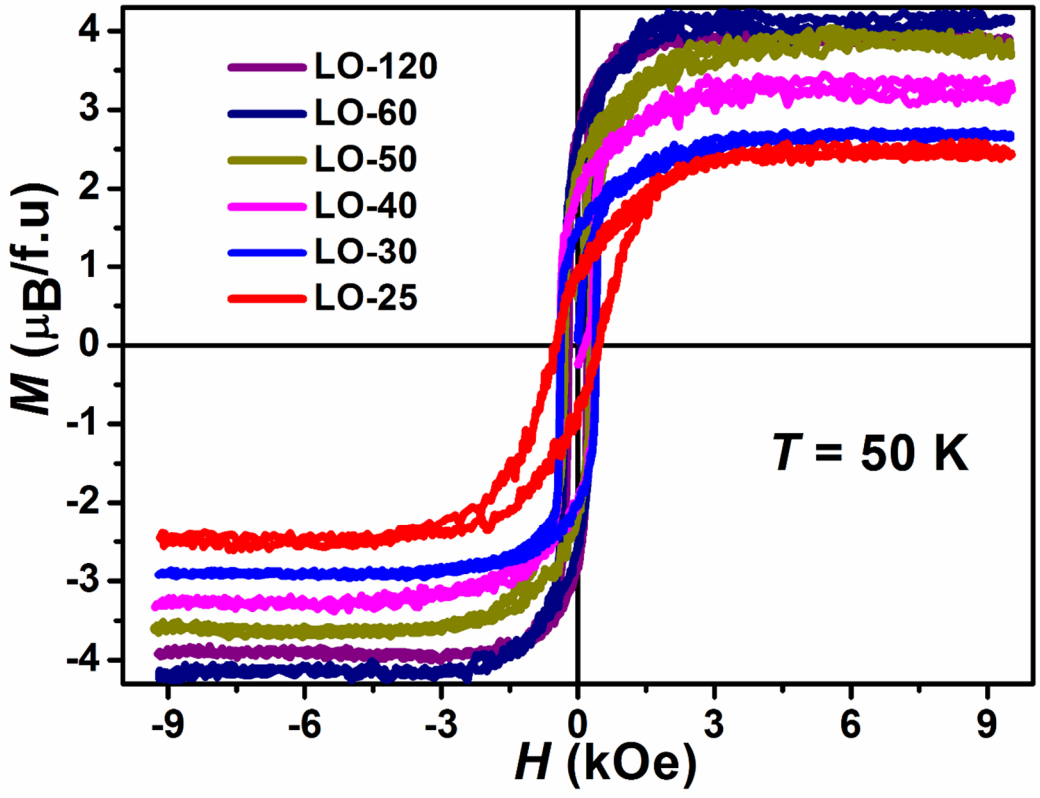

Figure 3.23: *MH*-loops recorded at 50 K.

TH-1726_11612111

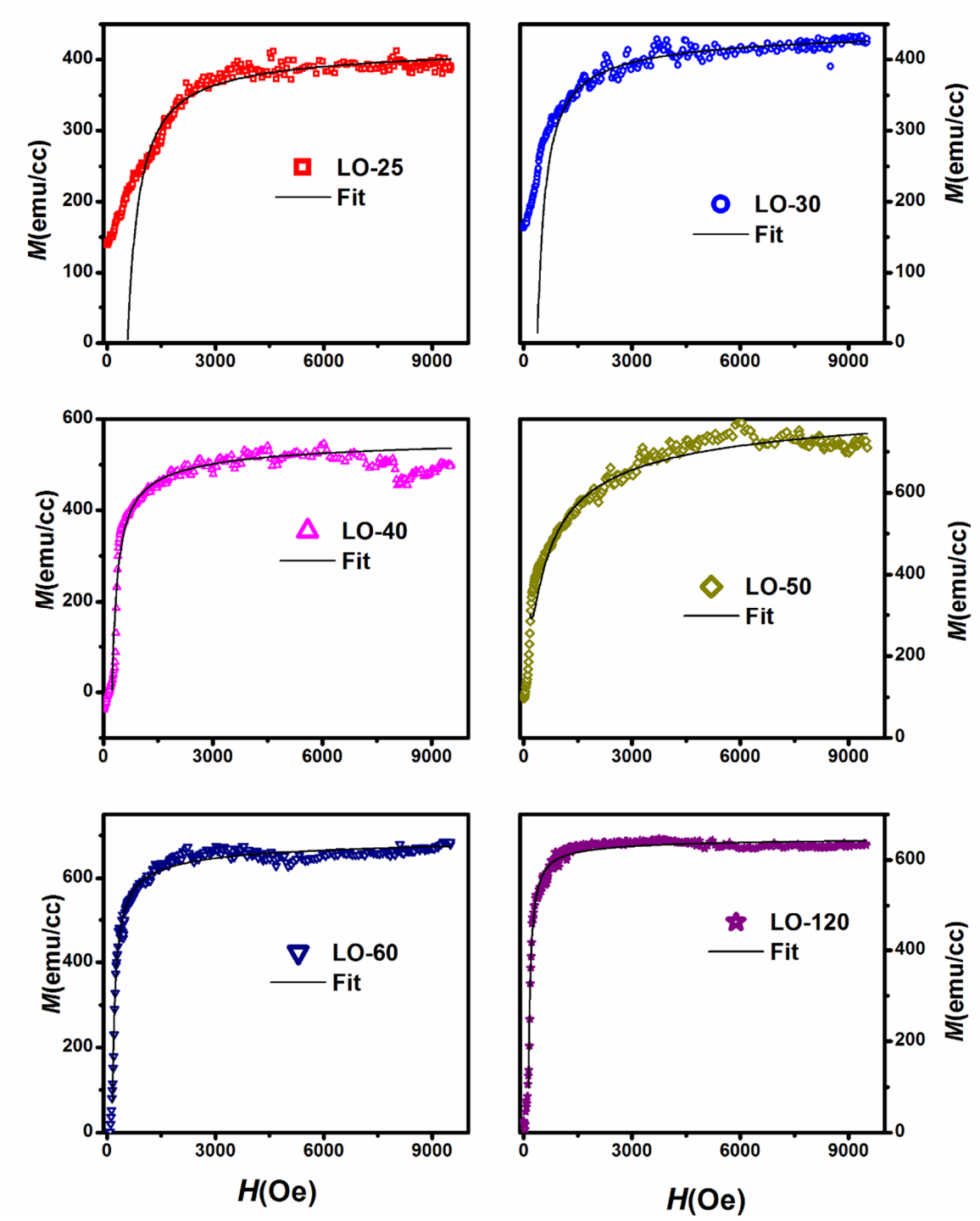

Figure 3.24: Initial magnetization curves fitted to the law of approach to saturation model (eq. 3.5) for different films.

TH-1726_11612111

3.5.5 Electrical Resistivity

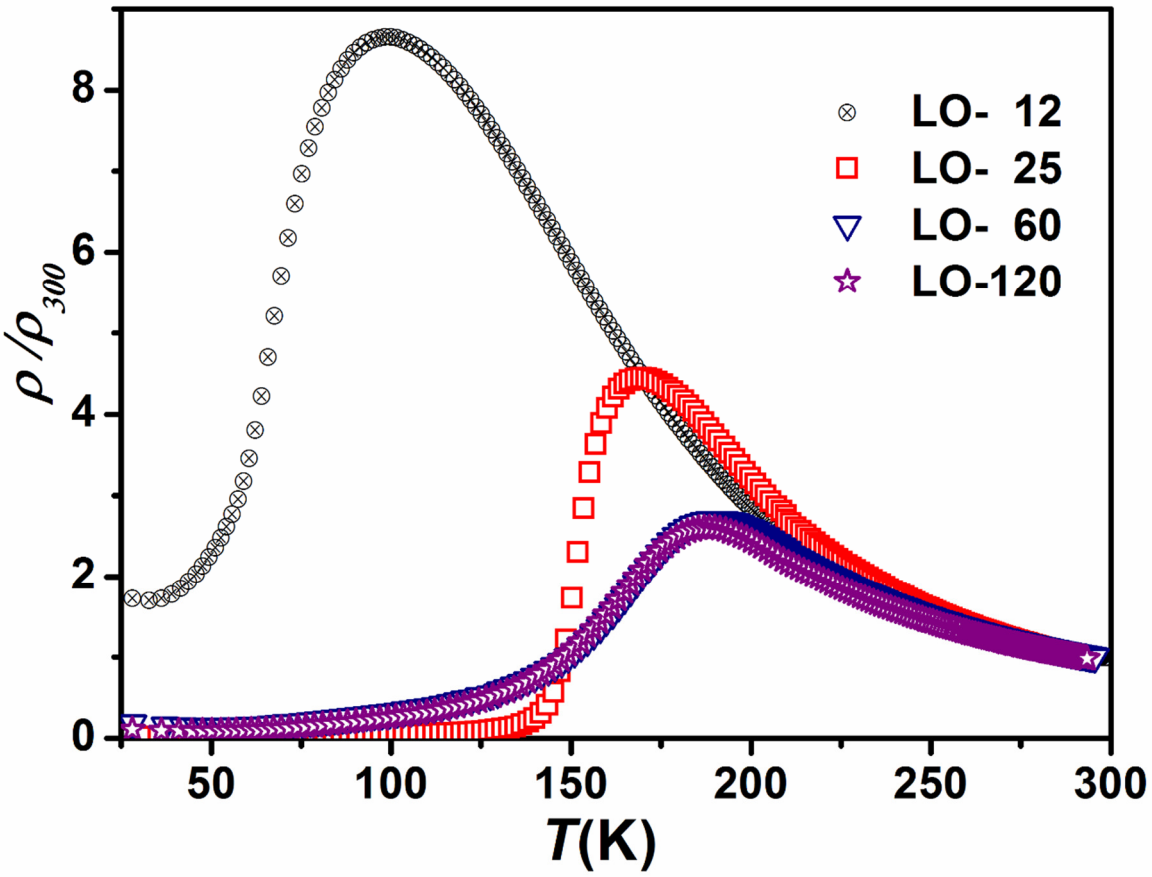

Figure 3.25: Electrical resistivity versus temperature plots for LO-12, LO-25, LO-60 and LO-120 films

Fig.3.25 shows the temperature variation of electrical resistivity of oxygen annealed NSMO films. We can see that all films including 12 nm thick film exhibit metal-insulator transition. Even though 12 nm film comes under magnetic dead layer, the appearance of metal-insulator transition highlights that electrical dead layer must be much lower than 12 nm. Borges *et al.* [193] have shown that electrical dead layer is quite small compared to magnetic dead layer due to the fact that magnetic spin polarisation requires larger thickness. According to them, the electrical and magnetic dead layer thickness for $La_{0.7}Sr_{0.3}MnO_3$ films on (001)-MgO substrate is 4 nm and 10 nm respectively. As the film thickness is increased from 12 nm to 60 nm, a sharp increase in T_{MI} close to that of bulk sample (200 K) is seen and for further increase in thickness, no appreciable increase in T_{MI} is seen. However T_{MI} values of 120 nm thick film is relatively smaller than that of 60 nm and this could due to oxygen off-stoichiometry in thicker films.

TH-1726_11612111

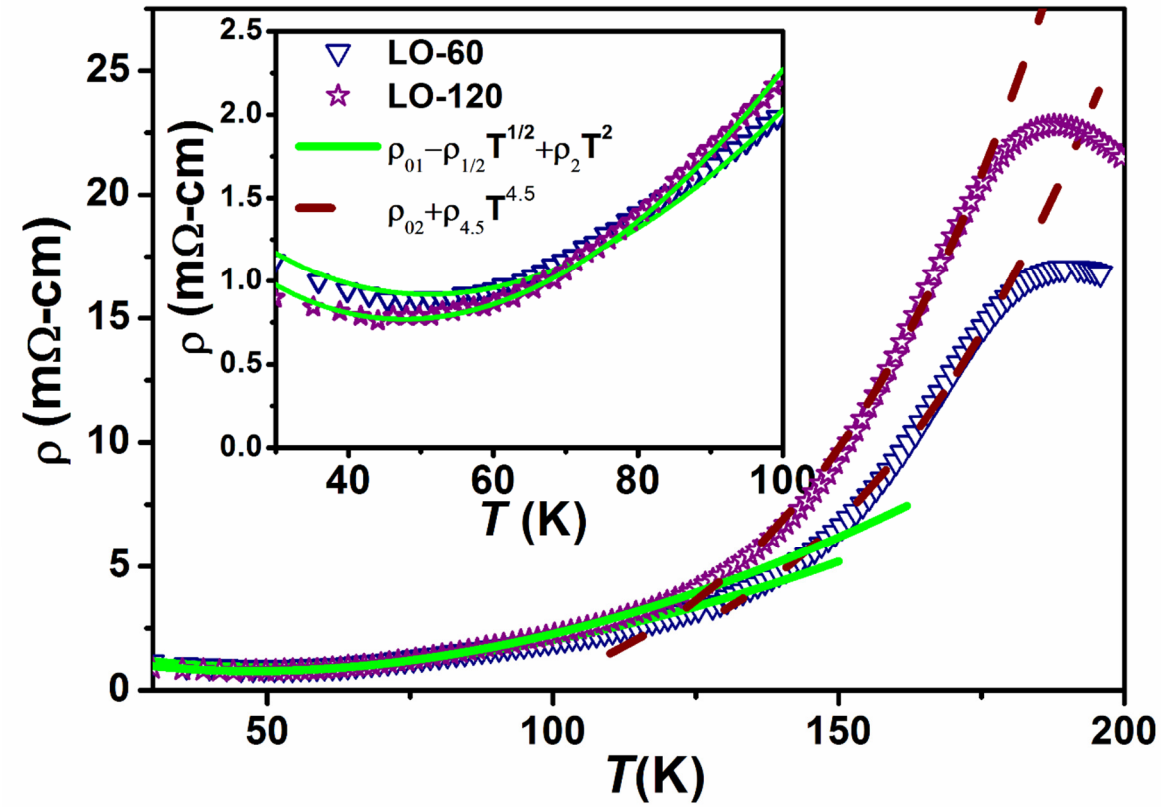

Figure 3.26: Resistivity versus temperature plots of LO-60 and LO-120 films for $T < T_{MI}$ .The solid line corresponds to fit to Eq.(3.11) and the dashed lines represent fit to Eq. (3.12). Inset shows the enlarged view of resistivity plot in the low temperature region.

The electrical resistivity data in the metallic region are generally fitted to the following empirical relation,

$$\rho = \rho_0 + \rho_m T^m + \rho_n T^n \qquad (3.10)$$

Here ρ_0 is the temperature independent residual resistivity due to the scattering by impurities, defects, grain boundaries, domain wall, etc. The exponents m and n take the values depending on the nature of scattering mechanism. Often more than one scattering mechanisms contribute to the electrical resistivity of manganites. T^2, T^3 and $T^{4.5}$ dependences are attributed to electron - electron scattering [198, 199], spin fluctuations [200] and electron-magnon [201] scattering respectively. In addition to the above scattering mechanisms, the low temperature upturn in the resistivity plot is taken care by including a term - $T^{1/2}$and it is attributed to weak localization effect [202, 203].

Typical plots of temperature variation of electrical resistivity in the metallic region for LO-60 and LO-120 films are shown in Fig.3.26. The resistivity values fall quite sharply as the temperature in reduced below T_{MI} and however, for $T \leq 125$ K, the resistivity

TH-1726_11612111

decreases only gradually. For clarity, the temperature dependence of resistivity for $T <$ 100 K is shown in the inset of Fig. 3.26, where a clear upturn is seen at low temperature. Thus the scattering mechanism governing the electrical resistivity in the vicinity of T_{MI} drastically differs from that in the low temperature region.

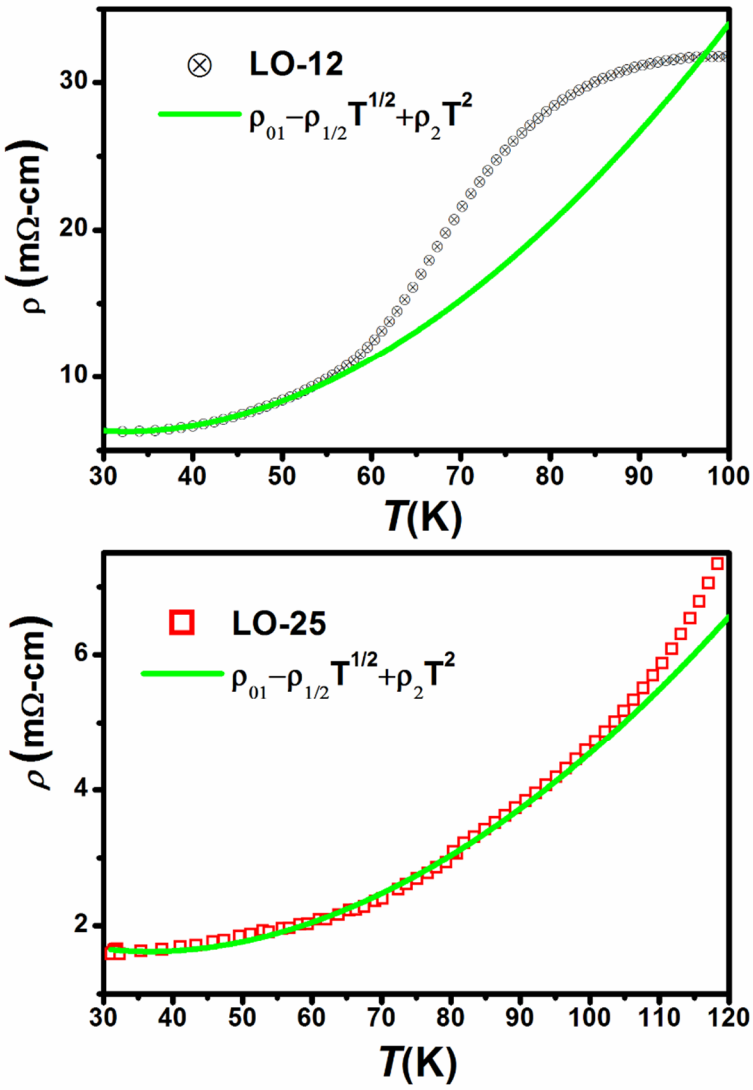

Figure 3.27: Resistivity versus temperature plots along with the fit to the eq.3.11 for the samples of LO-12 and LO-25 films in the metallic region.

The electrical resistivity data in the low temperature region ($T <$ 125 K) could be successfully fitted to the relation,

$$\rho = \rho_{o1} - \rho_{1/2}T^{1/2} + \rho_2 T^2 \qquad (3.11)$$

TH-1726_11612111

The fitted data are shown as solid line in Fig. 3.26 and the expanded view of ρ versus T upto 100 K including the fitted data are shown in the inset of Fig. 3.26. They closely follow the experimental data. Thus the electrical resistivity at low temperature region is governed by electron - electron scattering and weak localisation effect. However for T > 125K the above fit is found to deviate from the experimental data, so, the resistivity data in the vicinity of T_{MI} were fitted to the relation,

$$\rho = \rho_{02} + \rho_{4.5}T^{4.5} \tag{3.12}$$

The fitted data are shown as dashed lines in Fig.3.26. Thus the rather sharp rise in resistivity in the vicinity of T_{MI} could be explained by electron magnon scattering effect. The ρ_{02} values are found to be in the same order of magnitude as that of ρ_{01}. Unlike the thicker film ($d > 60\ nm$), the resistivity of 12 and 25 nm films follow only eq (3.11) in the temperature region of T < 60 K and T < 120 K respectively as shown in Fig.3.27. So, there is a predominant weak localization effect to the electrical resistivity. This can be understood in terms of defects and large strain in thinner films. A sharp decrease in residual resistivity is seen as the film thickness is increased from 12 nm (55 Ω-cm) to 60 nm (3.6 Ω-cm) and for further increase in film thickness, no appreciable variation in ρ_0 is obtained as given in table – 3.4. Similarly $\rho_{1/2}$ and ρ_2 values of 12 nm film are found to be about an order of magnitude larger than those of thicker films.

The electrical resistivity data in the insulating region ($T > T_{MI}$) were fitted the eq.3.3 [182]. Typical plots of lnρ versus $T^{-1/4}$ for LO-12, LO-25, LO-60 and LO-120 films are shown in Fig.3.28. They exhibit linear behaviour for $T > T_{MI}$, i.e. mostly in the temperature range of 220 to 300 K ($T^{-1/4}$ = 0.26 to 0.24). However 12 nm thick film exhibits linear behaviour down to around 100 K ($T^{-1/4}$ = 0.28) due to lower T_{MI} value. The fitting was carried out by allowing ρ_{0m} and T_{0m} as free parameters of the fit. The fitted data are shown as solid line in Fig.3.28. The fitted ρ_{0m} value was found to be in the order of 10^{-7} Ω-cm. From the fitted values of T_{0m} we have estimated hopping energy at 300 K using the eq. 3.4 [182]. The obtained values of E_h are given in table - 3.4. Unlike, the resistivity in the metallic region, here it is not very sensitive to substrate induced strain on the film. ρ_{0m}value is found to increase with increase in film thickness and it can be attributed to increase in the density of defects, as the film thickness is increased. This observation is consistent with the magnitude of resistivity at 300 K, which increases with

TH-1726_11612111

increase in thickness and on the other hand, the hopping energy in found to marginally decrease with increase in film thickness.

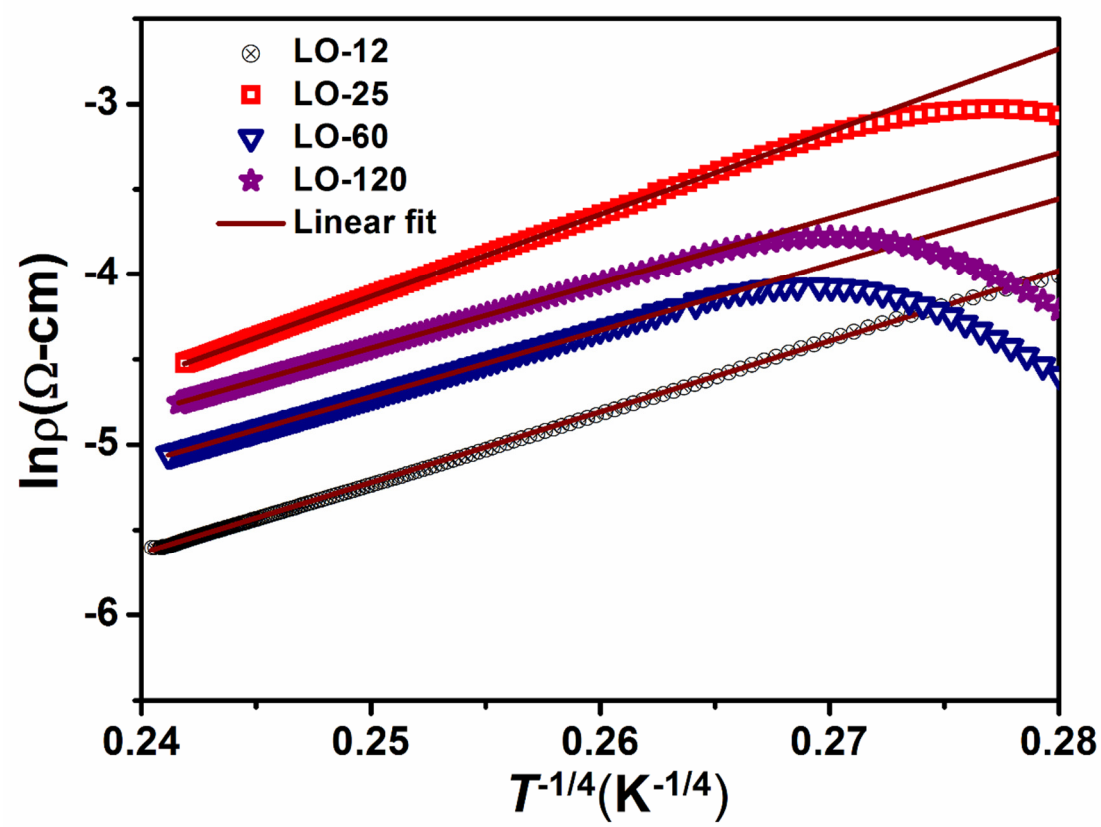

Figure 3.28: lnρ versus $T^{-1/4}$ plots along with fit to Mott-VRH model

Table 3.4: Parameters obtained from the analysis of electrical resistivity data.

Film	ρ_0 (mΩ-cm)	$\rho_{1/2}$ (mΩ-cmK$^{-1/2}$)	ρ_2 (μΩ-cmK^{-2})	$\rho_{4.5}\times10^{-6}$ (μΩ-cmK$^{-4.5}$)	E_h (meV)
LO-12	55	10.1	1.5	-	64
LO-25	3.9	5.0	0.5	-	61
LO-60	3.6	0.5	0.3	1.2	60
LO-120	3.5	0.5	0.4	1.7	59

TH-1726_11612111

3.5.6 Magneto-Resistivity of NSMO Films

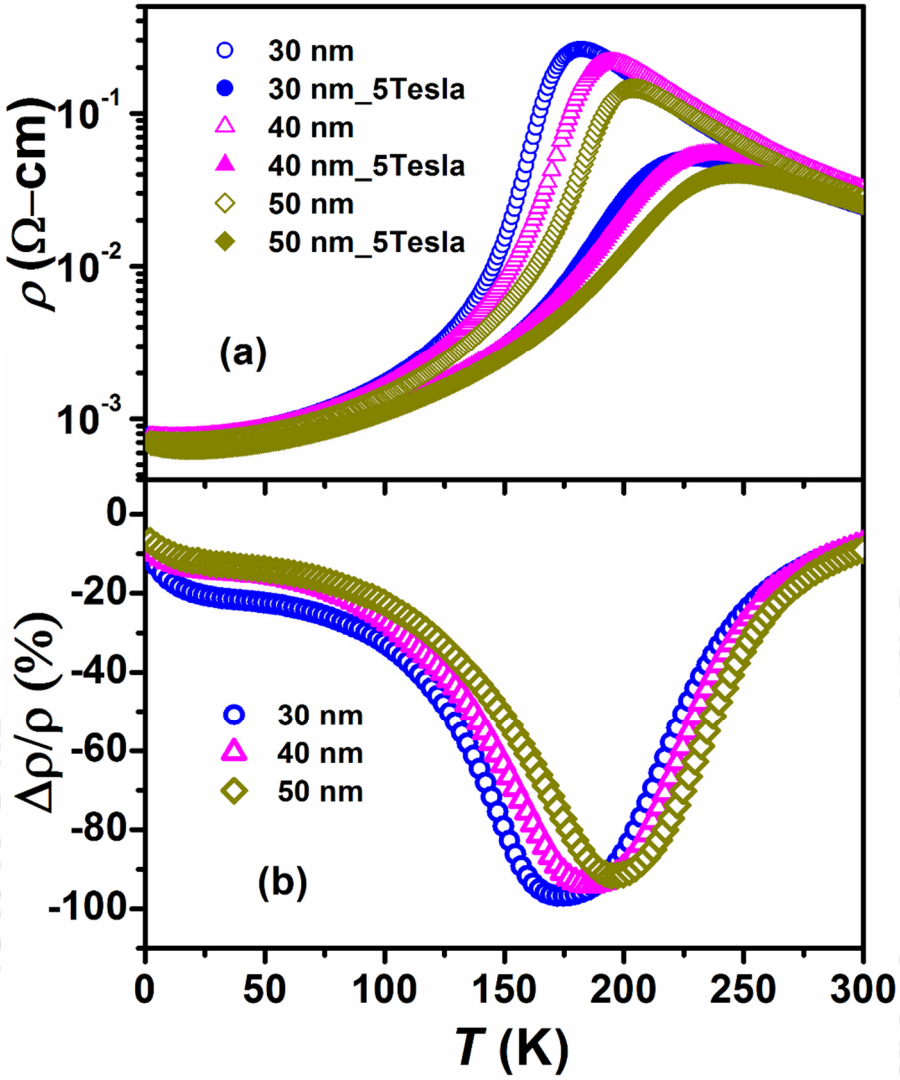

Figure 3.29: (a) Temprature variation of electrical resistivity in the absence of field and in the presence 5 T magnetic field.(b) Temperature variation of maagneto-resistivity for 30, 40 and 50 nm thick films.

The typical temperature dependence of electrical resistivity for 30, 40 and 50 nm films in the absence of applied field and in presence of applied magnetic field of 5 T are shown in Fig. 3.29(a). All films exhibit metal to insulator transition and this transition is shifted to higher temperture region in the presence of external magnetic field. The magnitude of electrical resisvity data drops when the films are exposed to the magnetic field. The magnetoresistivity (MR) was calculated from the relation:

$$\text{MR}\ (\%) = \left[\frac{\rho(H) - \rho(0)}{\rho(0)}\right] \times 100 \qquad (3.13)$$

TH-1726_11612111

where $\rho(0)$ and $\rho(H)$ are the values of resistivity in the absence and in presence of a magnetic field, respectively. The MR values of the NSMO/LAO thinfilms were obtained in the temperature range (2 – 300 K) for 5 T field. These data are plotted as a function of temperature as shown in Fig.3.29(b), where a clear increase in the magnitude of MR (%) with increase in film thickness is seen. The maximum magnitude of MR (%) values are obtained at a temperature close the metal-insulator temperature (T_{MI}). The best MR (~96%) was observed for 30 nm thick film at 177 K, and the lowest MR (92%) was found for the 50 nm thick at 197 K.

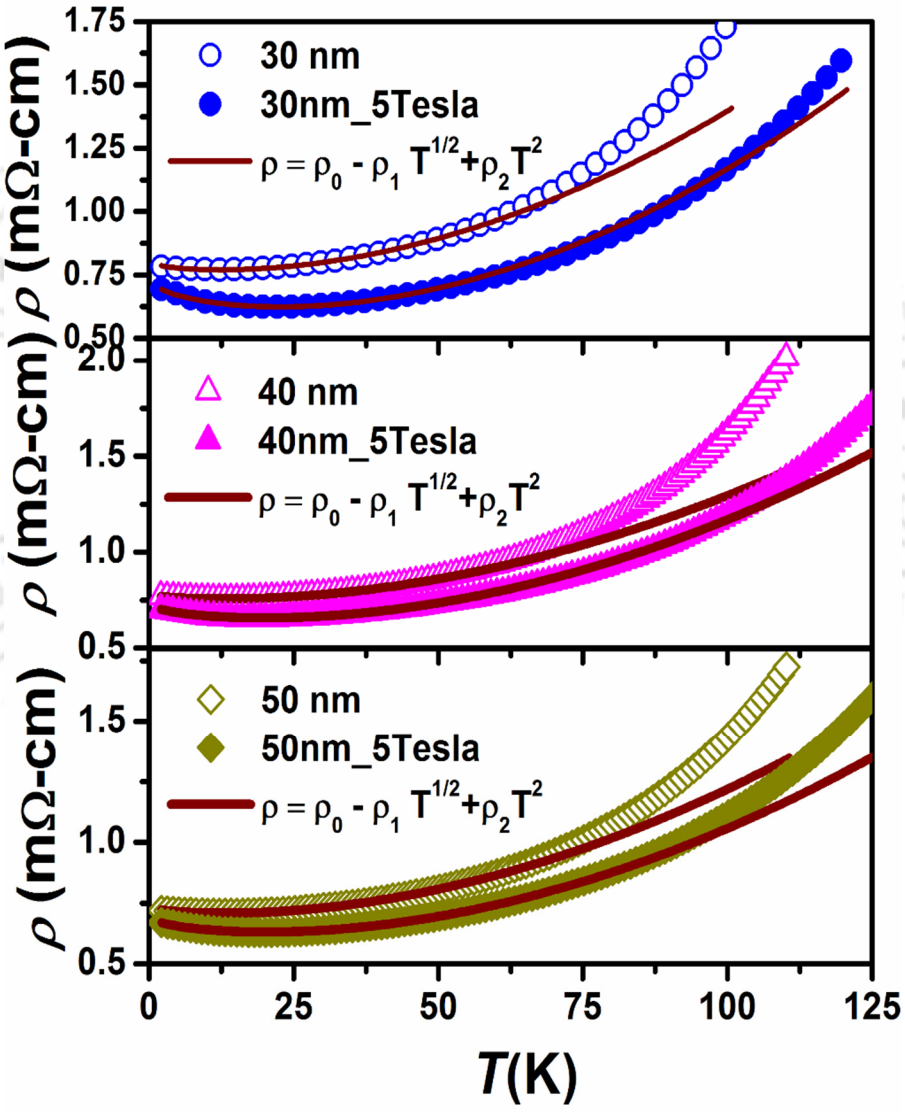

Figure 3.30: Fit of electrical resistivity data in the metallic region for H = 0 and 5 T field by using eq.3.11.

The resistivity data were analysed using the eq. 3.11 in the metallic region. The fitted data of the thin films are shown in Fig. 3.30 wherein the symbols are the experimental

TH-1726_11612111

data and the solid lines are the fitted data. It is seen that the data are fitted perfectly and the values of the parameters obtained from the fit are tabulated in Table-3.4. The fitted parameters such as residual resistivity and temperature coefficients of resistivity $\rho_{1/2}$ and ρ_2 are found to decrease with increase in film thickness both for H = 0 and 5 T fields. This signifies that the contribution of weak localization is suppressed with increase in film thickness. This supression could be achieved due to the relaxation of strain and the reorientation of grains with minimal defects at grain boudaries, etc. However with the application of magnetic field eventhough the residual resistivity is reduced considerably, the temperature coeffients of resistivity values are found to increase due to increased scattering of electrons due the external field. However, the above argument holds true only at temperatures far below T_{MI} at which data were analysed.

Table 3.5: Parameters obtained from the analysis of electrical and magneto-resistivity data.

Film	T_{MI} (K)	$\rho_0 \times 10^{-4}$ (Ω-cm)	$\rho_{1/2} \times 10^{-5}$ (Ω-cmK$^{-1/2}$)	$\rho_2 \times 10^{-8}$ (Ω-cmK^{-2})
30 nm (0 T)	184	8.02	1.17	7.21
30 nm (5 T)	232	7.41	3.26	7.54
40 nm (0 T)	196	7.86	1.16	6.17
40 nm (5 T)	240	7.37	2.40	6.72
50 nm (0 T)	205	7.35	0.96	5.25
50 nm (5 T)	248	7.00	2.27	6.33

The variation of T_{MI} with film thickness is shown in the Fig.3.31, where T_{MI} tends to saturate as the film thickness increases and approaches towards bulk T_{MI} (B). It is analysed in terms of scaling theory,

$$\left[\frac{[T_{MI}\ (B) - T_{MI}\ (t)]}{T_{MI}\ (B)}\right] = \left[\frac{k}{t}\right]^{\lambda} \qquad (3.14)$$

TH-1726_11612111

where k and λ are constants [204]. The fitted data by taking k and λ as free parameters of the fit and by taking T_{MI}(B) = 205 K are shown as solid line in Fig. 3.31. The estimated values of k and λ are found to be 8.4 nm and 1.79 respectively.

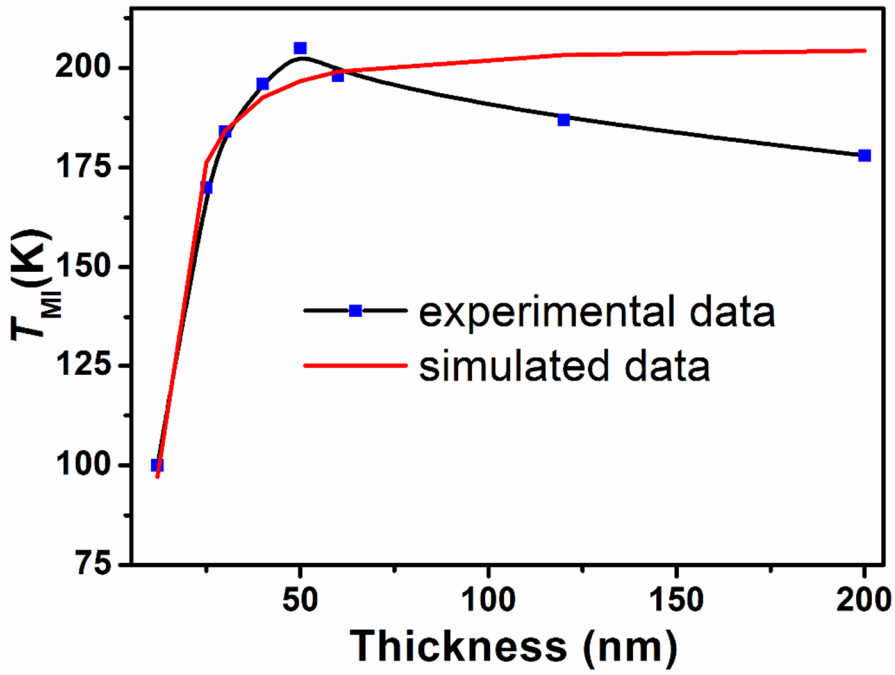

Figure 3.31: T_{MI} as a function of thickness (t) of NSMO along with fitted data

3. 5. 7 Conclusions

We have prepared c-oriented $Nd_{0.7}Sr_{0.3}MnO_3$ films on (001)oriented $LaAlO_3$ substrate by varying the thickness in the range of 12 nm to 120 nm. The lattice strain is found to relax with increase in film thickness. The Raman spectra analysis shows that for lower thickness of films intense Raman peaks due to rotational and stretching modes of MnO_6 octahedra are seen and their intensity is found to decrease with increase in film thickness. Magnetization measurements show that all films exhibit ferromagnetic transition with a maximum T_C of 200 K and it is close to that of bulk sample. Magnetic dead layer of about 12 nm is observed. The *M-H* loops measured at 50 K shows a maximum M_s value of about 4 μ_B. The analysis of *M-H* loop and the estimation of magnetic anisotropy constant shows that films of lower thickness exhibit larger anisotropy constant. Temperature variation of electrical resistivity of all films show metal-insulator transition. Films of higher thickness show larger T_{MI}. The resistivity in the metallic region was fitted by dividing them into two different regions, sharp decrease in resistivity in the vicinity of T_{MI} was fitted by considering the electron-magnon scattering mechanism but at low temperature the

TH-1726_11612111

combination of electron - electron scattering and weak localisation effect was taken into the account. The resistivity data in the insulating region were fitted to Mott-VRH model. The estimated hopping energy is found to decrease with increase in film thickness.

भारतीय प्रौद्योगिकी संस्थान गुवाहाटी • Indian Institute of Technology Guwahati •

TH-1726_11612111

Chapter 4
Deposition and Characterisation of $Nd_{0.7}Sr_{0.3}MnO_3/Nd_{0.8}Na_{0.2}MnO_3$ Bilayer Thin Films

TH-1726_11612111

TH-1726_11612111

4.1 Introduction

In this chapter we report the deposition of bilayer $Nd_{0.7}Sr_{0.3}MnO_3$ (NSMO) and $Nd_{0.8}Na_{0.2}MnO_3$ (NNMO) films and study of their electrical and magnetic properties. Here NSMO is a ferromagnetic material and NNMO is a charge ordered (CO) antiferromagnetic material. The functional properties of bilayers are studied by varying the thickness of NSMO layer. Here, we have deposited NSMO layer based on optimised condition discussed in the earlier chapter. Before the deposition of bilayers, we have optimized the deposition of charge ordered (CO) $Nd_{0.8}Na_{0.2}MnO_3$ thin films and studied their electrical transport and magnetic properties.

The e_g - electron bandwidth is known to be strongly influenced by the average ionic radius at rare - earth (R) site of $RMnO_3$ series. The bandwidth decreases with decrease in average ionic radius in the rare earth site and it leads to weakening of double exchange ferromagnetic interaction and the strengthening of competing charge ordering (CO) induced anti-ferromagnetism [205]. The charge ordering is the manifestation of real space ordering of Mn^{3+} and Mn^{4+} ions that overcome the kinetic energy of charge carriers such that e_g - electrons are localized and this arrangement gives rise to antiferromagnetic interaction. The charge ordering is generally observed in half doped rare-earth manganites $R_{0.5}A_{0.5}MnO_3$ (R = La, Nd etc.; A = Ca, Sr) [199, 206-209] or in narrow bandwidth systems like $Nd_{0.8}Na_{0.2}MnO_3$, $Pr_{0.8}Na_{0.2}MnO_3$ [194, 210].

Several authors have worked on CO materials in thin film form to optimise their electrical and magnetic properties towards potential applications in memory devices. Nakamura *et al.* have investigated the effect of lattice strain on charge and orbital ordered $Nd_{0.5}Sr_{0.5}MnO_3$ thin films grown on (001), (110) and (111) oriented $SrTiO_3$ substrates [211]. The suppression of CO is studied by varying the particle size, film thickness, applied electrical field and magnetic field [207, 212-216]. According to Prellier *et al.* [215], the CO in thinner films of $Pr_{0.5}Ca_{0.5}MnO_3$ could not be suppressed even for an applied field of H = 9 T and on the other hand in thicker films (110 nm), the CO is suppressed by a moderate field of 5T. However, Elovaara *et al.* [216] have reported that it is difficult to suppress the CO in thicker films of $Pr_{0.6}Ca_{0.4}MnO_3$ compared to that of thinner films. In view of the above contradicting reports and due to the lack of thickness dependent study of electrical and magnetic properties of (Nd, Na)MnO_3 series we have taken up a detailed study on $Nd_{0.8}Na_{0.2}MnO_3$ thin films.

TH-1726_11612111

$Nd_{0.7}Sr_{0.3}MnO_3$ (NSMO) is one of the interesting manganites having ferromagnetic and metal-insulator transitions in the vicinity of room temperature along with large magneto-resistance [217, 218]. Xiong *et al.* [219] have reported the MR of the order 10^6 % at 60 K for the applied magnetic field of 8 T in epitaxial NSMO films on $LaAlO_3$ substrate. Moreover, the film thickness and the substrate dependence of electrical and magnetic properties were investigated on NSMO films [80]. The electrical and magnetic properties of $Nd_{0.67}Sr_{0.33}MnO_3/Nd_{0.5}Ca_{0.5}MnO_3$ bilayers are reported to be quite sensitive to the thickness of films [220]. MR value of – 60 % at 270 K for a field of 8 T is reported in hetero-structure of $La_{0.67}Sr_{0.33}MnO_3/Nd_{0.67}Sr_{0.33}MnO_3$ films grown by pulsed laser deposition technique [221]. Hence, it would be interesting to study the effect of inter layer coupling of ferromagnetic $Nd_{0.7}Sr_{0.3}MnO_3$ (NSMO) with a charge ordered antiferromagnetic $Nd_{0.8}Na_{0.2}MnO_3$ (NNMO) films [222]. In the present work, we have deposited bilayer films of $Nd_{0.7}Sr_{0.3}MnO_3/Nd_{0.8}Na_{0.2}MnO_3$ by varying the thickness of NSMO layer and studied their structural, electrical and magnetic properties.

4.2 Preparation and Characterisation of Bulk $Nd_{0.8}Na_{0.2}MnO_3$

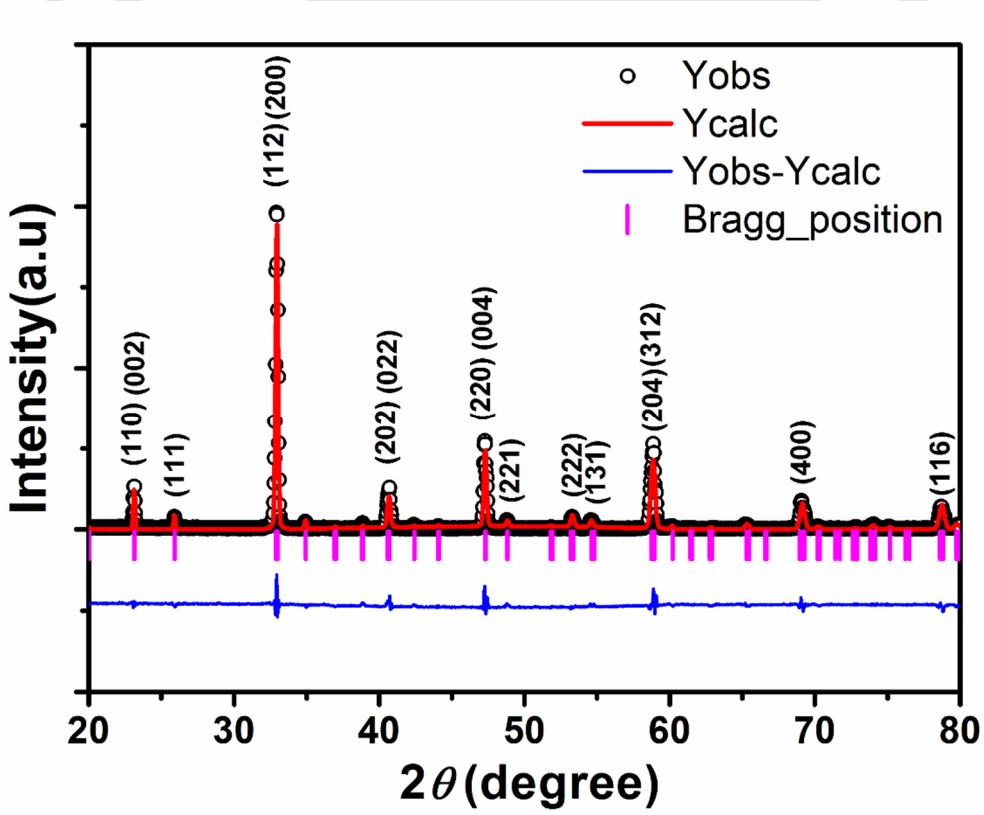

Figure 4.1: The XRD pattern of the polycrystalline bulk NNMO sample along with Rietveld refinement using Pbnm space group.

TH-1726_11612111

The bulk $Nd_{0.8}Na_{0.2}MnO_3$ (NNMO) compound was initially prepared by choosing the stoichiometric ratio of starting compounds Nd_2O_3, $C_4H_6MnO_4\ 4H_2O$ and Na_2CO_3 of purity better than 99%. They were grinded under acetone medium followed by pre-sintering in the temperature range of 400 - 700°C with an intermediate grinding between each annealing temperature. The pre-sintered powder was pressed into a 2 inch diameter target material and annealed at 800°C, followed by final sintering at 1200°C for 30 hrs in air.

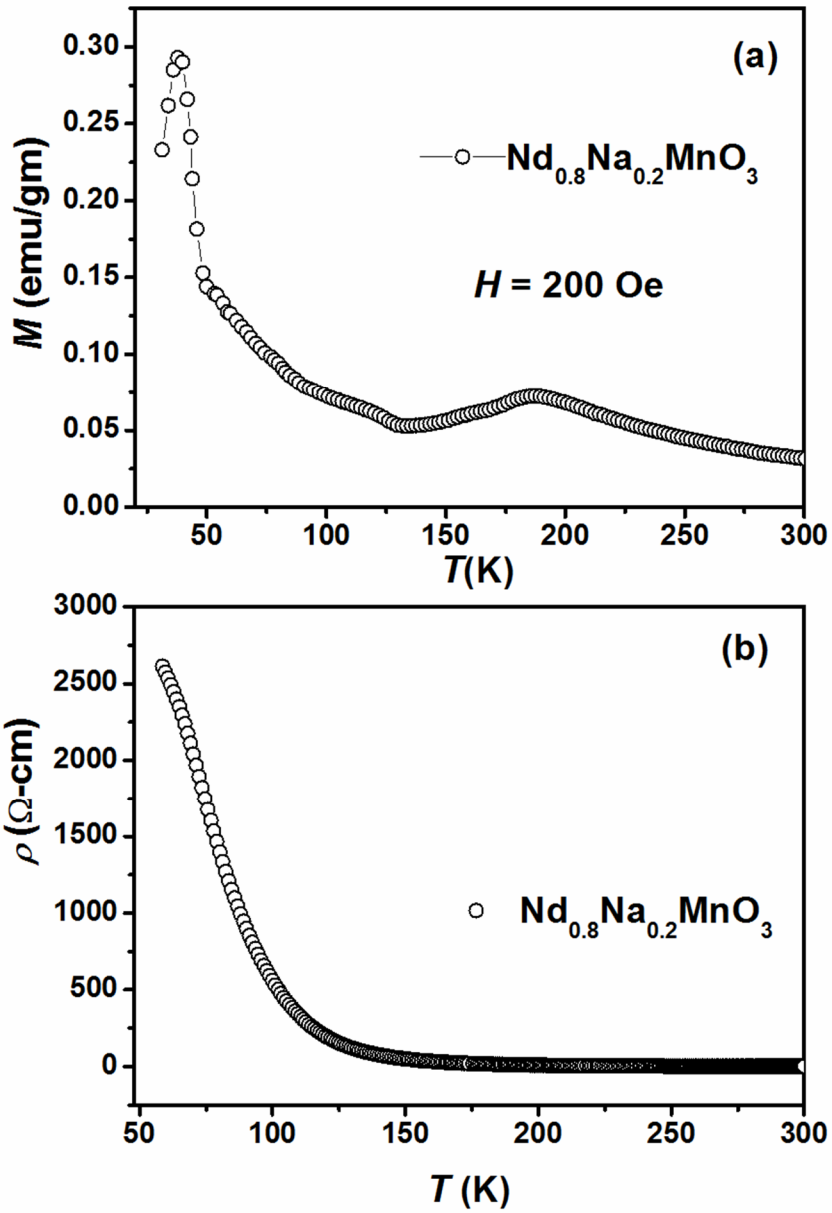

Figure 4.2: (a) Temperature variation of magnetization under zero field cooled condition and (b) temperature variation of electrical resistivity for the NNMO target.

The XRD pattern of $Nd_{0.8}Na_{0.2}MnO_3$ target material is shown in Fig.4.1 and as per the Rietveld refinement using Pbnm space group, it is found to be in single phase form with

TH-1726_11612111

lattice parameters a = 5.420 Å, b = 5.442 Å and c = 7.676 Å. The average pseudo cubic lattice parameter is deduced as c' (= c/2) = 3.838 Å using the lattice constant of the bulk target material. The temperature (T) variation of magnetization (M) measurement under zero field cooled condition for an applied magnetic field of 200 Oe is shown in Fig.4.2(a) and it shows a charge ordering transition around 188 K. However for T < 100 K, a secondary rise in magnetization is observed due to a possible low temperature ferromagnetic transition as shown in Fig.4.2. The characteristic feature of M - T plot is comparable to that reported in ref [223] for the CO bulk $Nd_{0.8}Na_{0.2}MnO_3$. The temperature variation of electrical resistivity data show a typical insulating behaviour as shown in Fig. 4.2(b).

4.3 Preparation and Characterisation of NNMO Thin Films

4.3.1 Preparation of NNMO Thin Films

Thin films were deposited by using RF-magnetron sputtering unit on (001)-$LaAlO_3$ substrate. The system was evacuated to a base pressure of 3 $\times 10^{-6}$ mbar and the substrate temperature was maintained at 650°C. The working pressure was maintained at 2.5 $\times 10^{-2}$ mbar by allowing the flow of Ar/O_2 gas mixture in 3:1 ratio. The RF power was maintained at 50 W during the deposition. By controlling the duration of deposition, films of thickness 30 nm, 40 nm, 50 nm, 75 nm and 100 nm were obtained. These films were post-annealed at 700°C for an hour in 0.5 mbar of oxygen environment.

4.3.2 Structural Properties

XRD patterns of NNMO thin films for thickness in the range of 30 nm to 100 nm are shown in Fig.4.3 with intensity in logarithmic scale. The evolution of (002) peak around $2\theta \approx 47°$ is clearly seen and it depicts the growth of films along the c-direction i.e. perpendicular to the plane of the film. The 2θ position of (002) peak is found to shift towards higher angle with increase in film thickness and the typical enlarged view of (002) peaks are shown in Fig.4.4 for 40, 75 and 100 nm films. The out-of-plane lattice constant value determined from (002) reflection is found to decrease with increase in film thickness as shown in table - 4.1. Such a trend of decrease of out-of-plane lattice constant and approaching towards bulk value highlights the presence of out-of-plane tensile strain. The lattice mismatch between the substrate and the sample is generally determined using the relation $(a_{sub}-a_{bulk})/a_{sub} \times 100\%$ where a_{sub} is the lattice constant of LAO. The lattice

TH-1726_11612111

mismatch is estimated to be -1.3% and it highlights the impending in-plane compressive strain and out-of-plane tensile strain. The substrate induced lattice strain (ε) was estimated using the relation

$$\varepsilon = \frac{(c_f - c')}{c'} \times 100\% \qquad (4.1)$$

Where c_f is the out-of-plane lattice constant of film and these values are tabulated in table - 4.1. The lattice is found to relax with increase in film thickness.

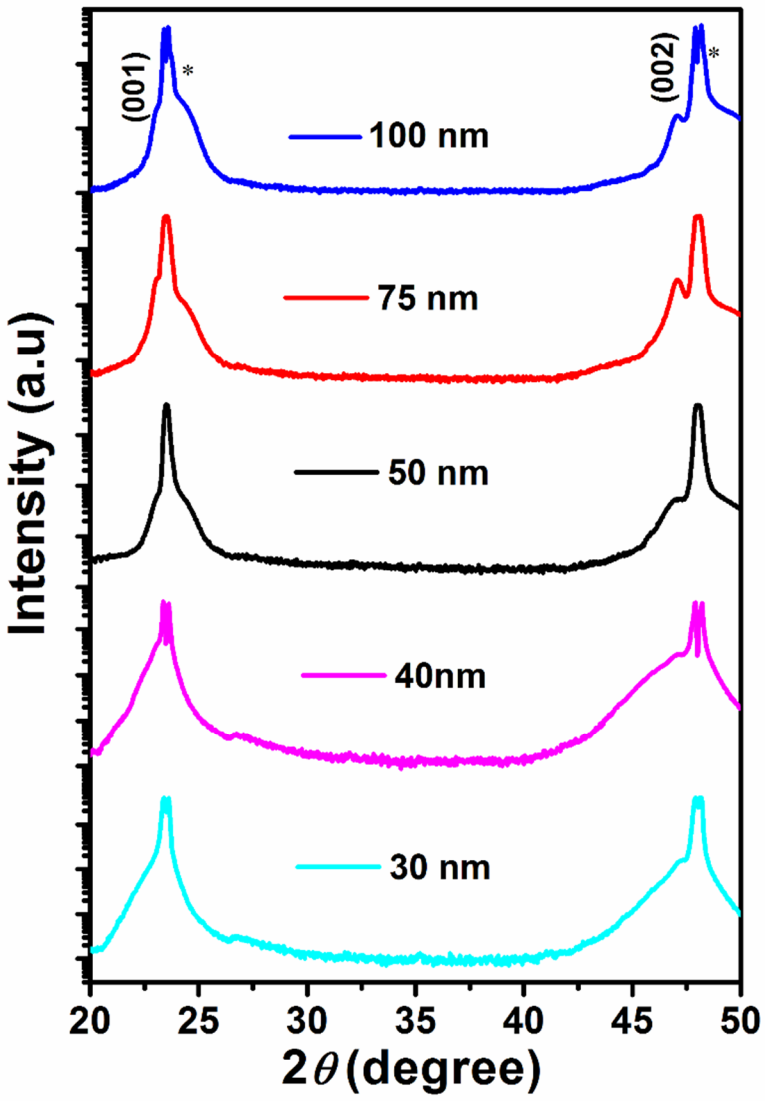

Figure 4.3: XRD patterns of NNMO films with thicknesses 30, 40, 50, 75 and 100 nm on LAO substrate. Star represents the (00*l*) reflections of the substrate.

TH-1726_11612111

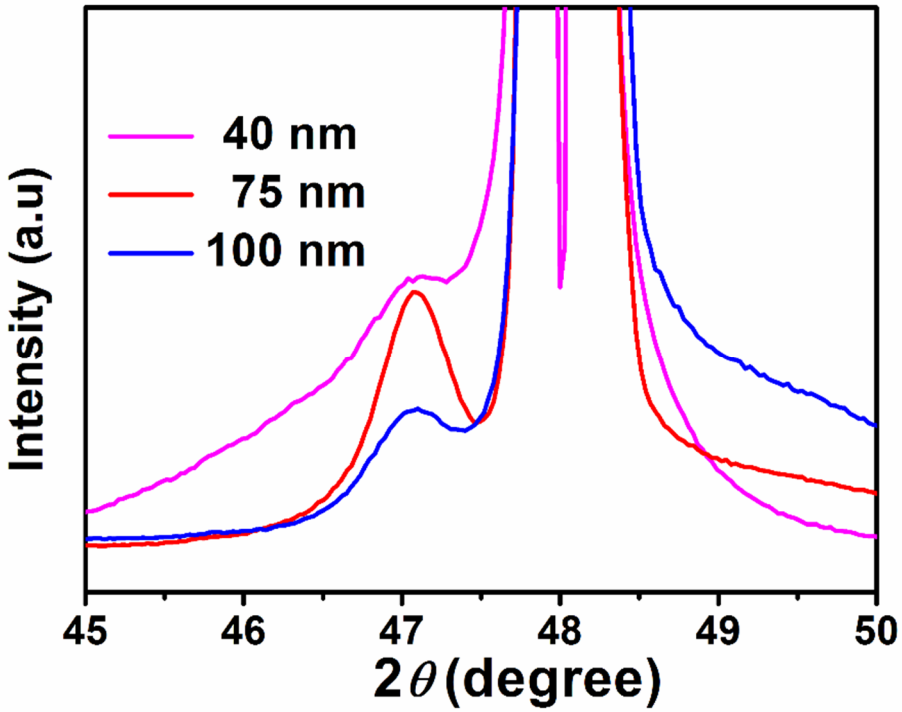

Figure 4.4: The enlarged view of the (002) peak of 40, 75 and 100 nm films on LAO substrate.

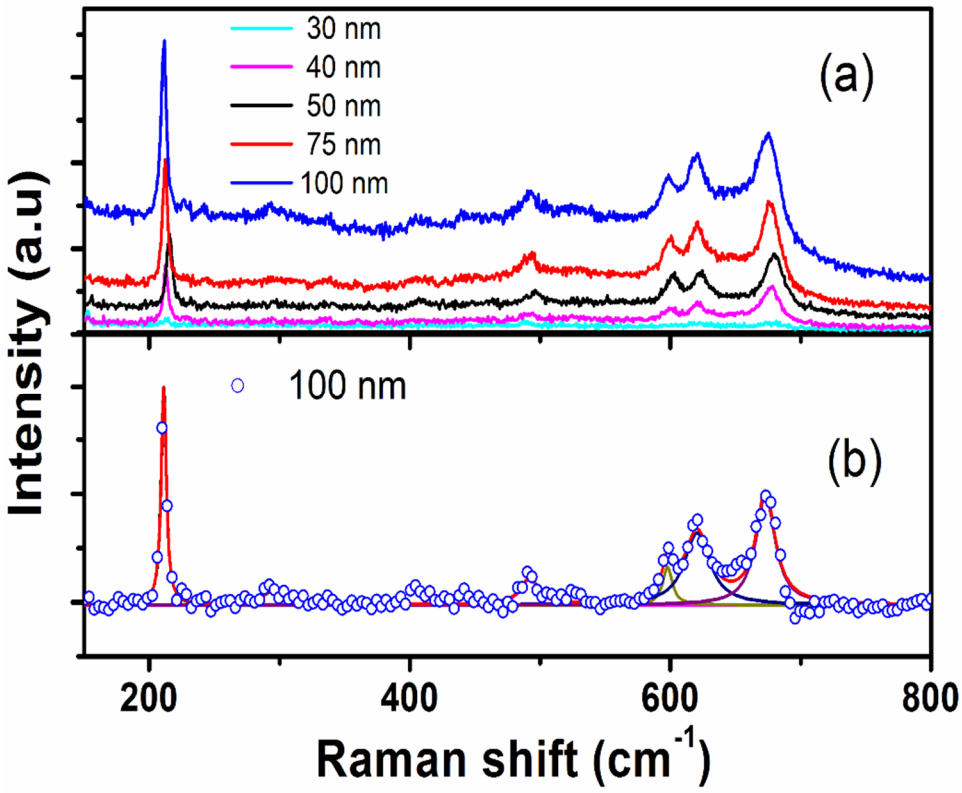

Figure 4.5 (*a*): The Raman spectra recorded at room temperature for films of different thicknesses. (b) The Raman spectrum of 100 nm film along with Lorentzian multiple peak fit.

TH-1726_11612111

The Raman spectra recorded at room temperature for different films are shown in Fig.4.5(*a*), where prominent peaks are observed at 211 cm^{-1}, 490 cm^{-1}, 601 cm^{-1}, 620 cm^{-1} and 680 cm^{-1} respectively. The peak positions were determined by carrying out Lorentzian fit and the typical Lorentzian fit along with experimental data for 100 nm film is shown in Fig.4.5(*b*). Even though group theoretical calculation predicts 24 Raman active modes for orthorhombic manganite with Pbnm space group only five prominent peaks are observed. The peak at low frequency, i.e., 211 cm^{-1} represents in-phase rotation of A_g mode and peak at 490 cm^{-1} is attributed to out-of-phase bending of $A_g(3)$ mode. The peak at ~ 601 cm^{-1} corresponds to Jahn-Teller stretching mode and it is reported to be related to CO phase [223]. The peak at 620 cm^{-1} corresponds to $B_{2g}(1)$ mode that occurs due to the interaction of oxygen and Mn ion in the octahedral site. The broad peak observed at 680 cm^{-1} can be attributed oxygen off-stoichiometry and its intensity is found to increase with increase in film thickness [224]. The peak at 211 cm^{-1} is found to shift towards lower frequency with increase in film thickness and this trend is consistent with decrease in out-of-plane lattice constant and hence possible increase in-plane lattice constant.

Table 4.1: Lattice parameter, strain (ε), ferromagnetic transition temperature (T_C), Curie temperature (θ_C),saturation magnetization (M_s) and activation energy (E_h) for 30, 40, 50, 75 and 100 nm thin films.

Thickness (nm)	c_f (Å)	Strain (ε%)	T_C (K)	θ_C (K)	M_s (μ_B/f.u)	E_h (meV)
30	3.862	0.59	-	-	-	61
40	3.859	0.55	-	-	-	57
50	3.858	0.52	82	87	2.47	53
75	3.855	0.44	72	81	2.41	71
100	3.853	0.39	71	77	2.24	47

4.3.3 Morphology of NNMO Thin Films

Fig. 4.6 shows the topographical images of NNMO films in a span of 2x2 $(\mu m)^2$ area. The root mean square (RMS) roughness values of the films are found to be around 1.4, 0.55, 0.53 and 0.45 nm, respectively for 30, 50, 75 and 100 nm films. The average particle size is found to be 55 nm, 70 nm, 38 nm and 50 nm for 30, 50, 75 and 100 nm thick films respectively. The 75 nm film is found show smaller particle size. The energy

TH-1726_11612111

dispersive spectrum was recorded by using EDS attached to Zeiss made (model: sigma) Field emission scanning electron microscope (FESEM). Here, the energy dispersive spectrum (EDS) is shown in Fig.4.7 for 30 nm film, and the estimated composition is $Nd_{0.66}Na_{0.19}MnO_x$ and is comparable to the starting composition.

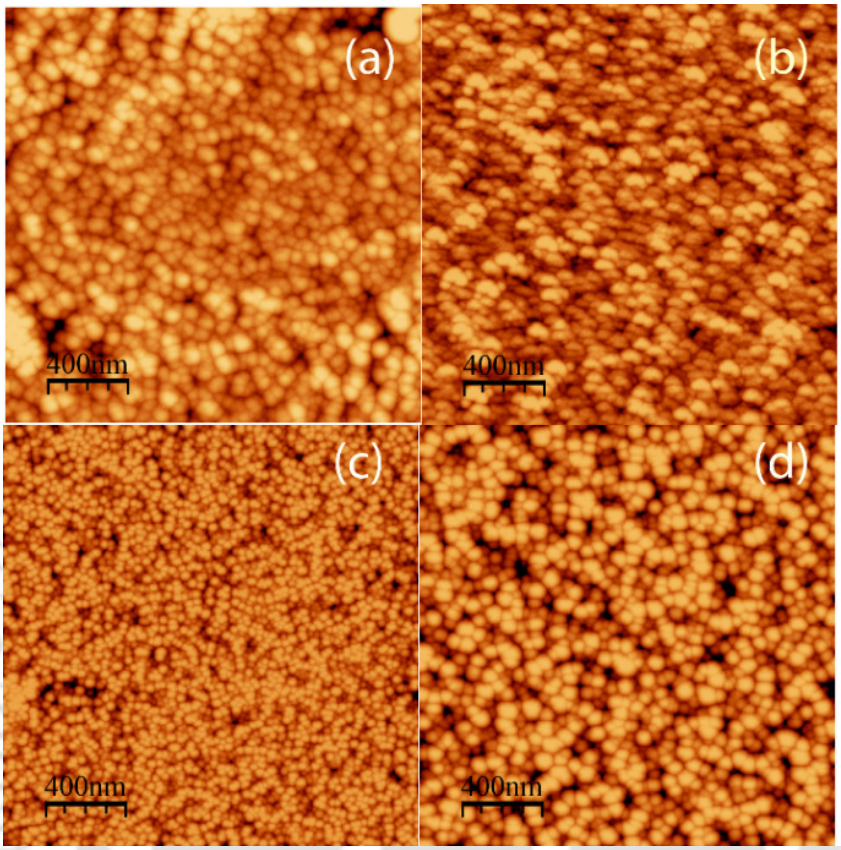

Figure 4.6: The topographical images of the films recorded using atomic force microscope for (a) 30 nm, (b) 50 nm, (c) 75 nm and (d) 100 nm films of NNMO

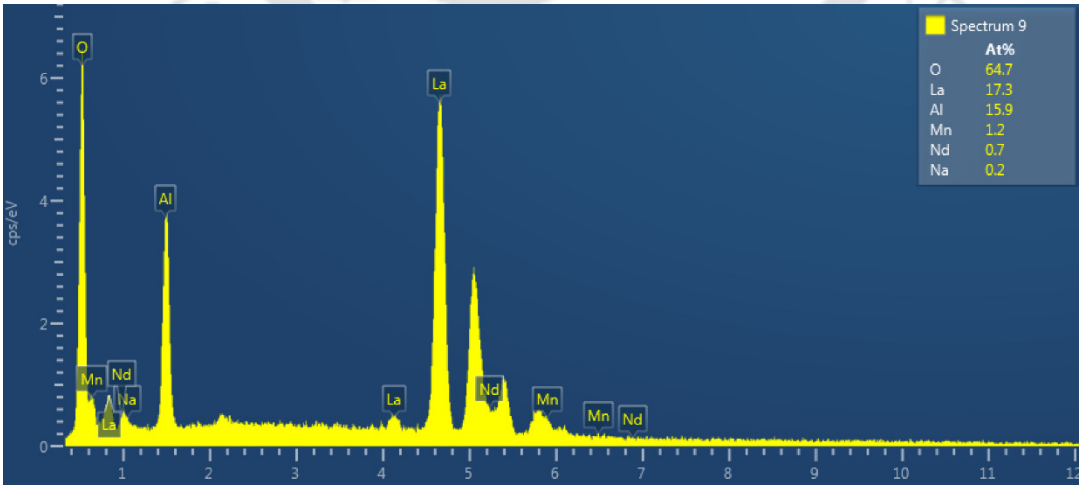

Figure 4.7: The EDS spectrum of 30 nm thick film.

TH-1726_11612111

4.3.4 Magnetic Properties

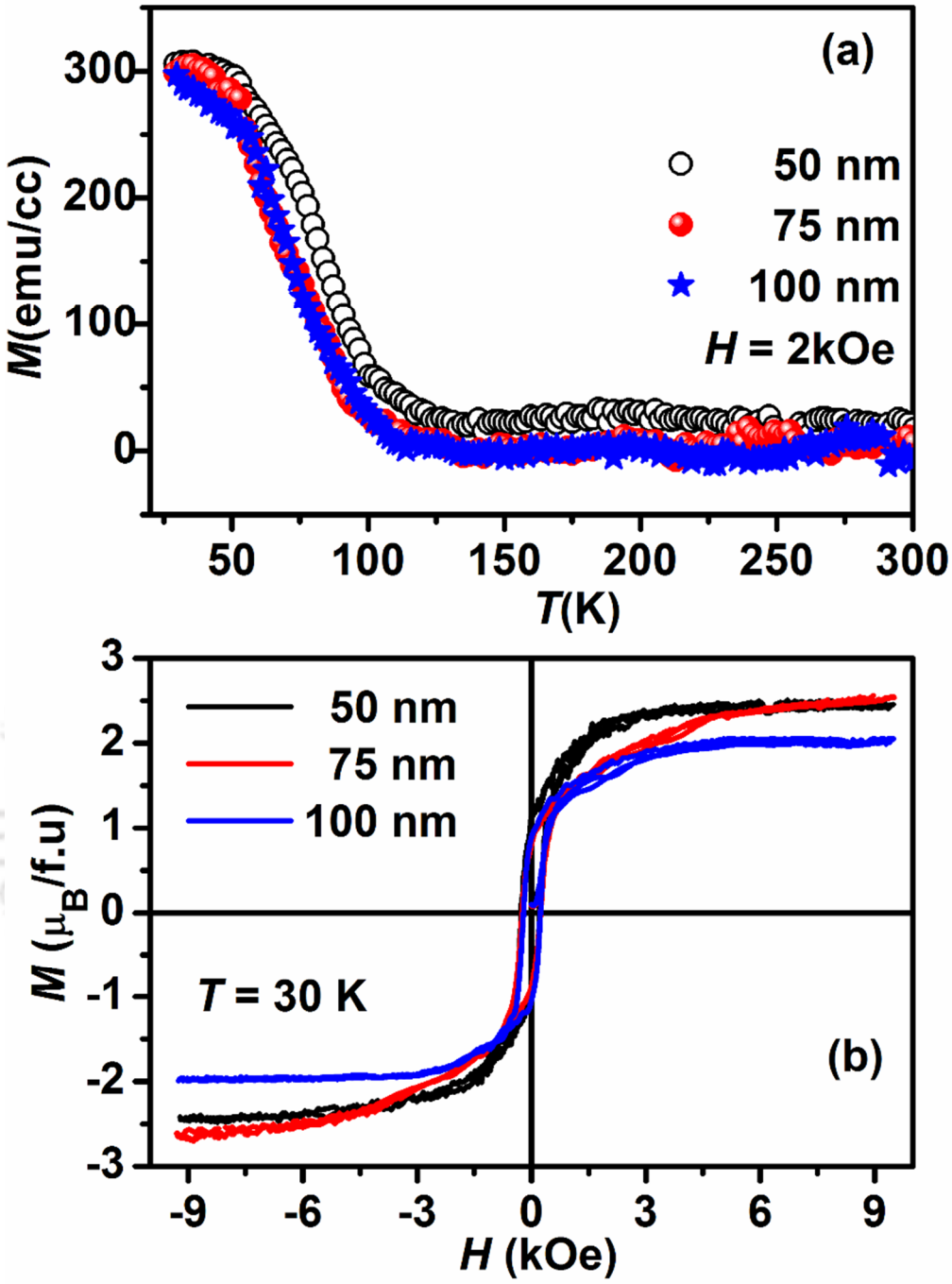

Figure 4.8: (a) Temperature variation of magnetization for an applied field of 2 kOe along the plane of 50, 75 and 100 nm films. (b) *MH*-loops recorded at 30 K for 50 nm, 75 nm and 100 nm films.

The plots of temperature variation of magnetization measured at H = 2 kOe for 50 nm, 75 nm and 100 nm films are shown in Fig.4.8(a). They all exhibit a board hump with small magnitude around 190 K and is comparable to that observed in bulk sample and as reported in ref [223]. This is attributed to CO transition. However as the temperature is

TH-1726_11612111

lowered below 100 K, the magnetization rises to a large value of the order of 300 emu/cc and it highlights the presence of ferromagnetic like behaviour. Such a low temperature ferromagnetic behaviour is reported in nano-crystalline powders of $Nd_{0.8}Na_{0.2}MnO_3$ especially when the average particle size is below 100 nm [194]. The average particle size in the present set of films fall in the above category as per atomic force microscope results. The ferromagnetic transition temperature (T_C) determined from the peak position of dM/dT versus temperature plot is tabulated in table-4.1. The T_C value is found to decrease with increase in film thickness. Thus in addition to particle size, the lattice strain plays a major role in quenching the CO at low temperature and strengthening the ferromagnetic interaction. We have not observed any meaningful magnetic moment in 30 nm and 40 nm films due to their thickness within the magnetic dead layer or due to the lack of sensitivity of VSM system for such a small thickness of CO phases.

The susceptibility in the paramagnetic region was analysed based on modified Curie-Weiss law,

$$\chi = \chi_0 + \frac{C}{(T-\theta_C)} \tag{4.2}$$

Here χ_0, C and θ_C are temperature independent susceptibility, Curie constant and Curie temperature, respectively. The estimated Curie temperature values are given in the table-4.1 and they follow the same trend as that of T_C.

In order to further understand the magnetic properties, we have recorded M-H loops at 30 K and they are shown in Fig.4.8(b). All films show ferromagnetic like behaviour with a maximum saturation magnetization value of the order of 2.47 μ_B/f.u. The saturation magnetization (M_S) value is estimated by fitting the initial magnetization curves to the law of approach to saturation magnetization [185], i.e.,

$$M = M_S\left[1 - \frac{a}{H^{1/2}} - \frac{b}{H^2}\right] \tag{4.3}$$

Here Ms is saturation magnetization, H represents the applied magnetic field, a and b are constants. It may be noted that 100 nm film shows smaller M_s value compared to that of other films. This is consistent with M-T measurement and is attributed to smaller lattice strain, where the CO-AFM contribution is expected to be considerable. The M-H loop of 75 nm film shows a distinct behaviour of two-step process, where larger field is required

TH-1726_11612111

for achieving the saturation. This can be explained by considering the large surface to volume ratio in this film and the corresponding contribution from uncompensated surface spins. This result is consistent with surface morphology image of 75 nm film. Similar trend is reported in nano-crystalline samples of $Nd_{0.8}Na_{0.2}MnO_3$ with comparable M_s values [194].

4.3.5 Electrical Resistivity

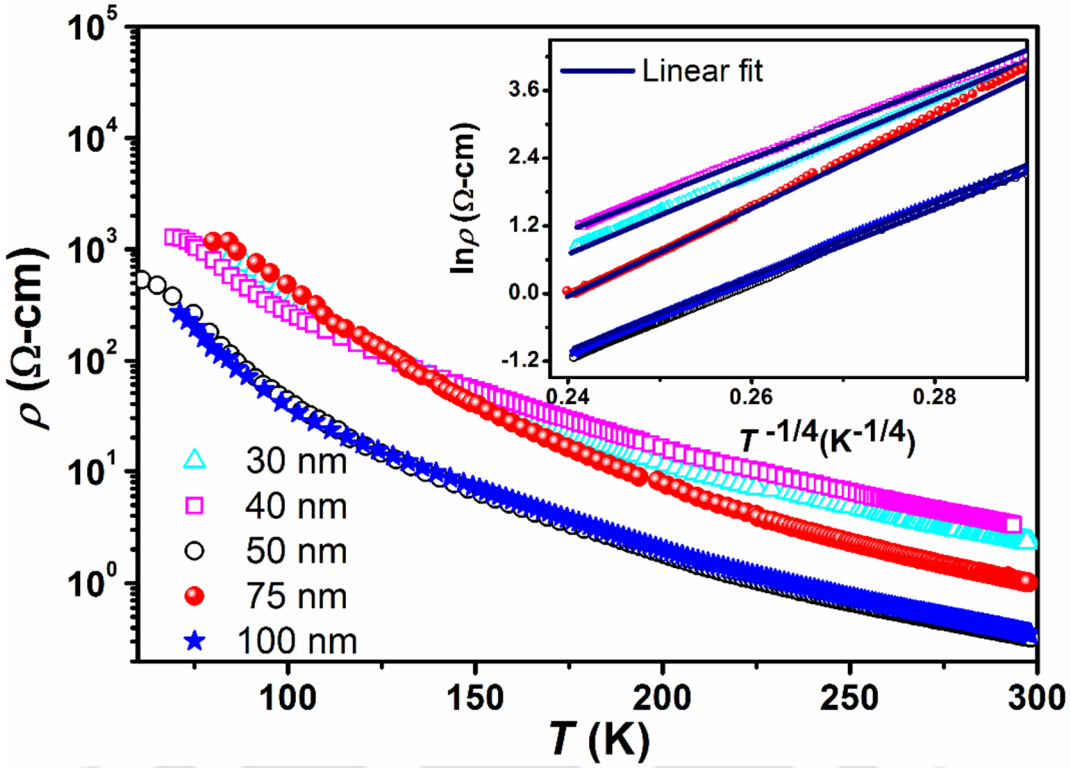

Figure 4.9: Plots of temperature variation of electrical resistivity for different films and the inset shows the lnρ vs $T^{-1/4}$ plots along with the fit to VRH model.

Temperature variation of electrical resistivity in semi-logarithmic scale is shown in Fig. 4.9 for different films. They all follow semiconductor like behaviour. The electrical resistivity at a given temperature is found to decrease with increase in film thickness barring an anomaly for 75 nm film. The relatively large resistivity observed in 75 nm film can be attributed to smaller grain size and associated electron scattering across grain boundaries. Plots of lnρ versus $T^{-1/4}$ are shown in the inset of Fig.4.9 and they all exhibit linear behaviour in consistent variable range hopping (VRH) [182] model,

$$\boldsymbol{\rho} = \boldsymbol{\rho_0}\exp(T_{0M}/T)^{1/4} \qquad (4.4)$$

The fitted data are shown as solid line. The result is comparable to that of $Nd_{1-x}Na_xMnO_3$ for $x \geq 0.15$ reported by Lakshmi *et al*. [225]. The density of states of electrons ($N(E_F)$) in

TH-1726_11612111

the vicinity of Fermi level was estimated from the fitted parameter T_{0M} and using the relation,

$$k_B T_{0M} = \frac{18}{[L^3 N(E_F)]} \quad (4.5)$$

as per ref [182]. Here L represents the localisation length and k_B is the Boltzmann constant. The ($N(E_F)$) values are found to be in the order of 10^{26} $m^{-3}eV^{-1}$, however for 75 nm film it is found to be 9.0×10^{25} $m^{-3}eV^{-1}$. In the above calculation L is taken as 3.8 Å i.e. the approximate lattice constant of the films. Moreover from the fitted parameter $T_{0M,}$ the activation energy at 100 K was determined using the relation

$$E_h = \frac{1}{4} k_B T_{0M}^{1/4} T^{3/4} \quad (4.6)$$

and they are given in table-4.1. The E_h value is found to decrease with increase in film thickness barring an anomaly for 75 nm film.

4.3.6 Conclusions

We have studied the effect of film thickness on electrical and magnetic properties of $Nd_{0.8}Na_{0.2}MnO_3$ thin films deposited by RF-magnetron sputtering on 001-$LaAlO_3$ substrate. The XRD patterns show the c-axis oriented growth of films. The out-of-plane lattice constant systematically decreases with increase in film thickness due to the reduction in out-of-plane tensile strain as the film thickness is increased. The Raman spectra of the films show the signature of charge ordering related bands at 601 and 620 cm^{-1}. Magnetization measurements show that in addition to the signature of weak charge ordering around 190 K a low temperature (< 100 K) ferromagnetic transition is observed. The saturation magnetization is found to decrease with increase in film thickness due to the strengthening of charge ordering as the lattice strain is decreased. The electrical resistivity data follow semiconducting behaviour and they were analysed in terms of Mott-VRH model.

TH-1726_11612111

4.4 Study of $Nd_{0.7}Sr_{0.3}MnO_3$/ $Nd_{0.8}Na_{0.2}MnO_3$ Bilayer Films

4.4.1 Deposition of NSMO/NNMO Bilayer

NSMO/NNMO bilayer thin films were deposited on (001)-oriented LAO substrate by using a RF-magnetron sputtering system. The bilayer deposition was carried out in-situ by maintaining the substrate temperature at 650°C and the Ar and O_2 gaseous mixture in 3:1 ratio. The working chamber pressure was 2.5×10^{-2} mbar and 4.3×10^{-2} mbar for the deposition of NNMO and NSMO films, respectively. NSMO films of different thicknesses i.e. 12 nm, 30 nm, 60 nm, 80 nm and 100 nm on NNMO film of 120 nm thickness were grown on LAO substrate. They are named as BL-12, BL-30, BL-60, BL-80 and BL-100 respectively. Further, the deposited films were post-annealed at 700°C for an hour in oxygen environment at 1 atm pressure. We have also grown single layer films of NNMO with 120 nm thickness (NNMO(120)) and NSMO film of thickness 80 nm (NSMO(80)) on 001- LAO substrate for a comparison.

4.4.2 Structural Properties

XRD patterns of the bilayer as well as single layer thin films in logarithmic intensity scale are shown in Fig.4.10. XRD patterns of hetero-structure bilayer films (NSMO/NNMO) and single layer NSMO and NNMO films show only peaks corresponding to (00*l*) reflections including that of LAO substrate. This highlights the bilayer films are grown along the orientation of c-axis, which lies perpendicular to the plane of the film. The well resolved (002) peaks corresponding to NSMO (solid diamond) and NNMO (open diamond) are seen and the peak position is found to shift towards higher 2θ angle with increase in film thickness. Fig. 4.11 depicts the enlarged view of the (002) peaks of bilayer films of different thicknesses. The out-of-plane lattice constant (c) values of the NSMO layer are found to 3.890 Å, 3.880 Å, 3.878 Å and 3.876 Å for BL-30, BL-60, BL-80 and BL-100, respectively and the lattice constant of NNMO film is around 3.863 Å. The lattice strain was calculated using the eq.4.1 where c_f and c′ correspond the lattice constant of NSMO film along c-direction and the pseudo cubic lattice constant of bulk NSMO. These values decrease from 1.1 % for BL-30 to 0.73 % for BL-100. Thus the NSMO layer exhibits tensile strain along the *c* - direction i.e. perpendicular to the plane of the film and its value decreases with increase in film thickness. The pseudo-cubic lattice constant values for bulk NSMO, NNMO, and LAO are 3.848 Å, 3.838 Å, and 3.788 Å, respectively. Lattice mismatch between NSMO and LAO results in an in-plane compressive strain and that leads to out-of-plane tensile strain.

TH-1726_11612111

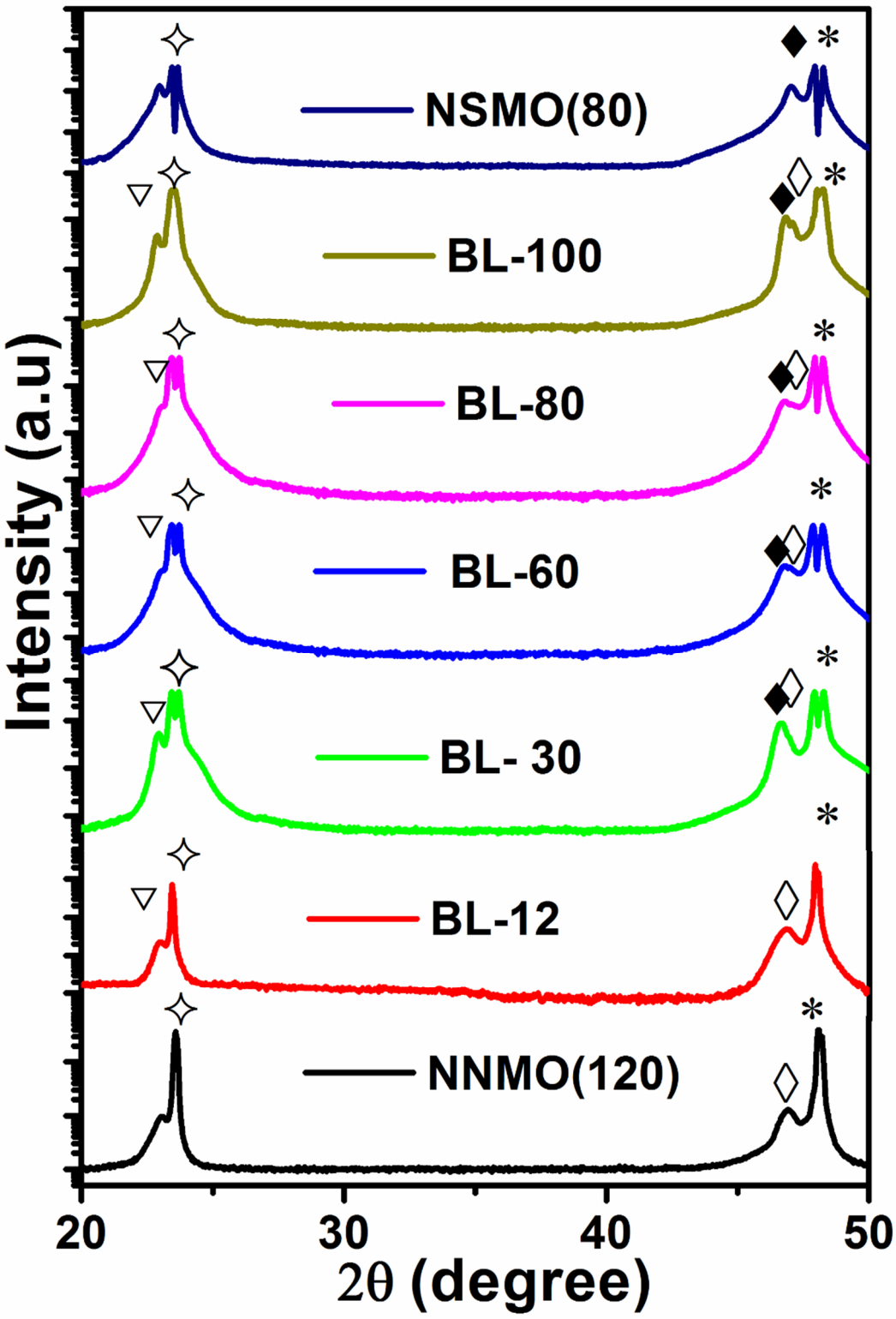

Figure 4.10: XRD patterns of NSMO/NNMO bilayer on 001-LAO substrate. Here, the intensity is shown in logarithmic scale to clearly display the peaks due to the film. The (002) peaks corresponding to the substrate, NNMO and NSMO are marked as stars, open diamond and solid diamond respectively. The (00l) peak of substrate and the bilayer films are marked as ✧ and ▽ respectively.

TH-1726_11612111

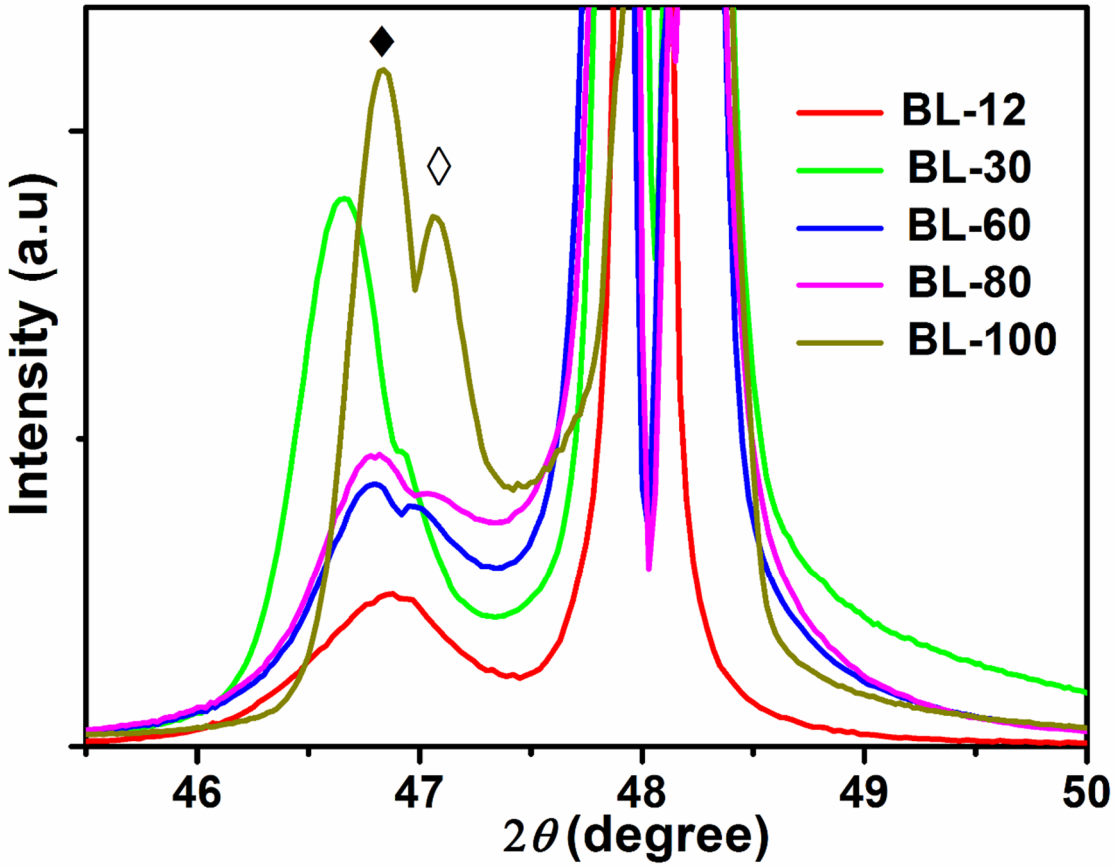

Figure 4.11: The enlarged view of (002) peak for bilayer films along with the substrate peak.

4.4.3 Magnetic Properties

Fig.4.12 illustrates temperature variation of magnetization under zero field cooled condition of bilayer films for a magnetic field of $H_{\|}$ = 500 Oe (along in-plane of the films). For a comparison, we have also included the *M-T* plots corresponding to single layer NNMO and NSMO films. They all undergo ferromagnetic transition with transition temperature (T_C) in the range of 62 K for BL-12 to 107 K for BL-100. On the other hand, T_C values are found to be 75 K and 180 K for NNMO and NSMO single layer films on bare substrate. The magnetization at a given temperature for $T < T_C$ is found to increase systematically with increase in film thickness. Thus the increase in T_C and magnetization with increase in film thickness suggests the strengthening of ferromagnetic interaction. The observed magnetization and ferromagnetic T_C for single layered NSMO film is found to be even larger than that of highest thickness (100 nm) of bilayered films. Single layer NNMO film shows ferromagnetic like transition at 75 K instead of antiferromagnetic behaviour. This can be attributed to the oxygen off-stoichiometry and the strong compressive strain induced distortion of MnO_6 octahedra. The smaller T_C observed in bilayer films can be

TH-1726_11612111

attributed to interface interaction and the associated lattice strain. The susceptibility in the paramagnetic region was analysed based on the modified Curie-Weiss law as given in eq.4.2. The θ_C is found to increase from 91 K for BL-12 film to 151 K for BL-100 film.

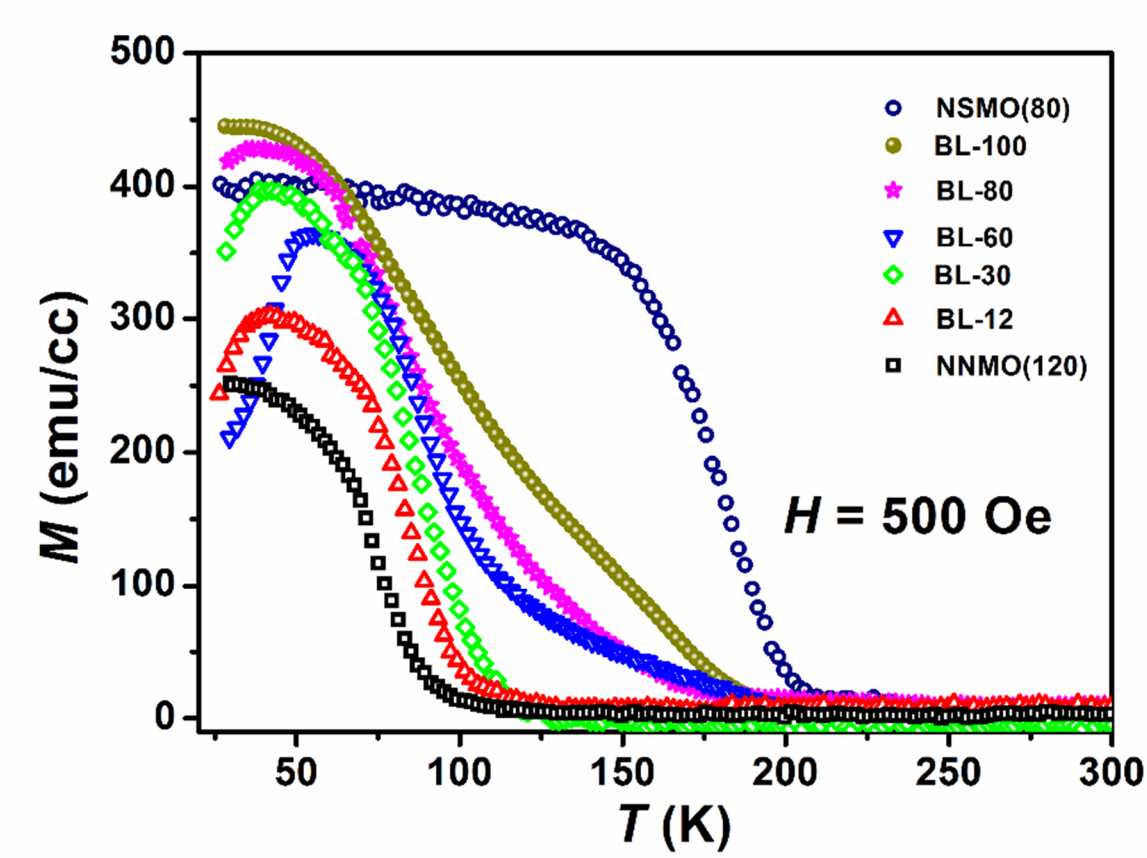

Figure 4.12: Temperature variation of magnetization for an applied field 500 Oe along in-plane of films for BL-12, BL-30, BL-60, BL-80 and BL-100 films along with single layer NNMO and NSMO films

In order to further understand the magnetic properties, *M-H* loops were recorded at 50 K and they are shown in Fig 4.13. All bilayered films show typical soft ferromagnetic behaviour, however the saturation magnetization is found to increase with film thickness. Moreover, the coercive field, H_c is found to be 180, 155, 280, 156 and 190 Oe, respectively for BL-12, BL-30, BL60, BL-80 and BL100 films. The saturation magnetization values of the films were determined with the help of law of approach to saturation magnetization [185] as given in eq.4.3. The determined M_s values are found to be 368, 436, 497, 544 and 560 emu/cc for BL-12, BL-30, BL-60, BL-80 and BL-100, respectively. The above variation of M_s can be understood in terms of reduction in lattice strain with increase in film thickness.

TH-1726_11612111

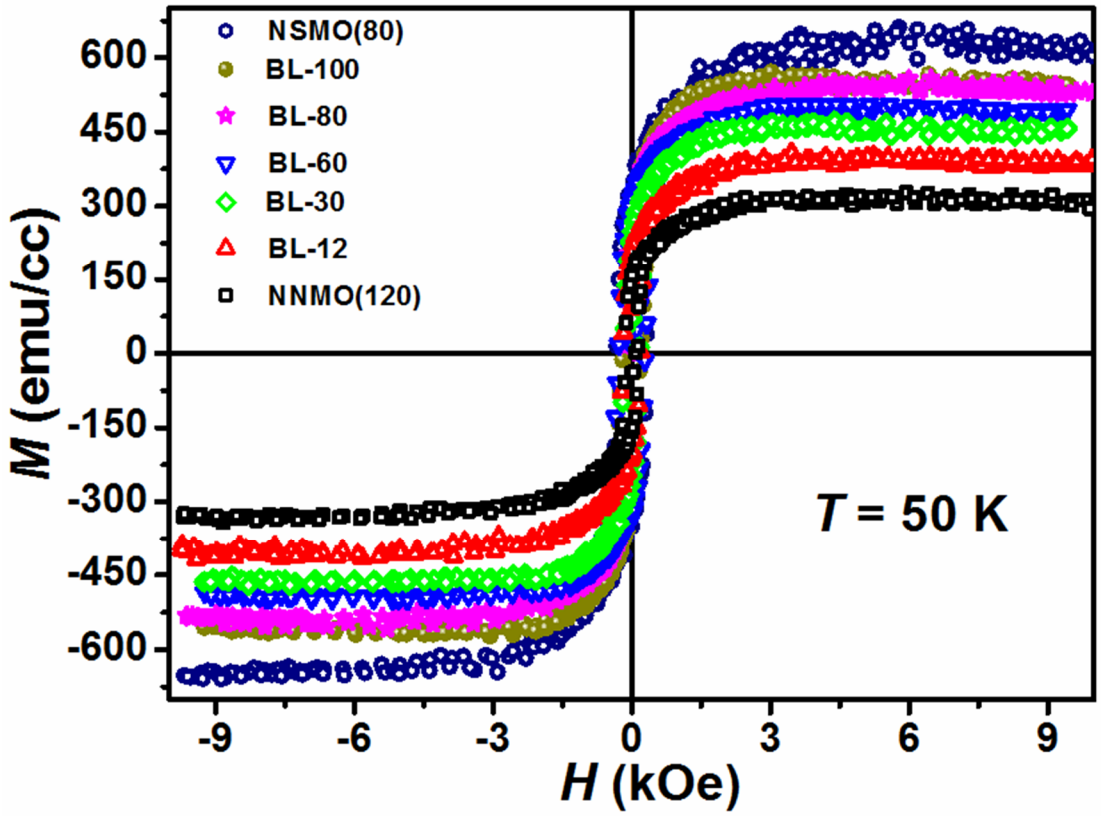

Figure 4.13: *MH*-loops of different bilayer films recorded at 50 K.

4.4.4 Electrical Resistivity

In order to understand the electrical transport of the hetero-structure bilayer films, we have measured the electrical resistivity as a function of temperature in the temperature range of 30 - 300 K and they are shown in Fig.4.14(a). Barring BL-12 and single layer NNMO, all other films show metal-insulator transition and the transition temperature (T_{MI}) value increases systematically with increase in NSMO thickness. The T_{MI} value is found to vary from 53 K for BL-30 to 176 K for BL-100. The T_{MI} value of BL-100 is found to be smaller than that of single layer NSMO film (202 K) and this can be attributed to interface interaction and lattice distortion in bilayer films. The improvement observed in the T_{MI} value of higher thickness films can be attributed to the strain relaxation of thicker films compared to those of thinner films. The variation of T_{MI} with film thickness (t) is analysed in terms of scaling theory,

$$\left[\frac{[T_{MI}\ (B) - T_{MI}\ (t)]}{T_{MI}\ (B)}\right] = \left[\frac{k}{t}\right]^{\lambda} \tag{4.7}$$

TH-1726_11612111

where, k and λ are constants [204]. The fitted data by taking k and λ as free parameters of the fit and by taking T_{MI} (B) = 185 K are shown as solid line in Fig.4.14(b). The estimated values of k and λ are found to be 22.6 nm and 1.13 respectively.

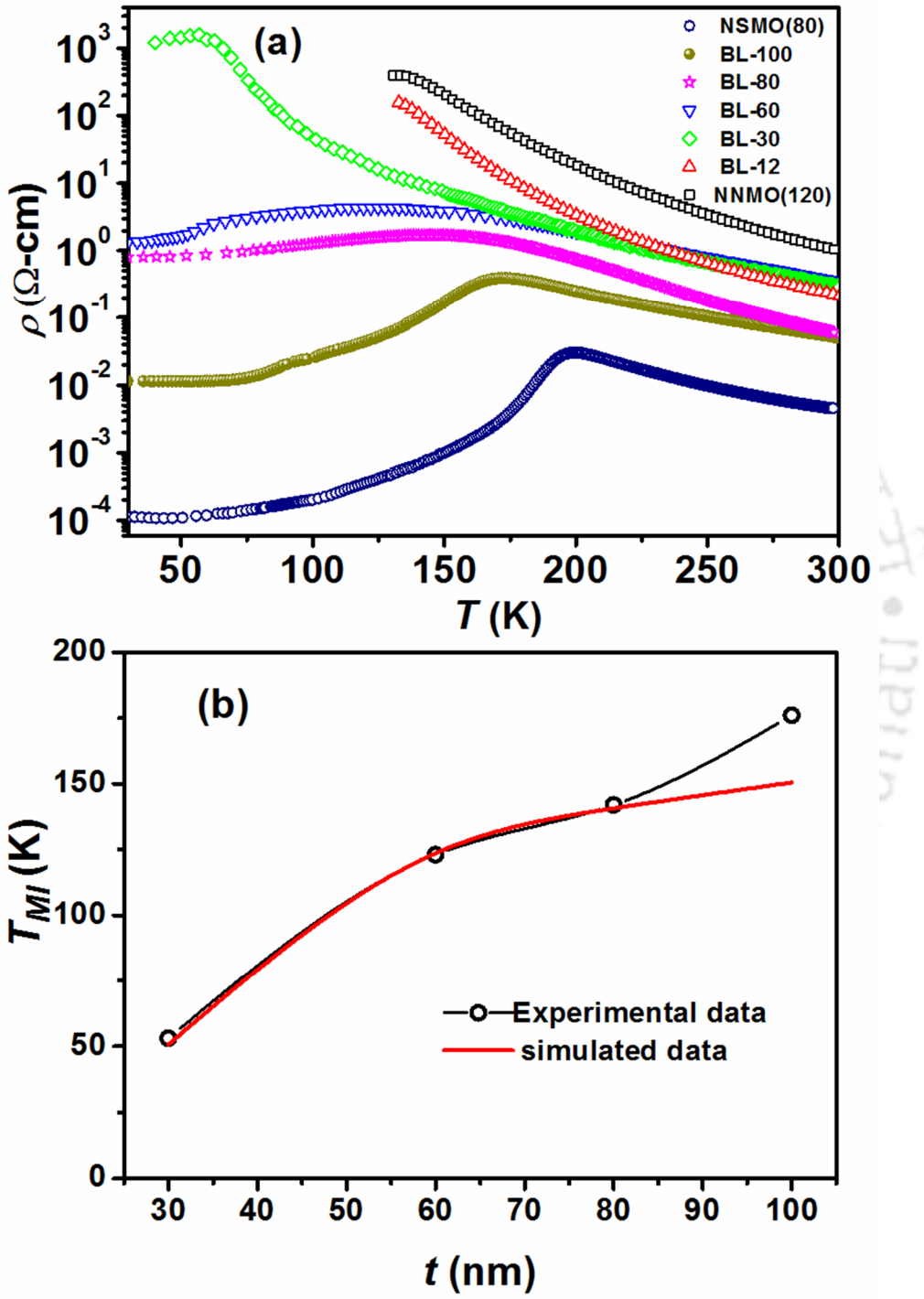

Figure 4.14: Temperature variation of electrical resistivity of bilayer films for NSMO thickness of 12, 30, 60, 80 and 100 nm, respectively along with single layer NSMO and NNMO films. (b) T_{MI} as a function of thickness (t) of NSMO layer along with fitted data.

TH-1726_11612111

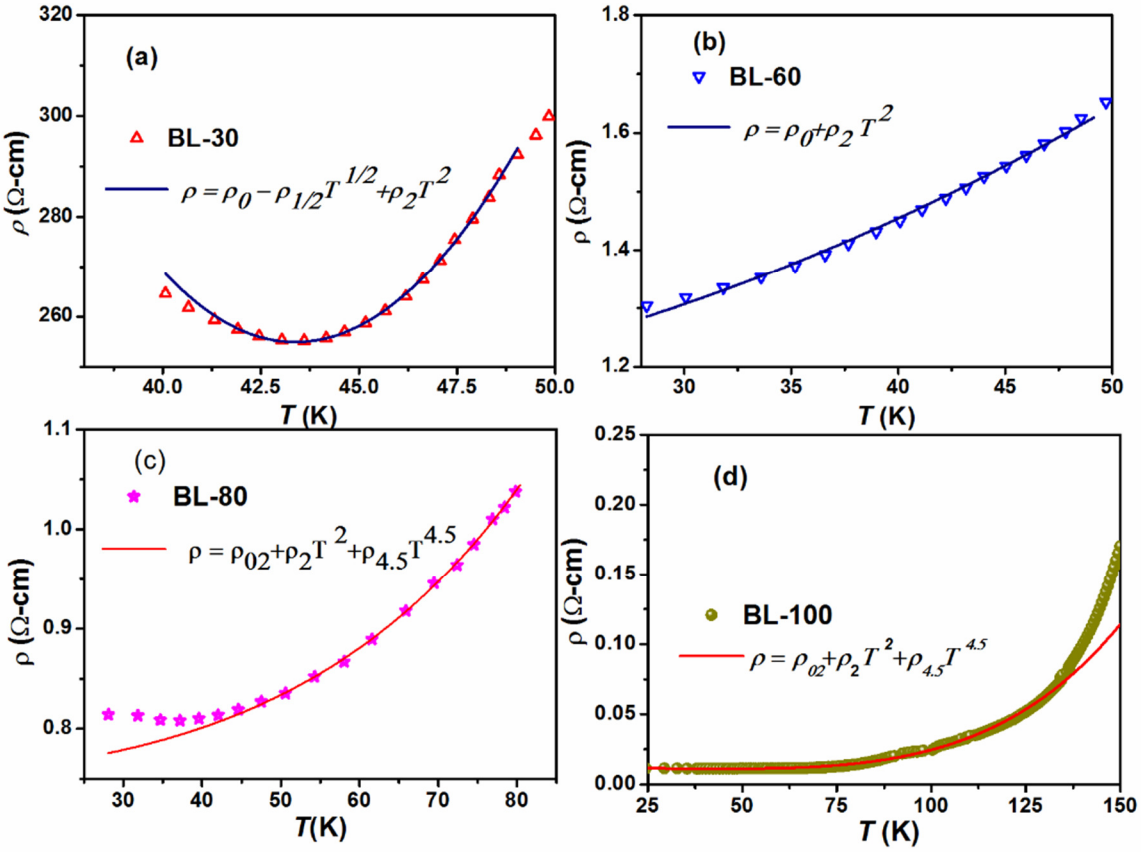

Figure 4.15: Electrical resistivity data along with their respective theoretical fit for bilayer films.

The resistivity plot of BL-30 exhibits an upturn in the low temperature region and it is analysed by considering the relation

$$\rho = \rho_{01} - \rho_{1/2}T^{1/2} + \rho_2 T^2 \qquad (4.8)$$

where ρ_{01} represents residual resistivity, T^2 – term refers to the electron – electron scattering [226] and the $T^{1/2}$ term corresponds to the weak localization effect [203]. The fitted values of ρ_{01}, $\rho_{1/2}$ and ρ_2 are found to be 4899 Ω-cm, 94 Ω-cm.K$^{-1/2}$ and 0.84 Ω-cm.K^{-2} respectively. However, for BL-60 sample, we have not observed such upturn and the resistivity data were analysed by just considering the electron-electron scattering (T^2) term as shown in Fig. 4.15 (b). The fitted values are found to be $\rho_0 = 1.12$ Ω-cm and $\rho_2 = 2.1\times 10^{-4}$ Ω-cm.K^{-2}. Fig. 4.15 (c) and (d) depict resistivity data of BL-80 and BL-100 film along with fitted data using the relation

$$\rho = \rho_{02} + \rho_2 T^2 + \rho_{4.5} T^{4.5} \qquad (4.9)$$

where an additional term due to electron – magnon ($T^{4.5}$- term) scattering is included [50, 201].The fitted values of ρ_{02}, ρ_2 and $\rho_{4.5}$ are found to be 0.75 Ω-cm, 2.6×10^{-5} Ω-cm.K^{-2} and

TH-1726_11612111

3.24×10^{-10} Ω-cm.$K^{-4.5}$ respectively for BL-80 film. These parameters for BL-100 are found to be 0.01 Ω-cm, 5.69×10^{-7} Ω-cm.K^{-2} and 1.85×10^{-11} Ω-cm.$K^{-4.5}$ for BL-100, respectively.

The electrical resistivity data in the paramagnetic insulating region were analysed by considering various models such as small polar hopping model with general relation

$$\rho = \rho_{sp} T^{n} \exp(-E_{SP}/k_B T) \qquad (4.10)$$

here E_{sp} is the activation energy of small polaron and n represents exponential term; here depending on the n value the scattering mechanism is called either adiabatic (n = 1) or (n = 3/2) non-adiabatic small polaron hopping model [227]. The resistivity data can also be analysed based on variable range hopping model, i.e. eq.4.4 [182]. We have analysed the resistivity data in the light of above two general relations and the data are found to be well fitted to Mott-VRH model as shown in Fig. 4.16. From the fitted T_{0M}, the activation energy values of the films were determined at T = 300 K using the relation given in eq.4.6 and they are found to decrease from 157 meV for BL-12 to 94 meV for BL-100.

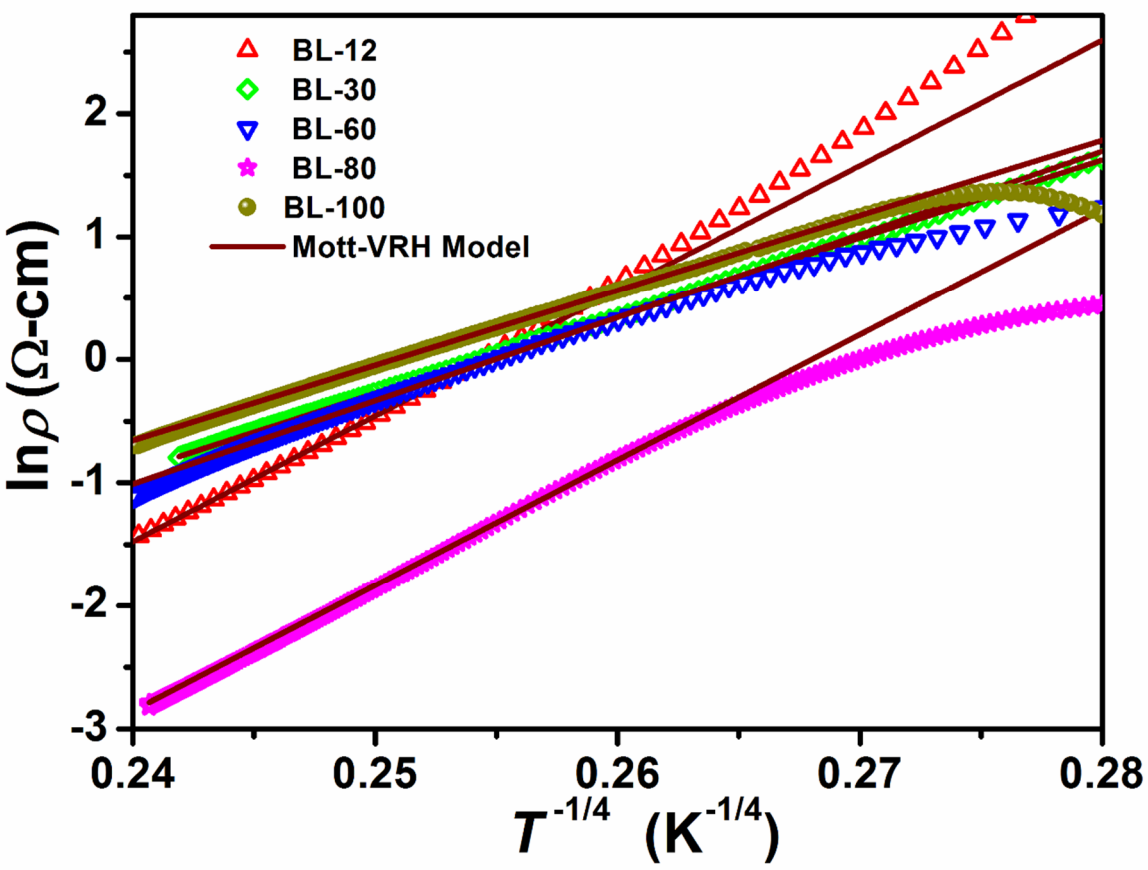

Figure 4.16: lnρ vs $T^{-1/4}$ curves along with the fit to the VRH model.

TH-1726_11612111

4.4.5 Conclusions

We have successfully fabricated c-axis oriented NSMO/NNMO films on (001)-LAO substrate for different thicknesses of NSMO layer in the range of 12 nm to 100 nm. The out-of-plane lattice constant of NSMO layer is found to vary from 3.890 Å for t = 30 nm to 3.876 Å for t = 100 nm and it depicts the presence of out-of-plane tensile strain whose value decreases with increase in film thickness. All bilayer films show ferromagnetic transition and whose transition temperature increases with increase in film thickness. They are explained in terms of lattice strain and the interface coupling at NSMO/NNMO surfaces. Electrical resistivity data show the metal-insulator transition with its transition temperature T_{MI} increasing with increase in film thickness. The resistivity data in the metallic region are explained in terms of combination of electron – electron and electron – magnon scattering. However for thinner film BL-30, a low temperature upturn in resistivity is seen and is explained by considering the weak localisation effect. The electrical resistivity data in the insulating region follow the Mott-VRH model.

TH-1726_11612111

Chapter 4

TH-1726_11612111

Chapter 5

Electrical Resistivity and Magnetic Properties of $La_{0.7}Sr_{0.3}MnO_3/LaFeO_3$ Bilayer Films

TH-1726_11612111

TH-1726_11612111

Chapter 5

5.1 Introduction

The deposition of bilayer and multilayer of ferromagnetic (FM) and anti-ferromagnetic (AFM) films and study of their electrical transport and magnetic properties are the subject of interest due to their potential applications in various spintronic and memory devices [228]. Moreover they are being studied to understand the coupling between the charges, spin and lattice degrees of freedom [151, 229]. The magnetic properties of $La_{0.7}Sr_{0.3}MnO_3$ (LSMO) and $La_{0.7}Ca_{0.3}MnO_3$ (LCMO) films grown with different capping layers have shown ferromagnetic transition and saturation magnetization similar to those of their respective bulk samples irrespective of nature of capping layers [146]. The controlled growth of LSMO films with a few nano-meter thickness on $BiFeO_3$ dielectric layer gives rise to multi-ferroic behaviour and they also exhibit magnetic as well as electrical exchange-bias behaviour [230]. Schumacher *et al.* [228] have reported that bilayer films of $La_{0.67}Sr_{0.33}MnO_3/SrTiO_3$ grown under low oxygen partial pressure (60 Pa to 200 Pa) exhibit the exchange bias behaviour. The hetero-structure configuration of an anti-ferromagnetic layer sandwiched between two ferromagnetic metallic layers efficiently serves as a spin valve device [231].

The magneto-resistance of tri-layered $LaFeO_3/La_{0.8}Ba_{0.2}MnO_3$ (LBMO)/$LaFeO_3$ film is found to be around 74 % larger than that of single layer LBMO film [59]. $LaFeO_3$ is one of the versatile anti-ferromagnetic insulators at room temperature with orthorhombic structure similar to that of ferromagnetic (La, Sr)MnO_3 compound [232]. Therefore the bilayer combination of LSMO and LFO is expected to show interesting electrical, magnetic and magneto-electrical properties. In this chapter, we have fabricated bilayer films of LSMO/LFO on (001) oriented $LaAlO_3$ substrate by using the RF-magnetron sputtering technique. The structural, electrical and magnetic properties of these films have been studied for different thicknesses of LSMO films on 120 nm thick LFO film.

5.2 Preparation and Characterisation of $La_{0.7}Sr_{0.3}MnO_3$ and $LaFeO_3$ Targets

5.2.1 Preparation and Characterisation of $LaFeO_3$ Target

The bulk $LaFeO_3$ was prepared by sol-gel technique. The stoichiometric amounts of La_2O_3 and Fe_2O_3 compounds of purity better than 99% were taken as starting compounds and they were converted into nitrates by adding nitric acid. These individual solutions were

TH-1726_11612111

mixed and converted into citrates by adding excess amount of citric acid followed by heating at a moderate temperature of 70°C until the precursor is formed. This mixture was pre-sintered at 600°C followed by final sintering at 1000°C in pellet form for 12h in air.

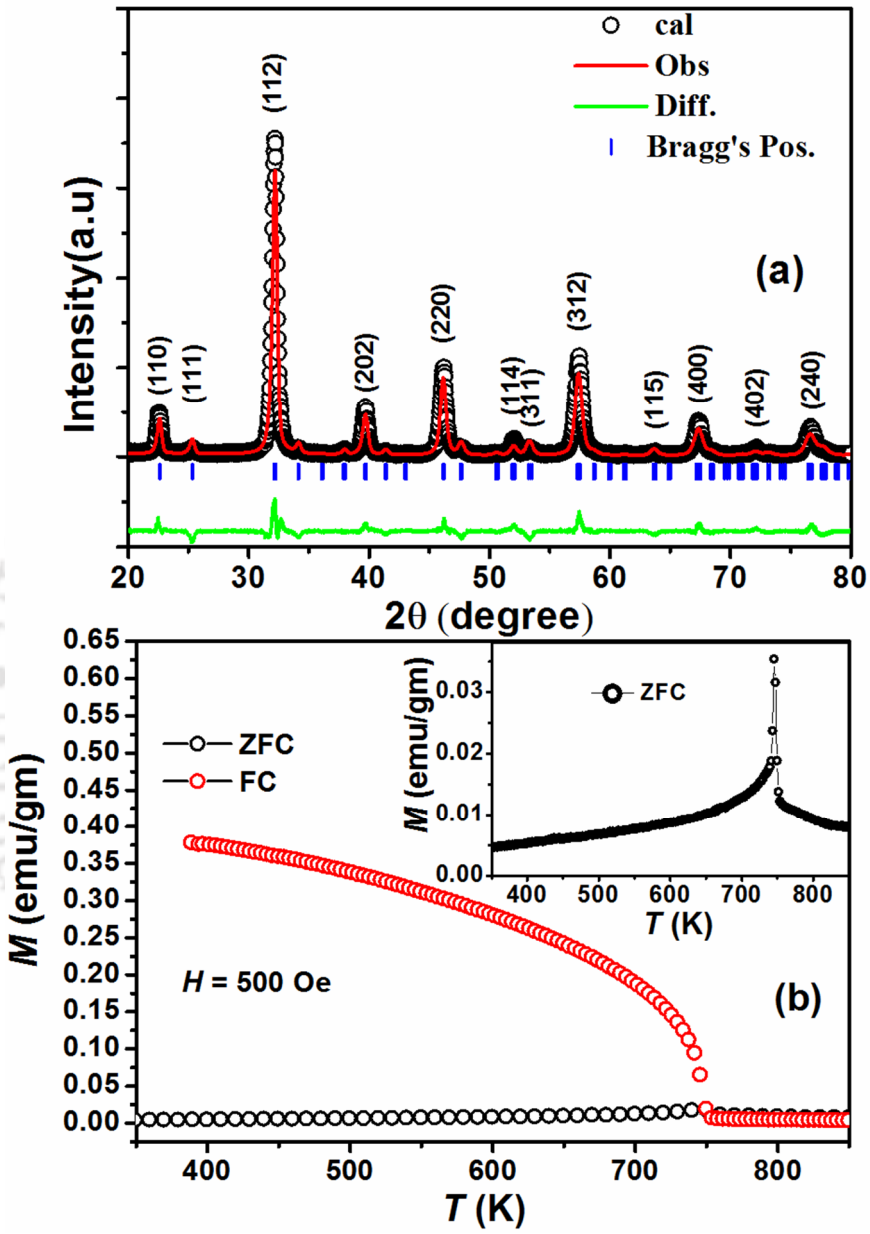

Figure 5.1**:** (a) XRD patterns of the LFO target along with the Rietveld refinement and (b) the temperature variation of magnetization under zero field and field cooled modes for an applied a field of 500 Oe. Inset of (b) represents the ZFC curve of LFO target.

XRD pattern of LFO target is shown in Fig.5.1(a). It is successfully refined by choosing Pbnm space group, i.e. with orthorhombic crystal structure. The refined data are shown as solid line in Fig.5.1(a). The lattice parameters for the LFO target are found to be a_1 = 5.555 Å, b_1 = 5.573 Å and c_1 = 7.868 Å. The pseudo cubic lattice constants of the LFO

TH-1726_11612111

are estimated as $a'_1 (= a_1/\sqrt{2}) = 3.928$ Å, $b'_1 (= b_1/\sqrt{2}) = 3.941$ Å and $c'_1 (= c_1/2) = 3.934$ Å. The above structural analysis shows that the LFO target material is prepared in single phase form.

Fig.5.1(b) illustrates the temperature variation of magnetization curves under zero field and field cooled conditions for the applied magnetic field of 500 Oe. The antiferromagnetic Neel temperature is found to be 745 K. It is comparable to the literature on $LaFeO_3$ [233].

5.2.2 Preparation and Characterisation of $La_{0.7}Sr_{0.3}MnO_3$ Target

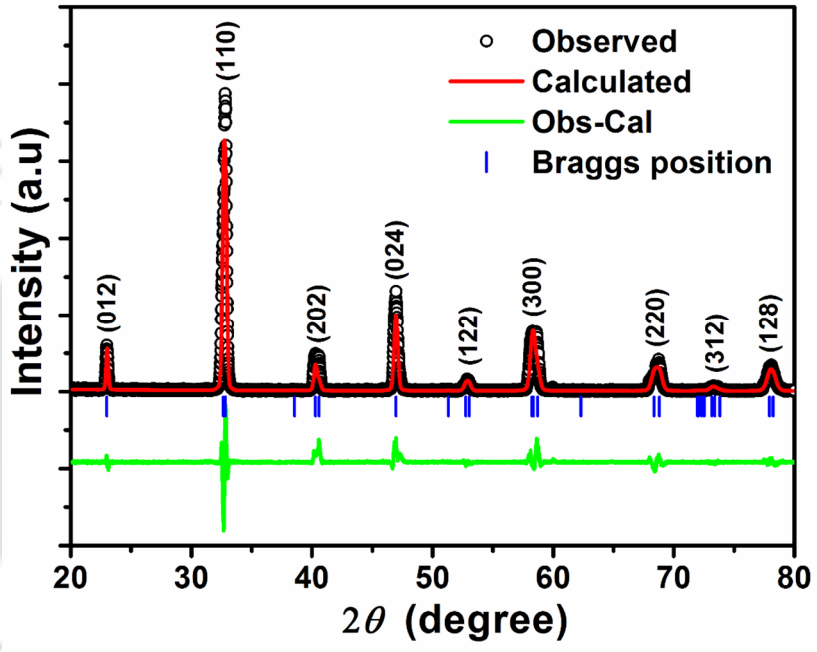

Figure 5. 2**:** XRD pattern of the LSMO target along with Rietveld Refinement

The bulk $La_{0.7}Sr_{0.3}MnO_3$ target was also prepared by using the sol-gel method. For this, the starting compounds were taken as La_2O_3, $SrCO_3$ and manganese acetate of purity better than 99%. The oxides were converted into nitrates by adding nitric acid. The mixture of the above solution was converted in to citrates by adding excess amount of citric acid and this mixture was heated in the temperature range of 75℃ to 100℃ with the help of a hot plate, until a gel was formed. The gel was converted into highly voluminous fine powder by heating at 300ºC using a rectangular muffle furnace. The above precursor was pre-sintered at 600℃ to decompose the remaining organic reagents. The obtained powder was further annealed at different temperatures in the range of 700ºC to 1000ºC along with

TH-1726_11612111

intermediate grinding. Then the powder pressed into a cylindrical target of 2 inch diameter and a thickness of about 3 mm was sintered at 1200℃ for 24 h in air.

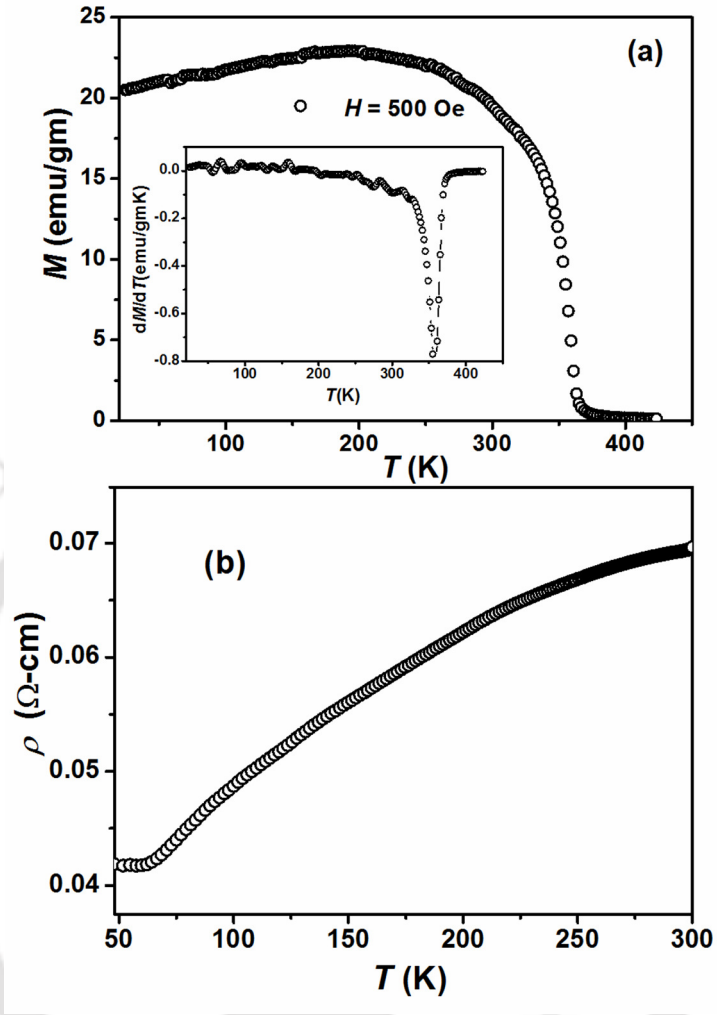

Figure 5.3: (a) Temperature variation of magnetization of LSMO target under zero field cooled condition for H=500 Oe and (b) Temperature variation of electrical resistivity of LSMO target. Inset of (a) shows the plot of dM/dT versus T for the target LSMO.

Fig.5.2 illustrates the XRD pattern of LSMO target. The pattern was Rietveld refined by choosing $R\bar{3}C$ space group i.e. with rhombohedra structure. As per the refinement, the LSMO target material is found to be in single phase form with their lattice parameters in hexagonal coordination as a =b= 5.491Å, and c = 13.337Å. The pseudo cubic lattice parameters of the target material are estimated as a' (= $a/\sqrt{2}$) = 3.883 Å, and c′(= $c/2\sqrt{3}$) = 3.849Å [234].

Temperature variation of magnetization measured for an applied field of 500 Oe is shown in Fig.5.3 (a) and the sample exhibits a clear ferromagnetic transition. Ferromagnetic

TH-1726_11612111

transition temperature of LSMO target was determined from the plot of d*M*/d*T* vs *T*. The transition temperature is found to be 358 K and this is almost comparable to the literature [226]. The temperature variation of electrical resistivity of the above sample is shown in Fig.5.3(b) down to 30 K. It exhibits metallic behaviour from room temperature to down to around 50 K. Its electrical resistivity at room temperature is found to be 69 mΩ-cm which is comparable to the previously reported value 0.1 Ω-cm [29, 201].

5.3 $La_{0.7}Sr_{0.3}MnO_3$ /$LaFeO_3$ Bilayer Films

5.3.1 Deposition of Bilayer Films

The bilayer films of $La_{0.7}Sr_{0.3}MnO_3$ (LSMO)/ $LaFeO_3$ were deposited on (001)-oriented $LaAlO_3$ (LAO) substrate by using a RF-magnetron sputtering system by maintaining a substrate temperature of 650°C. The bilayer deposition was carried out in situ with Ar and O_2 gas mixture in 3:1 ratio and by maintaining a working pressure of 2.5×10^{-2} mbar. The rate of deposition was calibrated to 8 nm/min and 4 nm/min for LFO and LSMO films, respectively by setting the RF power at 50 W. First, LFO layer with a thickness of 120 nm was deposited on LAO substrate and over which LSMO films of thicknesses 30 nm, 60 nm, 120 nm, 150 nm and 200 nm were grown separately and they are named as BL-30, BL-60, BL-120, BL-150 and BL-200 respectively. Further, the deposited films were post-annealed at 800℃ for an hour in oxygen environment at 1 atm pressure. Such post annealing is known to improve the magnetic and transport properties of LSMO films [235]. For a comparison, we have also grown single layer films of LFO with 120 nm thickness (SL-LFO-120) and LSMO film of thickness 60 nm (SL-LSMO-60) on 001- LAO substrate.

5.3.2 Structural Properties

XRD patterns of bilayer films for different thicknesses of LSMO layer are shown in Fig.5.4. Here the intensity is shown in logarithmic scale to clearly display the peaks due to films in the background of high intensity substrate peak. For a comparison, we also show the patterns of single layer LFO and LSMO deposited on 001 - LAO substrate. The growth of bilayer films along [001] direction with distinct (002) peaks corresponding to both LFO (closed diamond) and LSMO (open diamond) films appearing at $2\theta \approx 46.10°$ and 47° respectively can be clearly seen in Fig.5.4. The (001) peaks due to these films are almost merged at $2\theta \approx 23°$. The observed (001) and (002) peaks show that both LSMO and LFO

TH-1726_11612111

are grown as single crystalline films oriented along c-axis of the unit cell on (001)-LAO substrate.

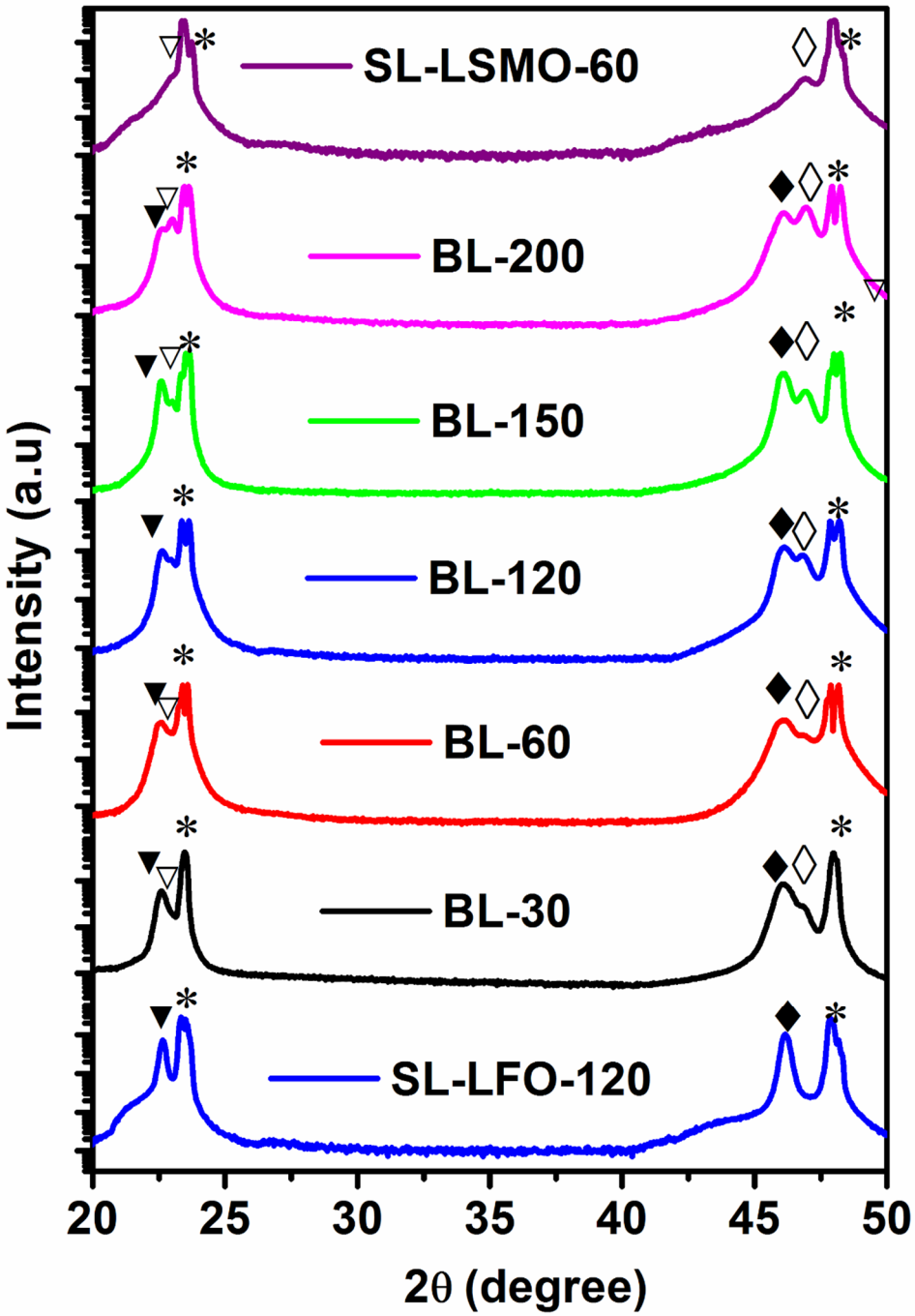

Figure 5.4: XRD patterns of LSMO/LFO bilayer on 001-LAO substrate. The intensity is shown in logarithmic scale to clearly display the peak due to the film. The (002) peaks corresponding to the substrate, LSMO and LFO are marked as stars, open diamond and closed diamond respectively

TH-1726_11612111

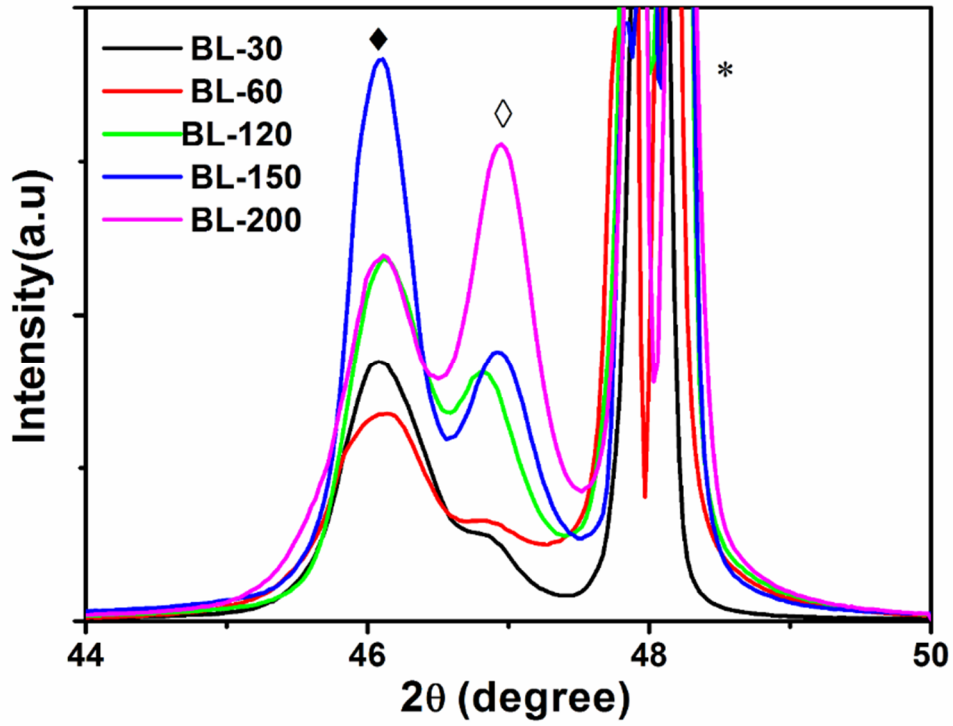

Figure 5.5: Enlarged view of (002) peaks of LSMO and LFO films along with LAO substrate.

The intensity of (002) peaks is found to systematically increase with increase in layer thickness of LSMO films as shown in Fig.5.5 in enlarged scale. The (002) peak position (46.10°) of LFO layer is found to be almost independent of thickness of LSMO layer. The out-of-plane lattice constant (c_{LFO}) of LFO layer is around 3.933 Å as shown in table-5.1, which is independent of LSMO layer thickness and moreover it is comparable to the bulk LFO sample. On the other hand, the (002) peak position of LSMO is found to shift towards higher 2θ value with increase in film thickness and thereby, its out-of-plane lattice constant (c_{LSMO}) systematically decreases from 3.887 Å for BL-30 to 3.868 Å for BL-200 as shown in table-5.1. So, with increase in film thickness, c_{LSMO} approaches towards its bulk value of $c' = 3.849$ Å. The lattice strain was calculated using the relation [104]

$$\varepsilon(\%) = \left(\frac{c_{LSMO} - c'}{c'}\right) \times 100 \qquad (5.1)$$

and these values are given in table-5.1. So, the LSMO layer exhibits tensile strain along the c - direction i.e. perpendicular to the plane of the film and its value is found to decrease from 0.98 % for 30 nm to 0.49 % for 200 nm thickness of LSMO layer. Such out-of-plane tensile or in-plane compressive strain can be understood in terms of smaller lattice constant ($c_{LAO} = 3.788$ Å) of LAO substrate compared to the LSMO film. Here, the lattice mismatch between LFO and LAO is -3.8% which indicates the presence of in-plane compressive

TH-1726_11612111

strain while the lattice mismatch between LSMO and LFO films is found to be 2.2%. Thus even though LSMO layer was deposited on LFO film, the LAO substrate influences the lattice strain and this can be understood as follows. The crystal growth occurs mostly during the post annealing process, where the LAO substrate plays a major role in controlling the crystal growth.

Table 5. 1: Out-of-plane lattice constant of bilayer films and the lattice strain of LSMO layer

Thickness (nm)	c_{LFO} (Å)	c_{LSMO} (Å)	Strain (ε_{LSMO}%)
BL-30	3.933	3.887	0.98
BL-60	3.934	3.886	0.96
BL-120	3.932	3.878	0.75
BL-150	3.934	3.871	0.57
BL-200	3.932	3.868	0.49

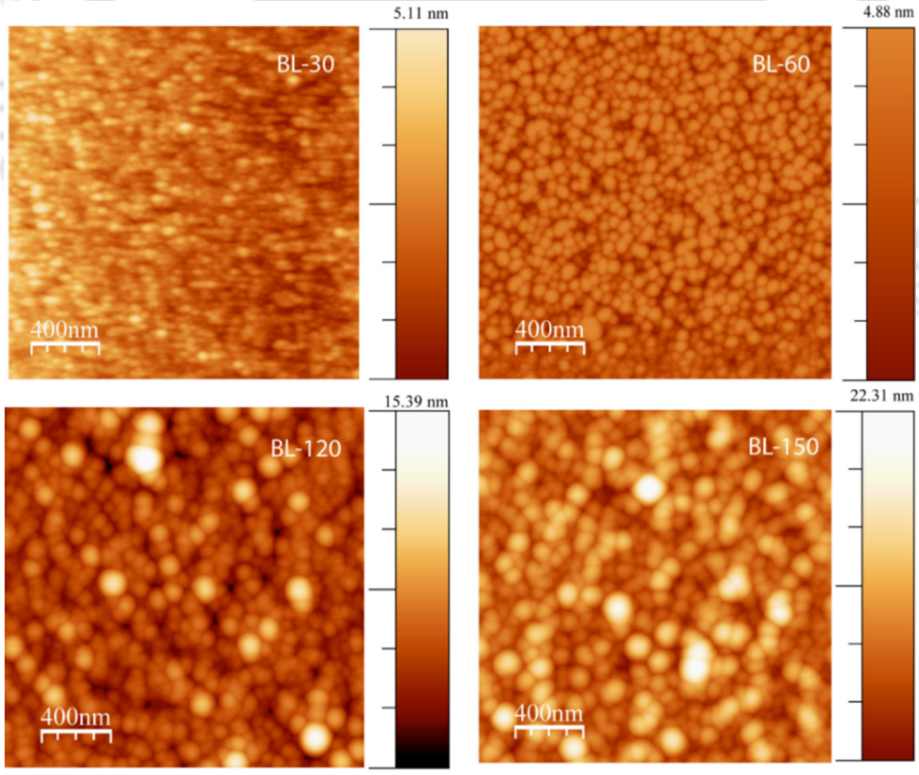

Figure 5.6: Surface morphology of bilayer films BL-30, BL-60, BL-120 and BL-150.

Fig.5.6 illustrates the surface morphology of bilayer films for the LSMO layer thickness of 30, 60, 120 and 150 nm and the scale, close to each of five images, represents

TH-1726_11612111

the height of grain. The surface roughness of the films is gradually increased from 0.8 nm for BL-30 sample to 3 nm for BL-150 sample. The average diameter of grain is found to increase from 40 nm for BL-30 to 120 nm with increase in film thickness.

5.3.3 Magnetic Properties

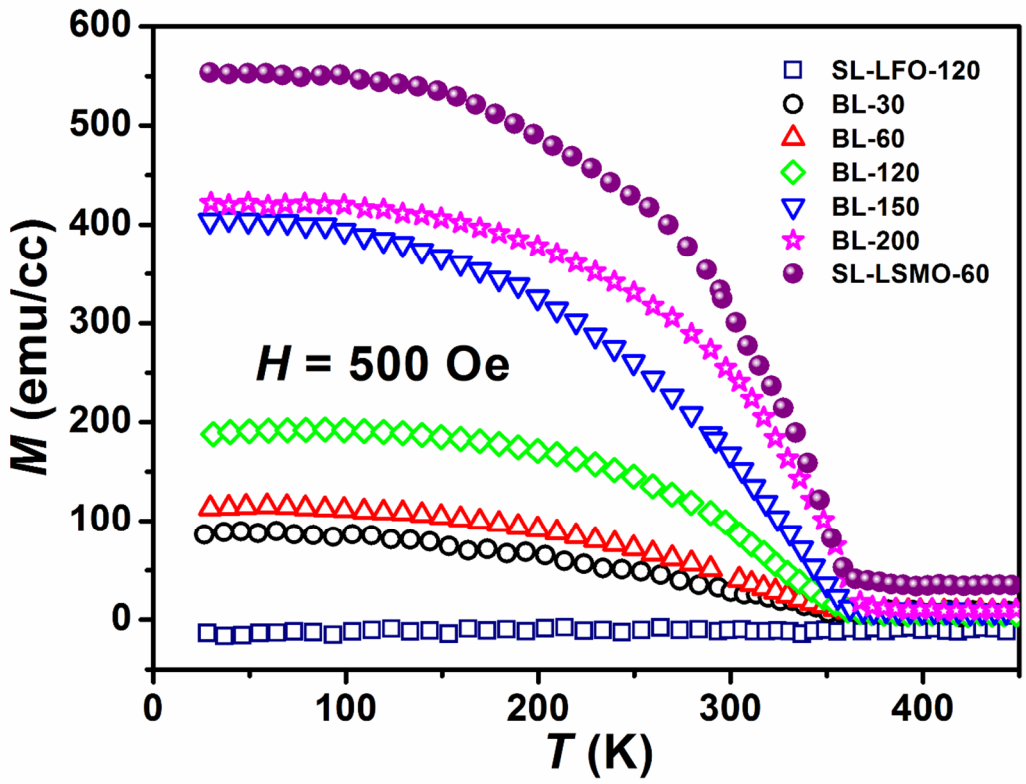

Figure 5.7: Temperature variation of magnetization under zero field cooled mode for an applied field of 500 Oe along in-plane of films for all bilayers and single layer LSMO film.

The temperature variations of magnetization of bilayer films under zero field cooled condition for a magnetic field of 500 Oe applied along in-plane of the film are shown in Fig. 5.7. For a comparison, we are also showing the M - T plots of single layer LFO and LSMO films. Here, all bilayer films show ferromagnetic transition and the transition temperature (T_C) was determined from the plot of dM/dT versus T. The width of the transition is found to decrease with increase in film thickness and the T_C is found to increase from 290 K for 30 nm film to 332 K for 200 nm film. The magnitude of magnetization for $T < T_C$ is also found to increase systematically with increase in LSMO thickness. The observed magnetization and ferromagnetic T_C for single layered LSMO film is found to be even larger than those of bilayer film of largest T_C. The above variation of T_C can be understood in terms of reduction in lattice strain with increase in film thickness. The magnetic moment of single layer LFO film is found to be mostly close to zero. Moreover,

TH-1726_11612111

the antiferromagnetic LFO layer is also found to considerably affect the ferromagnetic T_C of bilayer films due to possible magnetic frustration at FM/AFM interface.

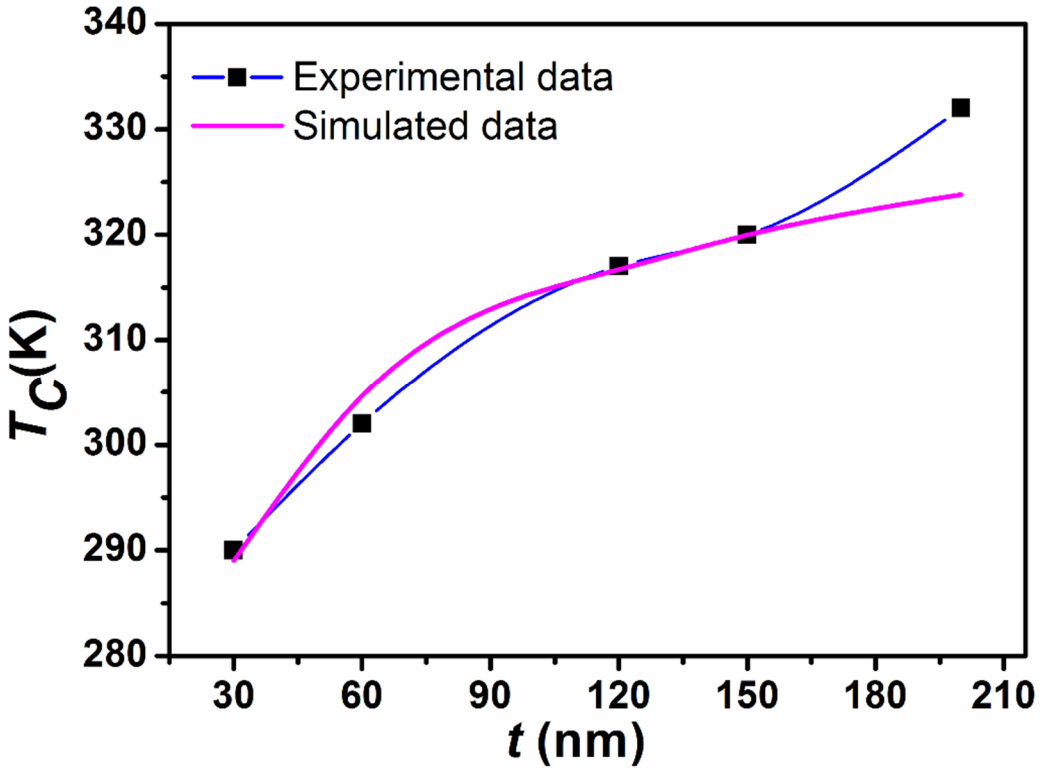

Figure 5.8: T_C as a function of thickness (t) of LSMO along with fitted data.

The variation of ferromagnetic T_C with film thickness is shown in Fig. 5.8, where T_C tends to saturate to the bulk value of T_C(B) as t is increased. It is analysed in terms of scaling theory,

$$\left[\frac{[T_C(B)-[T_C(t)]}{[T_C(B)}\right]=\left[\frac{k}{t}\right]^{\lambda} \quad (5.2)$$

where k and λ are constants [204]. The fitted data by taking k and λ as free parameters of the fit and by taking T_C (B) = 358 K are shown as solid line in Fig. 5.8.The estimated values of k and λ are found to be 0.4 nm and 0.37 respectively.

In order to further understand the magnetic properties, *M-H* loops were recorded at 50 K and they are shown in Fig. 5.9. All bilayer films show typical soft ferromagnetic behaviour, however the saturation magnetization is found to increase with film thickness. Moreover, the coercive field is found to decrease from 150 Oe for 30 nm film to 78 Oe for 120 nm film. The saturation magnetization (M_s) values of the films were determined with the help of law of approach to saturation magnetization [185], i.e.

TH-1726_11612111

$$M = M_S \left[1 - \frac{a}{H^{1/2}} - \frac{b}{H^2}\right] \quad (5.3)$$

Here, a and b are constants and they are taken as free parameters of the fit along with M_s. The determined M_s values are found to vary from 150 emu/cc for BL-30 to 490 emu/cc for BL-200. The above variation of M_s and H_c can be understood in terms of reduction in lattice strain with increase in film thickness. The T_C and M_s values of bilayer films are smaller than those of bulk samples and similar behaviour is reported in bilayer films of $La_{0.7}Sr_{0.3}MnO_3/BaTiO_3$ on LAO substrate [236]. As we have described that the in-plane tensile strain between the LSMO and LFO, would strongly stretch the Mn - O bond length along the plane of the films. As a result, the transfer of e_g electron is reduced between the Mn^{3+} and Mn^{4+} ions, thus the T_C and M_S values are diminished than the single LSMO layer film.

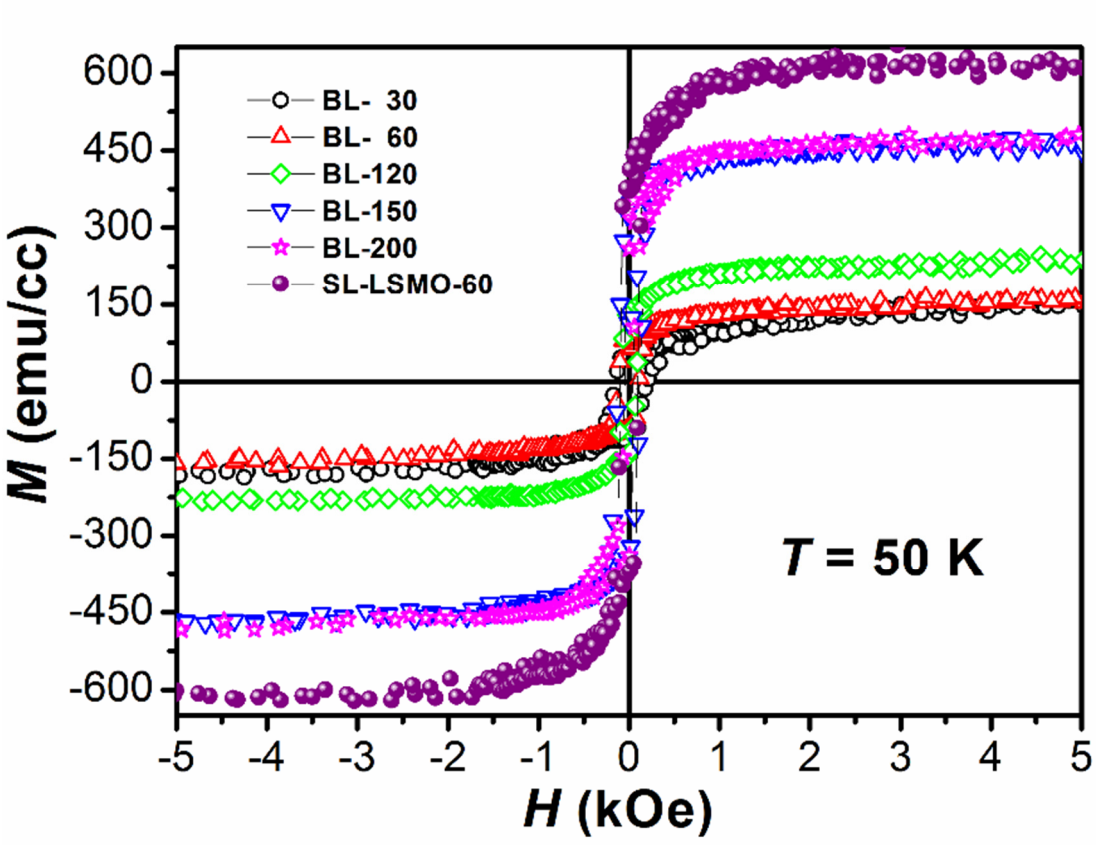

Figure 5.9: M – H loops of different bilayer films recorded at 50 K

TH-1726_11612111

Study of electron magnetic resonance (EMR) spectra gives additional information such as the presence of multiple or heterogeneous nature of ferromagnetic sample due to lattice strain, interlayer diffusion, etc. In this work, we have recorded the EMR spectra at room temperature and at 77 K by applying the dc magnetic field along and perpendicular to the film plane. In homogeneous paramagnetic material, one expects the resonance at

$$\frac{\omega}{\gamma} = H_r \tag{5.4}$$

where ω is the microwave frequency in resonance condition, which is fixed as 9.4 GHz in the X-band spectrometer. $\gamma = (g\mu_B/\hbar)$ the gyromagnetic ratio and H_r is the resonance field for the given paramagnet. However in ferromagnetic materials depending on the direction of applied dc magnetic field with respect to the plane of film, the following equations can be written [99, 237],

$$\left[\frac{\omega}{\gamma}\right]^2 = H_{||}[\ H_{||} + 4\pi M_s - H_a] \tag{5.5}$$

$$\left[\frac{\omega}{\gamma}\right] = [H_{\perp} - (4\pi M_s - H_{a1}\ )] \tag{5.6}$$

Here $H_{||}$ and $H_{\perp}$ are the resonance fields for applied fields along parallel and perpendicular to the plane of the films respectively. $4\pi M_s$ is the magnetization, which is influenced by the shape anisotropy. The anisotropy fields can be written as,

$$H_{\ a} = H_{a1} + H_{a2} \tag{5.7}$$

$$H_{\ a1} = \frac{2K_1}{M} \tag{5.8}$$

and $$H_{\ a2} = \frac{4K_2}{M} \tag{5.9}$$

Here K_1 and K_2 are the effective first-order and second order anisotropy constants respectively. According to eqs. (5.5) and (5.6), the resonance fields $H_{||}$ and $H_{\perp}$ are expected to be respectively smaller and larger than the H_r of paramagnet. The EMR spectra recorded at room temperature for in-plane applied fields are shown in Fig.5.10(a) for different bilayer films. A relatively broad ferromagnetic resonance spectrum is observed for BL-30 film at a resonance field of $H_{||}$ = 241 mT. As the film thickness is increased $H_{||}$ is found to shift towards lower field and in addition that the resonance peak is found to be sharper with increase in film thickness. It may be also noted that BL-120 shows the overlapping of two

TH-1726_11612111

spectra. Such overlapping of spectra cannot be ruled out for BL-30 and BL-60 films also due to their large width ($\Delta H_{\parallel}$) of the spectrum. The integrated intensity of these absorption signals was fitted to Lorentzian function and the estimated resonance fields corresponding to the prominent peak are shown in table-5.2. The above observed variation of $H_{\parallel}$ and $\Delta H_{\parallel}$ with increase in film thickness suggests that the lattice strain and AFM interface affect the magnetic properties significantly. The observed overlapping FMR signal for BL-120 can be attributed to the presence of two different ferromagnetic phases due to the possibility of formation differently strained regions.

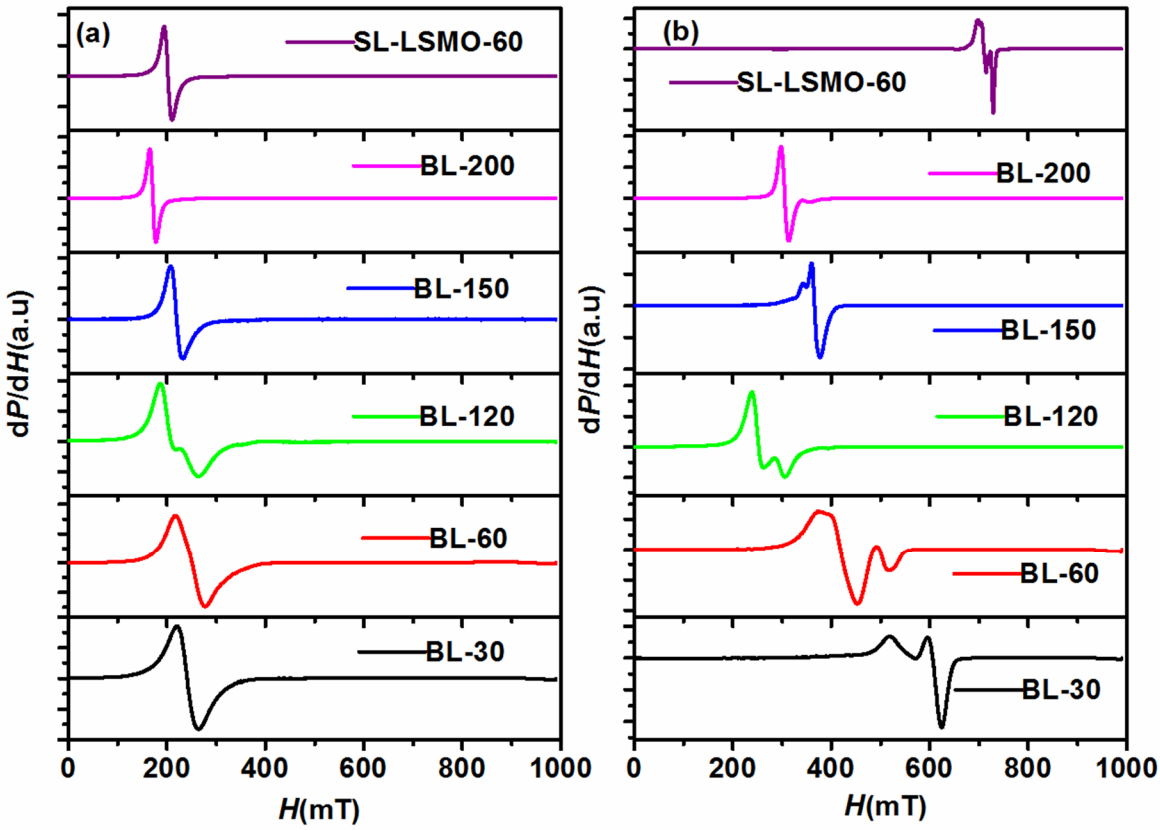

Figure 5. 10**:** FMR spectra of bilayers and SL-LSMO-60 recorded at room temperature for applied field along (*a*) in-plane and (*b*) for out-of-plane of the films.

TH-1726_11612111

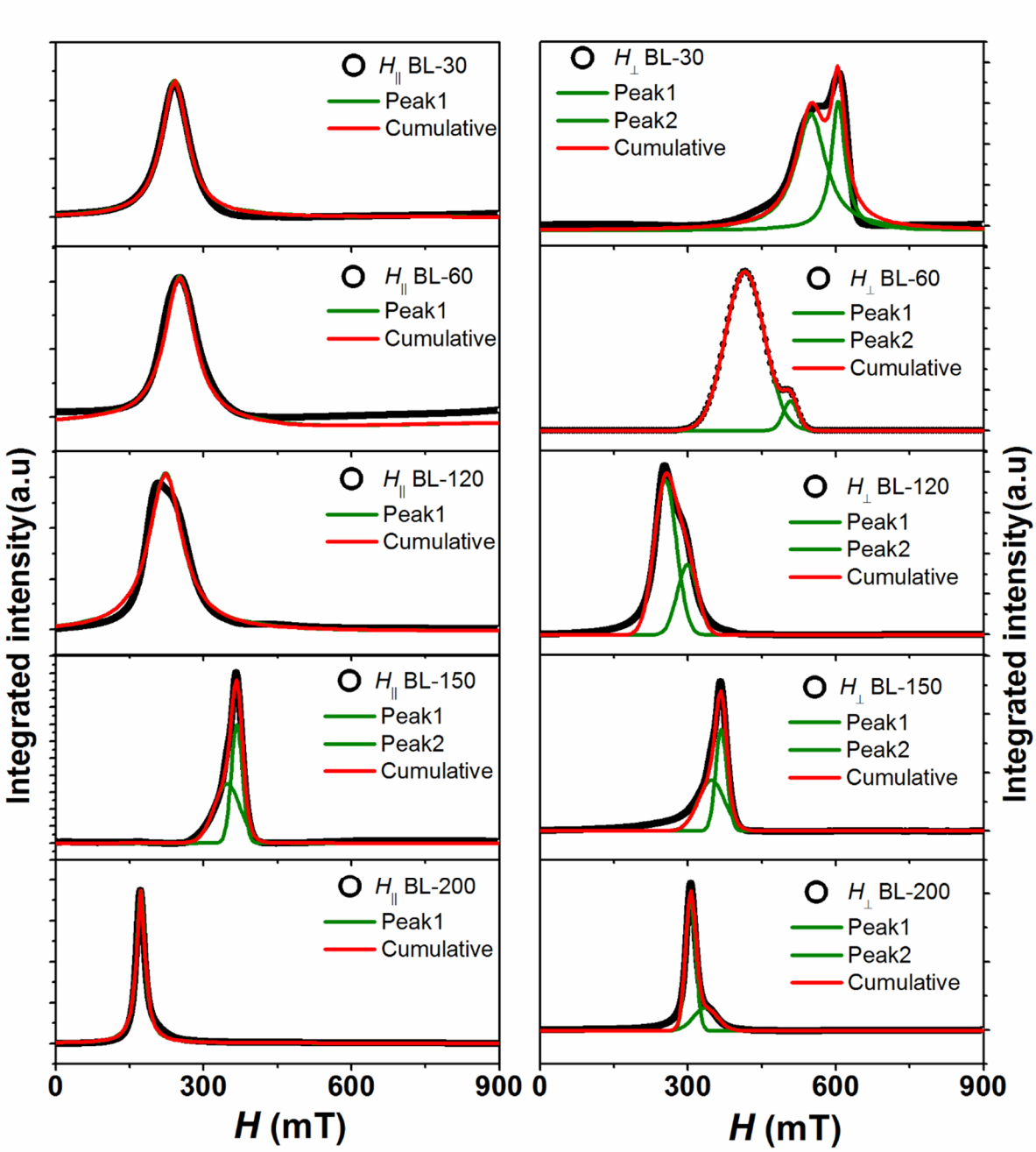

Figure 5.11: Integrated intensity of FMR signals of bilayer films along with fit to Lorentzian model.

The EMR spectra for field applied perpendicular to plane at room temperature are shown in Fig.5.10(b). Here as expected the resonance is shifted to higher fields. More interestingly for most of the films double resonance is observed and is consistent with the argument of presence of two types of ferromagnetic resonance [238]. For BL-30 one of the peaks ($H_{\perp}$ = 610 mT) can be assigned to the paramagnetic resonance (PMR) because of its T_C closer to room temperature and the secondary peak observed at lower resonance field ($H_{\perp}$ = 557 mT) can be assigned to the ferromagnetic resonance. Here, PMR is more

TH-1726_11612111

dominant signal than the ferromagnetic resonance at room temperature. In the case of films of BL-60, BL-120, BL-150 and BL-200, two overlapped resonance spectra resemble the existence of two ferromagnetic phases. Thus the perpendicular field clearly resolves these two FM signals, which are overlapped under parallel field condition. As the thickness of the film is increased, growth of lower field peak at the expense of higher field signal is seen due to the strengthening of one of the FM phase. Moreover the resonance field is found to shift towards the lower field with increase film thickness. Interestingly BL-200 film shows single resonance derivative as a result of relaxation of lattice strain. Thus for smaller film thickness, the lattice strain and the effect of AFM interface cause an additional ferromagnetic phase. Presence of such double resonance is seen even for single layered SL-LSMO-60 film. By fitting the integrated intensity to Lorentzian model as shown in Fig. 5.11, the resonance fields $H_{\perp}$ and the peak width $\Delta H_{\perp}$ at full-width half maxima were determined and they are given in table-5.2 especially for lower field peak. The higher field resonance peak is found to vary from $H_{\perp} = 610$ mT for BL-30 to $H_{\perp} = 355$ mT for BL-200. From the experimental resonance fields and magnetization, the anisotropy fields H_a and H_{a1} were estimated using the eqs. (5.7) and (5.8). The effective anisotropy constant K_v was determined by averaging the values of $K_1 = (1/2)\, MH_{a1}$ and $K_2 = (1/4)MH_{a2}$ and they are given in table-5.2.

Table 5.2: Resonance fields of electron magnetic resonance spectra for parallel ($H_{\parallel}$) and perpendicular ($H_{\perp}$) applied field to the films along with their respective full-width half maxima ($\Delta H_{\parallel}$, $\Delta H_{\perp}$) and anisotropy constant (K_v).

Thickness (nm)	$H_{\parallel}$(mT)		$\Delta H_{\parallel}$(mT)		$H_{\perp}$ (mT)		$\Delta H_{\perp}$(mT)		K_v $\times 10^3$(J/m^3)	
	300 K	77K	300 K	77K	300K	77K	300K	77K	300K	77 K
BL-30	241.3	-	76.9	-	557.2	-	105.0	-	6.1	-
BL-60	250.8	-	70.1	-	415.5	-	92.3	-	0.7	7.5
BL-120	227.3	269.2	28.8	67.2	253.9	897.1	53.2	55.0	0.2	12.2
BL-150	221.9	164.4	28.6	52.9	363.6	265.4	47.8	57.6	1.5	38.4
BL-200	172.2	135.1	25.5	57.1	305.2	212.6	24.5	49.4	1.5	36.5

TH-1726_11612111

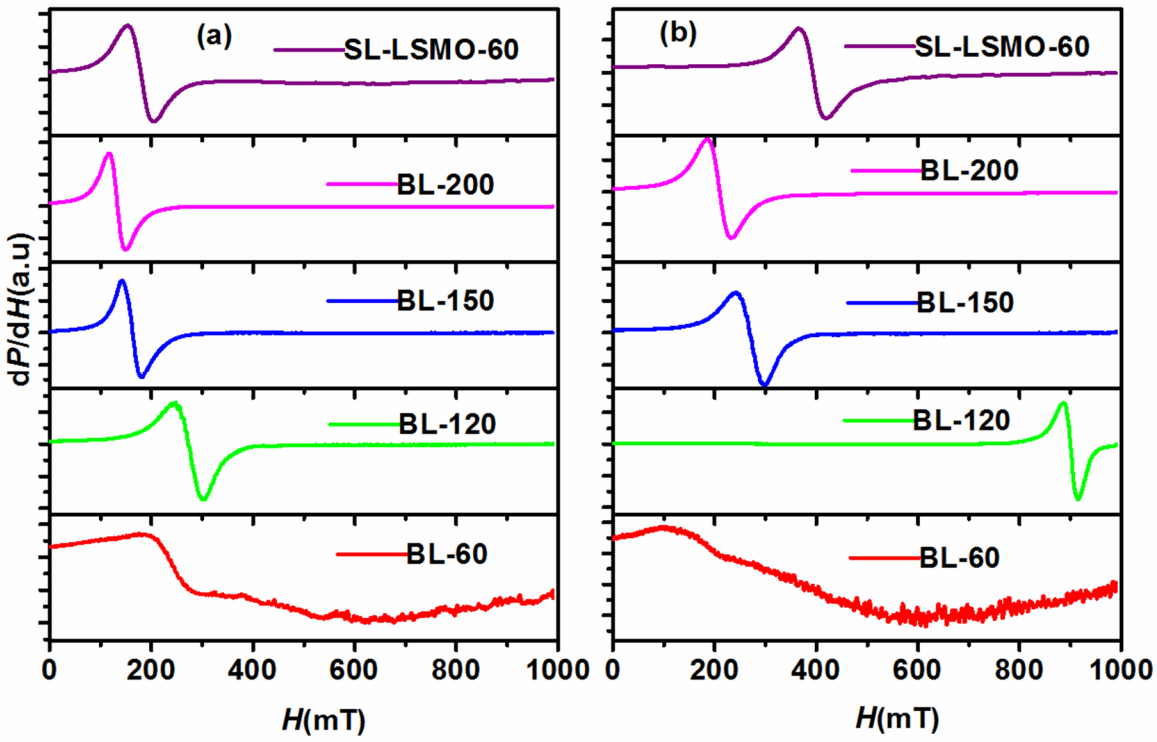

Figure 5.12: FMR spectra for field along the (a) in-plane and (b) out-of-plane of the films at 77 K for the bilayer films.

The EMR spectra recorded at 77 K under parallel and perpendicular field conditions are shown in Fig.5.12. Here the single layered film and films of higher thickness (≥ 150 nm) show the shifting of resonance fields towards lower field compared to their respective spectra at room temperature. This suggests the strengthening of ferromagnetic interaction at low temperature. Moreover, the $H_{\perp}$ values are higher than that of respective $H_{\parallel}$ values and this suggests the observed spectra are due to ferromagnetic resonance. However for BL-120 film, the resonance fields are relatively higher than those of room temperature values. One cannot also rule out the possibility of orbital-ordering induced AFM. For further decrease in film thickness to BL-60, we have not observed complete FMR signal due to the shifting of the peak towards very low field as well as due to very broad nature of resonance. The spectra of BL-30 at 77 K is found to be highly scattered and noisy, so, it is not shown. Thus for lower thickness films one cannot rule out the possibility of strengthening of competing AFM interactions at low temperature. The above argument can be also supported from the rather low values of M_s observed from M - H loops for these samples. The $\Delta H_{\parallel}$ and $\Delta H_{\perp}$ values at 77 K are determined from the integrated Lorentzian fit shown in Fig.5.13. They are tabulated in table-5.2 and they are found to be larger than those of respective parameter at room temperature. This can be attributed to wide distribution in ferromagnetic interaction. The anisotropy constant K_v estimated from the

TH-1726_11612111

EMR spectra at 77 K are shown in table-5.2 and they are found to be larger than that of their respective values at room temperature.

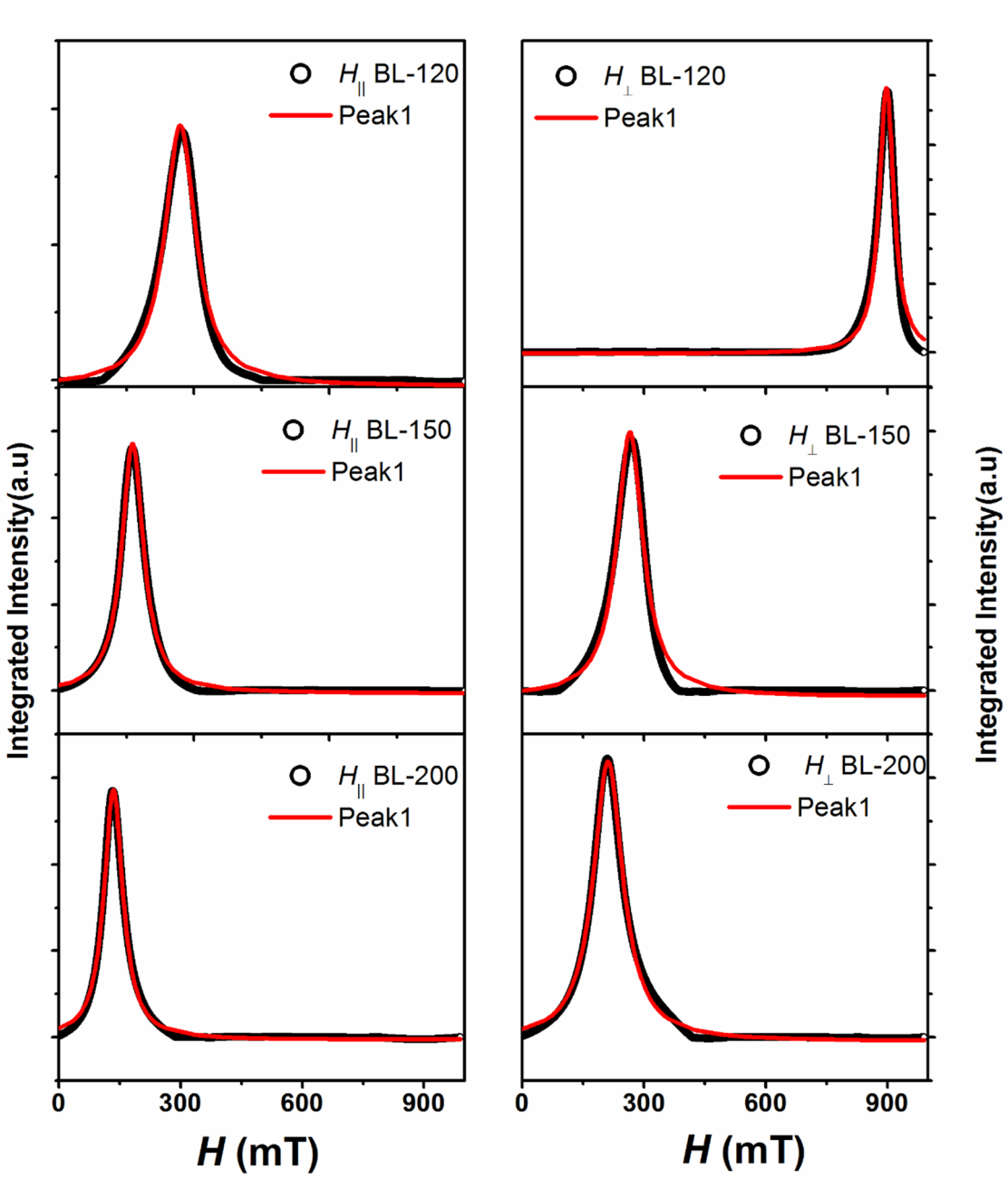

Figure 5.13: The integrated intensity fit of FMR spectra recorded at 77 K to the Loterzian model for the bilayer films.

TH-1726_11612111

5.3.4 Electrical Properties

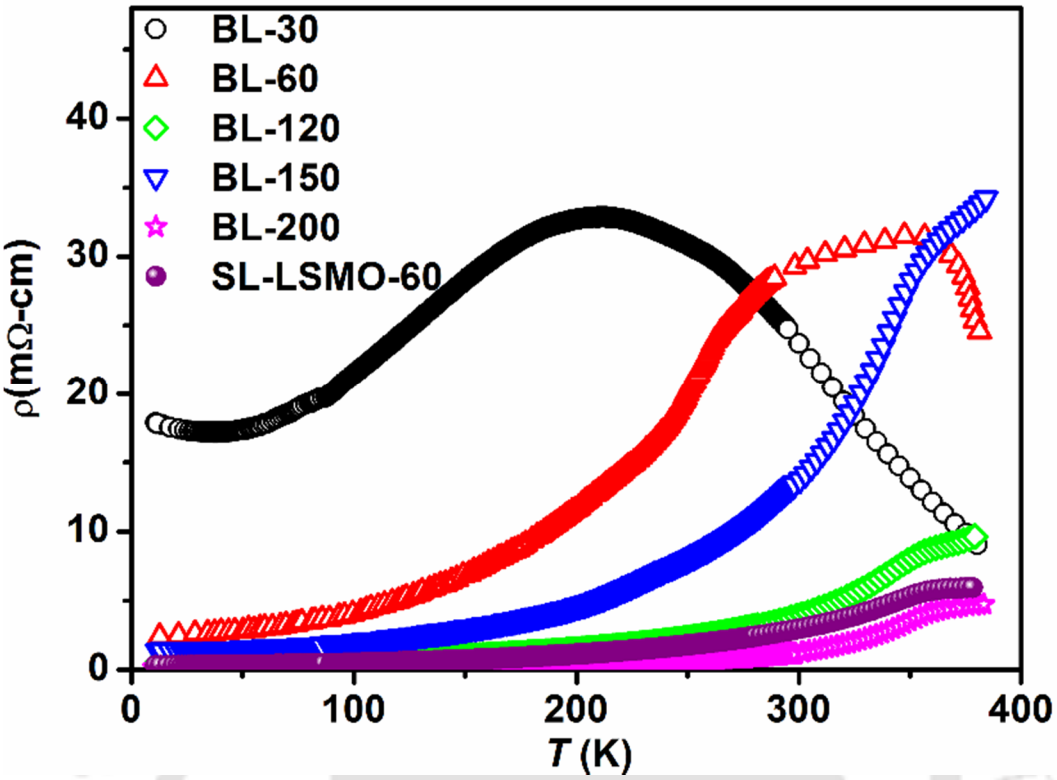

Figure 5.14: Temperature variation of electrical resistivity of bilayer films having LSMO layer thicknesses of 30, 60, 120, 150 and 200 nm along with single layer LSMO film.

In order to understand the electrical properties of hetero-structure films, we have measured temperature variation of electrical resistivity in the temperature range of 10 - 400 K for the bilayer as well as single layered LSMO films and they are shown in Fig.5.14. The samples BL-30 and BL-60 show metal-insulator transition (T_{MI}) and the remaining films exhibit metallic behaviour up to 400 K. The magnitude of resistivity value is found to drastically decrease with increase in LSMO layer thickness. The BL-30 film shows a very broad transition with T_{MI} at 210 K which is far below the FM T_C (290 K), and in addition to that it exhibits a low temperature (< 100 K) upturn in electrical resistivity. This feature clearly support the argument of presence of competing AFM as discussed under EMR spectra. The $\rho - T$ plot for BL-60 sample shows two distinct MI transition with T_{MI} = 289 and 353 K. This double transition is consistent with two FMR peaks and the presence of two FM interactions.

TH-1726_11612111

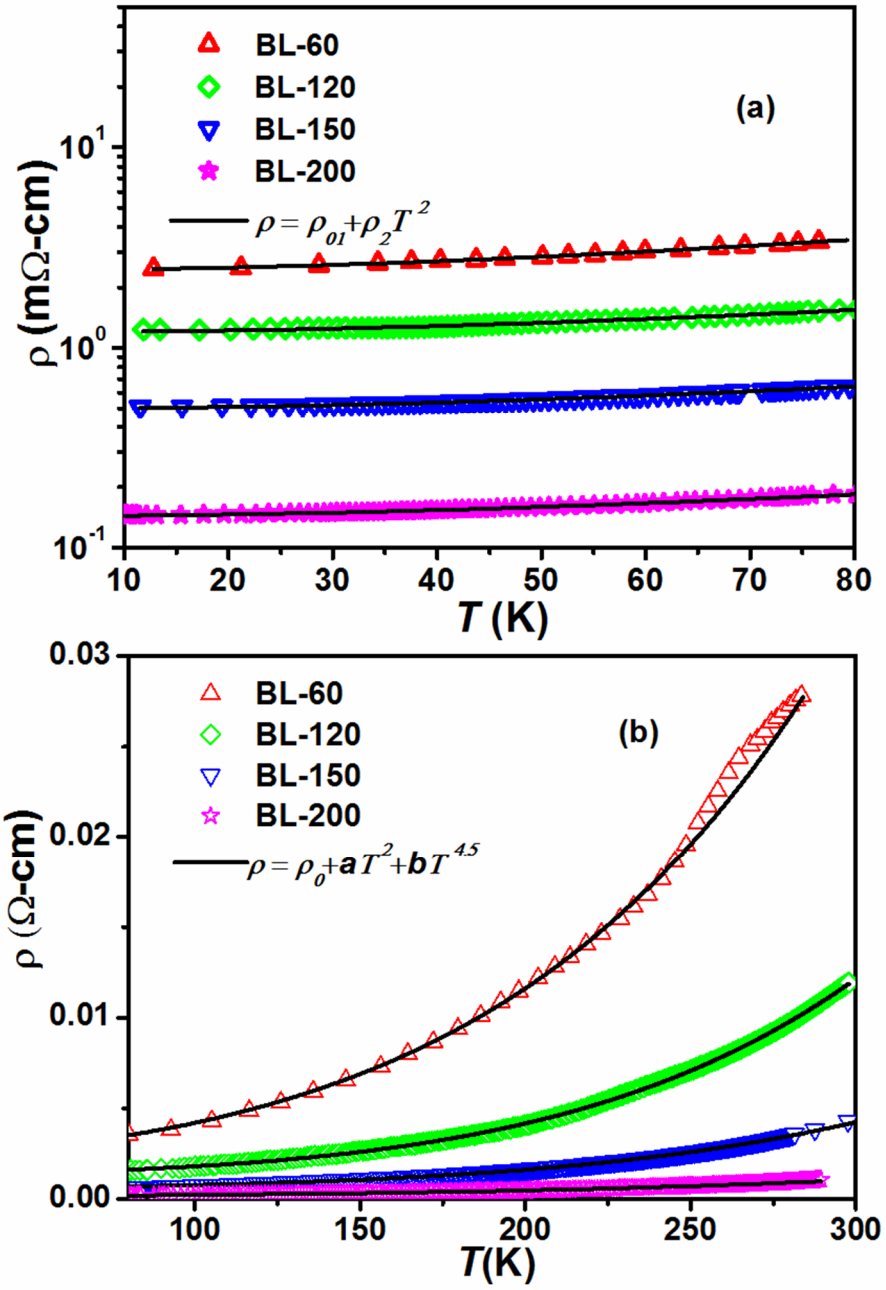

Figure 5.15: Electrical resistivity data in two different temperatures regions along with their respective theoretical fit.

The resistivity data in the low temperature region, for BL-30 sample, were analysed by using the relation [239]

$$\rho = \rho_0 - \rho_{1/2} T^{1/2} + \rho_2 T^2 \qquad (5.10)$$

where ρ_0 represents residual resistivity, T^2 term refers to the electron-electron scattering [226] and second term in the equation corresponds to the weak localization mechanism [203]. From the fit, the residual resistivity (ρ_0), $\rho_{1/2}$ and ρ_2 values are found to be 20.03

TH-1726_11612111

mΩ-cm, 639.33 μΩ-cmK$^{-1/2}$ and 0.75 μΩ-cmK^{-2} respectively. The obtained fitted values are almost comparable to the fitted values of $La_{0.7}Ba_{0.3}MnO_3$ thin films on the LAO substrate [240]. For the samples BL-60, BL-120, BL-150 and BL-200, the resistivity data were divided into two regions, i.e. 10 - 80 K and 80 – 300 K. The data in the low temperature region, i.e. 10 – 80 K, were analysed by using the relation $\rho = \rho_{01} + \rho_2 T^2$, i.e. by ignoring the second term in eq.5.10. The fitted data are shown as solid line in Fig.5. 15(*a*) and the corresponding fitted parameters are tabulated in table-5.3. Fig. 5.15(*b*) illustrates the analysis of resistivity data in the higher temperature region, (i.e. from 80 K to 300 K) by using the relation, [201, 181]

$$\rho = \rho_{02} + aT^2 + bT^{4.5} \qquad (5.11)$$

Which is a combination of the electron-electron scattering and electron-magnon interaction mechanism. Here ρ_{02} represents the residual resistivity, a and b are temperature dependent resistivity constants. $T^{4.5}$ term corresponds to the electron-magnon scattering mechanism [50]. The fitted parameters are given in table-5.3 and it is found that residual and temperature coefficient values decrease with increase in the film thickness. According to Pietambaram *et al*. [241], the electrical resistance of the manganite samples follow the eq. 5.11 due to the electron – magnon scattering by the lattice vibrations at low temperatures. Moreover, the low temperature resistivity data of $La_{0.67}Sr_{0.33}MnO_3/La_{0.67}Ca_{0.33}MnO_3$ multilayers was well explained by considering the electron - electron scattering with a coefficient of T^2 term in the order of ~ 10^{-8} Ω-cmK^{-2}which is comparable to the present result shown in table-5.3 [171].

Table 5. 3: Parameters obtained from the analysis of resistivity data in the metallic region.

Thickness (nm)	ρ_{01} (mΩ-cm)	ρ_2 (μΩ-cmK^{-2})	ρ_{02} (mΩ-cm)	a (μΩ-cmK^{-2})	b (μΩ-cmK$^{-4.5}$)
BL-60	2.45	0.16	2.40	0.171	0.11×10^{-8}
BL-120	1.20	0.05	1.31	0.042	4.9×10^{-8}
BL-150	0.49	0.02	0.56	0.017	1.4×10^{-8}
BL-200	0.14	0.006	0.13	0.006	2.1×10^{-9}

TH-1726_11612111

5.3.5 Conclusions

We have successfully fabricated c-axis oriented bilayer LSMO/LFO films on LAO substrate for different thickness of LSMO layer in the range of 30 nm to 200 nm. The out-of-plane lattice constant of LSMO layer is found to vary from 3.887 Å for t = 30 nm to 3.868 Å for t = 200 nm and it depicts the presence of out-of-plane tensile strain whose value reduces with increase in film thickness. Magnetization measurements and analysis show that all bilayered films exhibit ferromagnetic transition with increase in T_C from 290 K to 332 K and increase in saturation magnetization from 150 emu/cc to 490 emu/cc with increase in LSMO layer thickness. So, the lattice strain and the AFM LFO layer strongly affect the magnetic properties of LSMO layer especially for lower thickness. The EMR measurements show presence of FMR resonance whose resonance peak shifts towards lower field with increase in film thickness. Presence of double resonance peaks are also observed especially for lower thickness. Electrical resistivity data show the metal-insulator transition with its transition temperature T_{MI} increasing with increase in film thickness. The resistivity data of BL-30 film exhibit an upturn at low temperature. This was analysed in terms of the combination of electron – electron scattering and weak localisation mechanism. Remaining all samples were analysed over the temperature region 10 to 80 K in terms of electron –electron scattering. For T>80 K and upto 300K, resistivity data were analysed in terms of the combination of electron - electron scattering and electron – magnon scattering mechanism.

TH-1726_11612111

TH-1726_11612111

Chapter 6
Conclusions

TH-1726_11612111

TH-1726_11612111

Chapter 6

Conclusions

In this chapter, we summarize the results of structural, electrical and magnetic properties of single layer $Nd_{0.7}Sr_{0.3}MnO_3$ (NSMO) and $Nd_{0.8}Na_{0.2}MnO_3$ (NNMO) films and, the bilayer films of NSMO/NNMO. In addition to that the experimental results and the analysis of bilayer $La_{0.7}Sr_{0.3}MnO_3/LaFeO_3$ films are also given.

The bulk NSMO target was prepared by solid state reaction method and its diffraction pattern could be refined by using Pbnm space group in orthorhombic crystal with the lattice parameters a'= 5.544 Å, b'= 5.441 Å and c'= 7.697 Å. The temperature variation of magnetization and electrical resistivity measurements show that this bulk NSMO target material exhibits ferromagnetic and metal-insulator transition at T_C = 225 K and T_{MI} =185 K respectively.

In order to understand the role of post annealing we deposited 120 nm thick films of $Nd_{0.7}Sr_{0.3}MnO_3$ (NSMO) thin films on (001) oriented Al_2O_3 substrate followed by post-annealing at three different temperatures (700°C, 800°C and 900°C) in air environment. All films exhibit polycrystalline behaviour with single phase orthorhombic structure with typical lattice parameters a = 5.440 Å, b Å = 5.432 Å and c = 7.618 Å for the film annealed at 700°C. The lattice parameters increase with increase in annealing temperature. Room temperature Raman spectra show the signature of orthorhombic structure with A_g, B_{2g} and B_{3g} modes; one of the lines is found to be sensitive to lattice strain and it disappears upon annealing at 900°C. All films exhibit metal-insulator transition and the transition temperature (T_{MI}) is found to decrease from 144 K for 700°C annealing to 111 K for 900°C annealing. The resistivity data in the metallic region, i.e. for $T < T_{MI}$ could be fitted to the empirical relation $\rho = \rho_0 + \rho_{2.5}T^{2.5}$, while the resistivity data in the semiconducting region were fitted to Mott-VRH model. The ferromagnetic transition temperature (T_C) value obtained from the temperature variation of magnetization measurement is found to increase from 163 K for 700°C annealing to 192 K for 900°C annealing. The saturation magnetization values are also found to increase from 600 emu/cc for 700°C to 640 emu/cc 900°C. The improvement in the magnetic properties is attributed to reduced lattice strain and improved oxygen stoichiometry. However, the contradictory variation of T_{MI} can be explained in terms of growth of large grains or ferromagnetic islands weakly connected from each other due to weak grain boundary links or considerable grain boundary cracks

TH-1726_11612111

as a result of high temperature annealing of films. This can be substantiated from the increase in the roughness of film with increase in annealing temperature.

In order to study the effect of substrate induced lattice strains and its role on electrical resistivity and magnetic properties of NSMO thin films, we have deposited the films by choosing three different substrates namely (001) oriented Al_2O_3, MgO and $LaAlO_3$. The substrates are chosen such that they have different level of lattice mismatch with that of NSMO sample, i.e. 19.3%, 8.3% and -1.5% for ALO, MgO and LAO substrates respectively. NSMO films of 200 nm thickness were grown on these substrates and were separately annealed in air and oxygen environments at 700°C. Diffraction patterns of both air and oxygen annealed NSMO films on ALO and MgO are found to be in polycrystalline form with orthorhombic and cubic structure respectively. Their lattice parameters are found to be a = 5.449 Å, b = 5.433Å and c = 7.652Å and, a = 3.860 Å respectively for oxygen annealed films. On the other hand, NSMO films on LAO substrate are found to be in single crystalline form with growth orientation parallel to c-axis of the substrate with typical lattice constant of 3.851 Å. Magnetization measurements of all films show the ferromagnetic transition and the ferromagnetic T_C values of oxygen annealed films are higher than those of air annealed films. The maximum FM T_C of 194 K was observed for oxygen annealed film deposited on LAO substrate. However, the FM transition of films on ALO and LAO substrates is found to be quite broad due to the lack of uniform oxygenation of the films or the cubic structure of these films and associated restriction in Mn-O-Mn bond angle. *M-H* loops recorded at 50 K show ferromagnetic behaviour for all films and a maximum saturation magnetization value of 4.1 μ_B was observed in NSMO films on LAO substrate. Electrical resistivity data for both air and oxygen annealed films on three substrates show metal-insulator transitions; like magnetic transition, T_{MI} values of oxygen annealed films are higher than those of air annealed films. Moreover, the T_{MI} value of LO-200 film almost approches the bulk value. The magnitude of electrical resistivity of films deposited on LAO is found to be lowest compared to that of other two substrates. Hence, the oxygen annealing and the LAO substrate play a major role in tuning the electrical resistivity and magnetization properties of manganite film.

In order to understand the role of film thickness on electrical resistivity and magnetic properties we have deposited $Nd_{0.7}Sr_{0.3}MnO_3$ films of different thickness in the range of 12 nm to 120 nm on (001) oriented $LaAlO_3$ substrate. All films were post-annealed at 700°C in flowing oxygen gas environment. Analysis of XRD patterns show that all films

TH-1726_11612111

are grown with single crystalline cubic structure with their c-axis oriented perpendicular to the plane of the substrate. The out-of-plane lattice constant of NSMO films is found to decrease from 3. 870 Å for 12 nm to 3.851 Å for 120 nm thick film. This is attributed to the relaxation of out-of-plane tensile strain with increase in film thickness. Temperature variation of magnetization measurements under zero field cooled condition show that all films exhibit ferromagnetic transition and its transition temperature (T_C) is found to increase from 165 K for 25 nm to 200 K for 120 nm film thickness. The magnetic dead layer of about 12 nm is observed. The *M-H* loops measured at 50 K show the typical ferromagnetic behaviour with a maximum M_S value of 4 μ_B for 200 nm thick film. The increase in *Ms* value as the film thickness is increased can be attributed to the relaxation of lattice strain. The initial magnetization data were analysed in terms of law of approach to saturation. The effective magnetic anisotropy constant (*K*) estimated from the above analysis is found to decrease with increase in film thickness due to the relaxation of lattice strain. Electrical resistivity data of all films exhibit metal-insulator transition and the transition temperature value (T_{MI}) is found to increase from 101 K for 12 nm film to 200 K for 60 nm film. For thickness higher than 60nm no appreciable change in T_{MI} is observed. Variation of T_{MI} with the film thickness follows the finite size scaling theory relation $[T_{MI}(\mathrm{B})-T_{MI}(t)]/T_{MI}(\mathrm{B}) = (k/t)^{\lambda}$. The magneto-resistance values of the films are found be -96% at 177 K for 30 nm, -94% at 186 K for 40 nm and -92% at 194 K for 50 nm film thickness. The resistivity data in the low temperature region exhibit an upturn and they are analysed by considering the combination of weak localisation effect and electron – electron scattering mechanism. The resistivity data in the vicinity of T_{MI} were fitted by considering the electron – magnon scattering mechanism. Thus for NSMO film thickness above 60 m, the lattice strain almost relaxes and hence the T_C, T_{MI} and M_S values approach that of bulk sample.

$Nd_{0.8}Na_{0.2}MnO_3$ (NNMO) is one of the well known charge ordered (CO) antiferro-magnetic material with CO transition around 180 K. We wanted to study the bilayer of ferromagnetic NSMO and CO NNMO for potential applications in spintronic applications. As a first step, we wanted to optimize the deposition of NNMO films. So, we have prepared bulk NNMO target by using the solid state reaction method. The lattice parameters of the NNMO target are found to a = 5.420 Å, b = 5.442 Å and c = 7.676 Å. The average pseudo cubic lattice parameter is deduced as c' (= c/2) = 3.838 Å using the lattice constant of the bulk target material. Temperature variation of the magnetization under zero field cooled

TH-1726_11612111

condition shows the charge ordering transition around 188 K. The electrical resistivity data show the insulating behavior down to the low temperature.

We have studied the effect of film thickness on electrical and magnetic properties of NNMO thin films deposited on 001-$LaAlO_3$ substrate. The XRD patterns of the films show the single crystalline growth of the film along c- direction of the substrate. The typical lattice constant of the 30 nm thick film is 3.864 Å. Like NSMO films, the out-of-plane lattice constant of NNMO films systematically decreases with increase in film thickness due to the relaxation of out-of-plane tensile strain. We have noticed the signature of charge ordering related Raman bands at 601 and 620 cm^{-1} for spectra recorded at room temperature. Temperature variation of magnetization measurements show that in addition to the signature of charge ordering around 190 K a low temperature (< 100 K) weak ferromagnetic transition is observed. The saturation magnetization value is found to decrease with increase in film thickness due to the strengthening of charge ordering as the lattice strain is decreased. The electrical resistivity data of all samples follow semiconducting behaviour and they follow the Mott variable range hopping model.

The bilayer films of NSMO/NNMO were successfully deposited on 001-LAO substrate by keeping the thickness of NNMO layer as 120 nm and by varying the thickness of ferromagnetic NSMO layer from 12 nm to 100 nm. Both NSMO and NNMO layers are found to grow as single crystalline films with their orientation along the c-direction of the substrate. Like single layer NSMO films, the typical out-of-plane lattice constant (c_{NSMO}) of NSMO film in the bilayer is found to be 3.890 Å for 30 nm which is larger than the single layer NSMO film (3.867Å for 30 nm) due to the intermediate NNMO layer. c_{NSMO} value is found to vary from 3.890 Å for t = 30 nm to 3.876 Å for t = 100 nm and it depicts the presence of out-of-plane tensile strain whose value decreases with increase in film thickness. All bilayer films show a broad ferromagnetic transition and the T_C is lower than that of single layer film of same thickness. They all undergo ferromagnetic transition with T_C in the range of 62 K for 12 nm thick film to 107 K for 100 nm thick film. The lattice strain and the coupling of Mn – O – Mn ions at the interface of NSMO/NNMO impede the electron hopping in the DE networks and it leads to smaller FM T_C compared to that of single layer LSMO. Electrical resistivity data show the metal-insulator transition with the maximum transition temperature, T_{MI} of 172 K for 100 nm thick bilayer films. Like NSMO film, the bilayer film follows the finite size theory. The resistivity data in the metallic region is explained in terms of combination of electron – electron and electron – magnon scattering

TH-1726_11612111

mechanisms. However for thinner film (30nm), a low temperature upturn in resistivity is seen and is explained by considering the weak localisation effect.

We have also taken up the deposition of bilayer of $La_{0.7}Sr_{0.3}MnO_3$ (LSMO) and $LaFeO_3$ (LFO) on (001) oriented $LaAlO_3$ substrate due to the larger ferromagnetic T_C above room temperature of LSMO and the large Neel temperature (T_N = 745 K) of LFO phase for possible application in room temperature spintronics. Cylindrical bulk targets LSMO and LFO were prepared by the standard sol-gel technique. The XRD pattern of LSMO target shows the single phase rhombohedral structure and was refined by using $R\bar{3}C$ space group. The lattice parameters of bulk LSMO is found to be $a = b = 5.491$Å, and $c = 13.337$ Å. It exhibits ferromagnetic transition at 358 K as per magnetization measurement. The XRD pattern of bulk LFO was found to be in single phase form with orthorhombic crystal structure and was Rietveld refined by choosing Pbnm space group. The lattice parameters of LFO target are $a_1 = 5.555$Å, $b_1 = 5.573$Å and $c_1 = 7.869$Å. As per magnetization measurement at high temperature, it exhibits antiferromagnetic transition with a Neel temperature of 745 K.

We have successfully fabricated c-axis oriented single crystalline bilayer LSMO/LFO films on (001) oriented LAO substrate for different thickness of LSMO layer in the range of 30 nm to 200 nm. Here, the LFO layer thickness was kept fixed at 120 nm. The out-of-plane lattice constant of LSMO layer is found to vary from 3.887Å for t = 30 nm to 3.868 Å for t = 200 nm and it depicts the presence of out-of-plane tensile strain whose value reduces and then relaxed at higher film thickness. Magnetization measurements and analysis show that all bilayered films exhibit ferromagnetic transition with increase in T_C from 290 K to 330 K as the LSMO layer thickness in increased. Enhancement in T_C with film thickness perfectly follows the finite size theory. The saturation magnetization value is increased from 150 emu/cc for 30 nm to 490 emu/cc 200 nm LSMO layer thickness. So, the lattice strain and the AFM LFO layer strongly affect the magnetic properties of LSMO layer especially for lower thickness.

For further understanding the magnetic properties of bilayer films, we have recorded electron magnetic resonance (EMR) spectra and they show presence of ferromagnetic resonance (FMR) in bilayers. The resonance peak shifts towards lower field with increase in film thickness. A double resonance peak is seen when the film is exposed to the perpendicular dc magnetic field. This is due to the existence of two ferromagnetic

TH-1726_11612111

phases which are not clearly resolved for field applied parallel to the films. The anisotropy fields are estimated from the FMR spectra using the relation $[\omega/\gamma]^2 = H_{\parallel}[H_{\parallel}+4\pi M_s - H_a]$ for field applied parallel to the film surface and $\omega/\gamma = [H_{\perp} - (4\pi M_s - H_{a1})]$ for field applied in perpendicular the film surface.

Electrical resistivity data show the metal-insulator transition with its transition temperature T_{MI} increasing from 210 K for bilayer of 30 nm film to 353 K for 60 nm thick film and the remaining films exhibit metallic behaviour up to 400 K. The resistivity data in the metallic region for 30 nm film were analysed in terms of the combination of electron – electron scattering and weak localisation effect. All remaining films were analyzed in terms of electron – electron scattering and electron – Magnon scattering mechanism. Thus the bilayer films of LSMO/LFO with large thickness of LSMO layer shows the metal-insulator and ferromagnetic transition comparable to that of bulk samples.

Future Scope of Studies:

Following are the Future Scope of Studies in the Above Area.

- The bilayer films were studied by only varying the thickness of only the ferromagnetic NSMO or LSMO layers. It would be interesting to study by varying the thickness of antiferromagnetic layer such as NNMO and LFO layers. Moreover, it would be interesting to deposit the FM layers on the substrate followed by capping with AFM layers and study of their electrical and magnetic properties.
- It would be interesting to study the magneto-resistance of bilayer films to look for possible increase in magneto-resistance due to interlayer interaction.
- Moreover, it would be interesting to study the magneto-resistance of bilayer films by applying the fields both parallel and perpendicular to the flow of current.
- It would be also interesting to extend the studies on tri-layer films with two ferromagnetic layers separated by an intermediate anti-ferromagnetic layer.
- Study the magnetic tunnel junction behaviour of the tri-layer films.
- Extending the above bilayer and tri-layer studies by using a hard AFM material. This is expected to yield exchange bias behaviour. In the above prepared samples, we did not observe any exchange bias behaviour.

TH-1726_11612111

References

[1] C. W. Chu, P. H. Hor, R. L. Meng, L. Gao, Z. J. Huang, Wang, and Y. Q. *Phys. Rev. Lett.*, 58(4):405–407, 1987.

[2] S. N. Putilin, E. V. Antipov, O. Chmaissem, and M. Marezio. *Nature*, 362(4):226–228, 1993.

[3] J. G. Bednorz and K. A. Muller. *Z. Phys.*, B64:189–193, 1986.

[4] E. Dagotto, T. Hotta, and A. Moreo. *Phys. Rep.*, 344(1-3):1 – 153, 2001.

[5] J. M. D. Coey, M. Viret, and S. von Molnr. *Advances in Physics*, 48(2):167–293, 1999.

[6] A. P. Ramirez. *J. Phys.: Conden. Matt.*, 9(39):8171, 1997.

[7] Y. Tokura. *Colossal Magnetoresistive Oxides*. Advances in Condensed Matter Science. Taylor & Francis.

[8] C. N. R. Rao and B. Raveau. *Colossal Magnetoresistance, Charge Ordering and Related Properties of Manganese Oxides*. 1998.

[9] Y. Tokura. *Reports on Progress in Physics*, 69(3):797, 2006.

[10]T. A. Ho, N. T. Dang, T.-L. Phan, D. S. Yang, B. W. Lee, and S. C. Yu. *J. Alloys. Comp.*, 676(0):305 – 312, 2016.

[11]G. H. Jonker. *Physica*, 20(7):1118 – 1122, 1954.

[12]J. H. Van Santen and G.H. Jonker. *Physica*, 16(7):599 – 600, 1950.

[13]G. H. Jonker and J. H. Van Santen. *Physica*, 16(3):337 – 349, 1950.

[14]C. Zener. *Phys. Rev.*, 81(0):440–444, 1951.

[15]A. J. Millis, P. B. Littlewood, and B. I. Shraiman. *Phys. Rev. Lett.*, 74(25):5144–5147, 1995.

[16]V. M. Goldschmidt. Oxford University Press. 1958.

[17]J. P. Zhou, J. T. McDevitt, J. S. Zhou, H. Q. Yin, J. B. Goodenough, Y. Gim, and Q. X. Jia. *Appl. Phys. Lett.*, 75(8):1146–1148, 1999.

[18]V. M. Goldschmidt. GeoChemistry, Oxford University Press. 1958.

[19]H. Y. Hwang, S-W. Cheong, P. G. Radaelli, M. Marezio, and B. Batlogg. *Phys. Rev. Lett.*, 75(5):914–917, 1995.

[20]J. P. Zhou, J. T. McDevitt, J. S. Zhou, H. Q. Yin, J. B. Goodenough, Y. Gim, and Q. X. Jia. *Appl. Phys. Lett.*, 75(8):1146–1148, 1999.

[21]Y. Tokura and N. Nagaosa. *Science*, 288(5465):462–468, 2000.

[22]S. Blundell. Oxford Master Series in Condensed Matter Physics. OUP Oxford, 2001.

[23]J. B. Goodenough. *Phys. Rev.*, 100(2):564–573, 1955.

TH-1726_11612111

References

[24]J. Kanamori. *J. Phys. Chem. Solids*, 10(2):87 – 98, 1959.

[25]E. O. Wollan and W. C. Koehler. *Phys. Rev.*, 100(2):545–563, 1955.

[26]C. W. Searle and S. T. Wang. *Can. J. Physics*, 47(23):2703–2708, 1969.

[27]Z. Jirak, S. Vratislav, and J. Zajicek. *physica status solidi (a)*, 52(1):K39–K43, 1979.

[28]E. Pollert, S. Krupicka, and E. Kuzmicova. *J. Phys. Chem. Solids*, 43(12):1137 – 1145, 1982.

[29]C. H. Chen, S-W. Cheong, and A. S. Cooper. *Phys. Rev. Lett.*, 71(15):2461–2464, 1993.

[30]P. D. Battle, T. C. Gibb, and P. Lightfoot. *J. Solid. Stat. Chem.*, 84(2):271 – 279, 1990.

[31]C. H. Chen, S-W. Cheong, and H. Y. Hwang. *J. Appl. Phys.*, 81(8):4326–4330, 1997.

[32]H. Kuwahara, Y. Tomioka, A. Asamitsu, Y. Moritomo, and Y. Tokura. *Science*, 270(5238):961–963, 1995.

[33]Y. Tomioka, A. Asamitsu, Y. Moritomo, H. Kuwahara, and Y. Tokura. *Phys. Rev. Lett.*, 74(0):5108–5111, 1995.

[34]G. Xiao, E. J. McNiff, G. Q. Gong, A. Gupta, C. L. Canedy, and J. Z. Sun. *Phys. Rev. B*, 54(0):6073–6076, 1996.

[35]Y. Moritomo, H. Kuwahara, Y. Tomioka, and Y. Tokura. *Phys. Rev. B*, 55(12):7549–7556, 1997.

[36]V. Kiryukhin, D. Casa, J.P. Hill, B. Keimer, A. Vigliante, and Y. Tomioka, Y.and Tokura. *Nature*, 386(0):813–815, 1997.

[37]S. Parashar, E.E. Ebenso, A.R. Raju, and C.N.R. Rao. *Solid. Stat. Commun.*, 114(5):295 – 299, 2000.

[38]K. Miyano, T. Tanaka, Y. Tomioka, and Y. Tokura. *Phys. Rev. Lett.*, 78(22):4257–4260, 1997.

[39] C. N. R. Rao, A. Arulraj, A. K. Cheetham, and B. Raveau. *J. Phys.: Conden. Matt.*, 12(7):R83, 2000.

[40]J. M. D. Coey, M. Viret, L. Ranno, and K. Ounadjela. *Phys. Rev. Lett.*, 75(21):3910–3913, 1995.

[41]M. Ziese and Ch. Srinitiwarawong. *Phys. Rev. B*, 58(17):11519–11525, 1998.

[42]G. Jakob, W. Westerburg, F. Martin, and H. Adrian. *Phys. Rev. B*, 58(22):14966–14970, 1998.

[43]T. Akimoto, Y. Moritomo, A. Nakamura, and N. Furukawa. *Phys. Rev. Lett.*, 85(18):3914–3917, 2000.

[44]A. Urushibara, Y. Moritomo, T. Arima, A. Asamitsu, G. Kido, and Y. Tokura. *Phys. Rev. B*, 51(20):14103–14109, 1995.

[45]P. Orgiani, C. Adamo, C. Barone, A. Galdi, S. Pagano, A. Yu. Petrov, O. Quaranta, C. Aruta, R. Ciancio, M. Polichetti, D. Zola, and L. Maritato. *J. Appl. Phys.*, 103(9):093902, 2008.

[46]X. Wang and X.-G. Zhang. *Phys. Rev. Lett.*, 82(21):4276–4279, 1999.

TH-1726_11612111

References

[47]D. Schumacher, A. Steffen, J. Voigt, J. Schubert, Th. Brückel, H. Ambaye, and V. Lauter. *Phys. Rev. B*, 88(14):144427, 2013.

[48]Yu. A. Boukov and V. A. Danilov. *Physics of the Solid State*, 50(1):95–100, 2008.

[49]G. J. Snyder, R. Hiskes, S. DiCarolis, M. R. Beasley, and T. H. Geballe. *Phys. Rev. B*, 53:14434–14444, 1996.

[50]K. Kubo and N. Ohata. *J.Phys. Soc. Japan*, 33(1):21–32, 1972.

[51]M. Jaime, P. Lin, M. B. Salamon, and P. D. Han. *Phys. Rev. B*, 58(10):R5901–R5904, 1998.

[52]A. Ettayfi, R. Moubah, E.K. Hlil, S. Colis, M. Lenertz, A. Dinia, and H. Lassri. *J. Magn.Magn. Mater.*, 409(0):34 – 38, 2016.

[53]V. Strbik, B. Blagoev, E. Mateev, and T. Nurgaliev. *J. Phys.: Conf. Series*, 514(0):012042, 2014.

[54]H. Boschker, M. Huijben, A. Vailionis, J. Verbeeck, S. van Aert, M. Luysberg, S. Bals, G. van Tendeloo, E. P. Houwman, G. Koster, D. H. A. Blank, and G. Rijnders. *J. Phys. D: Appl. Phys.*, 44(20):205001, 2011.

[55]Q. X. Zhu, M. Zheng, M. M. Yang, X. M. Li, Y. Wang, X. Shi, H. L. W. Chan, H. S. Luo, X. G. Li, and R. K. Zheng. *Appl. Phys. Lett.*, 103(13):132910, 2013.

[56]P. G. de Gennes. *Phys. Rev.*, 118(1):141–154, 1960.

[57]J. F. Lawler, J. G. Lunney, and J. M. D. Coey. *Appl. Phys. Lett.*, 65(23):3017–3018, 1994.

[58]M. Ohtaki, H. Koga, T. Tokunaga, K. Eguchi, and H. Arai. *J.Solid. Stat. Chem.*, 120(1):105 – 111, 1995.

[59]J. M. D. Teresa, M. R. Ibarra, P. A. Algarabel, C. Ritter, C. Marquina, J. Blasco, J. Garcia, A. del Moral, and Z. Arnold. *Nature*, 386(0):256–259, 1997.

[60]T. T. M. Palstra, A. P. Ramirez, S-W. Cheong, B. R. Zegarski, P. Schiffer, and J. Zaanen. *Phys. Rev. B*, 56(9):5104–5107, 1997.

[61]N.F. Mott. *Conduction in non-crystalline materials*. 2nd edition. Oxford, Oxford university press, 1993.

[62]N.F. Mott. *Metal-Insulator transitions*. 2nd edition. London, Taylor & Francis, 1990.

[63]A. L. Efros and B. I. Shklovskii. *J. Phys. C: Solid. Stat. Phys.*, 8(4):L49, 1975.

[64]Y. Murakami, J. P. Hill, D. Gibbs, M. Blume, I. Koyama, M. Tanaka, H. Kawata, T. Arima, Y. Tokura, K. Hirota, and Y. Endoh. *Phys. Rev. Lett.*, 81(3):582–585, 1998.

[65]I. Dzyaloshinsky. *J. Phys. Chem. Solids.*, 4(4):241 – 255, 1958.

[66]T. Moriya. *Phys. Rev.*, 120(1):91–98, 1960.

[67]J.-P Renard and A Anane. *Mater. Sci. Eng. B*, 63(1):22 – 29, 1999.

TH-1726_11612111

References

[68]V. Skumryev, F. Ott, J. M.D. Coey, A. Anane, J.-P. Renard, L. Pinsard-Gaudart, and A. Revcolevschi. *Eur. Phys. J. B*, 11(3):401–406, 1999.

[69]A. Munoz, J. A. Alonso, M. J. Martinez-Lope, J. L. Garcia-Munoz, and M. T. Fernandez-Diaz. *J. Phys.: Conden. Matt.*, 12(7):1361, 2000.

[70]R. Kajimoto, H. Yoshizawa, H. Kawano, H. Kuwahara, Y. Tokura, K. Ohoyama, and M. Ohashi. *Phys. Rev. B*, 60(13):9506–9517, 1999.

[71]H. Kuwahara, Y. Tomioka, A. Asamitsu, Y. Moritomo, and Y. Tokura. *Science*, 270(5238):961–963, 1995.

[72]Y. Moritomo, T. Akimoto, A. Nakamura, K. Ohoyama, and M. Ohashi. *Phys. Rev. B*, 58(9):5544–5549, 1998.

[73]H. Kawano, R. Kajimoto, H. Yoshizawa, Y. Tomioka, H. Kuwahara, and Y. Tokura. *Phys. Rev. Lett.*, 78(22):4253–4256, 1997.

[74]B. Samantaray and S. Ravi. *J. Superconduct. Novel Magn.*, 24(1):809–814, 2011.

[75]X.J. Liu, E.Y. Jiang, Z.Q. Li, B.L. Li, W.R. Li, A. Yu, P. Wu, and H.L. Bai. *J. Magn.Magn. Mater.*, 305(2):352 – 356, 2006.

[76]X.J. Liu, E.Y. Jiang, Z.Q. Li, B.L. Li, W.R. Li, A. Yu, and H.L. Bai. *Physica B: Conden. Matt.*, 348(1-4):146 – 150, 2004.

[77]B. Samantaray, S. Ravi, A. Das, and S. K. Srivastava. *J. Appl. Phys.*, 110(9):093906, 2011.

[78]Z. Q. Li, H. Liu, X. J. Liu, X.D. Liu, H. L. Bai, C.Q. Sun, and E. Y. Jiang. *J. Magn.Magn. Mater.*, 284(1-3):133 – 139, 2004.

[79]M. Strikovski and J. H. Miller Jr. *Appl. Phys. Lett.*, 73(12):1733–1735, 1998.

[80]Y. Jin, X.-P. Cui, W.-H. Han, S.-X. Cao, Y.-Z. Gao, and J.-C. Zhang. *Phys. Chem. Chem. Phys.*, 17(19):12826–12832, 2015.

[81]Z. Q. Li, Y. Q. Gao, and E. Y. Jiang. *Appl. Phys. Lett.*, 254(21):6959 – 6961, 2008.

[82]K. Chahara, T. Ohno, M. Kasai, and Y. Kozono. *Appl.Phys.Lett.*, 63(14):1990–1992, 1993.

[83]E. S. Vlakhov, R. A. Chakalov, R.I. Chakalova, K. A. Nenkov, K. Dorr, A. Handstein, and K.-H. Muller. *J. Appl. Phys.*, 83(4):2152–2157, 1998.

[84]H. Tanaka and T. Kawai. *Appl. Phys. Lett.*, 76(24):3618–3620, 2000.

[85]J. Klein, C. Hofener, L. Alff, and R. Gross. *J. Magn. Magn. Mater.*, 211(1-3):9 – 15, 2000.

[86]B. Mercey, P. A. Salvador, Ph. Lecoeur, W. Prellier, M. Hervieu, Ch. Simon, D. Chippaux, A. M. Haghiri-Gosnet, and B. Raveau. *J. Appl. Phys.*, 94(4):2716–2724, 2003.

TH-1726_11612111

References

[87]J. Li, C. K. Ong, J.-M. Liu, Q. Huang, and S. J. Wang. *Appl. Phys. Lett.*, 76(8):1051–1053, 2000.

[88]J. Sakai, N. Ito, and S. Imai. *J. Appl. Phys.*, 99(8):08Q318, 2006.

[89]A. S. Ogale, S. R. Shinde, V. N. Kulkarni, J. Higgins, R. J. Choudhary, Darshan C. Kundaliya, T. Polleto, S. B. Ogale, R. L. Greene, and T. Venkatesan. *Phys. Rev. B*, 69(23):235101, 2004.

[90]H. Ni, D. Yu, K. Zhao, Y.-C. Kong, H. K. Wong, S. Q. Zhao, and W. S. Zhang. *J. Appl. Phys.*, 110(3):033112, 2011.

[91]T. Petrisor Jr., M. S. Gabor, A. Boulle, C. Bellouard, C. Tiusan, O. Pana, and T. Petrisor. *J. Appl. Phys.*, 109(12):123913, 2011.

[92]K. Dorr, J. M. De Teresa, K.-H. Muller, D. Eckert, T. Walter, E. Vlakhov, K. Nenkov, and L. Schultz. *J. Phys.: Conden. Matt.*, 12(31):7099, 2000.

[93]S. H. Seo, H. C. Kang, H. W. Jang, and D. Y. Noh. *Phys. Rev. B*, 71:012412, 2005.

[94]D. L. Proffit, H. W. Jang, S. Lee, C. T. Nelson, X. Q. Pan, M. S. Rzchowski, and C. B. Eom. *Appl. Phys. Lett.*, 93(11):111912, 2008.

[95]J. R. Sun, C. F. Yeung, K. Zhao, L. Z. Zhou, C. H. Leung, H. K. Wong, and B. G. Shen. *Appl. Phys. Lett.*, 76(9):1164–1166, 2000.

[96]B. Li, L. Yang, J. Tian, X.P. Wang, H. Zhu, and T. Endo. *J. Appl. Phys.*, 109(7):073922, 2011.

[97]C. Dubourdieu, M. Audier, H. Roussel, J. P. SÃ©nateur, and J. Pierre. *J. Appl. Phys.*, 92(1):379–384, 2002.

[98]P. M. Leufke, A. K. Mishra, A. Beck, D. W., Ch. KÃ¼bel, R. Kruk, and H. Hahn. *Thin Solid Films*, 520(17):5521 – 5527, 2012.

[99]E. Steinbei, K. Steenbeck, T. Eick, and K. Kirsch. *Vacuum*, 58(2-3):135 – 148, 2000.

[100]T. Li, B. Wang, H. Dai, Y. Du, H. Yan, and Yanpin Liu. *J. Appl. Phys.*, 98(12):123505, 2005.

[101]R. P. Borges, W. Guichard, J. G. Lunney, J. M. D. Coey, and F. Ott. *J. Appl. Phys*, 89(7):3868–3873, 2001.

[102]G. C. Xiong, Q. Li, H. L. Ju, S. M. Bhagat, S. E. Lofland, R. L. Greene, and T. Venkatesan. *Appl. Phys. Lett.*, 67(20):3031–3033, 1995.

[103]S. Y. Yang, W. L. Kuang, Y. Liou, W. S. Tse, S. F. Lee, and Y. D. Yao. *J. Magn. Magn. Mater.*, 268(3):326 – 331, 2004.

[104]A. V. Khoryushin, J. E. Mozhaeva, P. B. Mozhaev, V. V. Yurchenko, O. Stupakov, A. V. Pan, C. S. Jacobsen, and J. B. Hansen. *J.Magn. Magn. Mater.*, 333(1-3):53 – 62, 2013.

[105]F. S. Razavi, G. Gross, H.-U. Habermeier, O. Lebedev, S. Amelinckx, G. Van Tendeloo, and A. Vigliante. *Appl. Phys. Lett.*, 76(2):155–157, 2000.

TH-1726_11612111

References

[106]M. Izumi, Y. Konishi, T. Nishihara, S. Hayashi, M. Shinohara, M. Kawasaki, and Y. Tokura. *Appl. Phys. Lett.*, 73(17):2497–2499, 1998.

[107]B. Vengalis, A. Maneikis, F. Anisimovas, R. Butkut, L. Dapkus, and A. Kindurys. *J. Magn. Magn. Mater.*, 211(1-3):35 – 40, 2000.

[108]C. Adamo, X. Ke, H. Q. Wang, H. L. Xin, T. Heeg, M. E. Hawley, W. Zander, J. Schubert, P. Schiffer, D. A. Muller, L. Maritato, and D. G. Schlom. *Appl. Phys. Lett.*, 95(11):112504, 2009.

[109]Y.-M. Kang, A. N. Ulyanov, G.-M. Shin, S.-Y. Lee, D.-G. Yoo, and S.-I. Yoo. *J. Appl. Phys.*, 105(7):07, 2009.

[110]F. Sanchez, I.C. Infante, U. Luders, Ll. Abad, and J. Fontcuberta. *Surf. Sci.*, 600(6):1231 – 1239, 2006.

[111]C. J. Lu, Z. L. Wang, C. Kwon, and Q. X. Jia. *J. Appl. Phys.*, 88(7):4032–4043, 2000.

[112]N. L. Guo, J. Li, Y. F. Wei, Y. Zhang, L. M. Cui, L. Zhao, Y. R. Jin, H. Y. Tian, Hui Deng, G. P. Zhao, and D. N. Zheng. *J. Appl. Phys.*, 112(1):013907, 2012.

[113]V. Stankevic, c. Simkevicius, S. Balevicius, N. Zurauskiene, P. Cimmperman, A. Abrutis, and V. Plausinaitiene. *Thin Solid Films*, 540(0):194 – 201, 2013.

[114]D. Pesquera, G. Herranz, A. Barla, E. Pellegrin, F. Bondino, E. Magnano, F. Sanchez, and J. Fontcuberta. *Nature Comm.*, 3(0):1189, 2012.

[115]S. Jain, H. Sharma, A.K.r Shukla, C.V. Tomy, V.R. Palkar, and A.Tulapurkar. *Physica B: Conden. Matt.*, 448(1):103 – 106, 2014.

[116]D. G. Schlom, L.-Q. Chen, X. Pan, A. Schmehl, and M. A. Zurbuchen. *J. Amer. Ceram. Soc.*, 91(8):2429–2454, 2008.

[117]G. Van Tendeloo, O.I. Lebedev, and S. Amelinckx. *J. Magn. Magn. Mater.*, 211(1-3):73 – 83, 2000.

[118]A. M. Haghiri-Gosnet, J. Wolfman, B. Mercey, Ch. Simon, P. Lecoeur, M. Korzenski, M. Hervieu, R. Desfeux, and G. Baldinozzi. *J. Appl. Phys.*, 88(7):4257–4264, 2000.

[119]B. Wiedenhorst, C. Hofener, Y. Lu, J. Klein, M. S. R Rao, B.H. Freitag, W. Mader, L. Alff, and R. Gross. *J. Magn. Magn. Mater.*, 211(1-3):16 – 21, 2000.

[120]W. Prellier, Ch. Simon, A. M. Haghiri-Gosnet, B. Mercey, and B. Raveau. *Phys. Rev. B*, 62:R16337–R16340, 2000.

[121]A. Barman and G. Koren. *Appl. Phys. Lett.*,77(11):1674–1676, 2000.

[122]Y. Suzuki, Yan Wu, J. Yu, U. Ruediger, A. D. Kent, T. K. Nath, and C. B. Eom. *J. Appl. Phys.*, 87(9):6746–6748, 2000.

[123]F. Tsui, M. C. Smoak, T. K. Nath, and C. B. Eom. *Appl. Phys. Lett.*, 76(17):2421–2423, 2000.

[124]A. J. Millis, T. Darling, and A. Migliori. *J. Appl. Phys.*, 83(3):1588–1591, 1998.

TH-1726_11612111

References

[125]M. Angeloni, G. Balestrino, N. G. Boggio, P. G. Medaglia, P. Orgiani, and A. Tebano. *J. Appl. Phys*, 96(11):6387–6392, 2004.

[126]M. Spankova, A. Rosova, E. Dobrocka, S. Chromik, I. Vavra, V. Strbik, D. Machajdik, A.P. Kobzev, and M. Sojkova. *Thin Solid Films*, 583(0):19 – 24, 2015.

[127]E. Dagotto, T. Hotta, and A. Moreo. *Phys. Rep.*, 344(1-3):1 – 153, 2001.

[128]M. M. Saber, M. Egilmez, F. Schoofs, O. Ofer, M. Mnsson, J. W. A. Robinson, M. Blamire, K. H. Chow, and J. Jung. *Appl. Phys. Lett.*, 100(25):252408, 2012.

[129]Z. Konstantinovic, J. Santiso, D. Colson, A. Forget, Ll. Balcells, and B. Martinez. *J. Appl. Phys.*, 105(6):063919, 2009.

[130]C.M. Xiong, J.R. Sun, and B.G. Shen. *Solid. Stat. Commun.*, 134(7):465 – 469, 2005.

[131]Z.-H. Wang, H. Kronmuller, O. I. Lebedev, G. M. Gross, F. S. Razavi, H. U. Habermeier, and B. G. Shen. *Phys. Rev. B*, 65:054411, 2002.

[132]Q. Qian, T. A. Tyson, C. Dubourdieu, A. Bossak, J. P. SÃ©nateur, M. Deleon, J. Bai, G. Bonfait, and J. Maria. *J. Appl. Phys.*, 92(8):4518–4523, 2002.

[133]M.-H. Jo, N. D. Mathur, Jan E. Evetts, M. G. Blamire, M. Bibes, and J. Fontcuberta. *Appl. Phys. Lett.*, 75(23):3689–3691, 1999.

[134]H. L. Ju, K. M. Krishnan, and D. Lederman. *J. Appl. Phys.*, 83(11):7073–7075, 1998.

[135]D. Dale, A. Fleet, J. D. Brock, and Y. Suzuki. *Appl. Phys.s Lett.*, 82(21):3725–3727, 2003.

[136]H.-D. Zhang, Z.o-J. Li, Y.-Z. Long, H.-W. Xie, B. Sun, H.-B. Lu, and Z.-H. Mai. *J. Crys. Growth.*, 366(0):39 – 42, 2013.

[137]M. Bibes, Ll. Balcells, S. Valencia, J. Fontcuberta, M. Wojcik, E. Jedryka, and S. Nadolski. *Phys. Rev. Lett.*, 87(6):067210, 2001.

[138]M. Bibes, S. Valencia, Ll. Balcells, B. Martnez, J. Fontcuberta, M. Wojcik, S. Nadolski, and E. Jedryka. *Phys. Rev. B*, 66(13):134416, 2002.

[139]A. Gupta and J.Z. Sun. *J. Magn. Magn. Mater.*, 200(1-3):24 – 43, 1999.

[140]F. Tsui, M.C. Smoak, T.K. Nath, and C.B. Eom. *Appl. Phys. Lett.*, 76(17):2421–2423, 2000.

[141]K. Steenbeck, T. Eick, K. Kirsch, K. O Donnell, and E. Steinbei. *Appl. Phys. Lett.*, 71(7):968–970, 1997.

[142]R. B. Praus, B. Leibold, G.M. Gross, and H.-U. Habermeier. *Appl. Surf. Sci.*, 138-139:40 – 43, 1999.

[143]H. W. Zandbergen, S. Freisem, T. Nojima, and J. Aarts. *Phys. Rev. B*, 60(14):10259–10262, 1999.

[144]A. Biswas, M. Rajeswari, R. C. Srivastava, Y. H. Li, T. Venkatesan, R. L. Greene, and A. J. Millis. *Phys. Rev. B*, 61(14):9665–9668, 2000.

TH-1726_11612111

References

[145]J. Zhang, H. Tanaka, T. Kanki, J.-H. Choi, and Tomoji Kawai. *Phys. Rev. B*, 64(18):184404, 2001.

[146]S. Valencia, Ll. Balcells, B. Martinez, and J. Fontcuberta. *J. Appl. Phys*, 93(10):8059–8061, 2003.

[147]J. Dvorak, Y. U. Idzerda, S. B. Ogale, S. Shinde, T. Wu, T. Venkatesan, R. Godfrey, and R. Ramesh. *J. Appl. Phys.*, 97(10):10C102, 2005.

[148]M. Paranjape, J. Mitra, A. K. Raychaudhuri, N. K. Todd, N. D. Mathur, and M. G. Blamire. *Phys. Rev. B*, 68(14):144409, 2003.

[149]D.-W Kim, T.W Noh, H Tanaka, and T Kawai. *Solid. Stat. Commun.*, 125(6):305 – 309, 2003.

[150]H. Kumigashira, D. Kobayashi, R. Hashimoto, A. Chikamatsu, M. Oshima, N. Nakagawa, T. Ohnishi, M. Lippmaa, H. Wadati, A. Fujimori, K. Ono, M. Kawasaki, and H. Koinuma. *Appl. Phys.s Lett.*, 84(26):5353–5355, 2004.

[151]H. Yamada, Y. Ogawa, Y. Ishii, H. Sato, M. Kawasaki, H. Akoh, and Y. Tokura. *Science*, 305(5684):646–648, 2004.

[152]F. Yang, M. Gu, E. Arenholz, N. D. Browning, and Y. Takamura. *J. Appl. Phys.*, 111(1):013911, 2012.

[153]Hans Schmid. *Ferroelectrics*, 161(1):1–28, 1994.

[154]M. Fiebig. *J.f Phys. D: Appl. Phys.*, 38(8):R123, 2005.

[155]W. Eerenstein, N. D. Mathur, and J. F. Scott. *Nature*, 442(7104):759–765, 2006.

[156]L. You, B. Wang, X. Zou, Z. S. Lim, Y. Zhou, H. Ding, L. Chen, and J. Wang. *Phys. Rev. B*, 88(18):184426, 2013.

[157]S. S. Rao, J. T. Prater, Fan Wu, C. T. Shelton, J.-P. Maria, and J. Narayan. *Nano Letters*, 13(12):5814–5821, 2013.

[158]L. W. Martin, Y.-H. Chu, M. B. Holcomb, M. Huijben, P. Yu, S.-J. Han, D. Lee, S. X. Wang, and R. Ramesh. *Nano Letters*, 8(7):2050–2055, 2008.

[159]J. Z. Sun, W. J. Gallagher, P. R. Duncombe, L. Krusin-Elbaum, R. A. Altman, A. Gupta, Yu Lu, G. Q. Gong, and G. Xiao. *Appl. Phys. Lett.*, 69(21):3266–3268, 1996.

[160]M. Wahler, N. Homonnay, T. Richter, A. Muller, C. Eisenschmidt, B. Fuhrmann, and G. Schmidt. *Sci. Rep.s*, 6(0):28727, 2016.

[161]S. M. Wu, Shane A. Cybart, P. Yu, M. D. Rossell, J. X. Zhang, R. Ramesh, and R. C. Dynes. *Nat Mater*, 9(9):756–761, 2010.

[162]T. Li, M. Zhang, B. Wang, and H. Yan. *Solid. Stat. Commun.*, 140(6):289 – 293, 2006.

[163]H. Tanaka and T. Kawai. *J. Appl. Phys.*, 88(3):1559–1565, 2000.

[164]H. Tanaka and T. Kawai. *Solid. Stat. Commun.*, 112(4):201 – 205, 1999.

TH-1726_11612111

References

[165]E. Folven, A. Scholl, A. Young, S. T. Retterer, J. E. Boschker, T. Tybell, Y. Takamura, and J. K. Grepstad. *Phys. Rev. B*, 84(22):220410, 2011.

[166]G. K. Wehner. *Phys. Rev.*, 112(4):1120–1124, 1958.

[167]G. S. Anderson. *J. Appl. Phys.*, 38(4):1607–1611, 1967.

[168]K. Wasa, M. Kitabatake, and H. Adachi. *Thin Film Materials Technology: Sputtering of Compound Materials*. Elsevier Science, 2004.

[169]M. Ohring. *Materials Science of Thin Films*. Elsevier Science, 2001.

[170]B. D. Cullity and S. R. Stock. *Elements of X-ray Diffraction*. Pearson Education, Limited, 2013.

[171]M. Jain, Y. Li, M. F. Hundley, M. Hawley, B. Maiorov, I. H. Campbell, L. Civale, Q. X. Jia, P. Shukla, A. K. Burrell, and T. M. McCleskey. *Appl. Phys. Lett.*, 88(23):232510, 2006.

[172]M. Ziese, H. C. Semmelhack, K. H. Han, S. P. Sena, and H. J. Blythe. *J. Appl. Phys.*, 91(12):9930–9936, 2002.

[173]L. Ranno, A. Llobet, R. Tiron, and E. Favre-Nicolin. *Appl. Surf. Sci.*, 188(1-2):170–175, 2002.

[174]V. B. Podobedov, D. B. Romero, A. Weber, J. P. Rice, R. Schreekala, M. Rajeswari, R. Ramesh, T. Venkatesan, and H. D. Drew. *Appl. Phys. Lett.*, 73(22):3217–3219, 1998.

[175]N. Malde, P. S. I. P. N. de Silva, A. K. M. Akther Hossain, L. F. Cohen, K. A. Thomas, J. L. MacManus-Driscoll, N. D. Mathur, and M. G. Blamire. *Solid. Stat. Commun.*, 105(10):643–648, 1998.

[176]M. Pattabiraman, G. Rangarajan, and P. Murugaraj. *Solid. Stat. Commun.*, 132(1):7 – 11, 2004.

[177]G. Venkataiah and P. Venugopal Reddy. *J. Magn. Magn. Mater.*, 285(3):343 – 352, 2005.

[178]Z. H. Sun, S. Dai, Y. L. Zhou, L. Z. Cao, and Z. H. Chen. *Thin Solid Films*, 516(21):7433 – 7436, 2008.

[179]M. N. Iliev, M. V. Abrashev, H. G. Lee, V. N. Popov, Y. Y. Sun, C. Thomsen, R. L. Meng, and C. W. Chu. *Phys. Rev. B.*, 57(5):2872–2877, 1998.

[180]M. Pattabiraman, G. Rangarajan, K. Y. Choi, P. Lemmens, G. Guentherodt, G. Balakrishnan, D. M. Paul, and M. R. Lees. *Pramana-Journal of Physics*, 58(5-6):1013–1017, 2002.

[181]J. M. De Teresa, M. R. Ibarra, J. Blasco, J. Garcia, C. Marquina, P. A. Algarabel, Z. Arnold, K. Kamenev, C. Ritter, and R. von Helmolt. *Phys. Rev. B.*, 54(2):1187–1193, 1996.

[182]D. K. Paul and S. S. Mitra. *Phys. Rev. Lett.*, 31(16):1000–1003, 1973.

[183]S. El Helali, K. Daoudi, M. Boudard, A. Schulman, C. Acha, H. Roussel, M. Oumezzine, and M. Oueslati. *J. Alloys. Comp.*, 655:327 – 335, 2016.

[184]A. Banerjee, S. Bhattacharya, S. Mollah, H. Sakata, H. D. Yang, and B. K. Chaudhuri. *Phys. Rev. B*, 68(18):186401, 2003.

TH-1726_11612111

References

[185]H. Kronmuller. *IEEE Transactions on Magnetics*, 15(5):1218–1225, 1979.

[186]Y. M. Xiong, T. Chen, G. Y. Wang, X. H. Chen, X. Chen, and C. L. Chen. *Phys. Rev. B*, 70(9):094407, 2004.

[187]D. Mishra, A. Perumal, and A. Srinivasan. *J. Phys. D: Appl. Phys.*, 41(21):215003, 2008.

[188]G. Hadjipanayis, D. J. Sellmyer, and B. Brandt. *Phys. Rev. B*, 23(7):3349–3354, 1981.

[189]C. M. Xiong, J. R. Sun, and B. G. Shen. *Solid State Communications*, 134(7):465 – 469, 2005.

[190]F. Family. *Physica A: Stat. Mech. Appl.*, 168(1):561–580, 1990.

[191]Y.-C. Liang and Y.-C. Liang. *J. Crys.Growth*, 304(0):275 – 280, 2007.

[192]T. L. Phan, N.V. Khiem, N. X. Phuc, and S. C. Yu. *J. Magn. Magn. Mater.*, 304:e334 – e336, 2006.

[193]R. P. Borges, W. Guichard, J. G. Lunney, J. M. D. Coey, and F. Ott. *J. Appl. Phys.*, 89(7):3868–3873, 2001.

[194]B. Samantaray, S.K. Srivastava, and S. Ravi. *J. Magn. Magn. Mater.*, 323(21):2622 – 2626, 2011.

[195]H. Boschker, M. Huijben, A. Vailionis, J.Verbeeck, S. van Aert, M. Luysberg, S. Bals, G. van Tendeloo, E. P. Houwman, G. Koster, D. H. A. Blank, and G. Rijnders. *J. Phys. D: Appl. Phys.*, 44(20):205001, 2011.

[196]X. Y. Xiong, T. R. Finlayson, and B. C. Muddle. *J. Phys. D: Appl. Phys.*, 34(18):2845, 2001.

[197]Y. Suzuki, H. Y. Hwang, S-W. Cheong, and R. B. van Dover. *Appl. Phys. Lett.*, 71(0):140–142, 1997.

[198]M. Jaime, M. B. Salamon, M. Rubinstein, R. E. Treece, J. S. Horwitz, and D. B. Chrisey. *Phys. Rev. B*, 54:11914–11917, 1996.

[199]P. Schiffer, A. P. Ramirez, W. Bao, and S-W. Cheong. *Phys. Rev. Lett.*, 75(18):3336–3339, 1995.

[200]N. Furukawa. *J. Phys. Soc. Japan*, 69(0):1954–1957, 2000.

[201]G. Jeffrey Snyder, Ron Hiskes, Steve DiCarolis, M. R. Beasley, and T. H. Geballe. *Phys. Rev. B*, 53(21):14434–14444, 1996.

[202]P. A. Lee and T. V. Ramakrishnan. *Rev. Mod. Phys.*, 57(2):287–337, 1985.

[203]Y. K. Lakshmi and P. V. Reddy. *J. Magn. Magn. Mater.*, 321(9):1240–1245, 2009.

[204]M. E. Fisher and M. N. Barber. *Phys. Rev. Lett.*, 28(23):1516–1519, 1972.

[205]Y. Tomioka, T. Okuda, Y. Okimoto, A. Asamitsu, H. Kuwahara, and Y. Tokura. *J. Alloys. Comp.*, 326(1-2):27–35, 2001.

[206]H. Kuwahara, Y. Tomioka, A. Asamitsu, Y. Moritomo, and Y. Tokura. *Science*, 270(5238):961–963, 1995.

TH-1726_11612111

References

[207]Y. Tomioka, A. Asamitsu, H. Kuwahara, Y. Moritomo, and Y. Tokura. *Phys. Rev. B.*, 53(4):R1689–R1692, 1996.

[208]M. Tokunaga, N. Miura, Y. Tomioka, and Y. Tokura. *Phys. Rev. B.*, 57(9):5259–5264, 1998.

[209]L. Liu, C.-F. Pai, Y. Li, H. W. Tseng, D. C. Ralph, and R. A. Buhrman. *Science*, 336(6081):555–558, 2012.

[210]J. Hejtmanek, Z. Jirak, J. Sebek, A. Strejc, and M. Hervieu. *J. Appl. Phys.*, 89(11):7413–7415, 2001.

[211]M. Nakamura, Y. Ogimoto, H. Tamaru, Makoto Izumi, and K. Miyano. *Appl. Phys. Lett.*, 86(18):182504, 2005.

[212]W. Prellier, A. M. Haghiri-Gosnet, B. Mercey, Ph. Lecoeur, M. Hervieu, Ch. Simon, and B. Raveau. *Appl. Phys. Lett.*, 77(7):1023–1025, 2000.

[213]T. Elovaara, T. Ahlqvist, S. Majumdar, H. Huhtinen, and P. Paturi. *J. Magn. Magn. Mater.*, 381:194–202, 2015.

[214]A. Asamitsu, Y. Tomioka, H. Kuwahara, and Y. Tokura. *Nature*, 388(6637):50–52, 1997.

[215]W. Prellier, Ch Simon, A. M. Haghiri-Gosnet, B. Mercey, and B. Raveau. *Phys. Rev. B.*, 62(24):R16337–R16340, 2000.

[216]T. Elovaara, H. H., S. Majumdar, and P. Paturi. *Appl. Surf. Sci.*, 381:17–21, 2016.

[217]J. F. Wang and J. Gao. *J. Appl. Phys.*, 109(7):07D708, 2011.

[218]H. Wang, X. Zhang, M. F. Hundley, J. D. Thompson, B. J. Gibbons, Y. Lin, P. N. Arendt, S. R. Foltyn, Q. X. Jia, and J. L. MacManus-Driscoll. *Appl. Phys. Lett.*, 84(7):1147–1149, 2004.

[219]G. C. Xiong, Q. Li, H. L. Ju, S. N. Mao, L. Senapati, X. X. Xi, R. L. Greene, and T. Venkatesan. *Appl. Phys. Lett.*, 66(11):1427–1429, 1995.

[220]J. Laverdiere, S. Jandl, and P. Fournier. *Phys. Rev. B.*, 84(10):104434, 2011.

[221]S. Mukhopadhyay, I. Das, and S. Banerjee. *J. Phys.: Conden. Matt.*, 21:026017, 2009.

[222]B. Samantaray, S. K. Srivastava, and S. Ravi. *J. Magn. Magn. Mater.*, 323(21):2622–2626, 2011.

[223]A. Tatsi, E. L. Papadopoulou, D. Lampakis, E. Liarokapis, W. Prellier, and B. Mercey. *Phys. Rev. B.*, 68(2):024432, 2003.

[224]Y. M. Xiong, T. Chen, G. Y. Wang, X. H. Chen, X. Chen, and C. L. Chen. *Phys. Rev. B.*, 70(9):094407, 2004.

[225]Y. K. Lakshmi, K. Raju, and P. V. Reddy. *J. Appl.Phys.*, 113(16):163701, 2013.

[226]A. Urushibara, Y. Moritomo, T. Arima, A. Asamitsu, G. Kido, and Y. Tokura. *Phys. Rev. B*, 51:14103–14109, 1995.

TH-1726_11612111

References

[227]P. Orgiani, C. Adamo, C. Barone, A. Galdi, S. Pagano, A. Yu. Petrov, O. Quaranta, C. Aruta, R. Ciancio, M. Polichetti, D. Zola, and L. Maritato. *J. Appl. Phys.*, 103(9):093902, 2008.

[228]D. Schumacher, A. Steffen, J. Voigt, J. Schubert, Th. Brückel, H. Ambaye, and V. Lauter. *Phys. Rev. B*, 88:144427, 2013.

[229]S. M. Haidar, Y. Shiomi, J. Lustikova, and E. Saitoh. *Appl. Phys. Lett.*, 107(15):152408, 2015.

[230]S. M. Wu, Shane A. Cybart, P. Yu, M. D. Rossell, J. X. Zhang, R. Ramesh, and R. C. Dynes. *Nat Mater*, 9(9):756–761, 2010.

[231]M. Viret, M. Drouet, J. Nassar, J. P. Contour, C. Fermon, and A. Fert. *Europhys. Lett.*, 39(5):545, 1997.

[232] S. M. Selbach, J. R. Tolchard, A. Fossdal, and T. Grande. *J. Solid. Stat. Chem.*, 196:249 – 254, 2012.

[233]W. C. Koehler and E.O. Wollan. *J. Phys. Chem. Solids.*, 2(2):100 – 106, 1957.

[234]M. Zhang, X. L. Ma, and D. X. Li. *Philosophical Magazine*, 85(15):1625–1636, 2005.

[235]W. Yuan, Y. Zhao, C. Tang, T. Su, Q. Song, J. Shi, and W. Han. *Appl. Phys. Lett.*, 107(2):022404, 2015.

[236]T. X. Li, M. Zhang, F. J. Yu, Z. Hu, K. S. Li, D. B. Yu, and H. Yan. *J. Phys. D: Appl. Phys.*, 45(8):085002, 2012.

[237]C. Chappert, K. Le Dang, P. Beauvillain, H. Hurdequint, and D. Renard. *Phys. Rev. B*, 34(5):3192–3197, 1986.

[238]D. M. Polishchuk, D. I. Pod'yalovskii, A. I. Matviyenko, A. I. Tovstolytkin, M. I. Zakharenko, and M. P. Semen'ko. *J. Magn. Magn. Mater.*, 340(0):109 – 112, 2013.

[239]A. Tozri, J. Khelifi, H. Baaziz, E. Dhahri, and E. K. Hlil. *Materials Letters*, 131:61–63, 2014.

[240]B. Li, H. Zhu, Q. Liu, Z. Liu, and Y. Zhang. *J. Magn. Magn. Mater.*, 366(0):50 – 54, 2014.

[241]S. V. Pietambaram, D. Kumar, R. K. Singh, C. B. Lee, and V. S. Kaushik. *J. Appl. Phys.*, 86(6):3317–3326, 1999.

TH-1726_11612111

List of Publications

Publications in International Journals

1. Structural, optical and magnetic properties of $Nd_{0.7}Sr_{0.3}MnO_3$ thin films.

T.R. Gopalarao, T. Bora, S. Ravi and D. Pamu, Physica Procedia, 54 (2014) 70-74.

2. Effect of post-annealing process on electrical and magnetic properties of $Nd_{0.7}Sr_{0.3}MnO_3$ thin films.

T.R. Gopalarao, S. Ravi and D. Pamu, J. Supercond. Nov. Magn., 28 (2015) 1571-1576.

3. Electrical transport and magnetic properties of epitaxial $Nd_{0.7}Sr_{0.3}MnO_3$ thin films on (001)-oriented $LaAlO_3$ substrate.

T.R. Gopalarao, S. Ravi and D. Pamu, J. Magn. Magn. Mater. 409 (2016) 148-154.

4. Effect of film thin thickness in electrical resistivity and magnetic properties of $Nd_{0.7}Sr_{0.3}MnO_3$ thin films

T.R. Gopalarao, S. Ravi and D. Pamu, J. Supercond. Nov. Magn., 29 (2016) 2567-2572.

5. Effect of film thickness on electrical and magnetic properties of $Nd_{0.8}Na_{0.2}MnO_3$ thin films

T.R. Gopalarao and S. Ravi, J. Supercond. Nov. Magn., 30 (2017) 2465-2470.

6. Magnetic and electrical transport properties of $La_{0.7}Sr_{0.3}MnO_3/LaFeO_3$ bilayer thin films

T.R. Gopalarao, Bibhuti Dash and S. Ravi, J. Magn. Magn. Mater. 441 (2017) 531-536.

7. Study of electrical transport and magnetic properties of $Nd_{0.7}Sr_{0.3}MnO_3$/ $Nd_{0.8}Na_{0.2}MnO_3$ bilayer thin films

T.R. Gopalarao and S. Ravi, J. Supercond. Nov. Magn. 31 (2018) 1149-1154.

TH-1726_11612111

Publications

Conference Presentations

1. Deposition and characterisation of $Nd_{0.7}Sr_{0.3}MnO_3$ thin films

   T.R. Gopalarao, S. Ravi and D. Pamu presented in International Conference on Magnetic Materials and Applications (ICMAGMA-2013) held at IIT Guwahati, Guwahati, during 5th - 7th Dec 2013.

2. Magnetic and electrical properties of $Nd_{0.7}Sr_{0.3}MnO_3$ thin films deposited under different oxygen partial pressures.

   T.R. Gopalarao, S. Ravi and D. Pamu presented in International Conference on Nano Science and Engineering Applications (ICONSEA-2014) held at Jawaharlal Nehru technological University Hyderabad, during 26th-28th Jun 2014.

3. Magnetic and electrical properties of $Nd_{0.7}Sr_{0.3}MnO_3$ thin films upon post-annealing

   T.R. Gopalarao, S. Ravi and D. Pamu presented in International Conference on Magnetic Materials and Applications (ICMAGMA-2014) held at Pondicherry University, Pondicherry, during 15th - 17th Sept 2014.

4. Thickness dependent of electrical and magnetic properties of $Nd_{0.7}Sr_{0.3}MnO_3$ thin films

   T.R. Gopalarao, S. Ravi and D. Pamu presented in International Conference on Magnetic Materials and Applications (ICMAGMA-2015) held at VIT University, Vellore, during 2nd - 4th Dec 2015.

TH-1726_11612111